Politecnico di Torino

ScuDo
Scuola di Dottorato ~ Doctoral School
WHAT YOU ARE, TAKES YOU FAR

Doctoral Dissertation
Doctoral Program in Mechanical Engineering (34th Cycle)

Effects of Non-unique Friction Forces on the Dynamic Behavior of Turbine Bladed Disks with Contact Interfaces

By

Erhan Ferhatoglu

******

Supervisor:
Prof. Stefano Zucca

Doctoral Examination Committee:
Prof. Yevgen Pavlovich Petrov, Referee, University of Sussex, United Kingdom
Prof. Norbert Hoffmann, Referee, Hamburg University of Technology, Germany

Politecnico di Torino
May, 2022

Declaration

I hereby declare that, the contents and organization of this dissertation constitute my own original work and does not compromise in any way the rights of third parties, including those relating to the security of personal data.

Erhan Ferhatoglu

2022

* This dissertation is presented in partial fulfillment of the requirements for **Ph.D. degree** in the Graduate School of Politecnico di Torino (ScuDo).

Acknowledgments

This thesis is the outcome of an exciting journey that would not have been accomplished without the support of many people. I am taking this opportunity to thank those who have contributed to my PhD.

First of all, I am eternally grateful to my supervisor Prof. Stefano Zucca for his excellent guidance and mentorship. He has always given me freedom for what I would like to explore in my direction, while, at the same time prevented me from going astray with his technical expertise. I can never be thankful enough for his supportive, promoting and professional supervision.

I would like to express my sincere appreciation to Prof. Daniele Botto for his advice and help particularly on the experimental stuff. I have gained valuable insights during the development of my test structure with his beneficial comments and suggestions.

I would like to express my deepest gratitude to Prof. Matthew Brake and Prof. Malte Krack for hosting me in the Tribomechadynamics research camp held at Rice University in Houston. It was a fantastic period of time for me, during which I learned new concepts with different perspectives. I also take this opportunity to thank those colleagues and professors from various research groups for the collaboration we performed.

I also would like to thank Dr. Jury Auciello and Dr. Lorenzo Arcangeli for enabling me to become a part of the joint project carried out at Baker Hughes in Florence. I have greatly benefited from their experience while directly working on industrial turbines, which expanded my horizon in my research.

I cannot proceed forward without thanking the present and past members of our research group, AERMEC. I am grateful to all professors and colleagues who helped me to grow in this friendly environment. I will always remember the AERMEC Group as the place where all the past experiences gained within the

group are completely transferred to the future members. Not only did I learn how to carry out a research, but this group enabled me to expand my connections in the structural dynamics community. Thank you all for the great times we had altogether here. It was a pleasure for me to be a part of this family.

I wish to thank my parents and my brother for their unconditional love and endless support that I have always felt deep in my heart. They are the invisible authors of this thesis with what they have done for me throughout my life.

And, my spouse, Azime Burcu; I thank you for your perpetual support, love and patience. I do not have proper words to express my gratitude for all the sacrifices you have made. This journey has become colorful with you. To the new journeys together…

Erhan

May, 2022

Abstract

The mitigation of excessive vibrations is one of the essential design criteria in the turbomachinery applications. To meet this need, friction damping technologies introduce beneficial approaches such as the incorporation of secondary structures into main bodies via contact interfaces. Intentional implementation of friction into systems helps to reduce oscillatory responses; however, it also brings various challenging issues due to the complex physics of the problem accompanied by several uncertainties. In this thesis, one of these uncertainties, which is referred to as the non-uniqueness of contact forces, is addressed on the dynamics of frictionally constrained turbine bladed disks. More specifically, the fundamental mechanism of the nonlinear dynamic response variability is thoroughly elaborated in the context of non-unique static tangential friction forces. On the computational side of the current work, the non-repeatability of the nonlinear vibration behavior while keeping all user-controlled inputs same is first shown on an industrial turbine blade. Two novel approaches are then developed for the determination of nonlinear response boundaries of the variability range. The methods are demonstrated on an academic turbine bladed disk with contacts in the shrouds and blade-disk interfaces, and the results are validated with a test data previously recorded on under-platform dampers. In the experimental portion of the work, a novel test campaign, which aims to reveal the underlying kinematics of the non-unique friction force phenomenon, is designed for one another academic turbine blade coupled with mid-span dampers. It is shown that static force equilibrium achieved on the damper is non-unique, which leads to multiple dynamic response amplitudes, although all the user-controlled inputs are nominally same in the macro scale testing environment. Finally, the variability range measured in the experiments is computationally estimated by using the developed approach. The outcomes of this thesis contribute to the understanding of how non-unique contact forces affect the dynamic behavior of frictionally constrained turbine bladed disks.

Contents

List of Figures

List of Tables

Chapter 1

Introduction

1.1 A Brief Background about the State of the Art

Bladed disks are indispensable components of turbomachines which mostly operate under severe working circumstances. The demand of high performance in the harsh environmental conditions makes them to be driven around their mechanical limits. This is quite relevant from the engineering point of view to improve the efficiency, but this also imposes the bladed disks to undergo high mechanical loads and stresses. During the rotation of turbines, large vibration levels of the blades may trigger high cycle fatigue that may result in unexpected and sudden failures (Cowles, 1996; Srinivasan, 1997). Mitigation of these oscillatory loads is a challenge for the engineers.

Turbine bladed disks may expose to different vibration mechanisms (Krack et al., 2017), where the consideration of all is out of scope in this thesis. One of the most impactful effects on the steady state response can be seen during the resonance of bladed disks due to a periodic forced excitation which is inevitably caused by the pressure inhomogeneity on the blades during the rotation of the rotor hub (Ewins, 2010). This necessitates the modal and frequency response analyses to be performed in the design stage in order to be able to predict vibration levels, hence to stay in the safe zone while the turbine is in service. In case of large amplitudes obtained by analyses, different remedies can be applied.

One of the first solution methods to reduce dynamic response amplitudes is the so-called design iterations which mainly refers to the change of blade's natural frequencies with a design modification in order to avoid resonance regions as much as possible (Seinturier, 2007). Despite the fact that this seems as a straightforward approach, it is not too easy due to the high modal density of bladed disks and the wide spectrum of the external excitation force. In the case of an unavoidable coincidence of resonance frequencies, intentional implementation of additional damping into the system may help to decrease the vibration of the blades.

The use of friction damping technologies plays an important role in the dissipation of excessive energy in turbomachines. Starting from the first studies proposed in 1980s (Griffin, 1980; Menq & Griffin, 1985; Menq et al., 1986), engineers have developed several design solutions to be able to mitigate large oscillatory loads. Some examples are under-platform dampers (Cigeroglu et al., 2009; Denimal et al., 2021; Panning et al., 2004; Sanliturk et al., 2001; Zucca et al., 2013), ring dampers (Laxalde et al., 2010; Tang & Epureanu, 2017), mid-span dampers (Drozdowski et al., 2015; Szwedowicz et al., 2008) or the use of contacts in the shrouds (Mitra et al., 2016; Petrov & Ewins, 2003) and in the blade-disk interfaces (Charleux et al., 2006; Petrov & Ewins, 2006). All of these configurations have been successfully applied in the past and there are always ongoing studies where engineers and researchers always try either to optimize existing topologies or to develop new type of configurations in order to increase reliability with more robust design.

1.2 Problem Statement and Literature Survey

Great success of the friction damping in the reduction of vibration levels has promoted the researchers to further delve into the understanding of the underlying physics of the contacts. For this purpose, the number of experimental and computational studies has increased sharply over the last two decades. However, it has been shown that the nonlinear nature of friction brings various peculiarities and the interpretation of the response behavior is not easy and straightforward.

One interesting feature of the nonlinear response is its variability obtained under the same nominal conditions even if all the user controlled inputs are kept identical. In the literature, to explain the underlying reason of non-repeatable data, some of the tribological studies have studied the effect of asperities (Mulvihill et al., 2011) and roughness (Eriten et al., 2011) of the surfaces. It has been revealed

that the real touching area on the contact pairs has significant importance on the frictional behavior. In some other studies, the variability phenomenon has been associated to several uncertainties present at the contact interfaces (Butlin et al., 2019b; Yuan et al., 2021) or misalignments in the assemblies, manufacturing errors, residual stresses and etc. A detailed study about the observations of variability and repeatability in the frictional structures is performed by Brake et al. (2017). One of the reasons of the response variability comes from the uncertainty of friction forces (Yang & Menq, 1998a, 1998b). According to the Coulomb's friction law, tangential contact force value for a fully stuck contact should always stay within a range whose boundaries are determined by limit values obtained with a multiplication of the surface friction coefficient and the normal force on that surface. This fact generates non-unique tangential forces within a range, where all of the possibilities are true. In addition to this fully stuck interface; if there is at least one another slipping contact in the system, multiple steady state response for totally same system parameters is possible due to interaction between normal and tangential directions. Here, it is worth highlighting that the definition of the term *uncertainty* is slightly ambiguous in the literature. It is used as a very general term to explain different phenomena such as the uncertainty of friction parameters, uncertainties due to wearing in contact surfaces, the uncertainty in the measurements and etc. In this thesis, the *uncertainty* mainly refers to the non-uniqueness of tangential friction forces.

The first examples of non-uniqueness of static contact problem solutions have been attributed to the studies performed in the contact mechanics community (Janovský, 1981; Mitsopoulou & Doudoumis, 1987; Klarbring, 1990). In the structural dynamics community, the uncertainty phenomenon has been first shown analytically by Yang and Menq (1998a, 1998b) on wedge dampers. The authors have reported that non-unique steady state vibration amplitudes exist due to the uncertainty of the contact forces even if all the input parameters are kept same. Detailed investigation has then been performed on under-platform dampers by Zucca et al. (2008) stating different static balance of the damper leads a range of variability in the turbine dynamics. This phenomenon has been shown in many applications in the last decade (Firrone et al., 2011; Zucca et al., 2013; Zucca & Firrone, 2014). Stender et al. (2020) have also very recently shown that co-existing system solutions for friction-induced vibrations result in multiple steady state responses for different initial conditions. Contrarily, most of the time, the researchers in the structural dynamics community have presented their nonlinear response curves in the computational studies, probably unconsciously, as if they

are unique. However, in the literature, various multiple responses have been reported during tests of the same system in different installations (Sever et al., 2008) or frequency sweeps (Claeys et al., 2016). Moreover, recent experimental investigations performed exactly on the same conditions for under-platform dampers (Botto & Umer, 2018; Botto et al., 2018; Gastaldi et al., 2021) have shown that different initial state of the damper in successive tests give rise to a huge variability in vibration amplitudes and resonance frequencies. All these experimental and computational studies prove that the variability phenomenon cannot be ignored. Determination of an upper and a lower boundary of multiple responses may play an important role from an engineering point of view in the dynamic design process, because the turbine components are generally designed with respect to their maximum dynamic amplitudes obtained at resonance frequencies for different excitation levels.

Yang and Menq (1998a, 1998b) have offered an analytical technique for wedge dampers to estimate the highest oscillatory amplitudes. The authors have utilized geometric relations in contact state configurations for the computation of extreme friction forces, where the detailed information can be found in Yang's PhD thesis (1996). However, this approach is developed for a single point contact element at each side of dampers, which makes the method not suitable for the structures undergoing micro slip behavior. Zucca et al. (2013) have also offered a technique to obtain always the same single response curve among an infinite number of options. There are also various studies in the literature, which use statistical and stochastic approaches to be able to predict the response bounds in frictional systems (Butlin et al., 2019a, 2019b; Yuan et al., 2021). However, these studies are not directly relevant to the uncertainty and the variability terms used in the concept of this thesis. On the other hand, besides finding the limits methodically, one can also search for it manually by assigning a set of static displacements as an initial guess. This idea with some filtering algorithm is used by Gastaldi et al. (2021). Despite the simplicity of this approach, its feasibility is quite limited due to high computational burden. In addition, the selected initial set may not become sufficient to be able to capture all potential contact states, which can result to miss correct response boundaries. It should be noted that the state of the art in the literature for variability studies and for the frequency response limits has not reached its maturity level yet.

1.3 Objective and Scope of the Thesis

Structural dynamics community struggles to reasonably explain the non-repeatable response obtained under the same nominal conditions in frictional systems. There may be several reasons for the variation of the data, which is mostly due to an abundant amount of uncertainties present in the contact interfaces. However, in the literature, the amount of studies related to the non-uniqueness of contact forces uncertainty has been very limited, although this phenomenon has been firstly introduced more than two decades ago. Hence, the thesis aims to contribute to this open research area by developing novel techniques and applying them to realistic turbine bladed disks with contact interfaces. In line with this purpose, the following points are the main topics of the current study.

1- It is first aimed to understand and to reveal the underlying physics of the uncertainty phenomenon associated to the non-unique friction forces. Then, the next step is to demonstrate the effects of the uncertainty on the dynamic behavior of an industrial steam turbine bladed disk coupled with mid-span dampers, which is also a part of a joint project to be performed with Baker Hughes Company.

2- It is aimed to develop a numerical method for the applications with wedge dampers to the estimate the response limits among multiple solutions due to the uncertainty phenomenon, and then to show this method on a simple case. Having shown it, the main goal is to develop a generalized numerical method which should be applicable to all types of turbine bladed disks with contacts regardless of the system's complexity, in order to determine the boundaries of the response variability range caused by the uncertainty phenomenon, and to demonstrate the developed method computationally on an academic turbine bladed disk with different types of contacts.

3- It is finally aimed to validate the developed method with experiments. Firstly, the goal is to challenge the method, as a part of a joint project, with an extensive test data obtained previously for an academic turbine blade coupled with under-platform dampers. Having demonstrated it, the second goal is to develop a novel test setup for an academic turbine blade coupled with mid-span dampers and to further study the dynamics of the uncertainty phenomenon with additional test parameters. The final goal is to compare the experimental and computational results.

1.4 Outline of the Thesis

The organization of the thesis chronologically follows the steps performed during the research. It consists of seven chapters, where the first one is the introduction presented here and the rest is outlined as the following.

Chapter 2 gives the numerical background of the forced response determination procedure of tuned bladed disks coupled with contact interfaces. The standard nonlinear analysis is summarized with its all steps, since it can be considered as the main infrastructure of the thesis. The generic behavior of the bladed disk dynamics is illustrated via an industrial steam turbine with mid-span dampers.

Chapter 3 introduces the main concept of the thesis, which is the uncertainty phenomenon associated to the non-uniqueness of friction forces. Its effects on the dynamic behavior are shown via a lumped parameter system which represents a turbomachinery application with a wedge damper pressed against two vibrating adjacent blades. A numerical method is also proposed to determine the response limits of the variability range.

Chapter 4 describes the development of a novel numerical method for the determination of response boundaries in turbine bladed disks with contacts. The method is computationally demonstrated with an academic turbine coupled with different types of frictional interfaces.

Chapter 5 presents a comparison study performed to validate the proposed method with an extensive experimental data. This chapter is a part of a joint project, where the experimental data has been previously collected from an academic turbine blade coupled with under-platform dampers. Computational analyses are done in the scope of the thesis and several cases are shown to challenge the developed method.

Chapter 6 presents the design of a novel test rig to experimentally study the effects of the uncertainty on the dynamics of an academic turbine blade coupled with mid-span dampers. It experimentally unveils the underlying physics of the uncertainty phenomenon via a purposely defined loading procedure and different parameters measured during the tests. In the second part, the computational analyses are performed to see whether the developed method is able to capture the response variability obtained in the experiments.

Chapter 7 is the conclusion and it summarizes the novel parts of the thesis with its contribution to the literature. It also gives a prospective future research direction in the context of the non-uniqueness of friction force uncertainty.

Chapter 2

Forced Response of Tuned Bladed Disks with Contact Interfaces

This chapter[1] presents a general overview about the procedure of the determination of nonlinear response of tuned bladed disks with contact interfaces. All procedure is summarized from the beginning to the end. To illustrate the dynamic behavior of bladed disks with contacts, an industrial application of steam turbines coupled with mid-span dampers is investigated. The first observation of the response variability phenomenon is shown with this case study in the thesis.

2.1 Theoretical Background

Turbine bladed disks are large structures having complex three dimensional shapes with possibly several subcomponents as representatively shown in Figure 1a. It consists of n_s totally identical sectors divided evenly over a 2π angle under the assumption of absence of mistuning effects, i.e. variations of the system properties for each sector. This enables the application of the cyclic symmetry with proper boundary conditions on the sector interfaces. In this way, full bladed disk model can be reduced to a fundamental sector which is an isolated one as representatively shown in Figure 1b. This approach greatly facilitates to deal with

[1] Part of the work described in this chapter has been previously published:
"Ferhatoglu, E., Zucca, S., Botto, D., Auciello, J., & Arcangeli, L. (2022). Nonlinear vibration analysis of turbine bladed disks with midspan dampers. *Journal of Engineering for Gas Turbines and Power*. *144*(4), 041021"

large models with high computational burden. In this thesis, the bladed disk is assumed tuned and all of the theoretical derivations are presented for the fundamental sector.

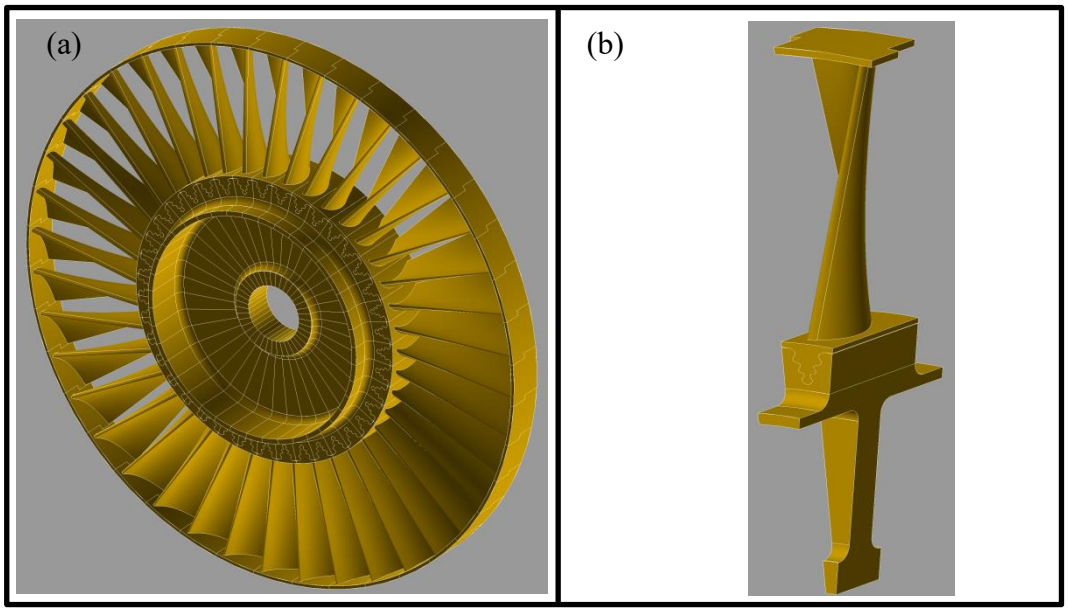

Figure 1: (a) A bladed disk, (b) The fundamental sector

2.1.1 The Governing Equation of Motion

The differential equation of the motion in time domain can be written for the fundamental sector under a periodic excitation as

$$\mathbf{M}\ddot{\mathbf{q}}(t)+\mathbf{C}\dot{\mathbf{q}}(t)+\mathbf{K}\mathbf{q}(t)+\mathbf{f}_n(\mathbf{q},\dot{\mathbf{q}},t)=\mathbf{f}_{ex}(t), \tag{2.1}$$

where $\mathbf{M}$, $\mathbf{C}$ and $\mathbf{K}$ are the mass, viscous damping and stiffness matrices of the linear system, respectively. $\mathbf{q}(t)$ represents the vector of generalized coordinates. $\mathbf{f}_n(\mathbf{q},\dot{\mathbf{q}},t)$ and $\mathbf{f}_{ex}(t)$ are the vector of contact force and the vector of external periodic force, respectively. Dot denotes the derivative with respect to time t.

The turbine bladed disks are subjected to a periodic travelling wave of forcing whose excitation frequencies are the integer multiples of the rotor's angular velocity, Ω. This implies a time delay between adjacent sectors with δt = T/ n_s, where T is the period of the excitation (T = $2\pi/\omega$). $\omega = eo \cdot \Omega$, being eo is the

fundamental engine order of the travelling wave excitation. Periodic excitation force can be decomposed to its harmonic components as

$$\mathbf{f}_{ex}(t) = \Re\left(\sum_{h=0}^{H} \hat{\mathbf{f}}_{ex}^{eo\cdot h} e^{ih\omega t} \right). \tag{2.2}$$

Here, $\hat{\mathbf{f}}_{ex}^{eo\cdot h}$ is the complex amplitude vector of the $eo\cdot h^{th}$ harmonic. H is the number of harmonics considered in the expansion. i represents the imaginary unit number.

In steady state conditions, periodic excitation force determines periodic response and periodic contact forces that can be written as

$$\mathbf{q}(t) = \Re\left(\sum_{h=0}^{H} \hat{\mathbf{q}}^{eo\cdot h} e^{ih\omega t} \right) \quad \text{and} \quad \mathbf{f}_n(t) = \Re\left(\sum_{h=0}^{H} \hat{\mathbf{f}}_n^{eo\cdot h} e^{ih\omega t} \right), \tag{2.3}$$

where $\hat{\mathbf{q}}^{eo\cdot h}$ and $\hat{\mathbf{f}}_n^{eo\cdot h}$ are the complex amplitude vectors of the response and contact forces corresponding to the $eo\cdot h^{th}$ harmonic, respectively. Substitution of Eqs. (2.2) and (2.3) into the Eq. (2.1), the following set of nonlinear algebraic equations in frequency domain can be obtained

$$\left(\mathbf{K}^{eo\cdot h} - (h\omega)^2 \mathbf{M}^{eo\cdot h} + ih\omega \mathbf{C}^{eo\cdot h} \right) \hat{\mathbf{q}}^{eo\cdot h} + \hat{\mathbf{f}}_n^{eo\cdot h} - \hat{\mathbf{f}}_{ex}^{eo\cdot h} = \mathbf{0} \qquad (h = 0, \cdots, H), \tag{2.4}$$

where both the static (h = 0) and the dynamic (h = 1$\cdots H$) balances are coupled to each other through the nonlinear contact forces, $\hat{\mathbf{f}}_n^{eo\cdot h}$, which directly depend on the response of the system, $\hat{\mathbf{q}}^{eo\cdot h}$. In Eq. (2.4), superscript $eo\cdot h^{th}$ referring to system matrices means that cyclic symmetry boundary conditions corresponding to the $eo\cdot h^{th}$ harmonic must be enforced.

2.1.2 Cyclic Symmetry

The complex amplitude vector of the fundamental sector, $\hat{\mathbf{q}}^{eo\cdot h}$, can be separated into three groups as $\hat{\mathbf{q}}^{eo\cdot h} = \left[\left({}_l\hat{\mathbf{q}}^{eo\cdot h} \right)^{\mathrm{T}}, \left({}_i\hat{\mathbf{q}}^{eo\cdot h} \right)^{\mathrm{T}}, \left({}_r\hat{\mathbf{q}}^{eo\cdot h} \right)^{\mathrm{T}} \right]^{\mathrm{T}}$, where superior T is the transpose operator. ${}_l\hat{\mathbf{q}}^{eo\cdot h}$ and ${}_r\hat{\mathbf{q}}^{eo\cdot h}$ are the vector of sector interface degrees of

freedoms lying on the left and right side, respectively, while ${}_i\hat{\mathbf{q}}^{eo\cdot h}$ is the remaining interior nodes, as representatively shown in Figure 2.

It should be noted that ${}_l\hat{\mathbf{q}}^{eo\cdot h}$ and ${}_r\hat{\mathbf{q}}^{eo\cdot h}$ are cyclically symmetric in tuned bladed disks and cyclic symmetry boundary conditions can be imposed to the fundamental sector interfaces as (Petrov, 2004)

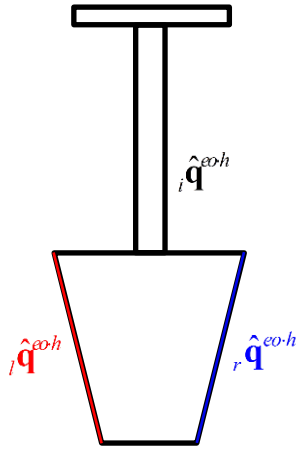

Figure 2 A schematic view of the fundamental sector with the interface and interior degrees of freedoms

$$\hat{\mathbf{q}}^{eo\cdot h}=\begin{Bmatrix}{}_l\hat{\mathbf{q}}^{eo\cdot h}\\ {}_i\hat{\mathbf{q}}^{eo\cdot h}\\ {}_r\hat{\mathbf{q}}^{eo\cdot h}\end{Bmatrix}=\underbrace{\begin{bmatrix}\mathbf{I} & \mathbf{0}\\ \mathbf{0} & \mathbf{I}\\ \mathbf{I}e^{i\varphi eo\cdot h} & \mathbf{0}\end{bmatrix}}_{\mathbf{T}_{\mathrm{CS}}^{eo\cdot h}}\begin{Bmatrix}{}_l\hat{\mathbf{q}}^{eo\cdot h}\\ {}_i\hat{\mathbf{q}}^{eo\cdot h}\end{Bmatrix}, \tag{2.5}$$

where φ is inter-blade phase angle, i.e. $\varphi=2\pi/n_s$. $\mathbf{T}_{\mathrm{CS}}^{eo\cdot h}$ is the transformation matrix and it can be used to obtain cyclically symmetric system matrices, which is given in Eq. (2.4), as

$$\mathbf{K}^{eo\cdot h}=\left(\mathbf{T}_{\mathrm{CS}}^{eo\cdot h}\right)^{*}\mathbf{K}\,\mathbf{T}_{\mathrm{CS}}^{eo\cdot h},\quad \mathbf{M}^{eo\cdot h}=\left(\mathbf{T}_{\mathrm{CS}}^{eo\cdot h}\right)^{*}\mathbf{M}\,\mathbf{T}_{\mathrm{CS}}^{eo\cdot h},\quad \mathbf{C}^{eo\cdot h}=\left(\mathbf{T}_{\mathrm{CS}}^{eo\cdot h}\right)^{*}\mathbf{C}\,\mathbf{T}_{\mathrm{CS}}^{eo\cdot h}, \tag{2.6}$$

where superscript * is the Hermitian conjugate operator.

2.1.3 Reduced Order Modeling

The use of cyclic symmetry largely reduces the size of the models; however, the number of Degrees of Freedoms (DOFs) even for one sector may be unmanageably large and needs to be decreased. Component Mode Synthesis techniques are extensively used to further reduce the model order to a reasonable level. In this thesis, the Craig-Bampton approach (Craig & Bampton, 1968) is used.

In this technique, the DOFs of the fundamental sector are split into two categories as $\hat{\mathbf{q}}^{eo\cdot h}=\left[\left(\hat{\mathbf{q}}_m^{eo\cdot h}\right)^{\mathrm{T}},\left(\hat{\mathbf{q}}_s^{eo\cdot h}\right)^{\mathrm{T}}\right]^{\mathrm{T}}$, where subscripts m and s refer to the master and slave coordinates, respectively. Here, the retained coordinates in the reduced order model are the master ones and they are selected as the contact, external force and response monitoring DOFs, while the rest in the full system is the slave coordinates. To find a relation between the master and slave coordinates for the transformation matrix, consider the governing equations by partitioning Eq.(2.4) with respect to the master and slave coordinates as

$$\left(\begin{bmatrix}\mathbf{K}_{mm}^{eo\cdot h} & \mathbf{K}_{ms}^{eo\cdot h}\\ \mathbf{K}_{sm}^{eo\cdot h} & \mathbf{K}_{ss}^{eo\cdot h}\end{bmatrix}-(h\omega)^2\begin{bmatrix}\mathbf{M}_{mm}^{eo\cdot h} & \mathbf{M}_{ms}^{eo\cdot h}\\ \mathbf{M}_{sm}^{eo\cdot h} & \mathbf{M}_{ss}^{eo\cdot h}\end{bmatrix}+ih\omega\begin{bmatrix}\mathbf{C}_{mm}^{eo\cdot h} & \mathbf{C}_{ms}^{eo\cdot h}\\ \mathbf{C}_{sm}^{eo\cdot h} & \mathbf{C}_{ss}^{eo\cdot h}\end{bmatrix}\right)\begin{Bmatrix}\hat{\mathbf{q}}_m^{eo\cdot h}\\ \hat{\mathbf{q}}_s^{eo\cdot h}\end{Bmatrix}+\begin{Bmatrix}\hat{\mathbf{f}}_{n,m}^{eo\cdot h}-\hat{\mathbf{f}}_{ex,m}^{eo\cdot h}\\ \mathbf{0}\end{Bmatrix}=\mathbf{0}. \tag{2.7}$$

The transformation matrix is constructed with two consecutive steps. First, the static relation between the master and slave coordinates is obtained by neglecting the inertial and damping forces. This is done by considering the second row of Eq. (2.7) that can be written as

$$\mathbf{K}_{sm}^{eo\cdot h}\hat{\mathbf{q}}_m^{eo\cdot h}+\mathbf{K}_{ss}^{eo\cdot h}\hat{\mathbf{q}}_s^{eo\cdot h}=\mathbf{0}, \tag{2.8}$$

which yields

$$\hat{\mathbf{q}}_s^{eo\cdot h}=\underbrace{-\left(\mathbf{K}_{ss}^{eo\cdot h}\right)^{-1}\mathbf{K}_{sm}^{eo\cdot h}}_{\boldsymbol{\Psi}_{sm}^{eo\cdot h}}\hat{\mathbf{q}}_m^{eo\cdot h}\ . \tag{2.9}$$

$\boldsymbol{\Psi}_{sm}^{eo\cdot h}$ is a matrix and its each vector is called as the constraint modes. A constrained mode is physically defined as the static deformation shape of the slave

coordinates due to a unit displacement applied to one of the master DOFs, while the rest of master DOFs is fixed and no force is applied to the slave DOFs.

The second step for the transformation matrix is the dynamic condensation. This is obtained by projecting the physical slave coordinates, $\hat{\mathbf{q}}_s^{eo\cdot h}$, to a set of modal coordinates, $\boldsymbol{\eta}_s^{eo\cdot h}$, by assuming the master DOFs are fixed. This is done in order to express the dynamic motion of the slave DOFs with its modal model which is much smaller than its spatial model. Eigenvalue problem can be obtained as

$$\mathbf{K}_{ss}^{eo\cdot h}\boldsymbol{\Phi}_{ss}^{eo\cdot h} = \boldsymbol{\lambda}_{ss}^{eo\cdot h}\mathbf{M}_{ss}^{eo\cdot h}\boldsymbol{\Phi}_{ss}^{eo\cdot h}. \tag{2.10}$$

Here, $\boldsymbol{\lambda}_{ss}^{eo\cdot h}$ and $\boldsymbol{\Phi}_{ss}^{eo\cdot h}$ are the matrices of square of the natural frequencies and the mode shapes, respectively. Dynamic part of $\hat{\mathbf{q}}_s^{eo\cdot h}$ can be written as a superposition of the mode shapes as

$$\hat{\mathbf{q}}_s^{eo\cdot h} = \boldsymbol{\Phi}_{ss}^{eo\cdot h}\boldsymbol{\eta}_s^{eo\cdot h}. \tag{2.11}$$

Then the full relation between master and slave coordinates can be written by using the constrained modes and the fixed interface mode shapes as

$$\hat{\mathbf{q}}_s^{eo\cdot h} = \boldsymbol{\psi}_{sm}^{eo\cdot h}\hat{\mathbf{q}}_m^{eo\cdot h} + \boldsymbol{\Phi}_{ss}^{eo\cdot h}\boldsymbol{\eta}_s^{eo\cdot h}. \tag{2.12}$$

This helps to create the transformation matrix, $\mathbf{T}_{\mathrm{CB}}^{eo\cdot h}$, as follows

$$\hat{\mathbf{q}}^{eo\cdot h} = \begin{Bmatrix} \hat{\mathbf{q}}_m^{eo\cdot h} \\ \hat{\mathbf{q}}_s^{eo\cdot h} \end{Bmatrix} = \underbrace{\begin{bmatrix} \mathbf{I} & \mathbf{0} \\ \boldsymbol{\psi}_{sm}^{eo\cdot h} & \boldsymbol{\Phi}_{ss}^{eo\cdot h} \end{bmatrix}}_{\mathbf{T}_{\mathrm{CB}}^{eo\cdot h}} \underbrace{\begin{Bmatrix} \hat{\mathbf{q}}_m^{eo\cdot h} \\ \boldsymbol{\eta}_s^{eo\cdot h} \end{Bmatrix}}_{\hat{\mathbf{q}}_{\mathrm{CB}}^{eo\cdot h}}. \tag{2.13}$$

Here, the physical master DOFs are completely retained and no reduction is performed on them. The main reduction comes from the slave coordinates. They are projected to their modal coordinates which is now included to the physical master DOFs as the second set of modal master nodes.

The system matrices of the reduced order model can also be obtained as

$$\begin{aligned}\mathbf{K}_{\mathrm{CB}}^{eo\cdot h} &= \left(\mathbf{T}_{\mathrm{CB}}^{eo\cdot h}\right)^{*} \mathbf{K}^{eo\cdot h}\, \mathbf{T}_{\mathrm{CB}}^{eo\cdot h} \\ \mathbf{M}_{\mathrm{CB}}^{eo\cdot h} &= \left(\mathbf{T}_{\mathrm{CB}}^{eo\cdot h}\right)^{*} \mathbf{M}^{eo\cdot h}\, \mathbf{T}_{\mathrm{CB}}^{eo\cdot h} \\ \mathbf{C}_{\mathrm{CB}}^{eo\cdot h} &= \left(\mathbf{T}_{\mathrm{CB}}^{eo\cdot h}\right)^{*} \mathbf{C}^{eo\cdot h}\, \mathbf{T}_{\mathrm{CB}}^{eo\cdot h}\end{aligned} \quad . \tag{2.14}$$

It should be noted that Eq. (2.4) now refers to DOFs of the reduced order model, but the subscript CB will be omitted and the same notation will be kept in the rest of the paper for clarity.

2.1.4 Contact Elements and Computation of Contact Forces

In the turbomachinery field, contact interfaces on the bladed disks are widely modeled with contacts elements. In this thesis, the model attributed to Jenkins (1962), as representatively shown in Figure 3, is utilized to represent the contact behavior. The contact element has a tangential and a normal direction perpendicular to each other, in which the contact forces are generated as Tangential Force, *T,* and Normal Force, *N*, respectively. A slider in tangential direction is used to pair the contact points. The local contact stiffness of the touching points is simulated using two linear springs, with the stiffness values of k_t and k_n, employing in tangential and normal directions, respectively.

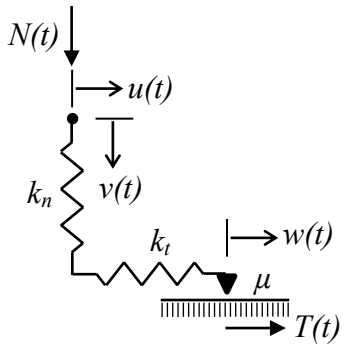

Figure 3: Contact element

The Coulomb friction law states that Tangential Force, *T(t)*, must be equal or lower than the limit value of $\mu N(t)$, being μ the friction coefficient, when the slider sticks. It starts slipping with respect to the ground with an amount of slip motion, *w(t),* when tangential force exceeds the limit value. The periodic relative tangential displacement, *u(t)*, and the periodic relative normal displacement, *v(t)*, of contact points determine the tangential and the normal forces for each contact

element. The normal and the tangential contact forces at time t is defined as follows

$$N(t) = \max\left(k_n v(t), 0\right) \quad , \quad T\left(t\right) = \begin{cases} k_t\left[u(t) - w(t)\right] & \text{stick state} \\ \mu N(t)\text{sign}\left(\dot{w}(t)\right) & \text{slip state} \\ 0 & \text{lift-off state} \end{cases} . \quad (2.15)$$

It can be seen from Eq. (2.15) that contact element is separated in case of negative relative normal displacements, due to the unilateral boundary condition at the contact point. It should be noted that the position of the slider at the stick state, *w(t)*, for a specific time instant t is an unknown parameter in advance. This prevents the direct computation of *T(t)*. To overcome this uncertainty, a four step predictor-corrector approach (Siewert et al., 2010) is followed in the calculation procedure as follows;

1- The contact is initially assumed in the stick state at time t regardless of its actual condition.

2- The value of the tangential force is estimated by using an arbitrary slip motion value, *w(t)*. One of the best alternatives for *w(t)* is the one computed at the previous time step, $w(t - \Delta t)$. Hence, the tangential force is predicted as follows

$$T^P(t) = k_t\left[u(t) - w^P(t)\right] = k_t\left[u(t) - w(t - \Delta t)\right]. \quad (2.16)$$

Here, $T^P(t)$ and $w^P(t)$ represent the predicted values of the tangential contact force and slip motion at time t, respectively. Δt is the time step.

3- The assumption of the step 1 is checked by comparing the value of the predicted tangential force with the limit value, $\mu N(t)$.

-The assumption becomes correct, if $T^P(t) \leq \mu N(t)$. This means that the predicted value in the step 2 is true.

- The assumption becomes wrong, if $T^P(t) > \mu N(t)$, i.e. the actual contact state is slip, as long as there is no lift-off.

4- The tangential force and the slip motion is then obtained as

$$T(t)=\begin{cases} T^{P}(t) & \text{stick state} \\ \mu N(t)\,\text{sign}\left(T^{P}(t)\right) & \text{slip state} \\ 0 & \text{lift-off state} \end{cases}$$
$$w(t)=\begin{cases} w(t-\Delta t) & \text{stick state} \\ u(t)-\mu N(t)\,\text{sign}\left(T(t)\right)/k_t & \text{slip state} \\ u(t) & \text{lift-off state} \end{cases} \quad . \tag{2.17}$$

Contact force values calculated by Eq. (2.15) are still in time domain and they are converted to the frequency domain with the Alternating Frequency/Time algorithm developed by Cameron and Griffin (1989). In this approach, time domain nonlinear responses, $\mathbf{q}(t)$, are first obtained by performing Inverse Fast Fourier Transform (IFFT) to Fourier coefficients, $\hat{\mathbf{q}}^{eo\cdot h}$. Nonlinear contact forces, $\mathbf{f}_n(t)$, are then calculated by using Eq (2.15). Lastly, the forces computed in time domain are transformed back to frequency domain by applying Fast Fourier Transform (FFT) to obtain complex amplitudes, $\hat{\mathbf{f}}_n^{eo\cdot h}$.The procedure is also summarized schematically in Figure 4.

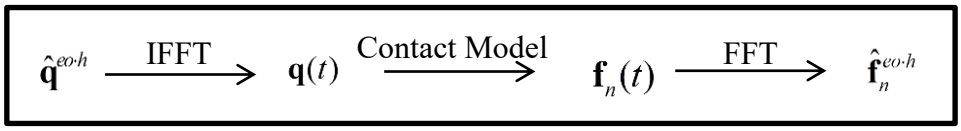

Figure 4: Alternating Frequency/Time approach

2.1.5 Receptance Notation and Partitioning of the Equations

Eq. (2.4) consists of system matrices whose inverse is needed in the solution process. This makes the computational burden one of the major problems, since the inverse operation at each iteration may take a large amount of time. Fortunately, a relieve may be possible with the use of receptance notation and by re-ordering the linear and nonlinear DOFs. However, it should be noted that the receptance cannot be defined for the 0^{th} harmonic of the balance equations, if there is a free body in the system, such as under-platform dampers. To bypass this problem, the system matrices for the 0^{th} harmonic are left as they are and receptance notation can be applied for the dynamic parts as

$$\begin{aligned} \mathbf{K}^0\hat{\mathbf{q}}^0 + \hat{\mathbf{f}}_n^0 - \hat{\mathbf{f}}_{ex}^0 &= \mathbf{0} \\ \hat{\mathbf{q}}^{eo\cdot h} + \boldsymbol{\alpha}^{eo\cdot h}\hat{\mathbf{f}}_n^{eo\cdot h} - \boldsymbol{\alpha}^{eo\cdot h}\hat{\mathbf{f}}_{ex}^{eo\cdot h} &= \mathbf{0} \quad \left(h = 1,\cdots,H\right) \end{aligned}. \tag{2.18}$$

Here, $\boldsymbol{\alpha}^{eo\cdot h}$ is the receptance matrix corresponding to the $eo\cdot h^{th}$ harmonics and can be calculated without performing any inverse operation as

$$\boldsymbol{\alpha}^{eo\cdot h} = \sum_{r=1}^{N_m} \frac{\phi_r^{eo\cdot h}\left(\phi_r^{eo\cdot h}\right)^*}{\left(\omega_r^{eo\cdot h}\right)^2 - h^2\omega^2 + i2\xi_r^{eo\cdot h}h\omega\omega_r^{eo\cdot h}}. \tag{2.19}$$

In Eq. (2.19), $\phi_r^{eo\cdot h}$, $\omega_r^{eo\cdot h}$ and $\xi_r^{eo\cdot h}$ represent the mode shape, natural frequency and the damping ratio for the r^{th} mode corresponding to the $eo\cdot h^{th}$ harmonics, respectively. N_m denotes the number of modes considered in the expansion and it is equal to the number of DOFs of the reduced order model.

The contact forces also only depend on the nonlinear DOFs. Thus, Eq. (2.18) can be partitioned by linear (with subscription l) and nonlinear (with subscription n) DOFs as

$$\begin{aligned} \begin{bmatrix} \mathbf{K}_{ll}^0 & \mathbf{K}_{ln}^0 \\ \mathbf{K}_{nl}^0 & \mathbf{K}_{nn}^0 \end{bmatrix}\begin{Bmatrix} \hat{\mathbf{q}}_l^0 \\ \hat{\mathbf{q}}_n^0 \end{Bmatrix} + \begin{Bmatrix} \mathbf{0} \\ \hat{\mathbf{f}}_n^0 \end{Bmatrix} - \begin{Bmatrix} \hat{\mathbf{f}}_{ex,l}^0 \\ \hat{\mathbf{f}}_{ex,n}^0 \end{Bmatrix} &= \mathbf{0} \\ \begin{Bmatrix} \hat{\mathbf{q}}_l^{eo\cdot h} \\ \hat{\mathbf{q}}_n^{eo\cdot h} \end{Bmatrix} + \begin{bmatrix} \boldsymbol{\alpha}_{ll}^{eo\cdot h} & \boldsymbol{\alpha}_{ln}^{eo\cdot h} \\ \boldsymbol{\alpha}_{nl}^{eo\cdot h} & \boldsymbol{\alpha}_{nn}^{eo\cdot h} \end{bmatrix}\begin{Bmatrix} \mathbf{0} \\ \hat{\mathbf{f}}_n^{eo\cdot h} \end{Bmatrix} - \begin{bmatrix} \boldsymbol{\alpha}_{ll}^{eo\cdot h} & \boldsymbol{\alpha}_{ln}^{eo\cdot h} \\ \boldsymbol{\alpha}_{nl}^{eo\cdot h} & \boldsymbol{\alpha}_{nn}^{eo\cdot h} \end{bmatrix}\begin{Bmatrix} \hat{\mathbf{f}}_{ex,l}^{eo\cdot h} \\ \hat{\mathbf{f}}_{ex,n}^{eo\cdot h} \end{Bmatrix} &= \mathbf{0} \quad \left(h = 1,\cdots,H\right) \end{aligned}. \tag{2.20}$$

After separating the linear and nonlinear DOFs, the first set of equations can be utilized to define linear DOFs as

$$\begin{aligned} \hat{\mathbf{q}}_l^0 &= \left(\mathbf{K}_{ll}^0\right)^{-1}\left(\hat{\mathbf{f}}_{ex,l}^0 - \mathbf{K}_{ln}^0\hat{\mathbf{q}}_n^0\right) \\ \hat{\mathbf{q}}_l^{eo\cdot h} &= \boldsymbol{\alpha}_{ll}^{eo\cdot h}\hat{\mathbf{f}}_{ex,l}^{eo\cdot h} + \boldsymbol{\alpha}_{ln}^{eo\cdot h}\left(\hat{\mathbf{f}}_{ex,n}^{eo\cdot h} - \hat{\mathbf{f}}_n^{eo\cdot h}\right) \quad \left(h = 1,\cdots,H\right) \end{aligned}, \tag{2.21}$$

and then the final set of equations to be solved iteratively can be written for the nonlinear DOFs as

$$\begin{aligned}\left(\mathbf{K}_{nn}^{0}-\mathbf{K}_{nl}^{0}\left(\mathbf{K}_{ll}^{0}\right)^{-1}\mathbf{K}_{ln}^{0}\right)\hat{\mathbf{q}}_{n}^{0}+\mathbf{K}_{nl}^{0}\left(\mathbf{K}_{ll}^{0}\right)^{-1}\hat{\mathbf{f}}_{ex,l}^{0}+\hat{\mathbf{f}}_{n}^{0}-\hat{\mathbf{f}}_{ex,n}^{0}=\mathbf{0}\\ \hat{\mathbf{q}}_{n}^{eo\cdot h}+\boldsymbol{\alpha}_{nn}^{eo\cdot h}\left(\hat{\mathbf{f}}_{n}^{eo\cdot h}-\hat{\mathbf{f}}_{ex,n}^{eo\cdot h}\right)-\boldsymbol{\alpha}_{nl}^{eo\cdot h}\hat{\mathbf{f}}_{ex,l}^{eo\cdot h}=\mathbf{0}\quad\left(h=1,\cdots,H\right)\end{aligned} \tag{2.22}$$

After obtaining the unknown response vector for nonlinear DOFs from Eq. (2.22), the response of linear DOFs can be easily obtained with Eq. (2.21) without performing any iteration.

It should be noted that leaving the system matrices in the equation set is suitable for the systems including free bodies. Although the above procedure is applicable also for the systems, in which the frictional interfaces are present on fixed structures such as shrouded frictional contacts, the inverse of the 0^{th} harmonic matrices can be taken for these systems. Hence, the receptance notation is applicable for the 0^{th} harmonic for constrained systems, as well.

2.1.6 Solution Procedure

In this thesis, the coupled set of Eq. (2.22) is solved simultaneously by using Newton-Raphson method with pseudo Arc-length Continuation (Chan & Keller, 1982). However, it should be noted that $\hat{\mathbf{q}}^{eo\cdot h}$, $\boldsymbol{\alpha}^{eo\cdot h}$, $\hat{\mathbf{f}}^{eo\cdot h}$ and $\hat{\mathbf{f}}_{ex}^{eo\cdot h}$ are complex quantities for $h \geq 1$, hence the set should be re-written with the real and imaginary parts as

$$\begin{aligned}&\left(\mathbf{K}_{nn}^{0}-\mathbf{K}_{nl}^{0}\left(\mathbf{K}_{ll}^{0}\right)^{-1}\mathbf{K}_{ln}^{0}\right)\hat{\mathbf{q}}_{n}^{0}+\mathbf{K}_{nl}^{0}\left(\mathbf{K}_{ll}^{0}\right)^{-1}\hat{\mathbf{f}}_{ex,l}^{0}+\hat{\mathbf{f}}_{n}^{0}-\hat{\mathbf{f}}_{ex,n}^{0}=\mathbf{0}\\ &\begin{Bmatrix}\Re\left(\hat{\mathbf{q}}_{n}^{eo\cdot h}\right)\\ \Im\left(\hat{\mathbf{q}}_{n}^{eo\cdot h}\right)\end{Bmatrix}+\begin{bmatrix}\Re\left(\boldsymbol{\alpha}_{nn}^{eo\cdot h}\right) & -\Im\left(\boldsymbol{\alpha}_{nn}^{eo\cdot h}\right)\\ \Im\left(\boldsymbol{\alpha}_{nn}^{eo\cdot h}\right) & \Re\left(\boldsymbol{\alpha}_{nn}^{eo\cdot h}\right)\end{bmatrix}\begin{Bmatrix}\Re\left(\hat{\mathbf{f}}_{n}^{eo\cdot h}-\hat{\mathbf{f}}_{ex,n}^{eo\cdot h}\right)\\ \Im\left(\hat{\mathbf{f}}_{n}^{eo\cdot h}-\hat{\mathbf{f}}_{ex,n}^{eo\cdot h}\right)\end{Bmatrix}+\\ &\qquad-\begin{bmatrix}\Re\left(\boldsymbol{\alpha}_{nl}^{eo\cdot h}\right) & -\Im\left(\boldsymbol{\alpha}_{nl}^{eo\cdot h}\right)\\ \Im\left(\boldsymbol{\alpha}_{nl}^{eo\cdot h}\right) & \Re\left(\boldsymbol{\alpha}_{nl}^{eo\cdot h}\right)\end{bmatrix}\begin{Bmatrix}\Re\left(\hat{\mathbf{f}}_{ex,l}^{eo\cdot h}\right)\\ \Im\left(\hat{\mathbf{f}}_{ex,l}^{eo\cdot h}\right)\end{Bmatrix}=\mathbf{0}\quad\left(h=1,\cdots,H\right)\end{aligned} \tag{2.23}$$

In this approach, frequency is also another unknown in addition to the nonlinear DOFs. The main aim is to make the residual of Eq. (2.23) is zero, which can be written as

$$\mathbf{R}\left(\Re\left(\hat{\mathbf{q}}_{n}^{eo\cdot h}\right),\Im\left(\hat{\mathbf{q}}_{n}^{eo\cdot h}\right),\omega\right)=\mathbf{0}\qquad\left(h=0,\cdots,H\right), \tag{2.24}$$

where $\Im\left(\hat{\mathbf{q}}_n^0\right)=0$. It is also worth noting that the residual of the 0th harmonic should be normalized in order not to face a convergence problem. This is necessary, because the residual of the 0th harmonic is defined in terms of force, while the one for the $eo\cdot h^{th}$ harmonics is in terms of displacement. Eventually, the residual can be written in the following form as

$$\mathbf{R}=[R^0,\Re(R^1),\Im(R^1),\cdots,\Re(R^H),\Im(R^H)]^{\mathrm{T}} \quad . \tag{2.25}$$

Iterative formula for the current solution point is then written as

$${}_{j+1}\mathbf{Y}={}_{j}\mathbf{Y}-\begin{bmatrix}\dfrac{\partial\mathbf{R}({}_{j}\mathbf{Y})}{\partial_{j}\hat{\mathbf{q}}_n^{eo\cdot h}} & \dfrac{\partial\mathbf{R}({}_{j}\mathbf{Y})}{\partial_{j}\omega}\\ \dfrac{\partial\mathbf{h}({}_{j}\mathbf{Y})}{\partial_{j}\hat{\mathbf{q}}_n^{eo\cdot h}} & \dfrac{\partial\mathbf{h}({}_{j}\mathbf{Y})}{\partial_{j}\omega}\end{bmatrix}^{-1}\times\begin{Bmatrix}\mathbf{R}({}_{j}\mathbf{Y})\\ \mathbf{h}({}_{j}\mathbf{Y})\end{Bmatrix}, \tag{2.26}$$

where

$${}_{j}\mathbf{Y}=\begin{Bmatrix}{}_{j}\hat{\mathbf{q}}_n^{eo\cdot h}\\ {}_{j}\omega\end{Bmatrix} \quad \text{and} \quad \mathbf{h}({}_{j}\mathbf{Y})=\mathbf{Z}^T(\mathbf{Y}_p-{}_{j}\mathbf{Y}). \tag{2.27}$$

Here, subscript j, $\mathbf{Z}$ and $\mathbf{Y}_p$ represent the iteration number, the unit vector tangent to the solution curve and predicted unknown vector before starting iterations, respectively. $\mathbf{Y}_p$ can be estimated as

$$\mathbf{Y}_p=\mathbf{Y}_k+s\mathbf{Z}. \tag{2.28}$$

In Eq.(2.28), $\mathbf{Y}_k$ and s represent the response vector converged at the previous solution point and the scalar arc-length parameter value that controls the length of the predictor, respectively.

In the computation of the jacobian matrix, the partial derivatives of contact forces with respect to the generalized coordinates can be written as follows

$$\frac{\partial \hat{\mathbf{f}}_n^{eo\cdot h}}{\partial \hat{\mathbf{q}}_n^{eo\cdot h}} = \begin{bmatrix} \mathbf{D}^{0,0} & \mathbf{D}^{0,1} & \cdots & \mathbf{D}^{0,H} \\ \mathbf{D}^{1,0} & \mathbf{D}^{1,1} & \cdots & \mathbf{D}^{1,H} \\ \cdots & \cdots & \cdots & \cdots \\ \mathbf{D}^{H,0} & \mathbf{D}^{H,1} & \cdots & \mathbf{D}^{H,H} \end{bmatrix}, \tag{2.29}$$

where

$$\mathbf{D}^{0,0} = \frac{\partial \hat{\mathbf{f}}_n^0}{\partial \hat{\mathbf{q}}_n^0}, \tag{2.30}$$

$$\mathbf{D}^{0,t} = \begin{bmatrix} \dfrac{\partial \hat{\mathbf{f}}_n^0}{\partial \Re(\hat{\mathbf{q}}_n^{eo\cdot t})} & \dfrac{\partial \hat{\mathbf{f}}_n^0}{\partial \Im(\hat{\mathbf{q}}_n^{eo\cdot t})} \end{bmatrix}, \quad \forall t \in [1, H] \tag{2.31}$$

$$\mathbf{D}^{m,0} = \begin{bmatrix} \dfrac{\partial \Re(\hat{\mathbf{f}}_n^{eo\cdot m})}{\partial \hat{\mathbf{q}}_n^0} & \dfrac{\partial \Im(\hat{\mathbf{f}}_n^{eo\cdot m})}{\partial \hat{\mathbf{q}}_n^0} \end{bmatrix}^{\mathrm{T}}, \quad \forall m \in [1, H] \tag{2.32}$$

$$\mathbf{D}^{m,t} = \begin{bmatrix} \dfrac{\partial \Re(\hat{\mathbf{f}}_n^{eo\cdot m})}{\partial \Re(\hat{\mathbf{q}}_n^{eo\cdot t})} & \dfrac{\partial \Re(\hat{\mathbf{f}}_n^{eo\cdot m})}{\partial \Im(\hat{\mathbf{q}}_n^{eo\cdot t})} \\ \dfrac{\partial \Im(\hat{\mathbf{f}}_n^{eo\cdot m})}{\partial \Re(\hat{\mathbf{q}}_n^{eo\cdot t})} & \dfrac{\partial \Im(\hat{\mathbf{f}}_n^{eo\cdot m})}{\partial \Im(\hat{\mathbf{q}}_n^{eo\cdot t})} \end{bmatrix} \quad \forall m, t \in [1, H]. \tag{2.33}$$

2.2 An Industrial Application: Steam Turbines with Mid-Span Dampers

In this case study, the dynamic behavior of the turbine bladed disks coupled with one of the special damper designs, the so-called Mid-Span Dampers (MSDs) that is commonly used in steam turbines of Baker Hughes Company, is thoroughly studied.

Mid-Span Damper (MSD) is a special type of friction dampers, which is extensively used at the Last Stage Blades (LSBs) of Baker Hughes' steam turbines. LSBs have very low stiffness due to their relatively thin airfoils with complex 3D shapes. Moreover, LSBs are exposed to very large centrifugal and aerodynamic forces during operation, which makes them to operate in a very severe condition (Yamashita et al., 2012). This requires a special type of friction dampers to be utilized and MSDs are particularly designed for LSBs. The design

of MSDs is historically based on a more traditional damping wire configuration in which a wire passes through a hole located on the blade (Jaiswal & Bhave, 1994; Drozdowski et al., 2016).

MSDs are metal devices with different design shapes such as pin or sleeve geometry. Figure 5 representatively shows bladed disks coupled with the pin geometry of MSDs which are placed approximately at 70% of the airfoil span and come into contact with LSBs by the centrifugal force acting during rotation. In the literature, MSDs are also known as the so-called friction bolt damping element (Drozdowski et al., 2015; Szwedowicz et al., 2008). Nonlinear vibration analysis of LSBs with integral connections has been conducted by Siewert et al. (2017) and Voldřich et al. (2015) and it has been shown that friction damping plays an important role for LSBs to be able to reduce stress levels and vibration amplitudes.

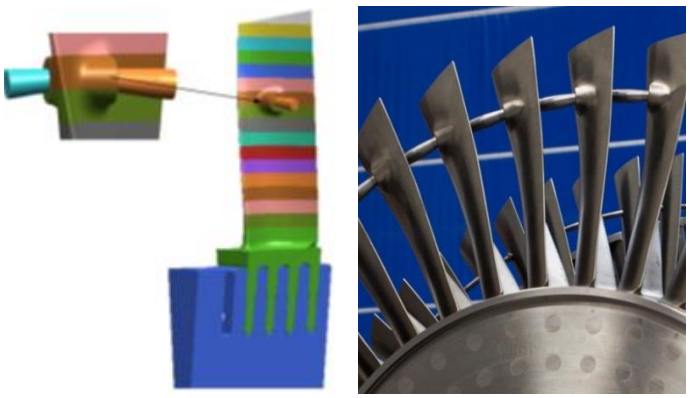

Figure 5: Bladed disks with mid-span dampers, *© 2020 Baker Hughes Company - All rights reserved*

2.2.1 Modeling Approach

Finite element model of the fundamental sector is constructed by utilizing one of the commercial software. Linear solid elements are used with a total of 2.5 million DOFs approximately in the full model. The models are shown in Figure 6.

The material of the structures is steel with Young's modulus E=210 GPa, Poisson coefficient ν=0.3 and density ρ=7800 kg/m^3. The MSD has a bi-conical shape, while the slots, where the damper penetrates into the blade, are cylindrical. Only some portion of the damper comes into contact with the blade pocket located approximately around 70% of the airfoil span. It should be noted that the friction damping generated at the blade root is neglected in this study and the blade–disk joint is modeled as perfectly linearly elastic.

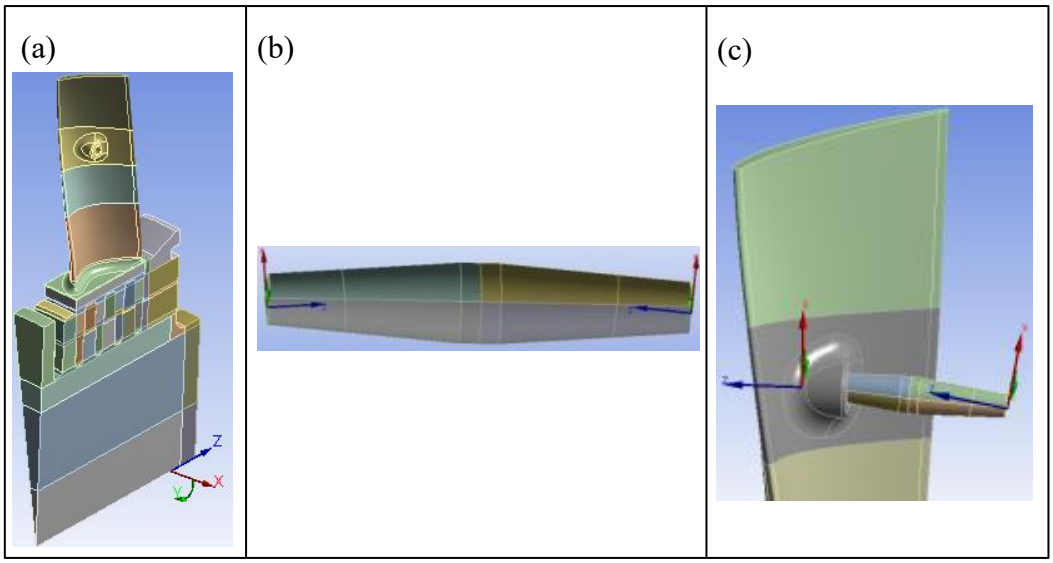

Figure 6: (a) Blade sector model, (b) Damper model, (c) Assembled view,

The static pre-load that simulates the centrifugal force and keeps the damper in contact with the blade during operation is applied on the damper model at 5 different nodes along the damper axis, as shown in Figure 7a. With this type of static forcing, upper portion of the MSDs touches to the blade. The contact surfaces between the blade and damper are precisely meshed so that the contact nodes of the blade and damper in the slot overlap and couple the system through contact elements. It has been shown by Zucca et al. (2016) that wear is generally localized along a line for a cylindrical contact surface. In addition, based on the previous experience of Baker Hughes Company, the cylindrical surface typically restricts the contact patch to a very limited region on a line. Hence, a theoretical line contact with 31 pair nodes at each side is assumed in the analyses. Each pair node has two tangential directions in the circumferential and axial direction of the damper, while the normal direction is defined radially from the rotor hub. Contact lines are shown in Figure 7b with a section view. Dynamic excitation force is distributed over the airfoil and applied from 19 different nodes as shown in Figure 7c. Unit force is exerted to each node from the direction of the nozzle axis. Linear viscous damping is used and 1% proportional damping ratio is assumed. The 0^{th} and the 1^{st} harmonics are used in the coupled Harmonic Balance equations. Displacement amplitude of the blade tip is presented in the results.

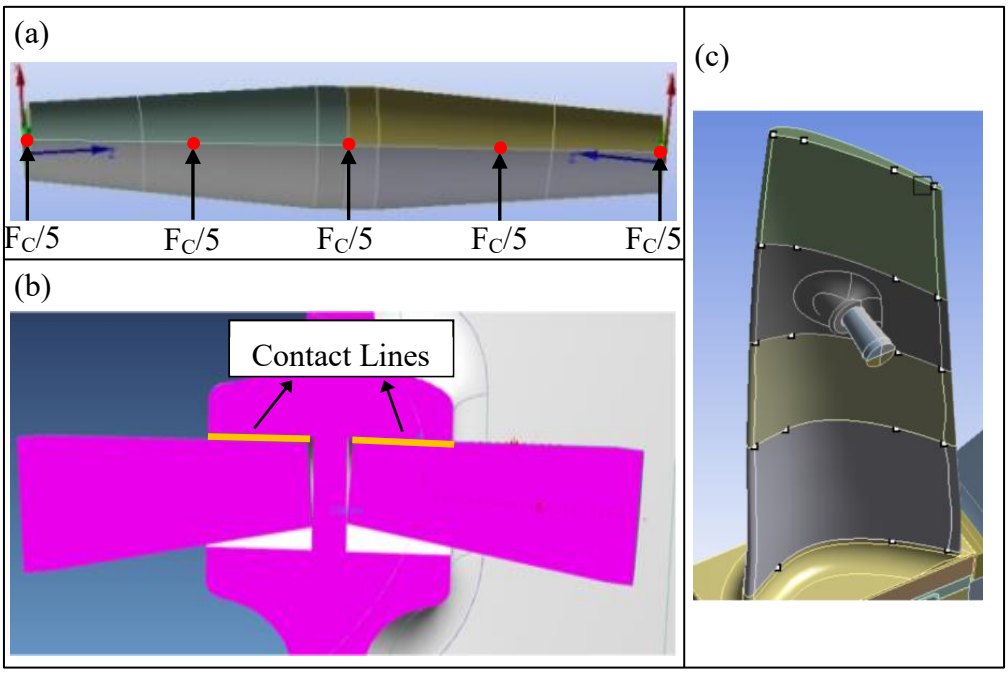

Figure 7: (a) Static pre-load on the damper, (b) Section view of the contact region, (c) Excitation force application nodes, *© 2020 Baker Hughes Company - All rights reserved*

Contact parameters play an important role on the dynamic characterization of dampers. Several studies have been performed in the last years (Allara, 2009; Lavella et al., 2011; Schwingshackl et al., 2012; Stingl et al., 2013) to correctly determine the contact properties. In this case study, the numerical approach developed by Allara (2009) is utilized to calculate the contact stiffness values. In this technique, the main principle of a flat indenter with rounded edges that is pressed onto an infinite half-space is used. However, since the contact surface is cylindrical in our case, the extent of the punch flat area is set equal to zero. It should be noted that contact stiffness values are directly dependent to centrifugal force in the turbomachinery applications. It increases with the rotor rotation speeding up, while it decreases with slowing down. Hence, it varies with different pre-load values. The overall contact stiffness value obtained for each surface is equally divided into number of contact nodes and shared by each contact element evenly. Eventually, the normal contact stiffness is obtained in the range of $1.24\times10^3 - 1.76\times10^3$ N/mm for the normal direction, and the tangential contact stiffness value is computed within the range of $1.19\times10^3 - 1.66\times10^3$ N/mm for the circumferential and axial directions. The coefficient of friction, μ, is assumed 0.5 and kept constant throughout the numerical simulations.

2.2.2 Dynamic Behavior of Last Stage Blades with Mid-Span Dampers

Nonlinear response analyses are performed with the 6th engine order around the first four resonances. The first four mode shapes of the sector for the 6th harmonic index are given in Figure 8a-d, respectively. The first one is in-plane bending mode. The second one is a coupled mode of the damper and blade, while the third one is a torsional mode. The fourth one is another coupled mode of the torsional and out-of-plane bending.

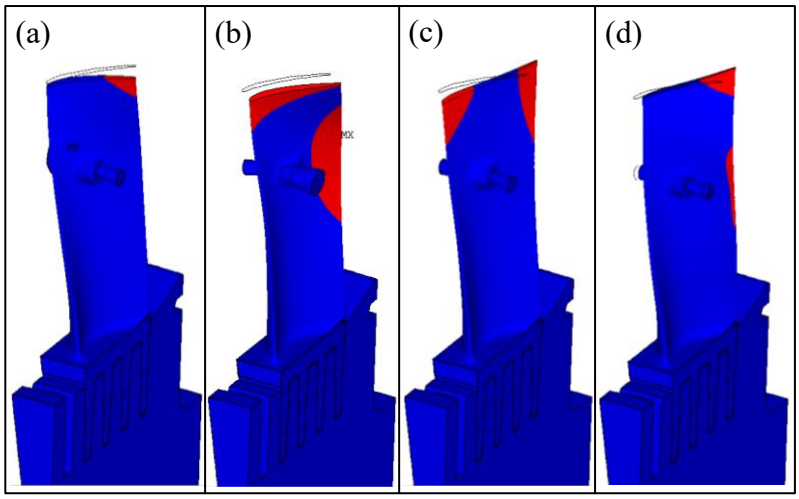

Figure 8: The first four mode shapes of the fundamental sector for the 6th harmonic index, *© 2020 Baker Hughes Company - All rights reserved*

Figure 9 shows the steady state vibration response obtained with different pre-loads around the first resonance. X and Y axes of the graph are normalized with respect to the first linear natural frequency value and the maximum free linear response value, respectively. The damper clearly dissipates energy and reduces vibration amplitudes. The response behavior shifts from the free linear response to the fully stuck linear response with the increase of static pre-load value, as expected. It should be noted that the natural frequency value of the fully stuck linear case is considerably higher than the free linear one. The reason for this high stiffening effect is that MSD is placed approximately 70% above from the blade root, which affects the system dynamics considerably and makes the coupled system much stiffer. This property of MSDs is highly critical in terms of the damper effect on the blade dynamics due to the location of the damper. Moreover, for the nonlinear analysis with the lowest pre-load (the orange curve), resonance

is obtained at a frequency that is smaller than the free linear natural frequency value. This shows for relatively low pre-loads that the damper mass is more dominant on the resonance value than the stiffness provided with the presence of the damper.

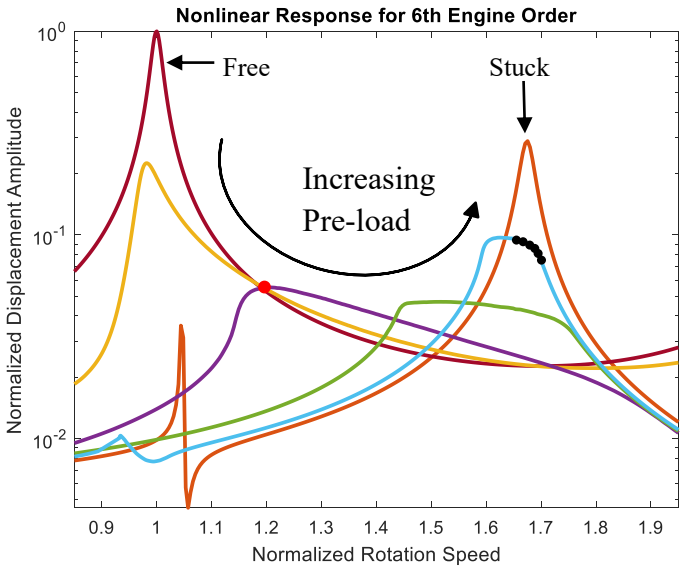

Figure 9: Frequency response curves around the 1st resonance with different pre-loads,

Contact maps give valuable information to visualize the partial slip behavior of the damper by monitoring the contact conditions. Figure 10a-f shows the contact states at six consecutive frequency points marked with black dots around $\omega = 1.7 \times \omega_n$ for a response curve that is close to fully stuck region of the first mode, i.e. light blue response curve shown in Figure 9. A cross section view of the upper line of the damper is simply visualized by highlighting the contact nodes with markers depending on the contact states. The red circle represents that the contact node is under fully stuck state, while the green stars indicate that there is an alternating stick-slip motion without separation during the cycle. Blue line in Figure 10 also represents the upper damper line that is not in contact with the blade. In this particular case, frequency sweep is performed from higher to lower values. Figure 10a is the contact map obtained at the first frequency just before slip starts, which means the damper is fully stuck. Figure 10b shows that partial slip initiates at the edge contact nodes for both sides and it is propagated through the inner nodes with progressing frequency values as shown in Figure 10c-f

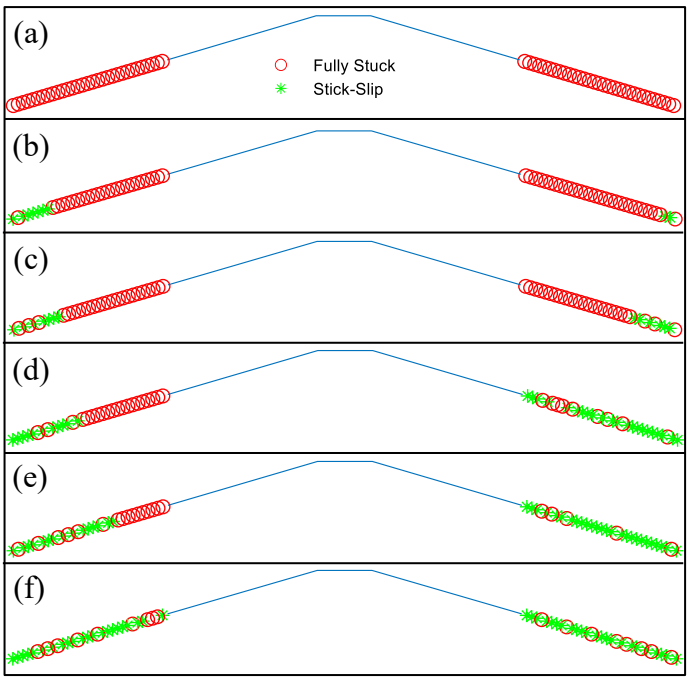

Figure 10: Contact conditions at six consecutive frequencies,

The responses obtained for different excitation values with the same initial pre-load around the 1st resonance are also shown in Figure 11. It can be seen that the damper is completely stuck for relatively low excitation values. There is just a frequency shift for this particular case and no damping supplied. The damper starts slipping and provides energy dissipation for the moderate excitation values. The MSDs are designed to operate in these regions, since most of the damping is achieved around these frequencies. The curves finally approach to the free linear case for the higher excitation values, in which the dissipation effect of the damper decreases.

A similar response behavior is obtained around the 2nd resonance region, as shown in Figure 12. It is also interesting to note that the change of contact stiffness due to different pre-loads can be clearly seen by comparing the resonance frequencies of two response curves close to the fully stuck region. The resonance frequency of the fully stuck linear response curve is slightly larger than the other one; because the centrifugal force is higher in the former, which results in a larger contact stiffness value. The same observation is also valid in the first resonance region as can be seen in Figure 9. All the analyses show that MSDs work very well around the first two resonances to reduce the vibration amplitudes.

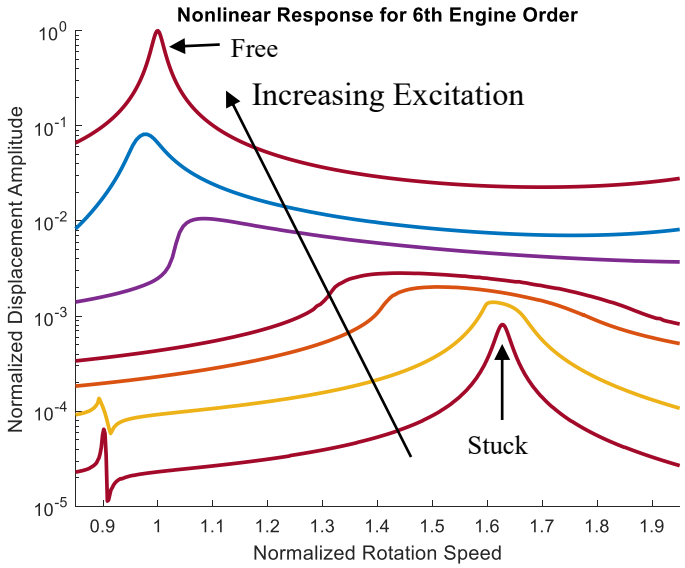

Figure 11: Frequency response curves around the 1st resonance with different excitations, © *2020 Baker Hughes Company - All rights reserved*

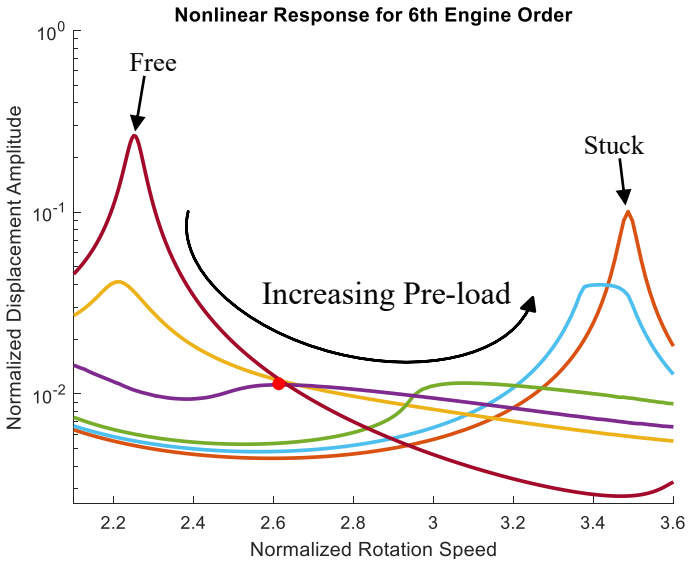

Figure 12: Frequency response curves around the 2nd resonance with different pre-loads, © *2020 Baker Hughes Company - All rights reserved*

Vibration responses obtained with different pre-loads around the 3rd and the 4th resonances are also given in Figure 13. Similarly, the damper is capable of reducing the vibration amplitudes with friction for both resonance regions. It is interesting to note that although there is a stiffening effect for the 3rd resonance region, this observation is not valid for the 4th resonance region. On the contrary,

the resonance frequency decreases due to the mass effect of the damper. This can be explained by the fact that the 4th mode of the sector (see Figure 8d) is a coupled mode of the torsional and out-of-plane bending, where the MSD and blade move together in the direction of out-of-plane. Thus, linear natural frequency of the free blade is not considerably affected by the presence of the damper, which prevents the stiffening effect.

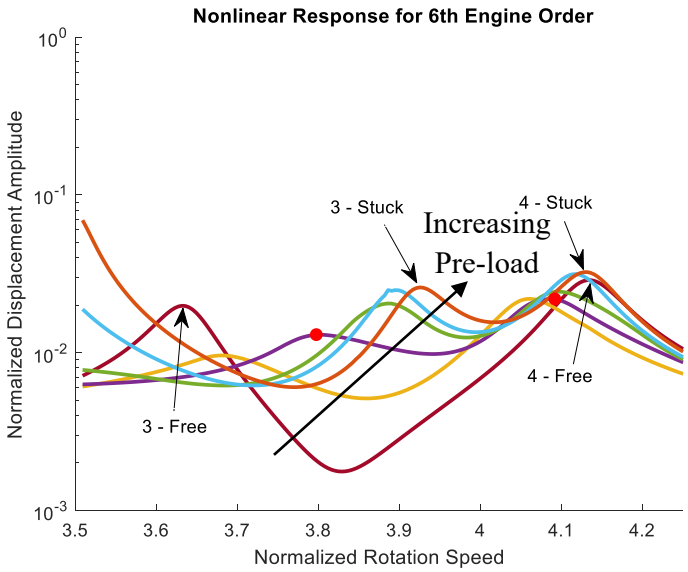

Figure 13: Frequency response curves around the 3rd and the 4th resonances with different pre-loads,

Contact conditions during the energy dissipation for different resonances play an important role on the characterization of damper kinematics. In this study, contact maps are extracted at the frequency points marked with red dots on the purple response curves. These points are intentionally selected; because, purple curves are obtained with a relatively low pre-load under which the damper provides a large vibration reduction. Figure 14a-d illustrate the contact conditions at $\omega = 1.2 \times \omega_n$, $\omega = 2.6 \times \omega_n$, $\omega = 3.8 \times \omega_n$ and $\omega = 4.1 \times \omega_n$ for the first four resonance regions, respectively. Figure 14a and Figure 14b show that a stick-slip-separation motion takes place in some of the contact nodes around the first and the second resonances, respectively. Partial slip behavior is observed for all resonances at the left side of the damper, while all the nodes on the right side makes a stick-slip motion except the first resonance. All contact maps show that MSDs are an efficient type of dampers to reduce the vibration amplitudes of LSBs with a partial slip behavior.

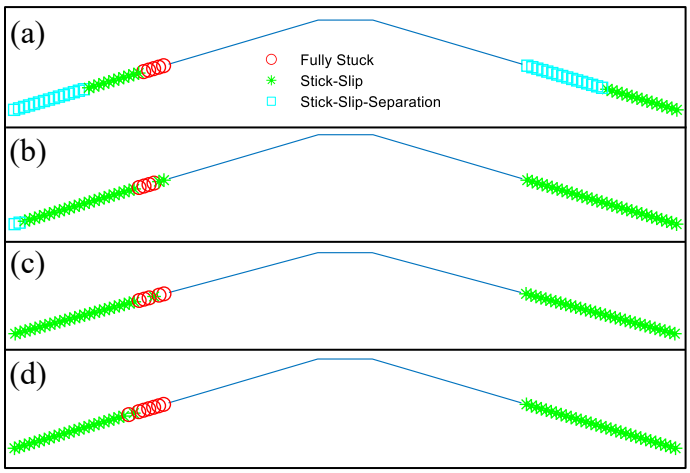

Figure 14: Contact conditions at four different resonances, © *2020 Baker Hughes Company - All rights reserved*

2.3.2 Observation of the Response Variability

The variability phenomenon under the same nominal conditions is observed in this case study as the first time throughout the thesis. Here, it is separately investigated in two particular cases with a low and a high pre-load. This allows identifying the kinematics of the variability under different conditions.

The first case is examined with a relatively low pre-load, where Figure 15 shows the response curves. The three nonlinear response curves are obtained by keeping all the system parameters exactly the same. The only difference between the analyses is the frequency step used during simulations. It is clearly seen from Figure 15 that the response may vary significantly. For this specific example, the responses are obtained by sweeping the frequency from higher to lower. The same initial guess value is assigned at the very first frequency ($\omega = 1.95 \times \omega_n$) in each analysis, which provided the same response value initially. However, the response curves are separated from each other after a certain frequency value. There is almost even ten times difference between the green and blue responses around $\omega = 1.15 \times \omega_n$ frequency value.

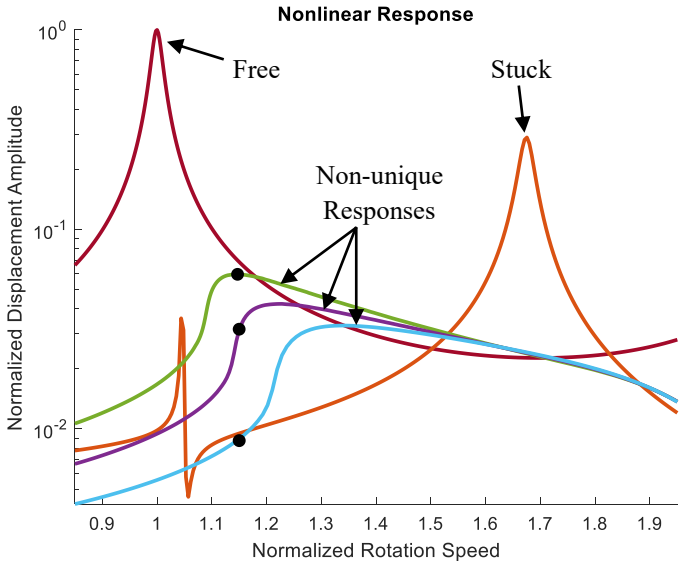

Figure 15: The variability of the frequency response for a relatively low pre-load, © *2020 Baker Hughes Company - All rights reserved*

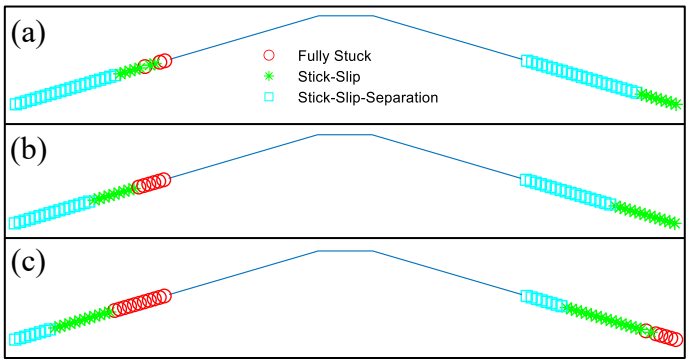

Figure 16: Contact conditions for the non-unique response with a relatively low pre-load, © *2020 Baker Hughes Company - All rights reserved*

In order to investigate the underlying kinematics of the variability, the contact states at frequency points marked in Figure 15 with black dots ($\omega = 1.15 \times \omega_n$) are studied. Figure 16a-c show the contact conditions for the green, purple and blue curves, respectively. It is seen that contact states at the same frequency are quite different in each case, although all the system parameters are kept same. The general pattern is similar, but non-unique tangential forces induced the contact states to propagate in a different way during the analyses. Partial slip is observed, as expected, since it is one of the main reasons for the variability. It is also interesting to note that the number of separating nodes in Figure 16a is higher than

the other ones. This provides a loss of stiffness and makes the green curve to be closer to the free linear response than the other ones.

The variability is also investigated with a higher pre-load. In this case, the non-unique nonlinear response is obtained close to the fully stuck linear one, as shown in Figure 17. It should be noted that the variability in the response is considerably smaller than the previous case and the curves almost overlap each other. The main reason of this fact can be better understood with the contact conditions. Figure 18a-c depicts the contact states for three curves around the resonance frequency marked with a black dot in Figure 17. The damper motion is dominated by an alternating stick-slip behavior on the contacts; thus, the uncertainty in the friction forces highly decreases due to the fact that it is originated by the fully stuck contacts. An almost unique response is obtained and a small difference in contact states causes a slight variation in the response curves as can be seen in Figure 17. It can be inferred from all of the results that if the damper is in gross slip or fully stuck, the nonlinear response approaches an identical pattern and becomes unique. On the other hand, once the partial slip is high, the response may vary considerably in different analyses with the same system parameters.

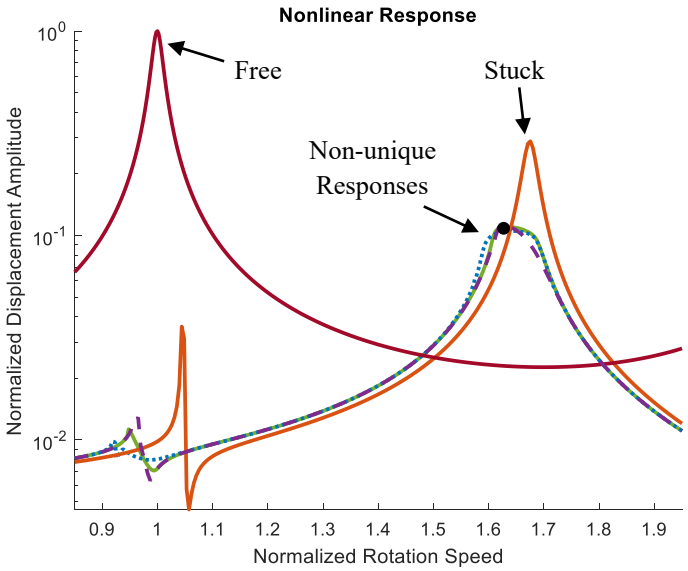

Figure 17: The variability of the frequency response for a relatively high pre-load, © *2020 Baker Hughes Company - All rights reserved*

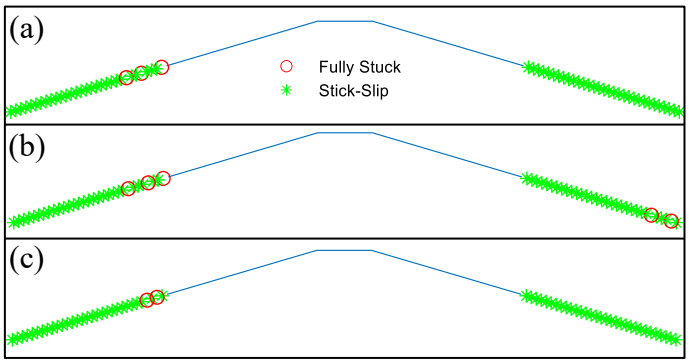

Figure 18: Contact conditions for the non-unique response with a relatively high pre-load,

2.3 Summary

This chapter depicts the full picture of performing a forced response nonlinear response analysis on the tuned bladed disks with contact interfaces. Each step is illustrated in detail to give an insight of followed procedures throughout the thesis. This chapter also presents a part of a joint project performed with the Baker Hughes Company. The dynamic response behavior of the steam turbines coupled with mid-span dampers, which is designed by Baker Hughes Company, is shown with the computational analyses performed in the scope of the thesis. The first observation of the dynamic response variability phenomenon is also presented on an industrial bladed disk with frictional constraints.

Chapter 3

Non-unique Contact Forces and Nonlinear Response Variability

This chapter[2] introduces the concept of non-unique contact forces which create an uncertainty in the frictional interfaces. This phenomenon may enable the computation of multiple responses under some conditions for the nominally same inputs. The variability of the nonlinear response is investigated and shown on a simplistic case study that imitates the turbine blades with wedge dampers. The periodic response limits are also determined with a numerical approach.

3.1 Non-unique Tangential Forces

Consider a generic Jenkins element with a variable normal load (see Figure 3) and assume a case where the input motion is relatively small so that the contact element has a stick state for the entire cycle. The Coulomb's friction law states that the resulting tangential force, $T(t)$, must always be bounded by an upper ($\mu N(t)$) and a lower ($-\mu N(t)$) limit. However, it should be noted that the static value of the tangential force, T^0, can vary within a range ($T^0_{min} \leq T^0 \leq T^0_{max}$). The limits for this range are determined by the static parts of maximum ($T_{max}(t)$) and minimum ($T_{min}(t)$) tangential forces, which make tangent to the positive and

[2] Part of the work described in this chapter has been previously published:
"Ferhatoglu, E., & Zucca, S. (2021). Determination of periodic response limits among multiple solutions for mechanical systems with wedge dampers. *Journal of Sound and Vibration*, *494*, 115900."

negative Coulomb's limit values, respectively. The variability range is representatively shown with corresponding time histories and hysteresis curves in Figure 19. It can be easily inferred that there is an infinite number of contact force curves that can be obtained within this range. It is worthy to note that although the static value differs for each curve, all of them must have the same dynamic components, since the variable part of tangential force is directly determined by the harmonic components of the input motion. This fact creates a non-uniqueness phenomenon in the computation of the tangential force for a fully stuck state. It should also be noted that although a varying normal is considered for this representative particular case, non-uniqueness of the static tangential force, within the range between T^0_{min} and T^0_{max}, also exists for contacts that exhibit a constant normal load.

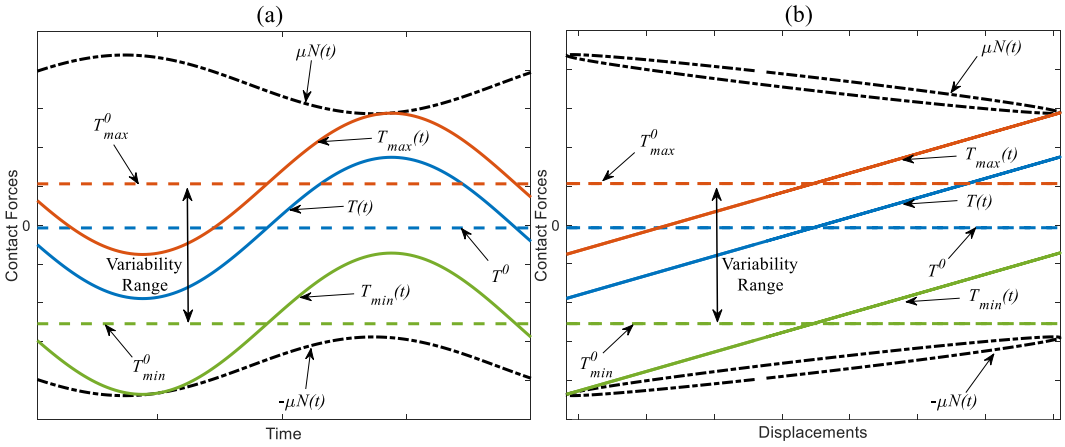

Figure 19: (a) Time histories and (b) Hysteresis curves for a full stick cycle

In order to clarify the situation further, consider Figure 20a showing the Jenkins contact element that is under a fully stuck condition with the given input motion, *u(t)*. The tangential force for a stick state can be computed by using the formula given in Eq. (2.15) which also includes the slider motion, *w(t)*. However, since the coordinate of the slider is an unknown parameter in advance, it can be hypothetically positioned within a range in such a way that the contact is always going to be in the stick state, as shown in Figure 20b and Figure 20c, in which the upper and lower limits are the points where positive and negative slips are about

to initiate. Since any position between limits is acceptable, an infinite number of periodic function *T(t)* then exists, as indicated in Figure 19.

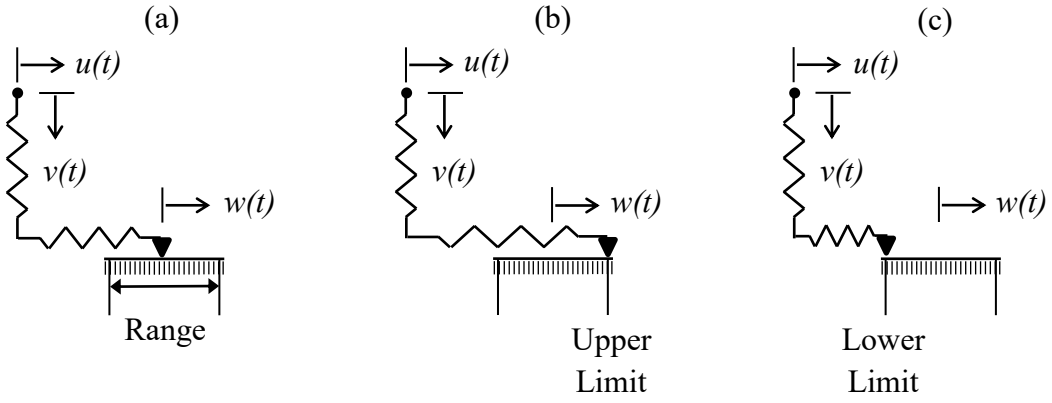

Figure 20: Contact element with different slider positions

It is also worth noting that non-unique values of the tangential contact force only occur for the fully stuck cycle. In case of an alternating stick–slip or an alternating stick–slip–lift-off cycle, only one single value for T^0 can be computed due to the fact that tangential force has already been confined by the limit. For example, consider Figure 21, which shows the time histories and hysteresis curve for an alternating stick–slip cycle. Tangential force starts to cycle in the negative slip state and directly takes the lower limit value. After transition to stick state, which is the time instant shown with blue dot, there is only one unique curve for the tangential force, which removes the uncertainty. Then, the condition again changes from stick to positive slip and this alternating motion continues until the end of the cycle. Similar behavior can be observed also for an alternating stick–slip–lift-off cycle as depicted in Figure 22, where the transition points between slip and lift-off states are shown with black dots. As a result, contact forces of a single Jenkins element are uniquely computed for both these cases. Hence, the uncertainty of the non-unique tangential contact force only exists for the contacts under fully stuck during the vibration cycle, i.e. the uncertainty in the system only exists if at least one of the contact points remains stuck during the vibration cycle.

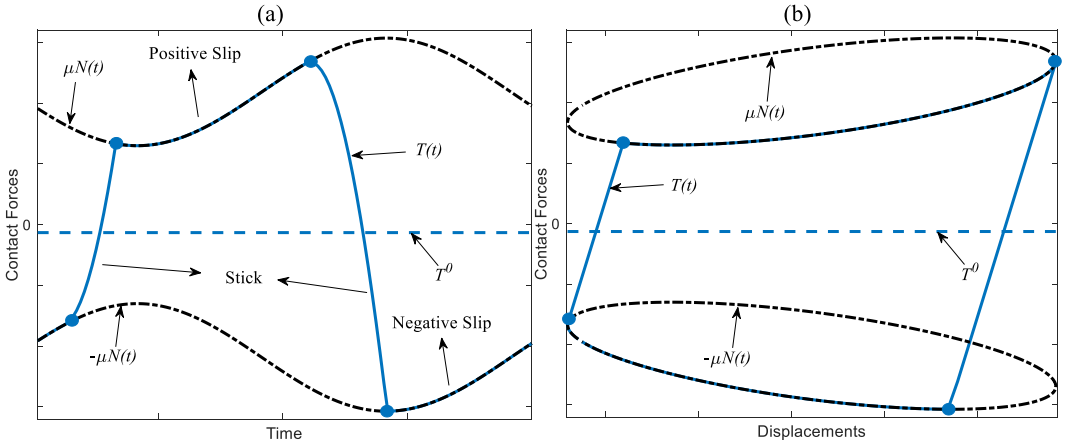

Figure 21: (a) Time histories and (b) Hysteresis curve for an alternating stick–slip cycle

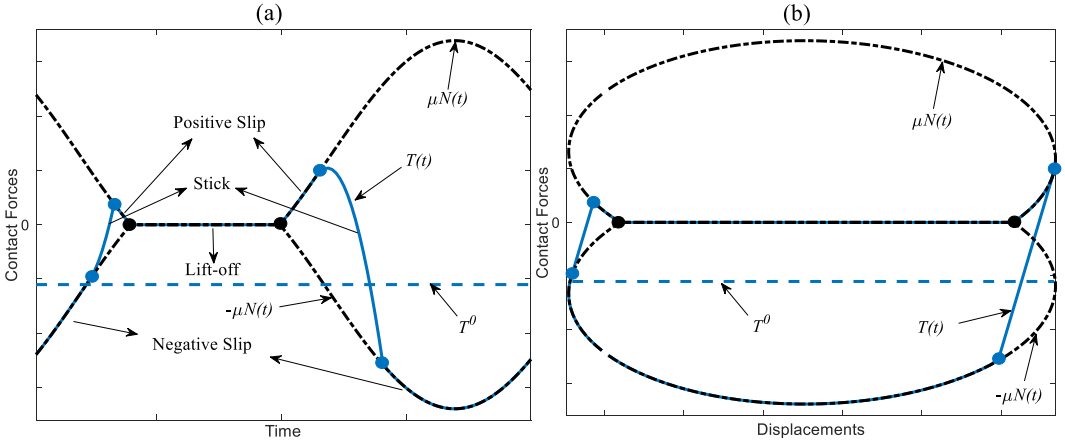

Figure 22: (a) Time histories and (b) Hysteresis curve for an alternating stick–slip–lift-off cycle

3.2 The Variability of the Nonlinear Response

3.2.1 Effective Stiffness and Equivalent Damping of a Contact Element

This section introduces the effective stiffness and equivalent damping concepts of a contact element. Basic expressions will be shown to simply illustrate the direct dependence of dissipative capabilities of a contact element to the normal force on it. In this way, the reader can better understand the main theory of the non-unique tangential forces that will directly affect the normal force of slipping contact elements, which, in turn, causes the response variability in the system.

Consider a single Jenkins element under a given periodic motion, $\mathrm{q}(t)$. Internal nonlinear force by dry friction, $\mathrm{f}_c(t)$, for the steady state motion can be expressed in a more general way as

$$\mathrm{f}_c(t) = \left(\mathrm{k}_{eq}(\hat{q}) + i\mathrm{c}_{eq}(\hat{q})\right) \times \mathrm{q}(t)\,, \tag{3.1}$$

where $\hat{q}$ represents the response amplitude. k_{eq} and c_{eq} are the effective stiffness and the equivalent damping terms of the contact element, respectively. For a better illustration, analytical expression of equivalent stiffness and damping terms for a representative 1D Jenkins element which is under a single harmonic input motion ($q(t) = \hat{q}\cos(\omega t)$) with a constant normal load, N_0, can be written as

$$\mathrm{k}_{eq} = \begin{cases} k_t & \text{full stick} \\ \dfrac{k_t}{\pi}\left(\varphi - \dfrac{\sin(2\varphi)}{2}\right) & \text{stick-slip} \end{cases}, \tag{3.2}$$

$$\mathrm{c}_{eq} = \begin{cases} 0 & \text{full stick} \\ \dfrac{4\mu N_0}{\pi\hat{q}}\left(1 - \dfrac{\mu N_0}{k_t\hat{q}}\right) & \text{stick-slip} \end{cases}, \tag{3.3}$$

where

$$\varphi = \arccos\left(1 - \frac{2\mu N_0}{k_t\hat{q}}\right). \tag{3.4}$$

These quantities, which are representatively shown in Figure 23, determine the contact elements' overall dissipative characteristics, which directly depend on the state conditions that the contact elements undergo during the full cycle. As can be seen in Figure 23a, k_{eq} starts from zero and saturates at a specific value, which means that the contact element becomes effective in the system with increasing pre-load and shifts the response graph from free linear case to the fully stuck linear case by adding stiffness to the structure. The contact state then becomes fully stuck after a certain pre-load and k_{eq} becomes equal to the contact stiffness

value. On the other hand, in Figure 23b, c_{eq} takes its maximum value for an intermediate pre-load that is defined as the so-called optimum point. After this point, the damping ability of the contact element decreases with increasing static pre-load and becomes zero at the fully stuck state condition. As a result, it can be understood that the dissipative characteristics of the contact element changes with the normal load on it. In the next section, this information will be used to show how the non-unique tangential forces of fully stuck contacts lead to different normal loads on slipping contact elements and correspondingly give rise to the multiple responses.

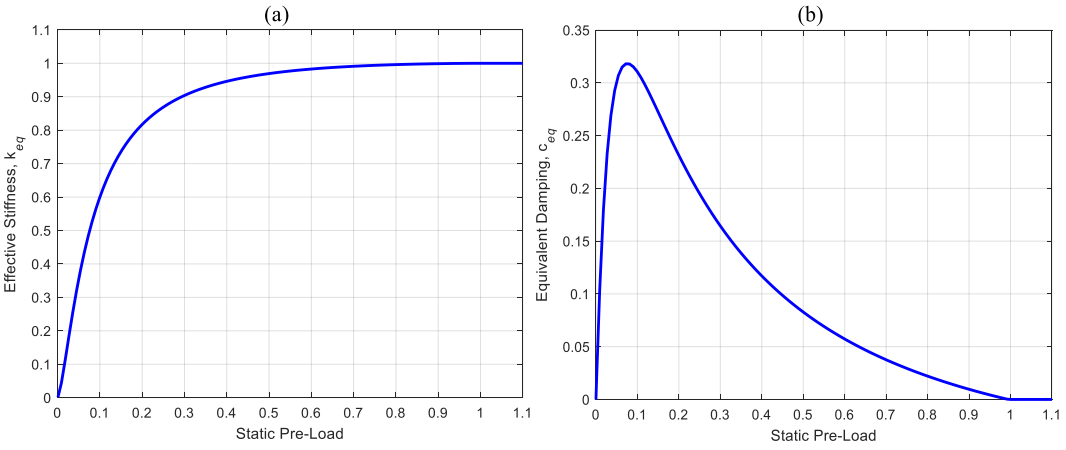

Figure 23: (a) Effective stiffness and (b) Equivalent damping for a dry friction element

3.2.2 Multiple Responses of Mechanical Structures with Frictional Interfaces

Computation of multiple nonlinear responses is shown on a non-complex system for simplicity, despite the fact that the variability phenomenon is a general matter of fact for engineering systems with dry friction.

Consider a mechanical system with an asymmetric wedge damper pressed between two vibrating bodies as shown in Figure 24a. Each damper side can be coupled to the adjacent body by means of a Jenkins element. Assuming the macro slip conditions while the system is under a periodic excitation, three different cases can be achieved during the steady state motion. These cases can be as follows.

1- Both sides may be fully stuck. In this case, there is an uncertainty in the static tangential force on both sides. However, the system behaves as a linear system. Hence, this case provides no friction damping to the system, which leads to obtain unique vibration amplitude.

2- Both sides may undergo an alternating stick–slip cycle or an alternating stick–slip–lift-off cycle. In this case, static tangential forces are uniquely defined on both sides as shown in Figure 21 and Figure 22. Hence, there is no variability in the contact forces, which enables to obtain only one unique response, as well.

3- One side may be under a fully stuck case, while the other one shows an alternating stick–slip or an alternating stick–slip–lift-off behavior. In this case, the non-uniqueness of static tangential forces applies to the fully stuck side. To investigate this case further, consider the static force balances on the wedge damper in x and y directions, which are representatively shown in Figure 24b. They can be written for this configuration as

$$\begin{aligned} {T^0}_R\cos(\alpha_R) - {N^0}_R\sin(\alpha_R) - {T^0}_L\cos(\alpha_L) + {N^0}_L\sin(\alpha_L) &= 0 \\ {T^0}_R\sin(\alpha_R) + {N^0}_R\cos(\alpha_R) + {T^0}_L\sin(\alpha_L) + {N^0}_L\cos(\alpha_L) &= F^0 \end{aligned}. \tag{3.5}$$

For the simplicity, assume, without any loss of generality, that the left damper side (with subscription L) is in full stick cycle while the right damper side (with subscription R) shows an alternating stick–slip or an alternating stick–slip–lift-off behavior. It can be clearly inferred that the uncertainty in ${T^0}_L$ directly affects the system behavior with the coupling that is present in Eq. (3.5). Different values of ${T^0}_L$ result non-unique ${N^0}_R$, which leads to obtain a variable steady state k_{eq} and c_{eq} for the right side of the damper due to different normal load values. This makes the dynamic behavior of the system to have a variable pattern as if the structure is forced by the same dynamic excitation but with different static pre-loads; because, simultaneous solution of Eq. (2.24) provides a coupling between the static and the dynamic parts. For each possible value of non-unique contact forces, it can be said that the force balance in the system is achieved in a non-unique way. Physically, it means that the different force equilibria occur on the damper, and these non-unique conditions create multiple dynamic responses due to the static-dynamic coupling in the system. As a result, multiple solutions of the system eventually exist for case 3. This phenomenon will be also illustrated experimentally in Chapter 5 and in Chapter 6, by showing non-unique force equilibrium on the real friction dampers.

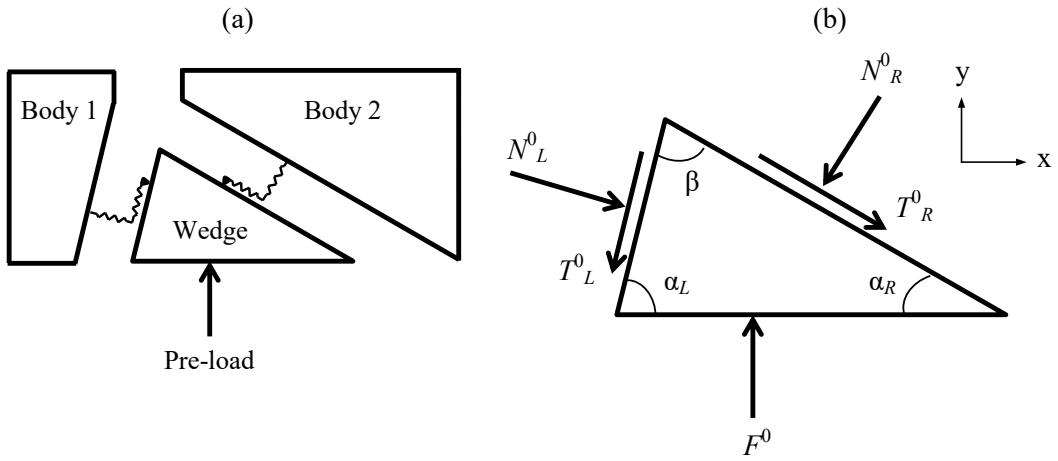

Figure 24: (a) An asymmetric wedge damper pressed between two inclined surfaces, (b) Static forces acting on the damper

Multiple solutions can be obtained changing the initial guess of the tangential contact force before starting the computation of friction forces. In this approach, the initial value of the tangential force at the very beginning of the predictor-corrector strategy (see Section 2.1.4) is set to an arbitrary value so that the Coulomb's law is satisfied. In a more general way, the tangential force value with a stick state assumption can be initially guessed at $t = t_{ini}$ for each contact element in the system as

$$T(t_{ini}) = m \times \mu N(t_{ini}) \tag{3.6}$$

where m is a multiplier coefficient and may be different for each contact element. It should also be noted that m can theoretically take a value in a range between –1 and 1, i.e. $-1 \le m \le 1$. After the predictor-corrector algorithm, if the contact element fully sticks at the end of the cycle, one of the multiple tangential forces in the variability range (see Figure 19) is computed. In this way, the non-unique contact forces can be obtained by simply changing the value of m in different analyses. Therefore, the multiple responses become possible with non-unique contact forces in the solution of Eq. (2.24).

Although an illustration of multiple responses is explained here for a very simple case, the uncertainty might also occur for a more complicated system with multiple contact elements. This phenomenon has already been shown in many studies both experimentally (Botto & Umer, 2018; Botto et al., 2018; Gastaldi et al., 2021) and computationally (Yang & Menq, 1998a; Firrone et al., 2011; Zucca et al., 2013). It should be noted that the amount of uncertainty is system

dependent. For example, there may be even 50 Hz resonance frequency difference between multiple responses obtained after two consecutive experiments as reported by Gastaldi et al. (2021). Moreover, ten times difference among multiple amplitudes at the same frequency is possible in industrial turbine bladed disks with mid-span dampers as shown in the previous chapter. Therefore, all of these previous studies also show that the uncertainty phenomenon is not a modeling artifact and it cannot be ignored in the design stage.

3.2.3 Response Limits

Numerical computation of multiple responses and the determination of upper and lower limits would take an interest in the design phase. Particularly, the upper bound at the resonance frequency may play the most important role from the engineering point of view. In this section, a numerical approach, which is able to provide the limit response curves that bound the multiple responses, is developed based on the following observations:

1- As a general fact, the physics of a slipping contact behavior implies that the contact approaches to the fully stuck condition if the static normal load exerted in normal direction increases. On the other hand, the lower the static normal load is, the closer the contact will be to the free condition, i.e. no friction forces.

2- The free and the fully stuck contact configurations determine the two limit dynamic configurations of the nonlinear system.

3- The static normal load acting on the right slipping side of the damper, $N^0{}_R$, has non-unique values because of the cross coupling between the two damper sides.

For the above mentioned reasons, it can be clearly concluded that the two configurations corresponding to the minimum and the maximum values of the static normal load over the slipping side ($N^0{}_R$ in this case) determine the boundaries of the response variability range at each excitation frequency. From the static force balances given in Eq. (3.5), $N^0{}_R$ can be derived as either

$$N^0{}_R = \frac{F^0 \sin(\alpha_L) + T^0{}_R \cos(\alpha_L + \alpha_R) - T^0{}_L}{\sin(\alpha_L + \alpha_R)} \tag{3.7}$$

or

$$N^0{}_R = F^0 \cos(\alpha_R) - N^0{}_L \cos(\alpha_L + \alpha_R) - T^0{}_L \sin(\alpha_L + \alpha_R). \tag{3.8}$$

It is known that the static tangential force on the left damper side, $T^0{}_L$, is not unique due to the uncertainty phenomenon. It should be noted that Eq. (3.7) or Eq. (3.8) cannot be solved alone since there are three unknowns in each one. However, the relationship between $N^0{}_R$ and $T^0{}_L$ is directly related through a divider or a multiplier factor of $\sin(\alpha_L+\alpha_R)$. It is also known for a wedge damper that $0 < \alpha_L+\alpha_R < \pi$, which shows the factor, $\sin(\alpha_L+\alpha_R)$, always takes positive values. As a result, the maximum value of the slipping side's normal load, $N^0{}_{max,R}$, corresponds to the minimum value of the sticking side's tangential force, $T^0{}_{min,L}$. Similarly, the minimum value of the slipping side's normal load $N^0{}_{min,R}$ corresponds to the maximum value of the sticking side's tangential force, $T^0{}_{max,L}$. Consequently, the boundaries of the response variability range, which are directly determined by the minimum and the maximum values of the static normal load over the slipping side, can be obtained by imposing the limit values of the static tangential force, $T^0{}_{max}$ and $T^0{}_{min}$, in the calculation of $T(t)$ on the sticking side.

It should be noted that the tangential force limits are unknown in advance before starting the computation of contact forces. However, it is known that $T(t) \equiv m \times \mu N(t)$, where m is bounded in [-1,1] due to the Coulomb's law for any t if there is no separation. In order to ensure to have the maximum tangential force limit, $T_{max}(t)$, at steady state, a large enough initial guess value for the tangential force, $T_{ini}(t)$, in the computation of the contact force procedure can be assigned at the very beginning. Numerically, since the limits are always bounded by the normal force components, $\mu N(t)$, in fully stuck conditions, initial prediction of the tangential force, $T_{ini}(t)$,can be set equal to at $t = t_{ini}$ as

$$T_{ini}(t_{ini}) = \mu N(t_{ini}). \tag{3.9}$$

Then, state-by-state simulation with the predictor-corrector approach, which is explained in Section 2.1.4 to calculate internal friction forces, will ensure that $T(t)$ is going to end up as $T_{max}(t)$ at steady state. From the physical point of view, this is the case where the steady state slider position of contact element, $w(t)$, is forced to stay at the farthest point just before the positive slip with respect to the relative displacement coordinate, $u(t)$, as shown in Figure 20b. On the contrary, the minimum force limit, $T_{min}(t)$, can be obtained with a similar procedure by initially assigning a sufficiently small value, numerically as

$$T_{ini}(t_{ini}) = -\mu N(t_{ini}). \tag{3.10}$$

This corresponds to a case that the steady state slider position is forced to stay at the farthest point just before the negative slip with respect to the relative displacement coordinate as shown in Figure 20c.

This numerical approach for the determination of response limits is specifically developed for mechanical systems with wedge dampers modeled by utilizing two point contact elements. A more generalized analysis for structures with more than two contact elements will be discussed in the next chapter. In the following section, the application of the proposed approach is presented by means of a simple hypothetical system that imitates a turbomachinery application with wedge dampers.

3.3 Case Study with a Simple System

In this section, a simplified model representing one of the most common types of friction dampers in turbomachinery applications, wedge dampers, is studied.

3.3.1 Lumped Parameter Model

The model investigated is constructed using an assembly with three lumped masses simulating two adjacent blades and a wedge damper interposed in between them as shown in Figure 25. The model utilized is a 6 degree-of-freedom (DOF) system where each mass has two different generalized coordinates allowing the horizontal and the vertical displacements in global x and global y directions, respectively. Two bodies with a mass value of m located at the left and the right hand-sides represent the bladed disk assembly itself and have exactly the same system properties as in the case of tuned bladed disks. Both of them are grounded with a spring whose stiffness value is k and have cross coupling between each other's x and y directions with a stiffness value of k_{12}. These springs physically represent the stiffness of large disks attached to rotor shaft and provide the coupling between vibrating bodies. It should also be noted that the motion of each mass in x and y directions are also coupled with a stiffness value of k_{xy}. These springs are also attached here to simulate and to capture the blade dynamics in this simple system. Each body has one contact point located on an inclined surface with the damper that is pressed against to the vibrating bodies with a static pre-load, F^0. This load corresponds to the centrifugal force that presses the damper to the blades in turbomachinery applications. The damper itself is modeled as a free

body without applying any boundary condition, allowing for rigid body motions. Its x and y displacements are also coupled to each other by means of a spring with a value of k_D, which is not explicitly sketched in Figure 25 for a clear view. Its image can be visualized exactly the same as the spring with stiffness k_{xy}, but on the damper. k_D physically corresponds to internal stiffness of the free wedge damper that involves into the bladed disk system as a secondary structure. A more compact expression of the generalized coordinates, linear system and damper matrices (with subscription D) and dynamic excitations are as

$$\mathbf{q}=\begin{Bmatrix} x_1 \\ y_1 \\ x_2 \\ y_2 \end{Bmatrix},\quad \mathbf{M}=\begin{bmatrix} m & 0 & 0 & 0 \\ 0 & m & 0 & 0 \\ 0 & 0 & m & 0 \\ 0 & 0 & 0 & m \end{bmatrix},\quad \mathbf{C}=\begin{bmatrix} c & 0 & 0 & 0 \\ 0 & c & 0 & 0 \\ 0 & 0 & c & 0 \\ 0 & 0 & 0 & c \end{bmatrix},$$

$$\mathbf{K}=\begin{bmatrix} k+k_{xy}+k_{12} & -k_{xy} & -k_{12} & 0 \\ -k_{xy} & k+k_{xy}+k_{12} & 0 & -k_{12} \\ -k_{12} & 0 & k+k_{xy}+k_{12} & -k_{xy} \\ 0 & -k_{12} & -k_{xy} & k+k_{xy}+k_{12} \end{bmatrix},\quad \mathbf{F}_{exc}=\begin{Bmatrix} F_{x,1} \\ F_{y,1} \\ F_{x,2} \\ F_{y,2} \end{Bmatrix}.$$

$$\mathbf{q}_D=\begin{Bmatrix} x_D \\ y_D \end{Bmatrix},\ \mathbf{M}_D=\begin{bmatrix} m_D & 0 \\ 0 & m_D \end{bmatrix},\ \mathbf{C}_D=\begin{bmatrix} 0 & 0 \\ 0 & 0 \end{bmatrix},\ \mathbf{K}_D=\begin{bmatrix} k_D & -k_D \\ -k_D & k_D \end{bmatrix},\ \mathbf{F}_{exc,D}=\begin{Bmatrix} 0 \\ 0 \end{Bmatrix}.$$

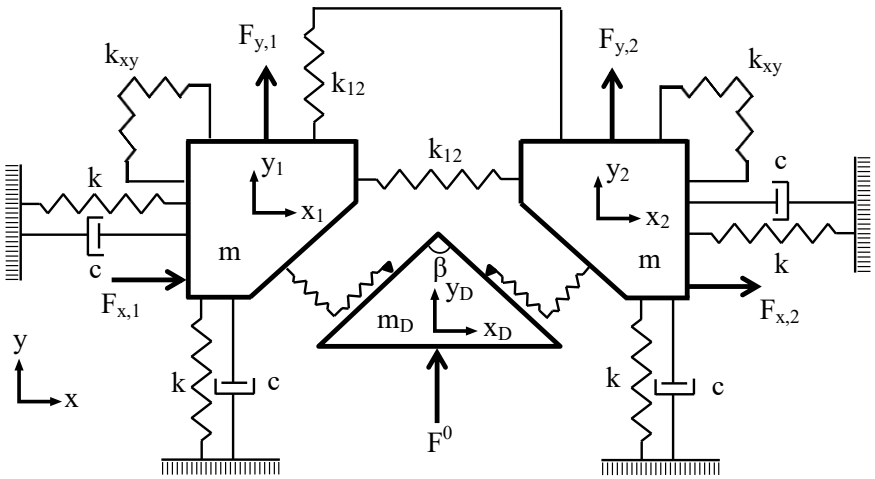

Figure 25: Full view of the lumped parameters system

The model is harmonically forced in y and x directions from the first and the second masses, respectively. This type of forcing is intentionally applied in order

to excite several modes of the system. Therefore, it enables the investigation of the damper kinematics and the variability of the nonlinear responses under different contact conditions. All of the system parameters are given in Table 1. It should be noted that despite the model simplicity, it can be considered as a general framework for the construction of highly specialized and detailed FE models of mechanical structures having joint interfaces and showing frictional behaviors.

Table 1: Lumped system and excitation parameters

Parameter	Value	Parameter	Value
m	1 kg	k_D	$3x10^5$ Nm^{-1}
m_D	0.1 kg	$F_{x,1}$	0
c	20 $N(m/s)^{-1}$	$F_{y,1}$	$20\sin(\omega t+\pi)$ N
k	$3x10^5$ Nm^{-1}	$F_{x,2}$	$5\sin(\omega t)$ N
k_{xy}	$3x10^5$ Nm^{-1}	$F_{y,2}$	0
k_{12}	$7x10^5$ Nm^{-1}		

The geometry of the damper model is intentionally selected as isosceles triangle with an apical angle β and base angles α as shown in Figure 25. This configuration gives an opportunity to examine the more general cases in which the static pre-load applied to the damper is not normal to the contact points. Furthermore, all the generalized coordinates will be coupled through this geometry in both x and y directions, which represents more realistic case scenario of real life applications with wedge dampers. It should also be noted that, in this way, a parametric study of the effect of different design alternatives by varying the angles β and α is also studied. The contact elements utilized in both sides share the same tangential (k_t) and normal (k_n) contact stiffness with a value $3x10^5$ Nm^{-1}. Coefficient of friction (μ) is taken 0.5. Fundamental harmonic is utilized in the dynamic balance equations.

Dynamic contact forces generated on the contact points are shown in Figure 26a. It should be noted that a coordinate transformation is needed from global to local in order to be able to calculate correct relative displacements and contact forces. The local coordinate systems (with superscription r) used in the calculations are also shown in Figure 26b. The transformations for both sides are applied as

$$\begin{Bmatrix} x_1^r \\ y_1^r \end{Bmatrix} = \begin{bmatrix} \cos(\alpha) & \sin(\alpha) \\ -\sin(\alpha) & \cos(\alpha) \end{bmatrix} \begin{Bmatrix} x \\ y \end{Bmatrix} \text{ and } \begin{Bmatrix} x_2^r \\ y_2^r \end{Bmatrix} = \begin{bmatrix} \cos(\alpha) & -\sin(\alpha) \\ \sin(\alpha) & \cos(\alpha) \end{bmatrix} \begin{Bmatrix} x \\ y \end{Bmatrix}. \quad (3.11)$$

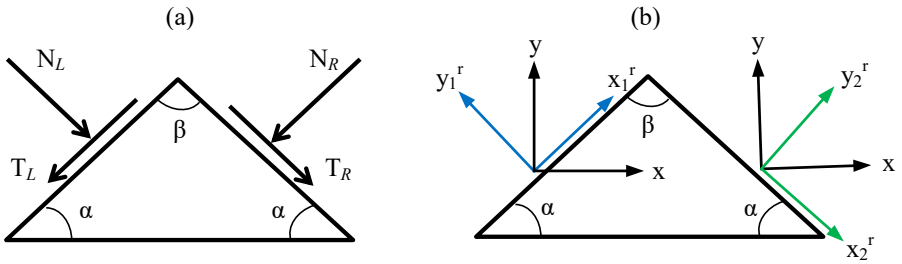

Figure 26: (a) Contact forces on the damper, (b) Coordinate systems

3.3.2 Multiple Responses and Limits

As mentioned in Section 3.2.2 that there should be a cross coupling between the tangential and the normal forces in the contacts in order to obtain multiple response phenomena. For this purpose, the generalized coordinates in the system are coupled to each other with the stiffness k_{xy}. In addition, the apical angle, β, and base angles, α, in the following analyses are set equal to 120° and 30°, respectively; which provides a damper induced cross coupling into to the system as generally explained in Eq. (3.5). In this way, the coupling strength that directly affects the multiple response range is increased. The following results are presented for the generalized coordinate of the right mass vertical displacement, y_2.

Figure 27 depicts the displacement amplitudes of the free linear (without damper) and fully stuck linear (with damper) cases for the entire frequency range. All the mode shape sketches of the free linear case are also shown in the same figure. Additionally, eigenvector values for each mode are also presented in Table 2 for a better visualization of the linear system dynamics. The first mode is the one where in-phase motion takes place in the all coordinates. Thus, the presence of the damper for this mode is not effective at all since there is no relative displacement between the DOFs. Natural frequency for the first mode also slightly decreases due to the extra damper mass. However, for the second mode, although the system makes an in-phase motion with respect to x_1–x_2 and y_1–y_2 directions, out-of-phase motions that take place in x_1–y_1 and x_2–y_2 coordinates provides a relative displacement due to cross coupling provided by stiffness k_{xy}. Hence, the damper affects the linear system and introduces stiffness as in the cases of the third and the fourth modes, where the out-of-phase motions between the generalized coordinates are much clearer.

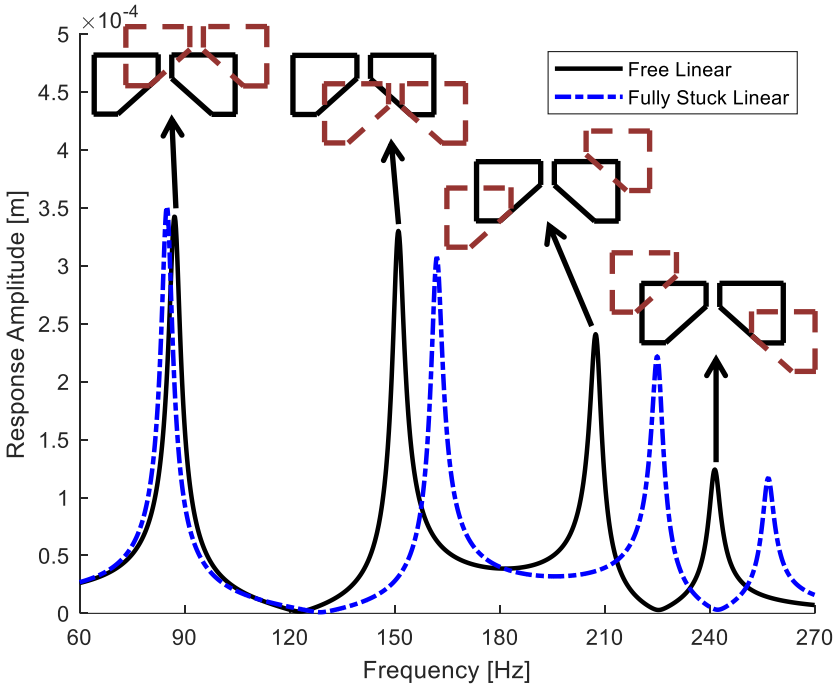

Figure 27: Frequency response for two linear cases without and with the damper

Table 2: Eigenvector values for each mode

Generalized Coordinates	1st Mode	2nd Mode	3rd Mode	4th Mode
x_1	1	1	-1	-1
y_1	1	-1	-1	1
x_2	1	1	1	1
y_2	1	-1	1	-1

Figure 28 shows the displacement amplitudes of the free Linear Response (LR), fully stuck LR and Nonlinear Responses (NLR) around the second and the third resonance regions. It should be noted that the response amplitudes presented in Figure 28 represent the amplitudes of dynamic components with excluded static components. Initial pre-load applied on the damper, F^0, is 120 N for each nonlinear case, which can be considered as a relatively high value and a moderate value for the second and the third resonances, respectively. This is expected since the dynamic external forces mostly excite the system's third mode. The damper efficiently dissipates the energy and damps the response in both resonance regions. However, it should be noted that the nonlinear responses shown in Figure 28 are obtained for the totally same system without changing any input parameters. Although the displacement amplitudes computed around the second

resonance overlap with each other, they vary in the third resonance region, which shows multiple solutions exist. It is worth noting that the iterations during the nonlinear analysis for each curve within the range are fully converged, which makes all the solutions true. The only parameter that is changed for each analysis is the initial guess of the tangential force for AFT scheme before starting the computation of the contact forces. Five different initial values for $T(t)$ at $t = t_{ini}$ within the range of $\mu N(t)$ and $-\mu N(t)$ end up with five particular converged responses, where the boundaries are indicated with red and brown dotted curves, respectively. The upper and the lower response limits are calculated with the limit tangential force criteria as explained in Section 3.2.3. The limiting cases, which give the boundaries, correspond to nonlinear analyses performed with $T_{max}(t)$ and $T_{min}(t)$, that are ensured to obtain by assigning the initial guess values as the limits ($\mu N(t_{ini})$ and $-\mu N(t_{ini})$) for $T(t)$, respectively, as explained in Eqs. (3.9) and (3.10). The other three curves staying within the range are obtained by using three intermediate arbitrary initial values for $T(t)$, which results to three different contact forces at steady state with the values of $T_{int1}(t)$, $T_{int2}(t)$ and $T_{int3}(t)$.

To check if the forces on the damper are under an equilibrium condition and the resultant force is zero for each harmonic, the force balance is investigated for each nonlinear analysis. The resultant forces in the global x and y directions (R_x and R_y) for the 0^{th} and 1^{st} harmonics are calculated as

$$\mathbf{R}^0 = \mathbf{K}_D \mathbf{q}_D + \mathbf{F}^0_{n,D} - \mathbf{F}^0_{ext,D}$$

$$\begin{Bmatrix} R^0_x \\ R^0_y \end{Bmatrix} = \begin{bmatrix} k_D & -k_D \\ -k_D & k_D \end{bmatrix} \begin{Bmatrix} x^0_D \\ y^0_D \end{Bmatrix} + \begin{Bmatrix} F^0_{x,n,D} \\ F^0_{y,n,D} \end{Bmatrix} - \begin{Bmatrix} F^0_{x,ext,D}=0 \\ F^0_{y,ext,D}=120 \end{Bmatrix}, \tag{3.12}$$

and

$$\mathbf{R}^1 = \left(\mathbf{K}_D - \omega^2 \mathbf{M}_D\right) \mathbf{q}_D + \mathbf{F}^1_{n,D} - \mathbf{F}^1_{ext,D}$$

$$\begin{Bmatrix} R^1_x \\ R^1_y \end{Bmatrix} = \begin{bmatrix} k_D - \omega^2 m_D & -k_D \\ -k_D & k_D - \omega^2 m_D \end{bmatrix} \begin{Bmatrix} x^1_D \\ y^1_D \end{Bmatrix} + \begin{Bmatrix} F^1_{x,n,D} \\ F^1_{y,n,D} \end{Bmatrix} - \begin{Bmatrix} F^1_{x,ext,D}=0 \\ F^1_{y,ext,D}=0 \end{Bmatrix}, \tag{3.13}$$

respectively.

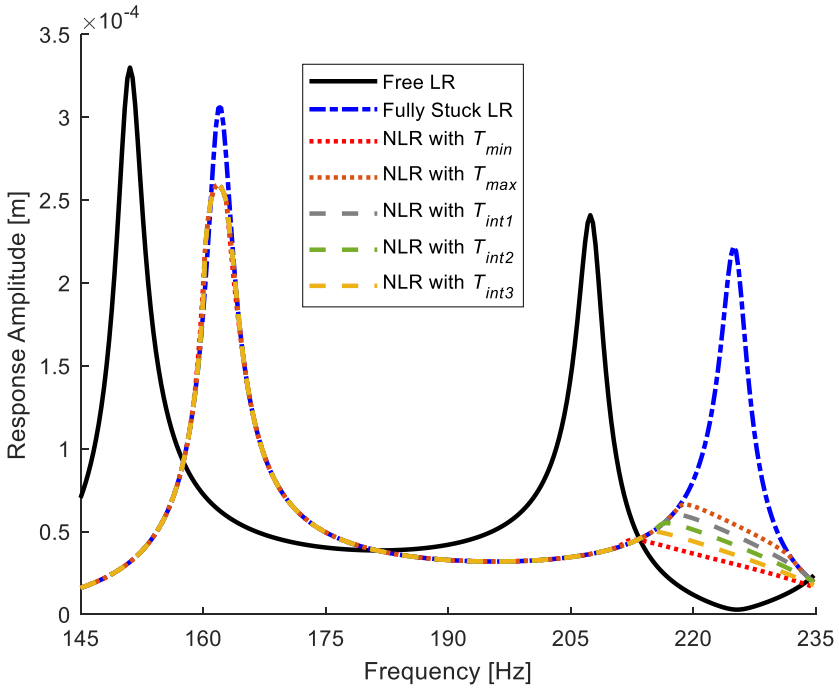

Figure 28: Nonlinear responses around the second and the third resonance regions

Figure 29a-e shows the resultant forces on the damper for five different nonlinear analyses presented in Figure 28, throughout the whole frequency range. This information is depicted just for a cross check of the nonlinear analyses to understand if the damper is both statically and dynamically in equilibrium. The results show that the damper is balanced properly, as expected, within all the analyses performed with different initial guess values of $T(t)$ at $t = t_{ini}$. Small deviations are due to round-off errors. These results physically mean that the force balance on the damper is achieved in a non-unique way, and this condition leads to the nonlinear response variability as shown in Figure 28.

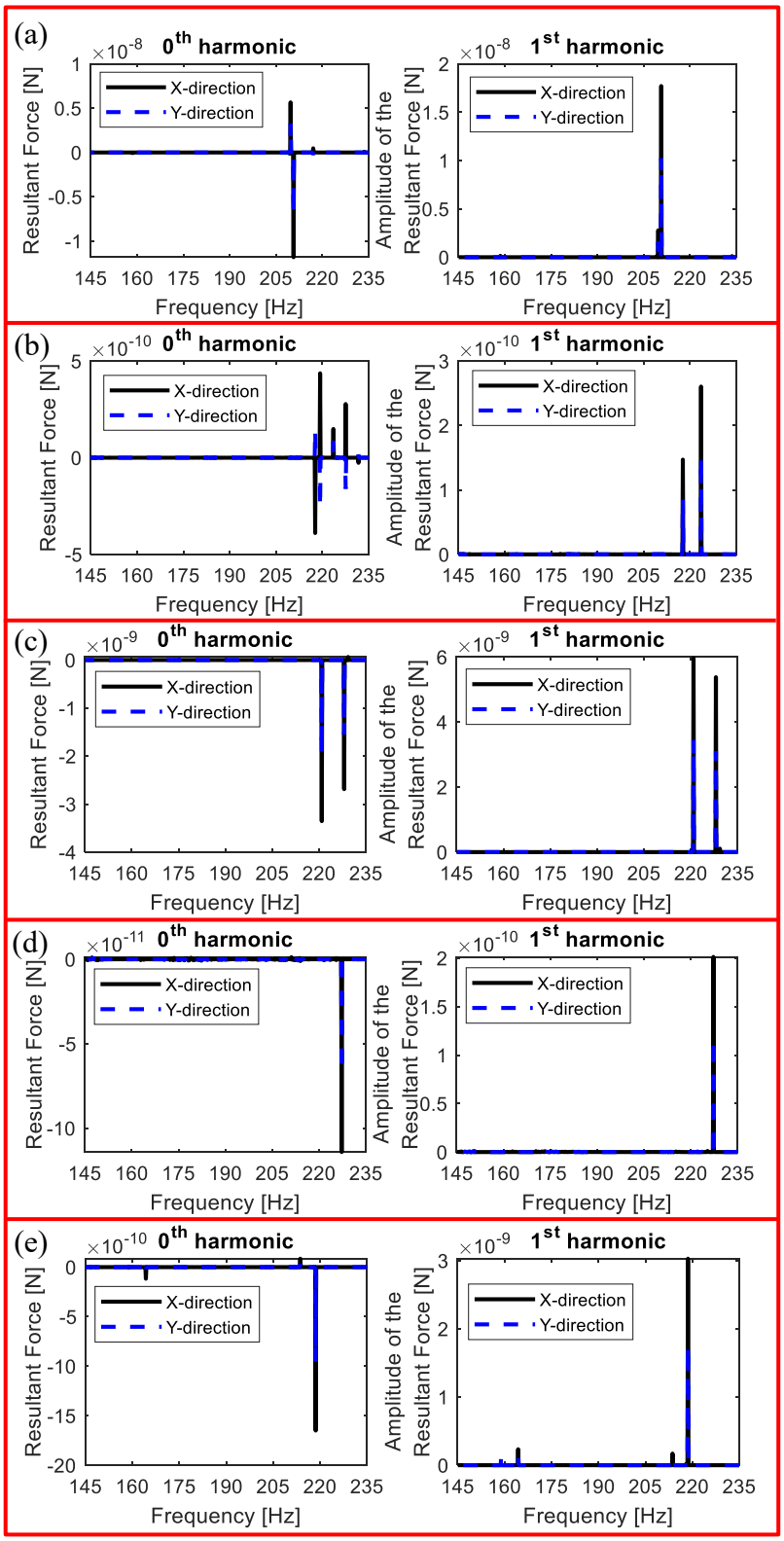

Figure 29: Resultant forces on the damper: (a) T_{min}, (b) T_{max}, (c) T_{int1}, (d) T_{int2}, (e) T_{int3}

It is interesting to note that the multiple solutions exist only around the third resonance region, which shows the uncertainty phenomenon of the tangential forces is not observed for the second resonance region. This phenomenon occurs due to different contact conditions, which changes the effective stiffness and the equivalent damping terms of the contact elements for particular resonances. For a better illustration, consider Figure 30 depicting the response graphs including the steady state contact states of the both dry friction elements throughout the frequency range considered in the nonlinear analysis. It is worth noting that the initial guesses of the tangential force in these analyses are assigned as an arbitrary value which is representatively selected among an infinite number of possible alternatives within the range. Figure 30a depicts one of the multiple displacement curves around the third resonance region, where one of the contacts is under fully stuck condition for the entire frequency interval, while the other contact makes an alternating stick–slip motion for a specific range. In a more detailed explanation, red circles represent the frequency points where both contacts are fully stuck; while green stars stand for the frequencies in which one of the contact elements slips during its cycle. The uncertainty of the first contact element's tangential force leads to obtain non-unique solutions for the frequency range shown by green stars. However, the second resonance region shown in Figure 30b shows that the first and the second contact elements make an alternating stick–slip and an alternating stick–slip–lift-off motion, respectively, for the frequency points highlighted by blue squares. These contact states remove the uncertainty phenomenon as shown in Figure 21 and Figure 22 since the friction forces become unique. Hence, the effective stiffness and the equivalent damping of the contact elements are the same for any initial guess value, which provides to compute a unique response at steady state.

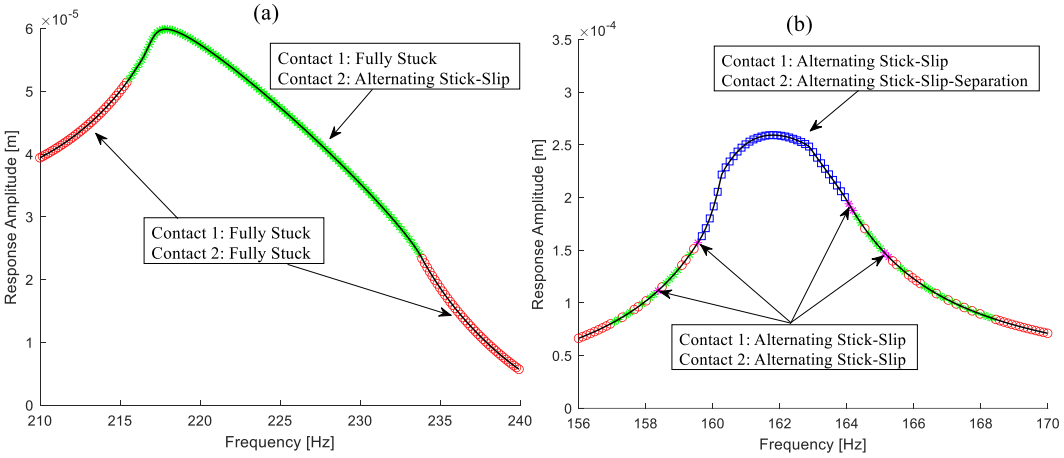

Figure 30: (a) Contact states around the third resonance region, (b) Contact states around the second resonance region

In Figure 31a, a general behavior of the nonlinear response curve corresponding to different static pre-loads applied on the damper is shown. The response is damped for the second and the third resonance regions as the pre-load decreases. The variability range is also highlighted around the third resonance region. It is seen that the range creates a closed region for relatively high pre-loads (400 N and 130 N). It shrinks with decreasing pre-loads and totally disappears after a certain value (60 N in this case). In order to explain this, it is worth mentioning that the effect of static pre-load on the maximum vibration amplitude is not regular. In particular, the maximum response amplitude starts decreasing with larger pre-loads from free linear case up to an optimum value. This observation is specific for low pre-loads. If the pre-load values keep rising beyond the optimum value, the response starts increasing again up to the fully-stuck case, where the system behaves as a linear one and no friction damping is provided by the damper. On the other side, the effect of static pre-load values on the resonance frequency is regular, where its value always increases as the pre-load becomes larger. As a result, for relatively high pre-loads (as 130 N and 400 N in Figure 31a), the upper and the lower response boundaries clearly create a closed region (colored in purple and green) where intermediate responses will end up to. On the other hand, for moderate pre-loads (60 N) at which the system would vibrate nearby the optimum configuration, the behavior is more complicated. The boundary response that corresponds to T_{max} is located on the right-hand side of the optimum, while the boundary response that corresponds to T_{min} stays on the left side, as shown in Figure 31b. In this case, it is not possible to clearly identify a closed region where the intermediate responses will end up to.

For instance, the resonance amplitudes of two intermediate curves computed by setting $T = T_{int1}$ and $T = T_{int2}$ lie outside the envelope of the two boundary responses. It should be stated that such a transition region is perfectly in line with the physics of frictionally damped dynamic systems.

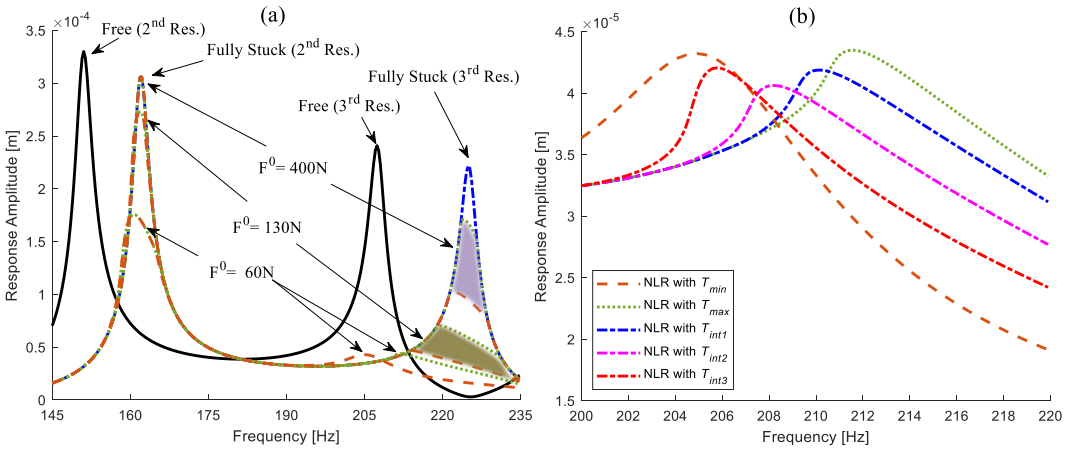

Figure 31: (a) Nonlinear responses for different static pre-loads, (b) Nonlinear responses for a moderate static pre-load, F^0 = 60N, nearby the optimum conditions

Figure 32a shows the limits of the optimal curve around the third resonance region. It can be seen that the maximum amplitude starts from the free linear case with low pre-loads and saturates at the fully stuck linear case with high pre-loads. The response range varies considerably, showing the uncertainty may result in huge differences in the maximum response amplitudes. As previously explained, optimal curves have a local minimum, the so-called optimum point, around 45-80 N, which corresponds to the transition region shown in Figure 31b. A closer view for this interval with three additional curves representing the ones obtained with intermediate values is given in Figure 32b. Due to the non-regular relationship between the pre-load and the maximum response amplitude, the two response boundary do not represent the maximum and the minimum limits at each frequency. Nevertheless, the response boundaries allow determining the range of static pre-load values at which the optimum response is expected. Figure 32c shows five different hysteresis curves obtained for the same static pre-load, F^0 = 80 N at the corresponding resonance frequencies. It can be seen that the slipping contact element has completely different hysteresis curves corresponding to the limits and some other intermediate tangential force values of the sticking element. This indicates that different transition points with non-unique tangential forces change the damping characteristic of the overall system since k_{eq} and c_{eq} eventually become different for each case. The resonance frequency limits are

also shown in Figure 32d. The lower and the upper limits start from the same initial resonance value since both of the contacts tend to make an alternating stick–slip motion for relatively low pre-loads. This condition removes the uncertainty phenomenon and allows computing a unique response. Similarly, the limits overlap each other for high pre-loads at the fully stuck linear resonance frequency.

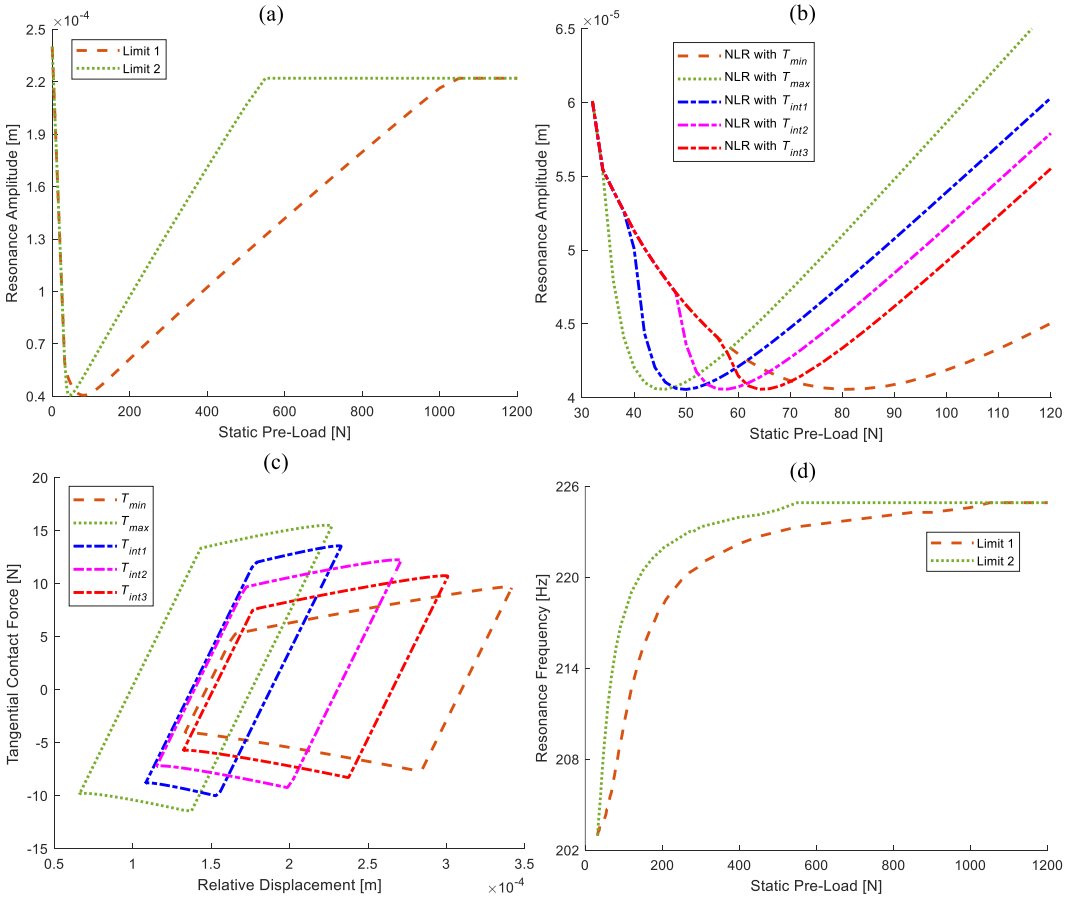

Figure 32: (a) Optimal curve limits, (b) Optimal curves for a smaller pre-load range, (c) Hysteresis curves for a static pre-load, F^0 = 80 N, (d) Resonance frequency limits

3.3.3 The Effect of Damper Geometry on Multiple Responses

In this section, the effect of different damper geometries by changing the apical angle, β, and base angles, α, on multiple response behavior and limits is investigated.

Damper induced cross coupling is directly determined by β and α. As the damper geometry changes, the interaction between the tangential and the normal forces varies. For this purpose, β and α are firstly set equal to 180° and 0°, respectively, where the damper becomes perfectly flat in horizontal direction. Figure 33a depicts the fully stuck linear and nonlinear displacement amplitudes around the third resonance region. Nonlinear response graphs represent the upper and lower limits of the variability range. The lower the static pre-load is, the more damped response obtained, as expected. However, comparing with the previous situation where β = 120°, the response variability in this case is extremely low. Almost unique response is obtained at steady state whichever initial guess value is used in the tangential force calculation. Because, the damper induced cross coupling is completely removed with flat damper and only interaction between x and y coordinates are provided by stiffness k_{xy}. Hence, the range for the multiple responses reduces substantially. Response variability is only obtained around very limited regions where one of them is enlarged for a closer view in Figure 33a. Figure 33b shows the contact states during the nonlinear analysis performed with F^0 = 250 N. It should be noted that the removal of damper induced cross coupling provides to obtain an alternating stick–slip motion in both contacts, which almost vanishes the uncertainty phenomenon and ends up to an unique response. The only frequency points in which the uncertainty is observed are the ones where one of the contacts is fully stuck while the other one makes an alternating stick–slip motion, which is highlighted with green stars. Multiple responses are possible for these small regions where one example is shown with a closer view in Figure 33a.

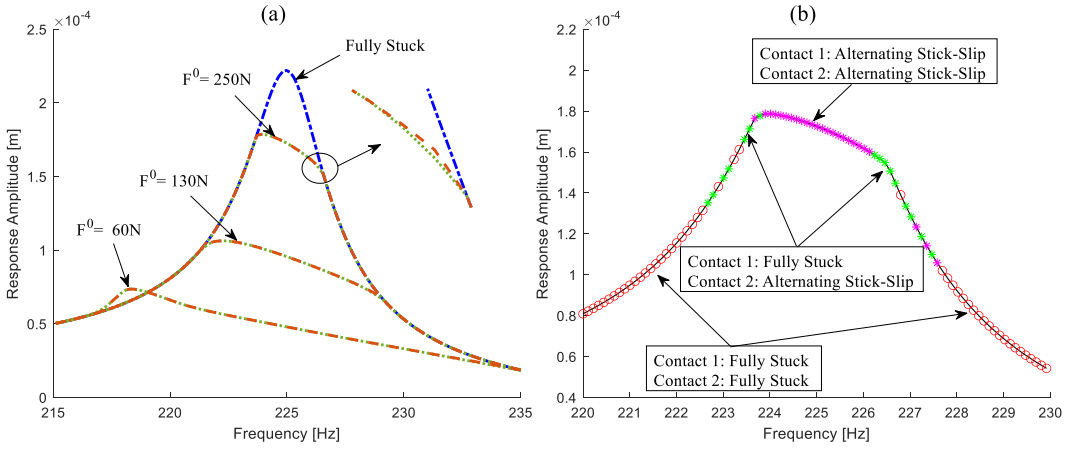

Figure 33: (a) Nonlinear responses for flat damper with different static pre-loads, (b) Contact states around the third resonance region with the static pre-load, F^0 = 250 N

Figure 34a presents a more general view about the range of the variability in the frequency response with different apical angles, β, for the values higher than 90°. The upper and the lower curves with the same color for the same angles represent the limits. It is noted that as the apical angle increases from 90° to 180°, i.e. from isosceles right triangle shape to flat damper geometry, the response variability range decreases substantially. The largest range is obtained in case of 90° apical angle due to the fact that the damper induced cross coupling in contact forces is the most effective on the uncertainty phenomenon with this geometry. On the other hand, the response is almost obtained unique when β is 180°. Moreover, it should be noted that there is no monotonic decrease in the variability range as β increases from 90° to 180°. The range obtained when β = 160° is larger than the one obtained with β = 150° as can be seen in the closer view shown in Figure 34a. This indicates that the change of the damper geometry with different angles is not the only parameter affecting the pattern of the variability range. This observation leads that the static and the dynamic parts in the force balance equations cannot be separated in order to make a prior prediction for the behavior of the variability range. Full dynamic analysis is required to correctly observe the pattern change in the range with different geometries. It is also worth noting that all the nonlinear analyses for different angles in Figure 34a are performed with particular pre-defined static pre-loads applied on the damper. The change of the variability range in optimal curves is also given in Figure 34b, where the resonance displacement amplitudes are shown with increasing static pre-load. The upper and the lower limits for the flat geometry, i.e. β = 180°, lies on the same line. They are separated from each other as the angle decreases and the range reaches to the maximum width when β = 90°. However, the same non-monotonic behavior as in the case of frequency response graph is valid here, as well. The range for β = 150° is larger than the one obtained for β = 160°, which breaks the monotonic behavior in the variability pattern. It should also be noted the higher pre-loads result in a wider range, while all the curves show similar behavior for relatively low pre-loads that is squeezed in a narrow region. The reason for this fact is that both contacts tend to have an alternating stick–slip or an alternating stick–slip–lift-off motion under a low static pre-load, which removes the uncertainty and results with unique response.

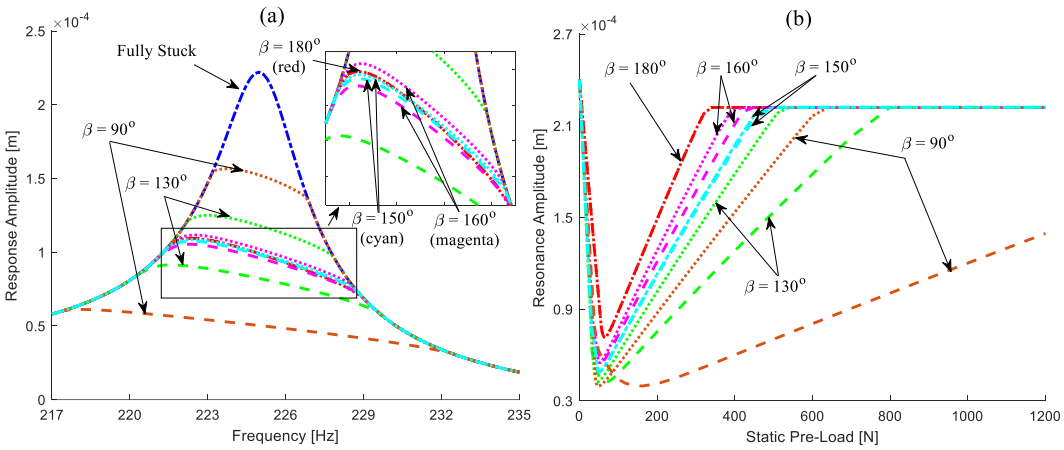

Figure 34: (a) The change of variability range in frequency response and (b) In optimal curves with different high apical angles, β

Figure 35a illustrates a straight diminishing behavior in the variability range as the apical angle, β, decreases from 90°. This shows that the effect of damper induced cross coupling on the uncertainty weakens with reducing β values. However, it is worth noting that when β is set equal to a value lower than 90°, increasing static pre-load makes the damper tend to have more slip motion instead of stick, as opposed to the previous cases. Because, in this case, the pre-load applied on the damper contributes to the tangential component of the contact force more than the normal force direction due to the orientation of the simple system used. Hence, the contacts between the damper and the system are totally lost after a certain value. In order to overcome this problem, in addition to the static pre-load exerted on damper, another static pre-load is applied on the first and the second masses in x_1 and $-x_2$ directions, respectively. In this way, it is simulated that the masses are pressed through the damper and the damper is squeezed in between the masses, which enables to have stick state and keeps the damper in contact with the system during the periodic motion. It is also worth noting that this type of force enforcement is applied in many applications of vehicle dynamics for the structures with wedge dampers. Resonance amplitude limits with respect to varying static loads applied on the masses, not on the damper, are presented in Figure 35b. These curves are defined in this study as pseudo-optimal curves, where the initial pre-load applied on the damper is kept constant at 500 N. The variability range becomes smaller with decreasing apical angle as obtained in Figure 35a. It should also be noted that the upper and the lower limits for each β value are parallel to each other since the pre-load on the damper is not a variable parameter anymore, which makes the response variability range constant with increasing pre-load until to reach fully stuck linear resonance response value.

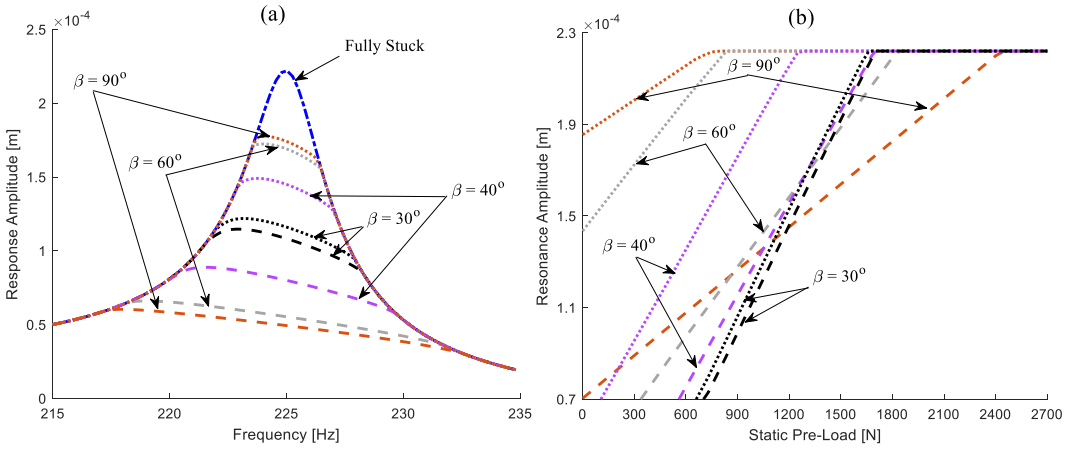

Figure 35: (a) The change of variability range in frequency response and (b) In pseudo-optimal curves with different low apical angles, β

3.4 Summary

This chapter presents the underlying physics of the uncertainty phenomenon and shows its effects on the nonlinear dynamic response behavior of structures with contacts. The variability is depicted by utilizing a simple lumped model that imitates a turbomachinery application with a wedge damper pressed against two vibrating adjacent blades. A numerical method is offered to determine the response limits among multiple solutions. Despite the model simplicity, this chapter presents the first numerical technique that can be utilized to determine the dynamic response limits among multiple solutions, in the context of non-unique friction force uncertainty.

Chapter 4

Determination of the Response Boundaries with a Systematic Approach

Multiple alternatives of possible steady state solutions bring much more complexity to the interpretation of the results. From the engineering point of view, the boundaries always take the core attention and need to be determined for complex structures. In this chapter[3], a generalized method which aims to detect the response boundaries regardless of the system's complexity is developed. The method is demonstrated on a realistic large turbine bladed disk having the contact on the blade tip with shrouds and in the root with blade-disk interfaces.

4.1 Theoretical Background

4.1.1 Multiple Responses

Even though the computation of multiple responses has been shown in the previous chapter, it is worth explaining it here briefly for more complex structures.

[3] Part of the work described in this chapter has been previously published:
"Ferhatoglu, E., & Zucca, S. (2021). On the non-uniqueness of friction forces and the systematic computation of dynamic response boundaries for turbine bladed disks with contacts. *Mechanical Systems and Signal Processing*, *160*, 107917."

Consider an arbitrary body with contact interfaces, modeled by means of multiple Jenkins elements, as the one shown in Figure 36. In this system, consider a steady state dynamic configuration, in which elements A and C are in a fully stuck cycle, while the other ones (B and D) are undergoing an alternating stick-slip motion. The static tangential components T^0_A and T^0_C are non-unique. This means that the static normal components of the slipping contact elements (N^0_B and N^0_D) can also be non-unique due to the static equilibrium of the body. As a result, the equivalent stiffness and damping at contacts B and D may change with different values of N^0_B and N^0_D (see Eqs. (3.2) and (3.3)). This leads to multiple contact force vectors, which in turn to multiple response levels for the same physical system under the identical excitation frequency and forces. It is important to note that multiple responses only exist in case of partial slip. If all the contact elements (A-D) are in a full stick cycle, k_{eq} and c_{eq} do not differ and the solution ends up a unique linear response. Similarly, if the contact undergoes a gross slip motion (i.e. all elements enter the slip and/or the separation state during the periodic motion), only one single solution occurs since the variability comes from the fully stuck elements.

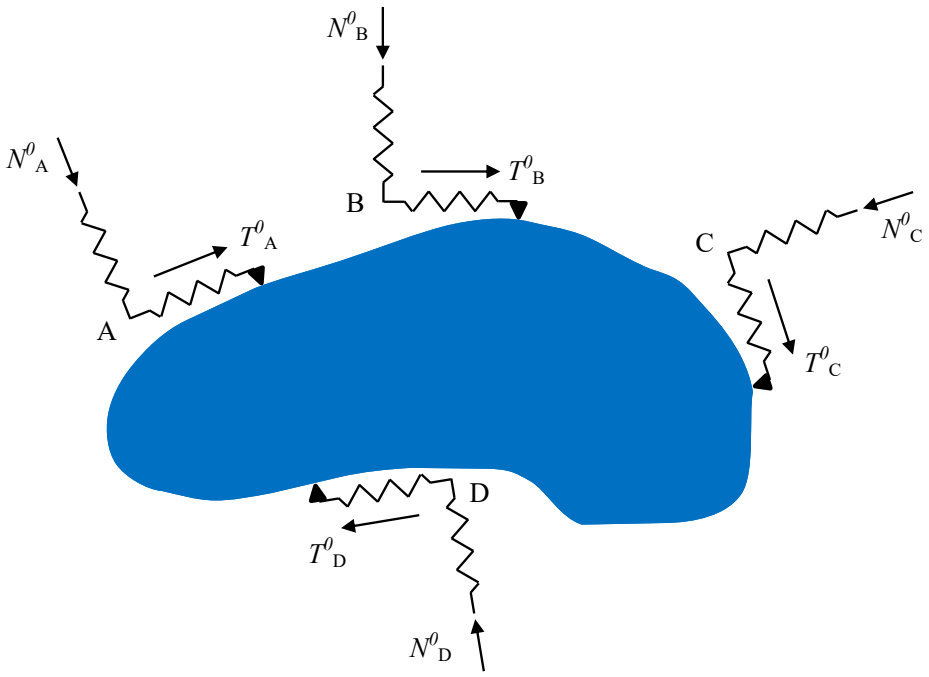

Figure 36: A body with multiple contact elements

4.1.2 Periodic Response Boundaries with an Optimization Algorithm

First, consider the work done by an external periodic force for the fundamental sector per one vibration cycle as

$$W = \int_0^{2\pi/\omega} \dot{\mathbf{q}}^{\mathrm{T}}(t)\,\mathbf{f}_{ex}(t)\,dt\,. \tag{4.1}$$

For a vibrating system under a steady state condition, the main energy input to system due to periodic excitation is equivalent to the work done, and it is balanced by the sum of dissipated energy, ΔW_{dis}, for the corresponding response amplitude level as

$$W = \Delta W_{dis}\,. \tag{4.2}$$

It should be noted that Eq. (4.2) is valid for a vibration-in-unison pattern, which means all of the system points reach their maximum oscillation amplitudes and pass through zero simultaneously. Reduction of the vibration response in frictional systems is associated with the dissipated energy. However, in turbine bladed disks, the amount of dissipated energy is not an absolute indicator for a meaningful interpretation of damping present in the system. In order to quantify damping, loss factor, η, defined as the proportion of the total energy dissipated over one cycle to the maximum potential energy, U_{pot}, corresponding to the vibration amplitude (Siewert et al., 2008) is used, and it is shown as

$$\eta = \frac{\Delta W_{dis}}{2\pi U_{pot}} = \frac{\Delta W_{visc} + \Delta W_{fric}}{2\pi\left(U_{blad} + U_{cont}\right)}\,, \tag{4.3}$$

where ΔW_{visc}, ΔW_{fric}, U_{blad} and U_{cont} represent the dissipated energy by viscous material damping, dissipated energy by friction damping, potential energy of the linear bladed disk without any contact and potential energy due to contacts, respectively.

Dissipated energy by viscous damping and potential energy for one sector of the bladed disk are directly related to linear matrices of the system and they can be calculated for one vibration period as (Siewert et al., 2008)

$$\Delta W_{visc} = \pi \times h\omega \times \left(\hat{\mathbf{q}}^{eo\cdot h}\right)^{*} \mathbf{C}^{eo\cdot h} \hat{\mathbf{q}}^{eo\cdot h}, \tag{4.4}$$

$$U_{blad} = \frac{1}{4}\left(\hat{\mathbf{q}}^{eo\cdot h}\right)^{*} \mathbf{K}^{eo\cdot h} \hat{\mathbf{q}}^{eo\cdot h}, \tag{4.5}$$

where superscript * is the Hermitian conjugate operator.

ΔW_{fric} and U_{cont} are the energy terms introduced by the contact. It should be noted that friction element has a complex contact force value, where the real part is associated with stiffness and imaginary part is related to damping. Hence, dissipated energy by friction damping and the potential energy due to contacts for one vibration period can also be computed as (Siewert et al., 2008)

$$\Delta W_{fric} = \pi \times h \times \Im\left(\left(\hat{\mathbf{q}}_n^{eo\cdot h}\right)^{*} \hat{\mathbf{f}}_n^{eo\cdot h}\right), \tag{4.6}$$

$$U_{cont} = \frac{1}{4}\Re\left(\left(\hat{\mathbf{q}}_n^{eo\cdot h}\right)^{*} \hat{\mathbf{f}}_n^{eo\cdot h}\right), \tag{4.7}$$

respectively. It has been shown in many studies that the loss factor, η, is the absolute parameter for quantifying the total damping in the system. Its numerical value in free or fully stuck linear cases, in which the only contribution is made by viscous damping, is expected considerably small since no dissipation is supplied by friction. When the slip takes place in contact interface, it starts increasing and may reach to its local maximum. Then, it can decrease to its minimum values. Detailed investigation of the behavior of loss factor with respect to changing several parameters can be found in the studies of Siewert et al. (2008) and Chen et al. (2021).

In the proposed approach, in addition to the unknown response vector, $\hat{\mathbf{q}}_n$, another variable unknown vector of multiplier coefficients, $\mathbf{m}$, is firstly defined as

$$\mathbf{m} = \left[m_1, m_2, \cdots, m_{N_c} \right]^T. \tag{4.8}$$

Here, N_c is the total number of sliders of the contact elements in the system. It is equal to the number of contact elements in case 1D Jenkins elements are used in

the system; while it is the double of the number of contact elements if 2D Jenkins elements are utilized. These multipliers do not directly appear in the nonlinear set of algebraic Eq. (2.4) as an unknown, but they can be considered as the so-called internal unknowns of the contact element. In particular, the i^{th} term of the vector, m_i, represents the ratio between the tangential force and the Coulomb limit force at the very beginning ($t = t_{ini}$) of the predictor-corrector loop used to determine the periodic contact forces in time domain as

$$T_i(t_{ini}) = m_i \times \mu N_i(t_{ini}) \qquad \left(i = 1, 2, \cdots, N_c\right), \tag{4.9}$$

with $-1 \le m_i \le 1$.

Once the number of 2D contact elements in the system is only one, two different multipliers (m_1 and m_2), which are the unknowns corresponding to two uncoupled in-plane tangential directions, need to be multiplied with the Coulomb limit force, separately. In this case, the response boundaries of the variability range are determined by setting $m_{1,2} = -1$ and $m_{1,2} = 1$, respectively, as developed in the previous chapter. On the other hand, if the number of 2D contact elements in the system is more than one, the response boundaries may not be determined manually by assigning some particular values to m; because, in this case, a huge number of combinations with different m values for each fully stuck element can occur. In order to overcome this limitation, an optimization algorithm to determine the response boundaries is proposed as

$$\begin{array}{ll} \text{minimize} & \eta \\ \text{with respect to} & [\hat{\mathbf{q}}^{\mathrm{T}}, \mathbf{m}^{\mathrm{T}}]^{\mathrm{T}} \\ \text{subject to} & \mathbf{R} = \mathbf{0} \end{array}, \tag{4.10}$$

where $\mathbf{R}$ is the residual of the nonlinear algebraic equations, as shown in Eq. (2.24).

In Eq. (4.10), η is the objective function to be minimized. Unknown variables of the optimization scheme are the response amplitudes of the fundamental sector, $\hat{\mathbf{q}}$, and the vector of multipliers, $\mathbf{m}$. The residual, $\mathbf{R}$, gets involved into optimization algorithm as the nonlinear constraints to be satisfied. The optimization algorithm given in Eq. (4.10) searches for the global minimum of the loss factor, which is the case for the lowest damping achieved in the system. Hence, the results of Eq. (4.10) give the upper boundary of the variability range in

response amplitudes. In order to find the lower boundary, the same logic can be used, but with the objective function corresponding to the opposite sign of the loss factor as

$$\begin{array}{ll} \text{minimize} & -\eta \\ \text{with respect to} & [\hat{\mathbf{q}}^{\mathrm{T}}, \mathbf{m}^{\mathrm{T}}]^{\mathrm{T}} \\ \text{subject to} & \mathbf{R} = \mathbf{0} \end{array} . \tag{4.11}$$

Nonlinear dynamic analysis of turbine bladed disks is computationally expensive due to the large number of contact points usually utilized in the models. The computational burden becomes even much higher with an additional optimization scheme, since the number of function evaluations severely increases. There are several optimization strategies in the literature for different purposes. In this thesis, the interior-point method is utilized. Basically, the interior-point approach approximates the original minimization problem as a sequence of equality constraint problems by adding a barrier function. Interested readers may refer to Byrd's papers (1999, 2000) for a more detailed description of the main theory of the interior-point algorithm. It is not presented here in this thesis. Implementation of the optimization process is performed by using *fmincon* built-in function in Matlab. The algorithm uses either a direct step or a conjugate gradient step to solve the approximate problem. The gradients are numerically computed by forward finite difference method. The convergence tolerance in the interior-point algorithm and the error tolerance for the nonlinear constraints are set to 10^{-8}. The whole solution process is briefly summarized in Figure 37.

It is worth mentioning that the main aim of this chapter is to develop a correct framework and to propose a systematic approach that determines the response boundaries with the help of an optimization algorithm. Offering a new numerical optimization method or assessing the most suitable optimization strategy for different problems is out of scope in this thesis. Here, the interior-point algorithm was sufficient for demonstration purposes of the developed methodology with satisfactorily accurate results and a manageable computational cost. However, there may be other optimization methods, which are more appropriate than the interior-point algorithm, for different applications. None of the optimization algorithms can be generalized and would give perfect results for each problem. Nevertheless, it can be said that the global optimization algorithms would be better in capturing the global minima of the objective function with an additional

computational cost. This can be seen as a trade-off between robustness and computational burden.

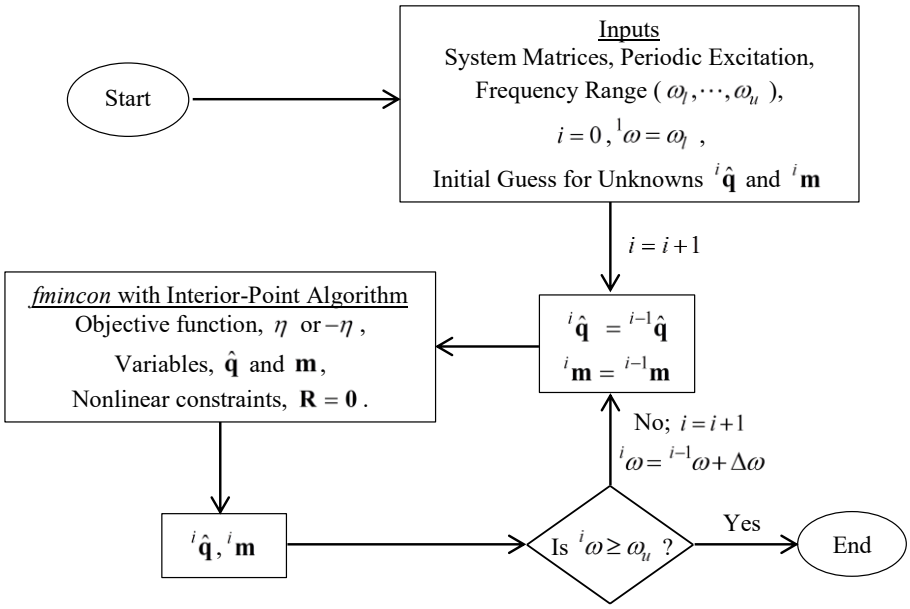

Figure 37: Flowchart of the solution scheme with the optimization algorithm

It is also worth mentioning that the objective function used in the scope of this thesis may not become the ultimate parameter that can be generalized for all the design analyses of turbine bladed disks; for instance, once the wear is also taken into account into analyses, or the nonlinear modal analysis is performed, different objective functions such as the dissipated energy itself or the maximum amplitudes may serve as a more generic choice. All these interpretations require further investigations. However, it should be underlined that the choice of the system's loss factor became satisfactorily successful in the determination of frequency response boundaries, as will be experimentally shown in the next chapters.

4.2 Application of the Proposed Method to the Turbine Bladed Disks

In this section, the proposed method is validated and demonstrated on a tuned turbine bladed disk. In order to show the general applicability of the method on different applications, possible source of friction damping at the shrouds and at the blade roots are investigated separately.

The model is constructed by using one of the commercial Finite Element programs. The following assumptions are made in the model:

- The bladed disk is considered totally tuned despite the fact that mistuning effects may play an important role on some special turbomachinery applications.

- Friction contacts are located at the blade shroud and at the blade root.

- The bladed disk considered in this study is constructed for the academic purposes and imitates a realistic geometry of industrial applications.

- The stiffening effect on the bladed disk structure due to rotation is neglected and the system matrices are assumed constant for the response computations within the entire rotational speed interval.

- Micro changes in the contact surfaces are neglected. Contact stiffness of the Jenkins element and friction coefficient of the surface (μ = 0.5) are assumed constant.

- Pre-loads and excitation forces are applied on discrete points.

- Linear damping matrix is created with Classical Rayleigh damping with only stiffness proportion, i.e. $\mathbf{C}_s = 10^{-5}\mathbf{K}_s$.

- The disk is considered rigid and excluded in the analyses. The blade is directly clamped from the root. Gyroscopic effects are neglected.

- In model order reduction with the Craig-Bampton approach, reduced system matrices are obtained by retaining the force nodes, response monitoring node and contact nodes as the master nodes as well as additional 50 modal coordinates.

It should also be noted that the coupled approach with the 0^{th} and the 1^{st} harmonics in harmonic balance equations is employed in the solution process. Influence of the higher harmonics on the system response accuracy is out of scope here and only the first harmonic is sufficient for the demonstration of the developed method.

4.2.1 Response Boundaries due to Friction Damping at the Blade Shrouds

The method is firstly applied to the shrouded blades, by assuming no friction damping at the blade roots. Figure 38a shows the FE model, boundary conditions, excitation nodes and response monitoring node. Since the blade root is clamped, cyclic symmetry only applies through the shroud contact nodes. Both static pre-load and dynamic excitation are applied from two forcing nodes located at the leading and at the trailing edge of a reference airfoil around 80% of the blade span. Two opposite axial static forces in z and –z directions, respectively, are applied in order to twist the blade and to establish contact at the shrouds during operation. In addition, periodic forces with 100 N amplitudes are applied from the same nodes in all three directions in order to excite multiple blade modes. Response node used to monitor the blade vibration is located in the center of the shroud.

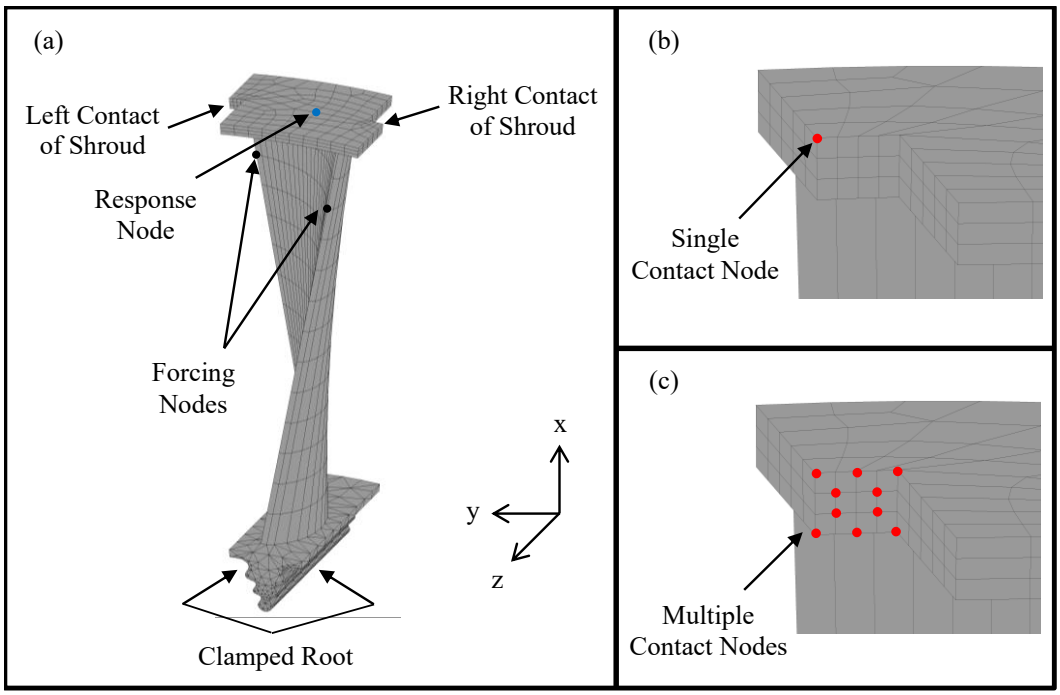

Figure 38: (a) Finite element model, (b) Single contact node on shroud surface, (c) Multiple contact nodes on shroud surface

Validation of the method is initially performed on the system with a single contact node as shown in Figure 38b. This first step is aimed to demonstrate that the proposed optimization algorithm is theoretically correct, since the developed method can capture the reference boundaries for a simple case whose solution can be found as explained in the previous chapter. Then, the number of contacts is increased and the results for a general case including several contact nodes, as depicted in Figure 38c, are presented. All the analyses are performed around the first bending resonance region with the 1st harmonic index. The deformed mode shape with the single contact node on the shroud is depicted for the whole turbine bladed disk and the fundamental sector in Figure 39a and Figure 39b, respectively. For a better illustration, a color variation is used to depict the mode deflection levels of different regions. Blue and red colors represent the minimum and maximum deflections, respectively, while the other colors show those in between them. In Figure 39a, the first nodal diameter among the blades can be clearly seen with the hypothetical blue line in the horizontal middle section of the assembly. In Figure 39b, the lateral bending mode is highlighted with an interference of the undeformed (black edge line) and the deformed mode shapes (colored).

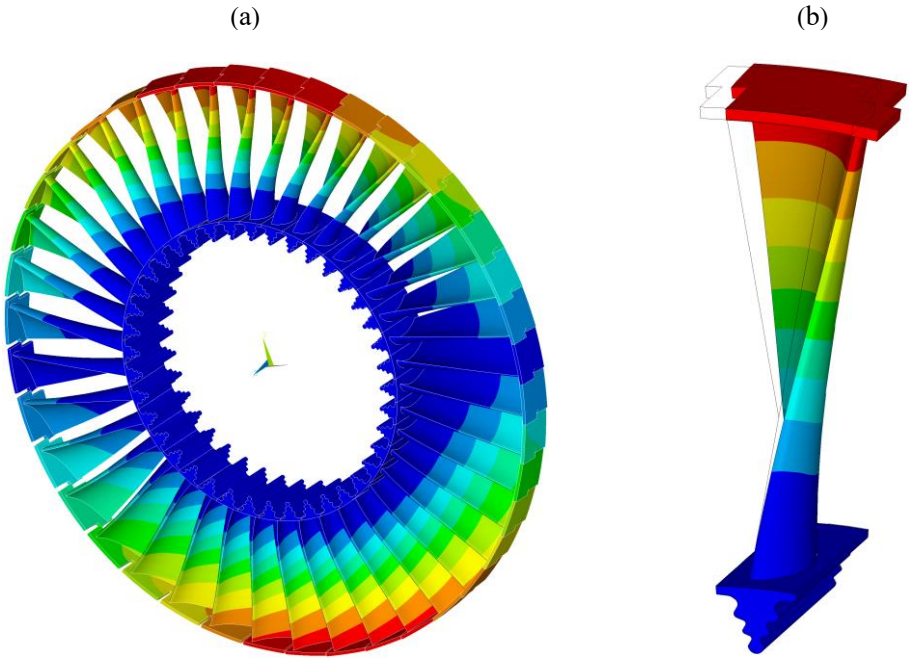

Figure 39: (a) Investigated mode shape of fully stuck linear system for the turbine bladed disk and (b) For the fundamental sector

A single contact in this case study includes one uncoupled 2D Jenkins element with two tangential forces in radial (x) and circumferential (y) directions and one normal force in the axial direction (z). As the normal of the contact surfaces is perfectly parallel with the global axial (z) direction, an extra local coordinate is not defined. The contact has a macro slip motion behavior on the shroud surface in both tangential directions separately. The value of the contact stiffness in tangential and normal directions is assumed same ($k_{t,1} = k_{t,2} = k_n$) and set to 1000 N/μm. It is known from the previous chapter that, in the presence of two sliders, when one contact pair is fully stuck, while the other one alternates either stick-slip or stick-slip-separation; multiple solutions exist due to uncertainty of the tangential forces. In these conditions, the response boundaries for macro slip contact behavior can be determined by using limit tangential forces in the fully stuck element. This strategy developed in the previous chapter is first used here to obtain the reference boundaries. Two nonlinear analyses are performed by setting $m_{1,2} = 1$ and $m_{1,2} = -1$, respectively, to find the upper and the lower boundaries without utilizing the proposed optimization algorithm.

Figure 40 shows the multiple responses with three different static forces applied on the system. Since the first mode shape of the fully stuck linear system is the lateral bending mode, circumferential displacement amplitudes are shown. Non-unique multiple responses and the variability range corresponding to all three static forces are clearly visible. The reason of this variability is that while the contact is slipping in the circumferential direction, it stays fully stuck in the radial one. Therefore, the uncertainty of the tangential forces in radial static component creates variability in dynamic response calculations. In Figure 40, the reference boundaries, which is obtained manually with limit tangential forces, and those computed with the optimization algorithm perfectly overlapped, confirming that the choice of the loss factor as the objective function of the optimization algorithm is correct. It should also be noted that, in frictionally damped systems, each contact surface is characterized by a case-dependent threshold F^0_T value, under which 2D gross slip occurs. Hence, the variability range in Figure 40 shrinks, in agreement with the results presented in the previous chapter, as the pre-load F^0 decreases tending towards the shroud threshold value (approximately 2 kN in this case).

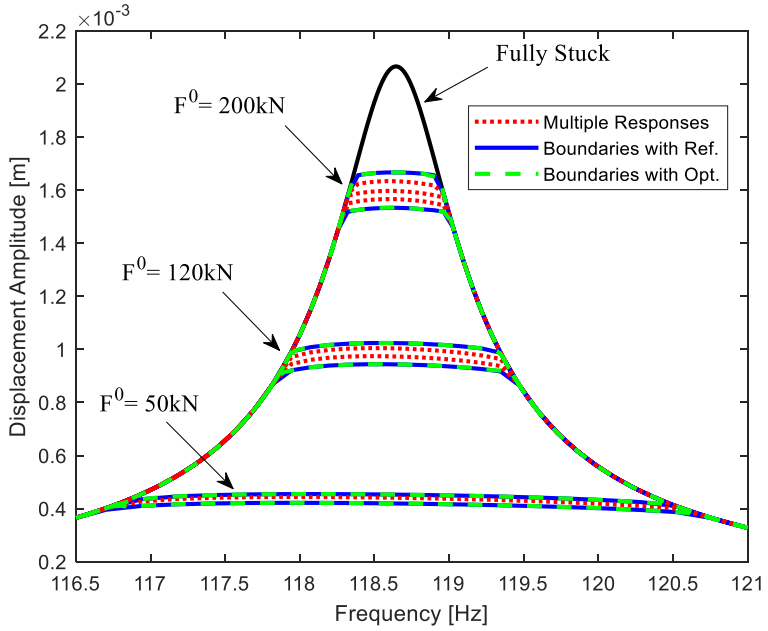

Figure 40: Multiple nonlinear responses with the boundaries

In the analyses performed with the reference method, m_1 and m_2 are kept constant throughout the entire frequency range and set to –1 and 1; while they vary in the optimization algorithm, since they are additional internal unknowns. For the sake of comparison, the values both m_1 (radial direction) and m_2 (circumferential direction) for the case with $F^0 = 200$ kN are shown in Figure 41a (lower boundary) and in Figure 41b (upper boundary). Zero initial guess for both multipliers in the optimization is assigned at the very beginning of the analyses and their actual values are obtained at the end of the iterative solution process. The only varying multiplier coefficient in the optimization algorithm is m_1, while m_2 values do not change with respect to initial guess. This indicates that the algorithm searches the global minimum of the loss factor in each analysis by only changing the m_1 value for a certain frequency interval, in which the initial and end points are marked by blue dots and an alternate stick-slip motion occurs in the circumferential direction.

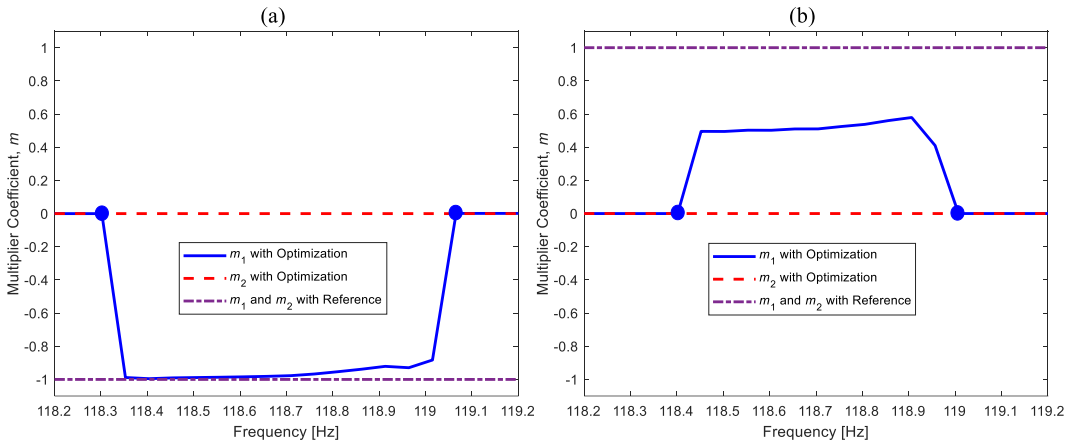

Figure 41: Values of the multiplier coefficients (F^0 = 200 kN): (a) Lower boundary analysis, (b) Upper boundary analysis

In Figure 41, it is also interesting to note that, when alternate stick-slip occurs and the system actually becomes nonlinear, the final value of m_1 computed by the optimization algorithm is different from the reference ($m_1 = \pm 1$). This result confirms that the reference solution strategy, which is proposed in the previous chapter in order to guarantee $T(t_{ini}) = \pm \mu N(t_{ini})$, is conservative with respect to the optimization algorithm. Intermediate guess values ($-1 < m < 1$) could be also enough in some cases to correctly compute the response boundaries. To confirm this observation, the upper response boundary analysis is repeated with the reference method, by setting $m_1 = m_2 = 0.6$. The same results are again obtained, confirming that, in this case, any initial guess with $m_1 \geq 0.6$ and $m_2 \geq 0.6$ allows computing the upper boundary.

Modeling friction interfaces by multiple contact elements introduces more uncertainty, since the number of potential fully stuck contact elements increases. As a result, a huge number of possible combinations is possible with different non-unique static tangential force at each stuck element. Hence, computation of the boundaries with a manual search could become totally infeasible. However, the optimization algorithm proposed in this thesis overcomes this problem.

Figure 42 shows the linear responses for free and fully stuck cases and the nonlinear response curves obtained for different pre-loads, F^0. It should be noted that since the turbine bladed disk used in this study is constructed just for academic purposes, the static pre-load applied represents only the twisting effect to retain contact in the shroud interfaces. Contact stiffness for each element in tangential and normal directions is assumed same and arbitrarily assigned to a

reasonable value of 100 N/µm. As can be seen from Figure 42, there are two response curves given in each case for different pre-loads, although the two curves either fully or partially overlapped in some cases. These nonlinear responses are computed by the optimization algorithm by minimizing the positive and negative of the loss factor, which results the upper and the lower boundaries, respectively. By doing that, the static and the dynamic balance equations are imposed as the nonlinear constraints. From a general view, the algorithm successfully satisfies these constraints almost in the entire frequency range, while the response jiggles at some particular points. This shows a slight convergence problem occurred at some specific frequencies during the iterations, while the general pattern is captured. This can be considered as one of the method's minor drawbacks despite its theoretical correctness. The optimization algorithm, which is implemented by using the *fmincon* function in Matlab, sometimes struggles to satisfy the nonlinear constraints. Nonetheless, the problem here is totally a numerical issue and it does not sharply affect the method's great success in capturing the boundaries.

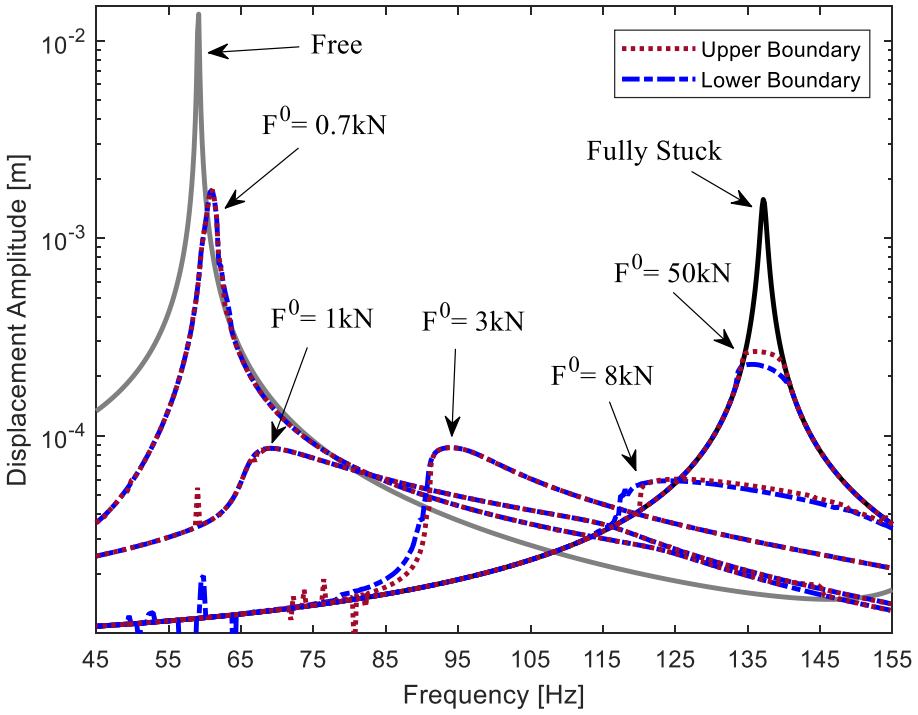

Figure 42: Frequency response curves with the boundaries

It is clearly seen from Figure 42 that the variability range throughout the entire frequency range is considerably small. There is even no variability and the

response boundaries totally overlap each other for the cases with low pre-loads. The deviation slightly increases with higher pre-loads where the difference between amplitudes and resonance frequencies become more apparent. The maximum range in the resonance amplitudes and the resonance frequencies are quite limited around 16% and 1% for the cases with 50 kN and 8 kN, respectively. This range is considerably smaller than those obtained in presence of either under-platform dampers (Gastaldi et al., 2021) or mid-span dampers (see the second chapter). The main reason for this fact is that under-platform dampers or mid-span dampers have two contact surfaces, where the uncertainty of tangential forces on fully stuck elements at one side strongly affects the other side's normal contact forces. This interaction is defined as the so-called damper-induced cross coupling, since it occurs due to the damper geometry. On the other hand, the frictional interfaces at the shrouds are free from the geometric cross coupling, since both surfaces on the left and right sides have the same contact kinematics and the same periodic contact forces, although shifted in time, due to cyclic symmetry. In this case, the only interaction between tangential and normal contact forces is provided by the dynamic coupling present in the system. Therefore, the effect of uncertainty is smaller, when compared to those of under-platform dampers and mid-span dampers. This observation is also completely coherent with the results presented in the previous chapter, where it is stated that the variability range is higher with wedge dampers (high cross coupling) with respect to flat dampers (low cross coupling).

A further explanation for the low variability range can also be deduced from the steady state contact maps depicted in Figure 43 for five nonlinear analyses. Since the main attention is generally focused on maximum amplitudes, contact conditions are presented around the corresponding resonance frequencies. Only one contact map is presented for each range due to the fact that the response variability is considerably small, which enables contact conditions not to differ too much within the range. In Figure 43a-e, contact nodes at the shrouds are highlighted with respect to their contact conditions. Since two uncoupled sliders in orthogonal tangential directions have been defined at each contact element, contact status information are provided for both radial (R) and circumferential (C) directions simultaneously. For instance, Figure 43a illustrates a map at $\omega = 60.9$ Hz for the case with $F^0 = 0.7$ kN. It is shown that all the nodes alternate stick-slip-separation in radial direction, while alternating slip-separation occurs in the circumferential direction. As a consequence, unique response exists and there is no variability in the response, as shown in Figure 42. A similar behavior is also

observed at higher pre-loads (F^0 = 1 kN and F^0 = 3 kN) in Figure 43b and Figure 43c, respectively. On the other hand, when the pre-load increases, some contact pairs enter fully-stuck condition during the periodic vibration. For instance, as shown in Figure 43d for F^0 = 8 kN, the whole shroud is in full stick in radial direction, while it is in gross slip in the circumferential direction. Hence, the uncertainty in the fully stuck contact elements produces non-unique responses. Due to the low coupling between tangential and normal forces, the variability of the response is small. As the pre-load further increases (Figure 43e, corresponding to F^0 = 50 kN), the number of fully stuck nodes becomes larger as well as the variability range. The variability vanishes when the shroud is in full stick condition in both directions and a linear behavior is obtained.

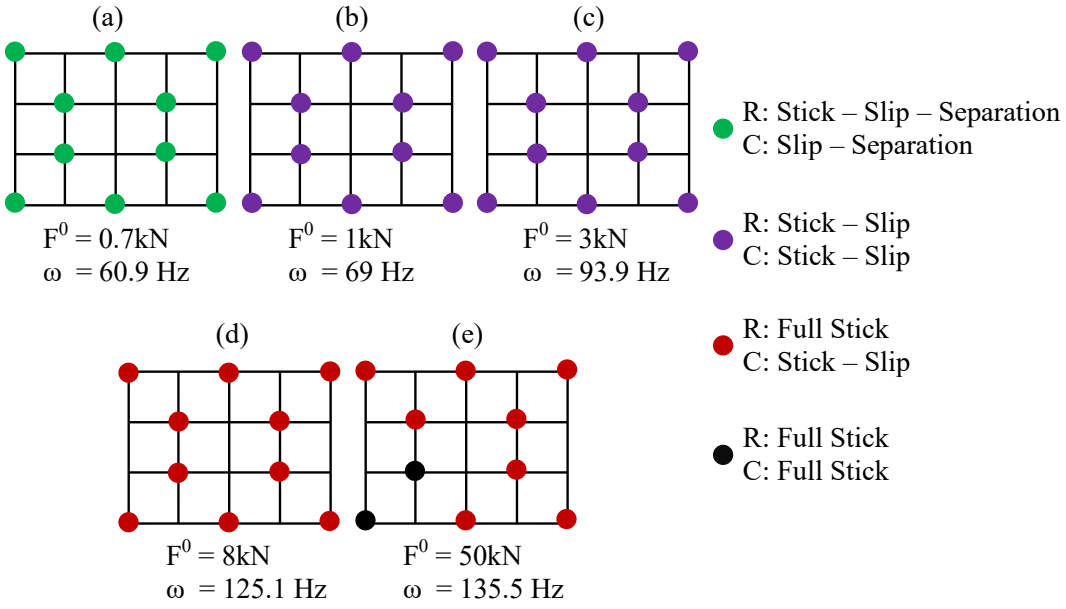

Figure 43: Contact conditions on the frictional interface of the shroud

The optimization algorithm proposed in this thesis overcomes the limitation of a manual search strategy that would imply a large number of simulations without any guarantee of detecting the boundaries. Instead, it represents a systematic approach, based on the minimization of a physical parameter that determines the damping ability of the system. However, the computational effort associated to the optimization algorithm is expected to be higher than the one of a single nonlinear analysis. Table 3 shows a performance comparison in terms of total number of iteration (N_{iter}), total number of function evaluations (N_{eval}) and computational times between the analyses of a manual one (without optimization)

and boundaries (with optimization). The values are presented for the overall computation of the analyses characterized by 350 frequency points within a quite wide frequency range (see Figure 42). All the analyses are performed by a computer with a 4–core processor (Intel(R) Xeon(R) CPU E3–1245 v5 @ 3.50 GHz) and 32 GB RAM. It can be noted that the total number of iterations and function evaluations are higher when the optimization algorithm is used. This also makes the computational cost more expensive. It roughly increases between 2.5 – 7 times for the analyses with different pre-load computations. There is no significant variation between lower and upper boundary analyses since the variability range is small. It should also be noted that *fmincon* function of Matlab is a black-box for the user. It uses either a direct step or a conjugate gradient step to solve the problem. On the other hand, the manual analysis is classically performed by using Newton Raphson with Arc-length Continuation technique. All the Jacobian matrices needed in the iterations for both cases (with and without optimization) are computed numerically with forward finite difference method. It is worth noting that all of the quantitative values shown here is system dependent and they may considerably vary in different systems with a more/less contact elements.

Table 3: Performance comparison of the analyses

F^0 [kN]	N_{iter}			N_{eval}			Comp. Time [min]		
	Manual Analysis	Lower Boundary	Upper Boundary	Manual Analysis	Lower Boundary	Upper Boundary	Manual Analysis	Lower Boundary	Upper Boundary
0.7	$1.7x10^3$	$2.7x10^3$	$2.6x10^3$	$3.6x10^5$	$6.1x10^5$	$5.9x10^5$	20	54	52
1	$5.9x10^2$	$2.2x10^3$	$3.5x10^3$	$1.6x10^5$	$5.1x10^5$	$7.8x10^5$	10	46	71
3	$6.3x10^2$	$2.7x10^3$	$2.3x10^3$	$1.7x10^5$	$6.1x10^5$	$5.2x10^5$	10	56	49
8	$1.1x10^3$	$3.5x10^3$	$2.9x10^3$	$2.5x10^5$	$7.6x10^5$	$6.5x10^5$	15	72	62
50	$3.7x10^2$	$1.6x10^3$	$1.9x10^3$	$1.3x10^5$	$3.8x10^5$	$4.4 x10^5$	8	36	39

4.2.2 Response Boundaries due to Friction Damping at the Blade Root

In the second case scenario, the blade is assumed to be cantilevered with contact elements (no engaged shrouds), in which the only source of friction damping is at the blade root. Since the disk is modeled as a rigid body, the contact elements ($k_{t,1} = k_{t,2} = k_n = 1000$ N/μm) couple the blade root directly to ground and the blade is a free-free beam without any cyclic symmetry boundary condition applied. Friction surfaces and the location of the contact nodes on each side are shown in Figure

44. In order to reduce the number of contact nodes and therefore the calculation time, only one lobe of the fir-tree root is used to connect the blade to the ground and 6 contact nodes per side are selected. On both root sides, tangential displacements in u_1 direction are parallel to rotation axis of the bladed disk, while tangential displacements in u_2 acts in the orthogonal direction, being v the normal displacement direction. A radial static force, corresponding to the centrifugal force of the blade, is applied at the forcing and response nodes. In addition, the same periodic excitation provided in the previous case is also applied here.

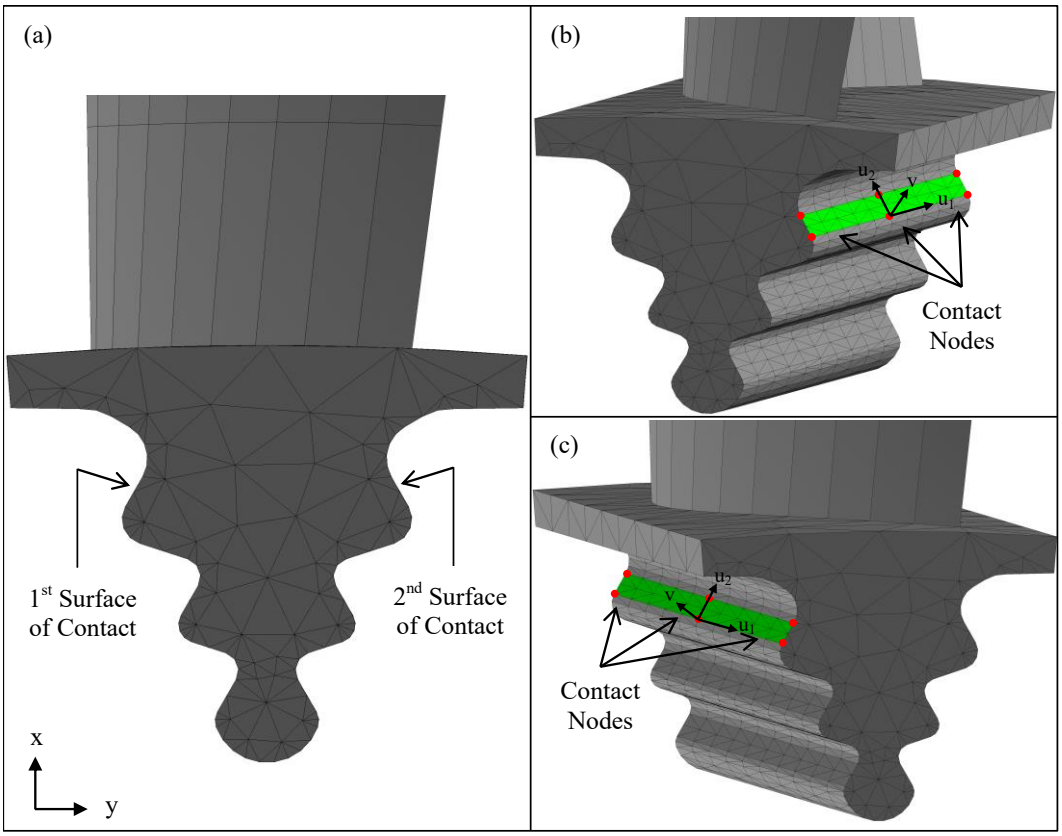

Figure 44: (a) Contact surfaces on the blade root, (b) Contact nodes on the 2nd surface, (c) Contact nodes on the 1st surface

The blade's first bending modes in circumferential and axial directions (see Figure 45) are investigated in order to show the applicability of the method at different resonance regions, characterized by different kinematics at the friction contacts. In order to activate the nonlinearity at the contact, two different values of radial force are applied in the two cases: 500 kN and 30 kN for the first and the second modes, respectively.

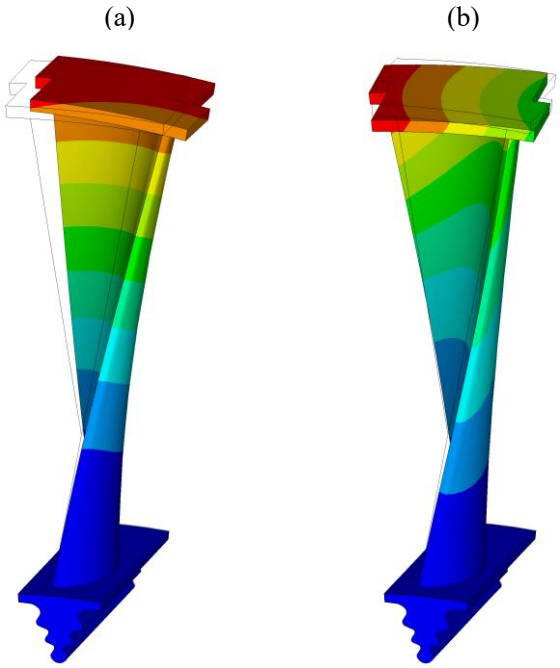

Figure 45: (a) The 1st bending (circumferential) mode shape, (b) The 2nd bending (axial) mode shape

In Figure 46a and Figure 46b, the nonlinear displacement amplitudes of the response node are shown around the first (circumferential) and the second (axial) resonance, respectively. For reference, in both cases, the linear response of the fully stuck blade is also shown. It should be noted that these boundaries represent the theoretical limits that the dynamic response may reach and multiple responses are possible in between them. It is evident that for both resonances, the variability of the response is much larger than the one for the shroud contacts, in terms of vibration amplitudes (8 times for the 1st resonance; 2 times for the 2nd resonance) and frequency shifts (2% and 5%, respectively). There are two main reasons for such a wide variability range. The first one is the geometric coupling between the tangential direction (u_2) of one root side and the normal direction (v) of the other one. This creates more interaction between the contact forces, hence increases the effect of non-unique static tangential forces on the response computation. The second one is the slip behavior at the contact surfaces. In order to explain this further, the contact status at different resonances is investigated in Figure 47a-d. The left and the right contact surfaces of the root are simply sketched, where the contact nodes are shown and their status is highlighted. A large partial slip characterizes both contact surfaces at each resonance. In all cases, almost half of the nodes are fully stuck in both local u_1 and u_2 directions. In Figure 47a-c, the

other half mostly alternates stick-slip in u_2 direction with a full stick motion in u_1 direction. There is full separation at some nodes in Figure 47d, which implies a loss of stiffness with a considerable resonance shift (see lower boundary in Figure 46b).

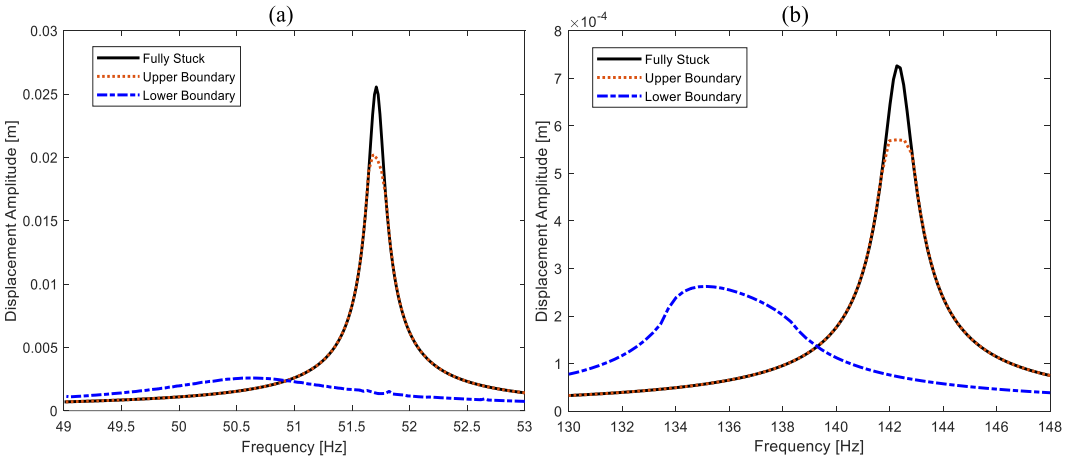

Figure 46: (a) Responses around the 1st resonance, (b) Responses around the 2nd resonance

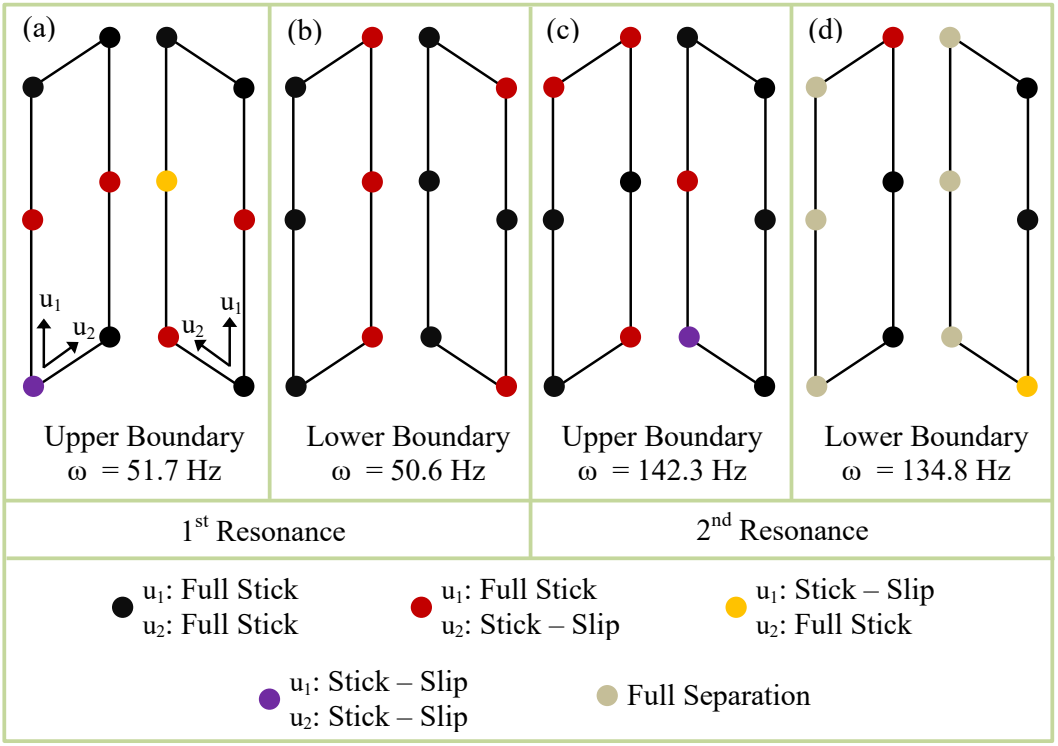

Figure 47: Contact conditions on the friction interface of the blade root

In Figure 47, it is interesting to note that the number of contact nodes that undergo an alternate stick – slip motion is higher at the upper boundary than at the lower one. This can be puzzling since the amplitudes are much higher in the former configuration. However, it should be stressed that the amount of time that contacts spend at each contact state considerably differs in the two cases. For instance, considering the map in the upper boundary calculation around the 1st resonance region (Figure 47a), only one slipping node (at the right side of the root) spends 20% of its periodic vibration cycle in slip state, while it stays 80% in stick state. The rest slipping nodes are actually almost fully stuck (1% and 99% for slip and stick states, respectively). This situation provides a very small amount of damping in the system. On the other hand, in Figure 47b, all slipping nodes spend approximately 65% and 35% of their cycles in slip and stick states, respectively. Therefore, although the number of slipping node is higher in the former, more damping is provided in the latter.

Another valuable information about the results can be extracted by quantitatively tracking the loss factor computed during the analyses, since it is the ultimate parameter that determines the total damping in the system. Figure 48a and Figure 48b illustrate the loss factor, used as the objective function in the optimization process, for the first and the second resonance regions, respectively. The lower boundary is characterized by higher loss factors than the upper one. This result is relevant since the response is more damped in the former, as shown in Figure 46. In Figure 48a, the loss factor for both boundaries is almost constant. However, this does not mean that the dissipated energy does not change in the system; because, the loss factor itself is the ratio between the amount of dissipated energy over the stored one. All the curves except the blue one in Figure 48a also show a bumpy behavior around the corresponding resonance frequencies, which indicates that slip begins and dissipated energy increases in the system. On the other hand, in the frequency interval considered, slip is always present for the lower boundary around the first resonance region. This is why the blue curve of Figure 48a does not have such kind of behavior, only showing a straight behavior with some jumps at some specific frequencies. It is worth stating here that, although the optimization algorithm successfully satisfies the nonlinear constraints, which means no convergence problem takes place, it finds some local minimum points in these frequencies. Actually, optimization algorithms are generally dependent to initial guess and they may converge to a local minimum point instead of global minimum solutions. The same phenomenon is observed here in this study, as well. Although this effect is not too impactful in this specific

case, there may be some other applications where this becomes more relevant. In those situations, one of the easiest remedies may be to change the initial points in order to be in the basin of attraction of the global minimum. This can be achieved by changing the step size and/or the sweep direction of the frequency. Another way is to perturb the objective function and constraints at various nearby points to check if better results can be obtained than the computed one. Moreover, computing the hessian matrix analytically may also help to obtain correct results, which requires a more sophisticated and further effort in the calculation of gradients. One another solution is to utilize a global optimization method, where an accompanying drawback of more expensive computational burden is accepted.

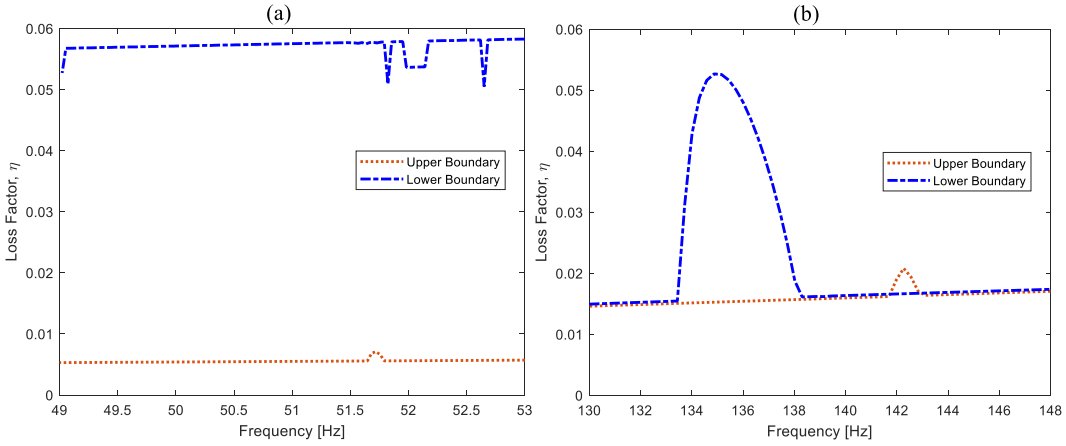

Figure 48: Change of the loss factor around (a) The 1st resonance region, and (b) The 2nd resonance region

As in the previous part, performance comparisons are presented in Table 4 for each analysis. Since the frequency interval considered here (see Figure 48) is narrow compared to shrouded blade case, the number of solution points is smaller (125 and 65 points for the 1st and the 2nd resonance, respectively). The optimization algorithm is considerably more expensive than the single non-linear analysis. This is expected since the number of iteration and function evaluation significantly increases in the optimization. It is also interesting to note that the lower boundary calculation takes more time than the upper one's since the contact in the latter is fully stuck for a larger frequency interval. This provides a unique response in most of the analysis and the algorithm can detect the upper limit faster. On the other hand, in the computation of lower boundary, the partial slip behavior in the contacts is observed for a wider frequency range. Thus, the optimization algorithm makes a significant number of iterations in the search for the global minimum, which increases the computational burden.

Table 4: Performance comparison for different resonances

	N_{iter}			N_{eval}			Comp. Time [min]		
	Manual Analysis	Lower Boundary	Upper Boundary	Manual Analysis	Lower Boundary	Upper Boundary	Manual Analysis	Lower Boundary	Upper Boundary
1st Res.	$1.9x10^2$	$3.2x10^3$	$5.0x10^2$	$3.2x10^4$	$4.4x10^5$	$8.2x10^4$	1.5	41	7
2nd Res.	$1.1x10^2$	$6.0x10^2$	$3.4x10^2$	$1.8x10^4$	$8.8x10^4$	$5.3x10^4$	1	7.5	5

As the optimization algorithm works at each excitation frequency in the considered frequency range, it is also useful to give the performance comparison only at several representative frequencies. For this purpose, three frequency points are particularly chosen for both resonance regions. Two of them are the resonance frequencies of the upper and lower boundaries (see Figure 46: 51.7 Hz and 50.6 Hz for the 1st resonance; 142.2 Hz and 135 for the 2nd resonance), while the third one is far away from the resonance regions. In this way, the efficiency of the method can be well compared with a manual nonlinear response analysis.

Table 5 shows the performance comparison for different resonances, but at particular frequency points. It is clear that the number of iterations and function evaluations increases around resonance regions. For the lower boundary analysis, the optimization algorithm makes more iteration than the one of the upper boundary. As explained before, this is relevant, because there is more partial slip in the lower boundary computation, and it takes time for the algorithm to capture the global minimum value of the objective function. Manual analysis also converges with the less number of iterations and function evaluations.

Table 5: Performance comparison for different resonances at particular frequency points

	Frequency [Hz]	N_{iter}			N_{eval}		
		Manual Analysis	Lower Boundary	Upper Boundary	Manual Analysis	Lower Boundary	Upper Boundary
1st Res.	50.6	1	219	2	218	30000	399
	51.7	12	35	65	985	4888	8910
	52.5	1	21	3	218	2866	532
2nd Res.	135	1	6	3	218	931	532
	142.2	8	8	16	765	1111	2194
	146	1	10	3	218	1484	532

Another valuable information is the residual values of the analyses to monitor the convergence of the processes. For the *fmincon* function (optimization algorithm), the *constraint violation* value is used; while for the *fsolve* function

(manual analysis), the sum of square of *fval* value is utilized, as the residual. Figure 49 depicts the residuals that are obtained in each analysis throughout the entire frequency range. The values are extremely small for the 1st resonance region, which indicates that all the analyses converged successfully. On the other hand, the residual value of the analysis of the upper boundary is 10^{-6} at the resonance (142.2 Hz). This indicates that full convergence is not achieved with respect to the tolerance (10^{-8}). Nevertheless, the residual is still very low, and there is no weird behavior in the response curve (see Figure 46b). These results show that the convergence efficiency of the analyses for these particular cases can be assumed sufficiently high.

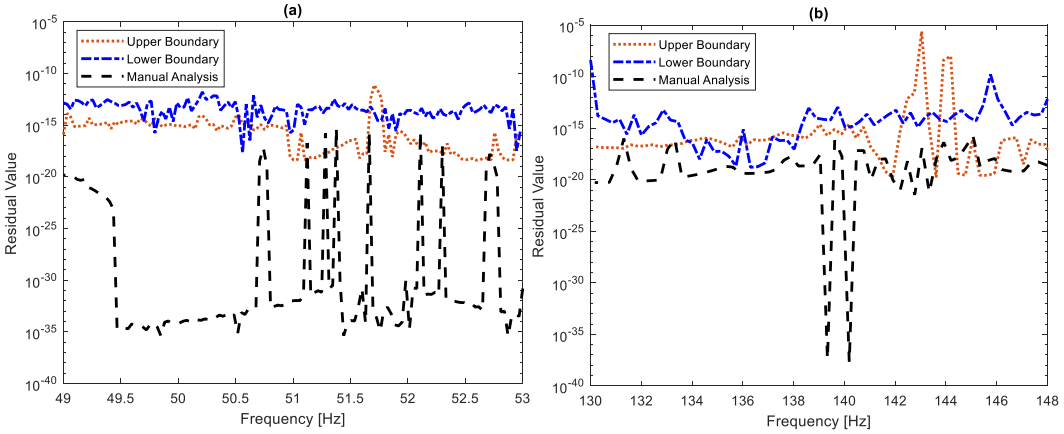

Figure 49: Convergence efficiency of the analyses: (a) The 1st resonance region, (b) The 2nd resonance region

It is shown in the case studies that the developed method is able to capture the boundaries systematically. However, the response curves computed with the reference method, which is developed in the previous chapter, may still attract the reader's attention, in case it will also work for systems with more than two contact elements. The blade root case study suits the best for this purpose, since the variability range is extremely large. Figure 50 shows the displacement amplitude responses obtained with the reference method, in addition to the ones already given in Figure 46a. The magenta and the green curves represent the nonlinear response (NLR) obtained by keeping the multiplier coefficient m constant at 1 and -1, respectively, for the entire frequency interval. Hence, the initial guess for the tangential contact force ($T(t_{ini})$) becomes $\mu N(t_{ini})$ and $-\mu N(t_{ini})$ for two different analyses, respectively, as proposed in the previous chapter. As can be seen in Figure 50, the reference method cannot capture the boundaries, which further highlights the advantage of the developed approach.

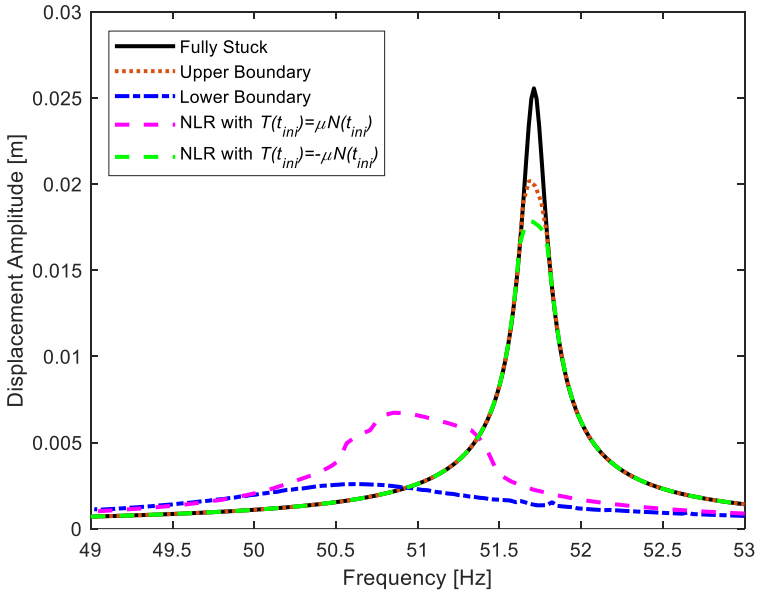

Figure 50: Response curves with the optimization algorithm and the reference method

4.3 Summary

This chapter describes a novel numerical method developed for the determination of the response boundaries of the variability range caused by the uncertainty phenomenon. The difference from the previous chapter is that the method proposed here is able to capture the boundaries regardless of the system's complexity level, while the previous one has been only suitable for systems undergoing macro slip friction motion.

The method is a generalized technique that utilizes an optimization algorithm to minimize an objective function, being the loss factor of the dynamic system. It is applicable to the different bladed disk configurations, characterized by different friction damping systems, such as blade roots, friction dampers, shrouds, etc. The method is validated and demonstrated on a realistic example by investigating the contact interfaces on the shrouds and on the blade-disk interfaces of an academic bladed disk. The results prove that the method is capable of capturing the periodic response boundaries. The method proposed is the first generalized approach to determine the response boundaries in the context of non-unique friction force uncertainty.

Chapter 5

Experimental Verification of the Developed Method on a Blade with Under-platform Dampers

This chapter[4] presents a collaboration study. It shows a comparison of an experimental and computational investigation on the dynamic response variability of a turbine blade with under-platform dampers. The main aim here is to challenge the optimization algorithm developed in the previous chapter with an experimental data set. The experimental campaign is designed by Botto and Umer (2018) and the data is recorded by Botto et al. (2018), while the computational analyses are performed in the scope of this thesis.

5.1 Brief Description of the Test Rig

Even though the experimental structure of this chapter is developed in one another study (Botto & Umer, 2018), it is described here very briefly for the sake of completeness.

[4] Part of the work described in this chapter has been previously published:
"Ferhatoglu, E., Gastaldi, C., Botto, D., & Zucca, S. (2022). An experimental and computational comparison of the dynamic response variability in a turbine blade with under-platform dampers. *Mechanical Systems and Signal Processing*, *172*, 108987"

Test setup had been designed such that the following main criteria are ensured during the test.

- The shape of the under-platform damper should ensure a cross coupling between the tangential force of one contact side and the normal force of the opposite side. This is an essential property to obtain response variability for the same nominal conditions with successive tests.

- In addition to frequency responses, the test rig should have the capability of measuring contact forces and relative displacements between contact surfaces. This feature enables the interpretation of the inherent contact dynamics in operation and provides the link between the recorded dynamic response and the specific set of contact forces that produced it.

- The blade root should be clamped properly in order to minimize an additional damping contribution. The only friction effect should be supplied by the contact between the blade and under-platform dampers.

Conventional test structures in laboratory conditions generally consist of one under-platform damper pressed between two blades (Pesaresi et al., 2017; Sanliturk et al., 2001). This architecture is quite popular due to its simplicity and it can be used to effectively investigate in-phase and out-of-phase blade motion, however it does not allow for contact forces to be measured. Instead, one blade with two under-platform dampers supported by auxiliary equipment is more convenient to this purpose. It enables the damper to be in contact with the blade on one side, while the other side can be used to measure friction forces. This is the strategy utilized also in the current case study and implemented in the test rig introduced by Botto and Umer (2018), where the reader may find all relevant details on its design and measuring procedures in their paper. For the sake of completeness, a brief description of the relevant features of the test rig follows.

Figure 51a shows the main assembly of the test rig. The blade is fixed from the root by applying a clamping force (F_{CLAMP}) with a purposely designed mechanism in the main block. Two under-platform dampers at each side are loaded with dead weights that simulate the static centrifugal force (CF) in real applications. It should be noted that under-platform dampers are positioned between the blade and an L-shaped force separator. In this way, the contact force on the non-blade damper side is decoupled along two perpendicular directions through the force separator, which is kept in place by a fixed side block. This

provides reaction forces (R) to be measured with load cells (LC) positioned in between the force separator and the fixed side block. The actual contact forces are then calculated by utilizing geometric relations (Botto & Umer, 2018). Figure 51b shows a closer top-view of the blade's under-platform. Two contact pads numbered with 1 and 2 are directly bolted to the blade and to the force separator, respectively. These pads are designed for practical reasons. They can be replaced easily to investigate different damper geometries without modifying the main setup. In this study, the geometry of the utilized damper (D) is flat on the blade side, while it is cylindrical on the force separator side. This ensures flat-on-flat and cylinder-on-flat contact surfaces on different damper sides, which enables the investigation of different kinematics. The blade is also excited with an electromagnetic shaker (F_{EXC}) from a slot close to the root. Figure 51c also representatively shows the static force balance on the left damper. Here, as mentioned above, the contact forces at the cylindrical side (T_{cyl} and N_{cyl}) were previously calculated with the load cell values, by utilizing a geometric relation between the contact pad 2 and the force separator. The contact forces at the flat side (T_{flat} and N_{flat}) are then derived through the force equilibrium by assuming the inertia of the damper is negligible. Interested readers may refer to the original study (Botto & Umer, 2018) for more detailed explanations about the entire test rig.

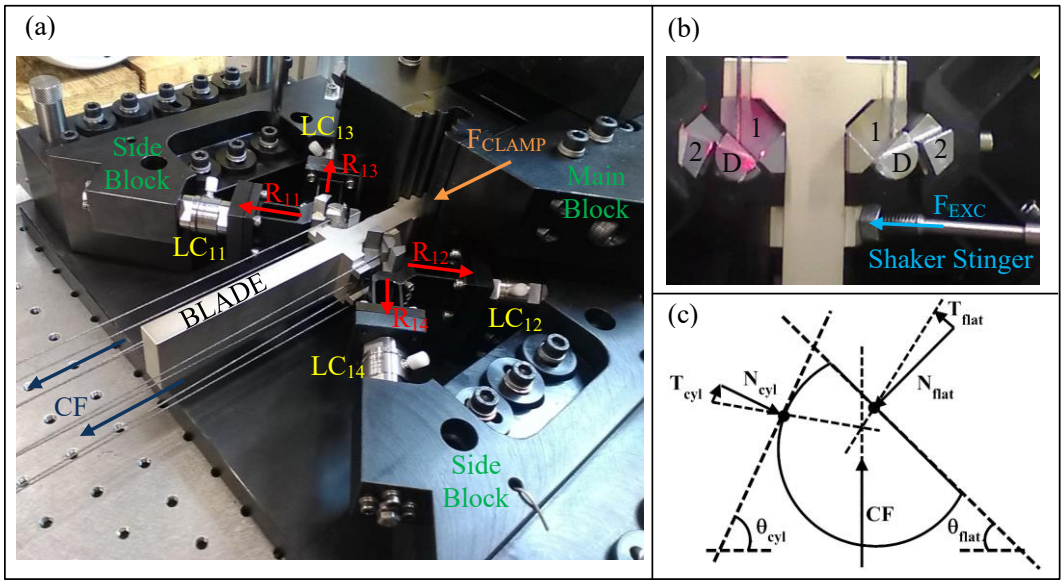

Figure 51: (a) Test rig setup, (b) A closer view of the blade's under-platform, (c) Force equilibrium on the damper

The blade has been designed only for academic purposes and it imitates real turbine blades in the industry in terms of frequency range for the first modes. The first natural frequency corresponding to the lateral bending mode is designated to lie in the 400-450 Hz range. The blade is free from modal coupling and has a well-separated first lateral bending mode. An investigation on the clamping force has also been performed before starting the experimental campaign. No influence of root attachment has been observed for the clamping force values greater than 40 kN. Hence, F_{CLAMP} is set to 50 kN for all experiments. A standard force controlled stepped-sine testing has been utilized in the experiments to measure nonlinear frequency response functions. Several sine sweeps have been performed with different excitation and centrifugal forces. The response of the blade tip is monitored with an accelerometer. Despite the fact that nonlinear FRFs are sufficient to observe the dissipation due to friction, the uncertainty phenomenon can only be interpreted in detail with the contact forces and hysteresis cycles. In order to measure these quantities, LCs are used to record contact forces as explained above, while a differential laser measures the relative displacement between the damper and contact pads. Figure 52 briefly summarizes the complete experimental setup and flowchart.

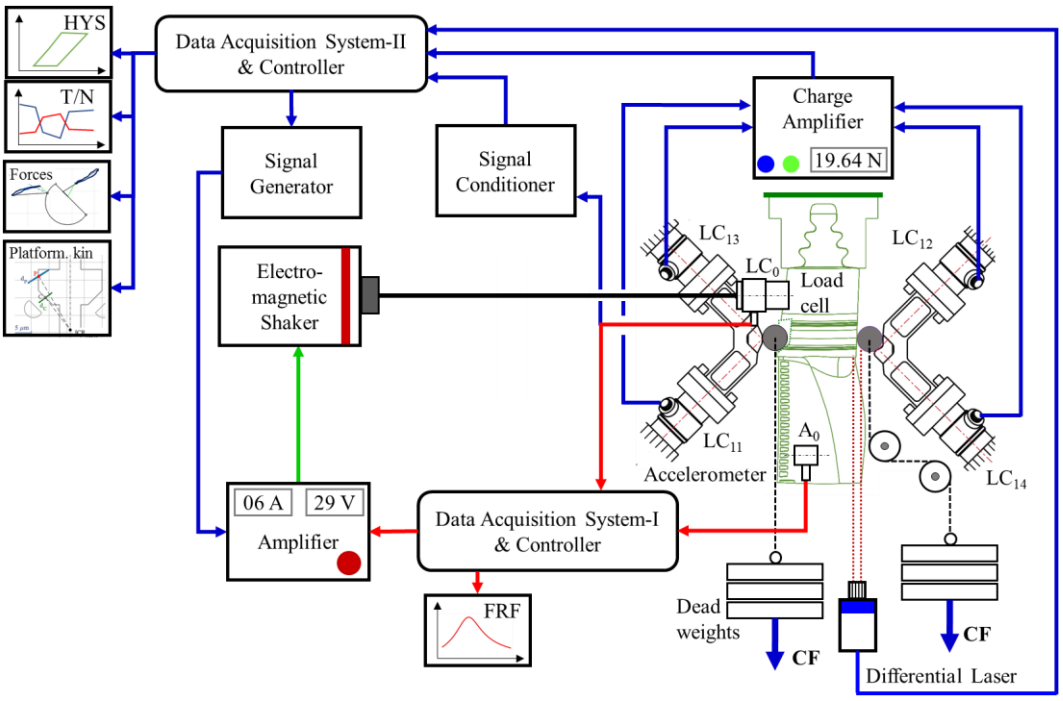

Figure 52: The flowchart of the experimental framework (Botto & Umer, 2018)

5.2 Modeling Approach

Finite Element Model of the structures is created to obtain system matrices in the scope of this thesis.

The blade, the damper and the other auxiliary parts are finely meshed with 3D solid elements as shown in Figure 53a. The blade and the contact pads (numbered 1 in Figure 51b) are merged in the finite element model, since they are tightly bolted in the tests. Similarly, the L-shaped force separator on both sides is also merged with the other contact pad (numbered 2 in Figure 51b) and load cells. These assumptions are confirmed by preliminary calibration experiments, where the differential laser head recorded zero displacements between contact pads and the respective host structures (either blade or force separator). Under-platform dampers are modeled with free-free boundary conditions owing to the fact that they are free to move. The rest of the test rig is considered rigid and excluded in the analyses. Consequently, the model consists of five different bodies. It should be noted that no contact element is imposed to the model in the finite element software. As the boundary conditions, the blade is clamped from the root, while the load cells are fixed from their far ends from the force separator. The Craig-Bampton approach (Craig & Bampton, 1968) is applied in order to obtain a reduced order model. Physical master nodes, i.e. excitation, static pre-load, response monitoring, and contact nodes, and 150 modal coordinates are retained as the master degrees-of-freedom in the reduction process.

Contact regions are shown in Figure 53b and Figure 53c for the dampers located at the left and right, respectively. Each damper has two different contact sides with the neighboring pads. The flat surface of the dampers has an area contact, while a line contact occurs at the cylindrical side. With this type of damper geometry, it has been shown by Botto et al. (2018) that the system kinematics mostly provides a micro slip and a full stick motion at the cylindrical and flat side, respectively. Correspondingly, in this study, different contact models are used at each contact interface to be able to better represent the contact conditions at each interface.

On the flat sides, the classical Jenkins element is used to model the frictional behavior. The number of contact pairs to be used in the final nonlinear analyses is determined with a pre-tuning process, where the effects of different quantities of Jenkins elements used at the flat sides are examined initially in the preliminary

nonlinear response analyses. It is concluded that increasing the number of elements does not increase the accuracy of the solutions, since the flat side is already fully stuck. As a result, five particular points are selected per each contact area (see Figure 53b and Figure 53c).

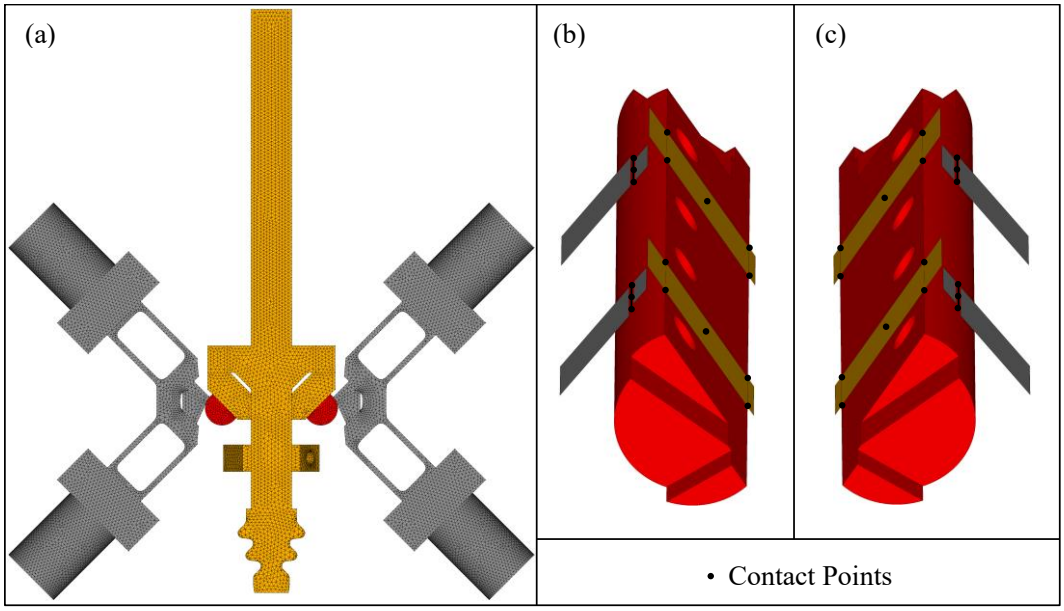

Figure 53: (a) Finite element model of the structure, (b) Left damper, (c) Right damper

On the other hand, a micro slip element is utilized for the line contact on the cylindrical side. The micro slip element is basically an array of concatenated macro slip elements. It has been firstly developed for non-conforming contact surfaces by Gastaldi and Gola (2015) and then validated experimentally on under-platform dampers (Gastaldi & Gola, 2016a). Its main principle is to capture the micro slip behavior by splitting the hysteresis cycle into several portions with linear stiffness elements. This idea has also been used previously (Ciğeroğlu & Özgüven, 2006; Jamia et al., 2021) and facilitates the imitation of the micro slip behavior with a simple strategy. In this case, the number of concatenated elements in a single micro slip element is five, and three distinct contact points are chosen on the line contact as shown in Figure 53b and Figure 53c. In this way, a total number of 15 macro slip elements are distributed over a relatively small contact line. This enables the computation of micro slip phenomenon with a satisfactory level of accuracy. It is also worth noting that 80 macro slip elements are used in total within the entire model of the structure, where 20 of them are located on the

flat sides and the rest on the cylindrical portions. It should also be noted that contact elements utilized in this chapter are 1D with the variable normal load, because another sensitivity analysis is performed in advance, and exactly the same responses are obtained separately with 2D and 3D contact elements. Hence, the tangential direction, which is parallel to the out-of-plane from a top view (see Figure 53a), is not considered in the analyses.

5.3 Linear Dynamic Characteristic of the Blade

The experimental linear behavior of the blade without engaged dampers can be used to extract the modal properties, i.e. natural frequency and damping ratio. These measured values are utilized to tune the linear model, before performing the experimental-numerical comparison on the nonlinear analyses.

The natural frequency of the blade may be severely affected by boundary conditions. Even though the blade root can be perfectly constrained in the computational model, the same condition may not be valid in laboratory conditions even if very large clamping forces are applied. Hence, a sensitivity analysis in the finite element model is firstly performed on the root boundary conditions in order to ensure a good match between the first natural frequency of the blade obtained numerically and its experimental counterpart. The natural frequency of the blade for the well-separated first bending mode is measured at 410 Hz in the experiments, and it is afterwards tuned to the same value in the numerical analyses with the sensitivity study. Figure 54a depicts the interested mode shape at 410 Hz.

Figure 54b shows the experimental and computational linear responses of the blade without under-platform dampers around the first resonance region. The accelerance amplitude of the blade tip is given. The responses almost overlap, thus providing an evidence of the fact that the linear behavior of the blade in the numerical model represents the real working conditions with a negligible amount of deviation. It should be noted that this verification is a key step that needs to be performed prior to nonlinear analyses; because, it prevents a potential artificial stiffness contribution from the root, which may introduce errors in the subsequent contact stiffness tuning at the platform-damper contact. It is also worth mentioning that although the damping ratio of the stand-alone blade model is estimated from the experimental result, the one corresponding to the entire system

and used in the nonlinear analyses is finely tuned after engaging the under-platform dampers in the next section.

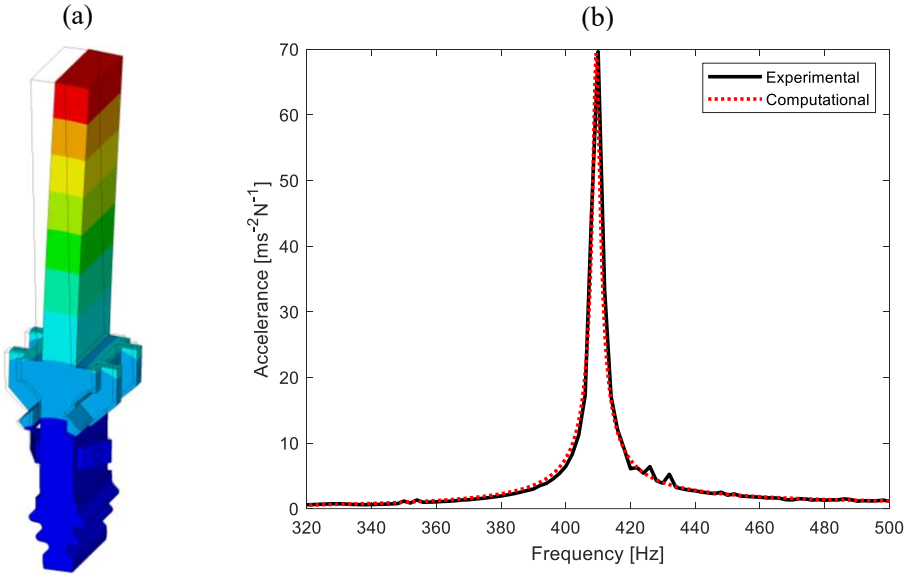

Figure 54: (a) The first lateral bending mode shape of the blade at 410 Hz, (b) Linear response of the blade tip without under-platform dampers

5.4 Nonlinear Behavior of the Blade with Under-Platform Dampers

Dynamic response variability of the blade with under-platform dampers is both computationally and experimentally investigated with various excitation levels (1-100 N) and three different pre-loads (2.6 kg, 4.6 kg and 6.6 kg). Before the nonlinear response computations, the linear damping ratio and contact parameters are calibrated in the numerical model.

A proportional damping ratio for the entire linear system with under-platform dampers is used. Its value is determined by the experimental results obtained with the lowest excitation force level, which gives the closest configuration to the fully stuck linear system. The damping ratio value is set to 0.8% and kept constant for the all analyses.

A preliminary analysis is performed for the characterization of contact elements in the model. First, the Jenkins element is used on both sides of the

damper (cylinder-on-flat and flat-on-flat contacts alike). However, the accuracy of the experimental-numerical match was deemed not satisfactory, especially for low excitation levels. One hypothesis to explain this discrepancy is the absence of a contact model capable of capturing the micro slip behavior at the cylinder-on-flat contact. In fact, a series of simple Jenkins elements evenly distributed along the line contact observed at the cylinder-on-flat side cannot capture partial slip phenomena, especially for a bending mode. Then, the micro slip array element is utilized at the cylindrical side, while the Jenkins elements are still kept at the fully stuck flat side. This new configuration significantly improves the experimental-numerical match.

The contact parameters are tuned to three sets of values, one for each pre-load case. This approach is relevant, since the contact pressure on the frictional surfaces in the experiments is different for each pre-load. The numerical values of the contact parameters utilized here are determined with a two-step procedure. First, a possible range of values is defined by considering the values extracted in the previous studies where the damper geometry of this work has been manufactured many times using the same material and studied separately (Gastaldi & Gola, 2015, 2016a, 2016b; Gastaldi, 2018; Botto et al., 2018). These values are taken as a starting reference point. Then, they are finely tuned to optimize the experimental-numerical match, keeping into account the variability due to the different static conditions. The final values are given in Table 6 and kept constant during the analyses. A further proof of the model consistency is that contact stiffness values tend to increase with increasing pre-load values, i.e. contact pressure, as expected.

Table 6: Contact parameter sets for different cases of pre-load

Applied Pre-load	Damper Side	Tangential Stiffness [N/μm]	Normal Stiffness [N/μm]	Coefficient of Friction
1st set for 2.6 kg	Flat	20	50	0.6
	Cylindrical	45	260	0.4
2nd set for 4.6 kg	Flat	25	65	0.6
	Cylindrical	45	260	0.4
3rd set for 6.6 kg	Flat	35	75	0.6
	Cylindrical	35	260	0.4

It should be highlighted once again that the main goal here is not to perform additional tests to experimentally extract the contact parameters used in the

computational analyses. The calibration and validation of these properties has already been deeply investigated and presented in the previous studies for the damper geometry utilized in this work. Here, the final values are tuned after a considerable amount of effort, so that they remain within the ranges demonstrated previously and they represent the most optimized ones that give a satisfactory level of accuracy for the comparison of experimental-numerical match. In the next parts, the results are presented and discussed in three different subsections. In the first one, the largest amount of data is collected and a thorough comparison is performed with 4.6 kg pre-load case. The numerical method is then challenged with further experimental data obtained at 6.6 kg and 2.6 kg of pre-load cases in the second and the third sections, respectively.

5.4.1 Multiple Nonlinear Responses with the Variability Range and Non-Unique Contact Forces for 4.6 kg Pre-Load Case

There may be various parameters that affect the repeatability of the response in frictional structures, as mentioned previously in the introduction. It is always challenging to eliminate all factors that are out of user control. One of the relevant approaches to identify the underlying reason of the non-repeatability is to keep macro scale testing conditions as similar as possible and to repeat the experiments under the same nominal conditions. Then, the only variable parameter in the different repetitions gives an insight on the cause of the variability. This idea has been applied also in the current work. Before presenting the response variability, it is first intended to demonstrate the main factor of non-repeatable data obtained in the experiments. For this purpose, a purposely defined strategy has been followed by Botto et al. (2018). In particular, a first set of the experiments is performed with an increasing order of excitations from 1 N to 100 N; and then in the second set, the same logic is applied but with the opposite direction decreasing back to 1 N from 100 N. In all the tests, the pre-load is kept constant at 4.6 kg. All sweeps performed with 20 N excitation are then collected and studied.

Figure 55 and Figure 56 show the contact forces measured on the right and left dampers, respectively, in four different runs with 20 N excitation and 4.6 kg pre-load. Tangential and normal forces are shown in one full vibration cycle at the corresponding resonance frequencies for both flat and cylindrical sides. It is seen that the contact forces of the first (before 100 N excitation) and second (after 100 N excitation) sets closely gather within themselves, but with an offset from each other. Dynamic parts of contact forces oscillate around non-unique static

components in different runs. This is an indication of different static balances achieved in each set, although the applied pre-load is nominally same. It can be said that the micro conditions in the frictional interfaces is blindly modified from a macro scale environment with the followed strategy, by keeping all user-controlled inputs identical. The uncertainty phenomenon provides the system to have a non-unique static force balance pattern, even if all the inputs are nominally same. As a result, it can be inferred that the response variability observed in the experiments is due to the non-uniqueness of friction forces, since the contact forces balance the equilibria with different static components in each run.

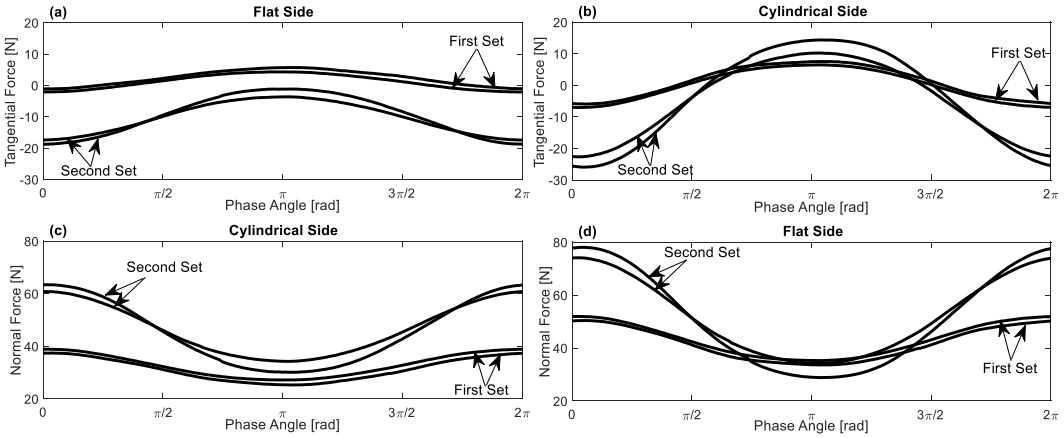

Figure 55: Experimental contact forces on the right damper for 20 N excitation case in one full vibration cycle at the corresponding resonance frequencies

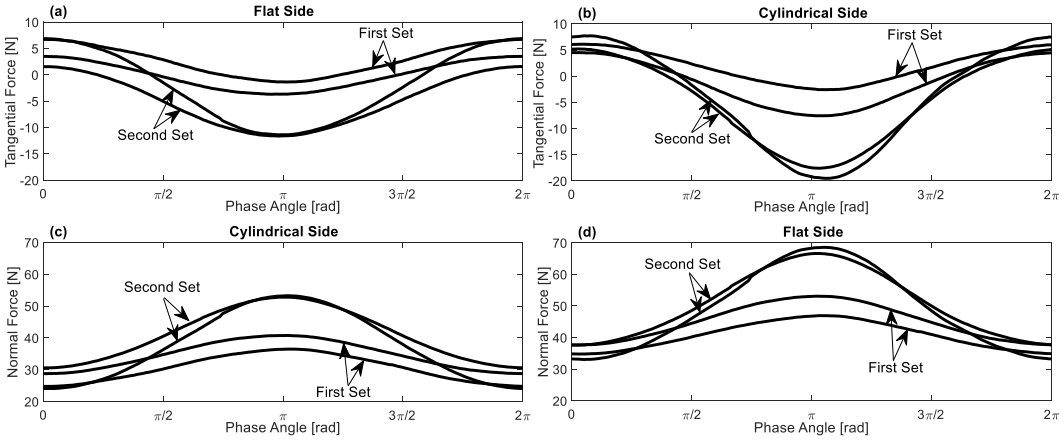

Figure 56: Experimental Contact forces on the left damper for 20 N excitation case in one full vibration cycle at the corresponding resonance frequencies

Figure 57 depicts the complete picture of the nonlinear response data for the pre-load with 4.6 kg. Normalized response amplitudes are grouped and presented in six different subplots with respect to the excitation. For instance, Figure 57a shows eight different responses corresponding to 1 N excitation, where three of them (solid black curves) are measured in the experiments, and the rest is obtained in the computational simulations. The experiments for each excitation set are performed under the same nominal conditions by keeping all the user-controlled inputs identical. The response variability obtained in the experiments cannot be explained with abrasion or wear, since the test durations are considerably short. Instead, different static force equilibria corresponding to each run induce a change in the equivalent stiffness and damping of the frictional contacts, leading to multiple responses for the same nominal conditions. On the computational side, analyses are performed in two different ways. The first one uses a non-linear solver developed in MATLAB, and calculates the steady state vibration amplitude of the system, as generically explained in the second chapter. This gives one of the multiple responses (dotted red curves) in each analysis shown in Figure 57a-f. The variation of the steady state response here is provided with different initial guess values of the static tangential forces during the computation of contact forces within the AFT algorithm. The second way utilizes the optimization algorithm proposed in the previous chapter and estimates the boundaries (dash-dotted green curves). The loss factor of the system is used as the objective function in the optimization. The upper and lower limits are predicted with the minimum and maximum values of the loss factor in two different analyses, respectively.

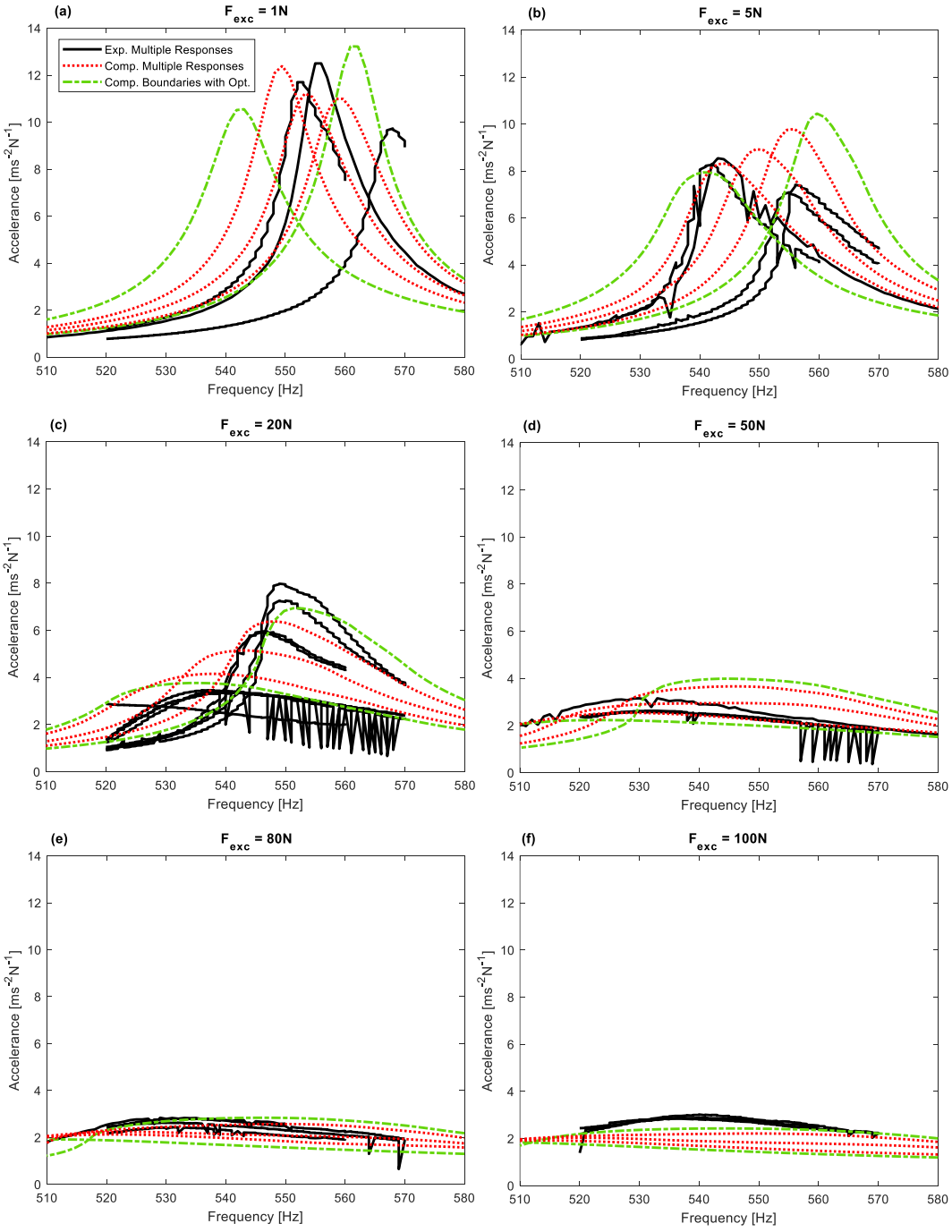

Figure 57: Nonlinear response amplitude of the blade tip for different excitation levels with 4.6 kg pre-load

The results show that the experimental limits of the variability range as well as the nonlinear dynamics of the blade with under-platform dampers are

satisfactorily captured by the numerically estimated boundaries and multiple responses, respectively. This verifies the adequacy of the optimization method proposed in the previous chapter to predict the response boundaries. A minor deviation between experimental and computational results is visible in some cases, i.e. the 100 N excitation shown in Figure 57f. The 100 N excitation case is the one where the nonlinearity is very high due to the large slip. This probably raises some additional issues, which take place in the experiments, but cannot be captured in the numerical model. One possible explanation is that the effect of the shaker stinger on the system becomes dominant in the experiments with the largest excitation, while the stinger-system interaction is not included in the model. It should be noted that the normalized experimental response has a trend for the cases from 1 N to 80 N, where it softens and decreases with increasing excitation. However, experimental results with 100 N do not comply with this observation. It can be observed that an additional stiffness contribution is present, potentially introduced by the shaker stinger, while the normalized computational response continues to soften since no additional stiffening effect is modeled.

It should also be noted that some of the experimental results, especially those in Figure 57b-d, display an oscillating or *jiggling* trend, i.e. sudden amplitude changes occur at consecutive frequency steps. This is caused by a limit in the shaker force controller, which sometimes struggles to keep the force amplitude at the predefined constant value for some specific frequencies. Nevertheless, the response behavior is apparent and this problem does not affect the results readability. Another observation is that the variability range is larger for lower excitation cases, while it shrinks with increasing levels of forcing. This can be considered as the second proof of the fact that the response variability in the experiments is mainly due to the non-uniqueness of friction forces. This observation is perfectly consistent with the theoretical hypothesis which defines the non-uniqueness of the solution as a phenomenon that arises from fully stuck points. Once the amount of slip increases in the system, the dynamic behavior converges towards a unique response and the variability range disappears with the gross slip. If there was one another factor that is dominant on the non-repeatability of the response in the experiments, it would have affected the data sharply for higher excitation cases, as well. This can also be illustrated more intuitively by directly comparing the resonance amplitudes with respect to the increasing excitation levels, as shown with the corresponding variability range in Figure 58.

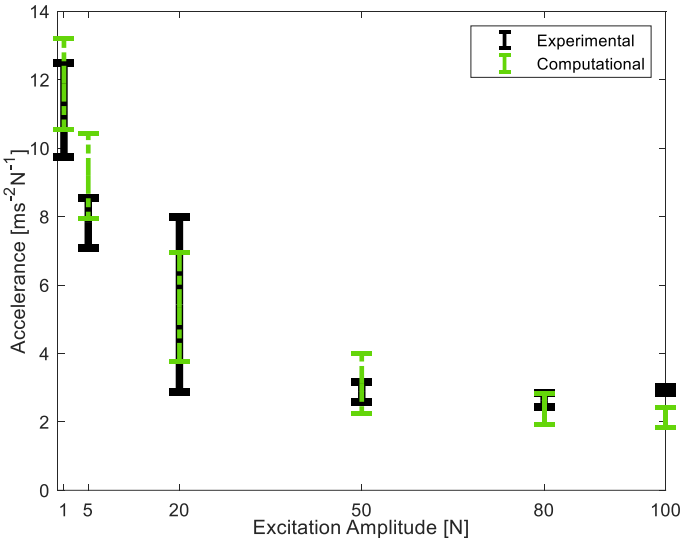

Figure 58: The variability range of resonance response amplitudes for different excitation levels with 4.6 kg pre-load

The inherent kinematics of the response variability can be understood better with the contact forces, which is one another valuable output of the current test rig. It is worth first mentioning that the experiments of the current work have been previously performed by Botto et al. (2018) to investigate mainly the dissipation capability of the under-platform dampers; hence, the contact force signals are recorded only for the frequency steps across the resonance to be able to limit the size of the time data collected. During the sweep, the recording of the signals is activated just a few frequency steps before the resonance, whose values are approximately estimated from previous experiments; and then it is stopped after the resonance is surpassed. Since the main attention of the tests has not been focused directly on the uncertainty phenomenon, there is a lack of multiple contact force data for a fixed frequency at a prescribed excitation level and pre-load; hence, one sample of contact forces will be given in the following experimental results. Nevertheless, this condition can still be considered sufficient to make a comparison between experimentally and computationally obtained contact forces, since the main goal here is to numerically capture the boundaries of the variability range in which there is at least one experimental data. It should also be mentioned that recorded time signals are found consistent and repeatable across a single resonance, but the details about the post-processing are not shown here for brevity.

Contact forces are measured for the majority of investigated cases, but two of them, 80 N and 20 N excitation cases, are presented in detail here. These cases are intentionally selected to investigate different kinematics. They serve as demonstrators, as the variability is lower in the former, while it is much larger in the latter. Another motivation for selecting these cases is also that the experimental and computational results of the response match quite accurately and this enables a close comparison of contact force results.

- Contact Forces for 80 N Excitation Case

The uncertainty phenomenon is directly related to the contact conditions, since the non-uniqueness of tangential forces occurs only in fully stuck points. Hence, first, the contact status on the frictional interfaces is investigated, particularly around the resonance frequency (ω = 529 Hz). Figure 59 shows the proportion of contact forces on each side of the right damper for one full vibration cycle. In addition to the experimental result, computational ones are also given. The resultant force is computed by summing all the forces obtained with the contact elements located at the same contact surfaces. This summation is done in the time domain for the corresponding frequency over a one vibration period.

It can be deduced from Figure 59a that the force ratio (T/N) at the flat side exhibits a behavior that is close to a sinusoidal motion. This indicates that gross slip is never achieved, which is a case also verified computationally by monitoring the status of the contact points. A great majority of the contact elements on the flat side are fully stuck; while a few ones have a stick-slip contact condition, but largely dominated by the stuck state. On the other hand, Figure 59b shows that a gross slip occurs on the cylindrical side, since the force ratio becomes equal to the coefficient of friction, i.e. $T/N = \mu$, in some portions of the cycle, as indicated by the labels in Figure 59b. This behavior is clearly visible in the computational analyses with a perfect straight line, while it has a more rounded shape in the experimental counterpart. Nevertheless, the transition between the stick and slip states is visible for both cases and is further highlighted in Figure 59b through the use of red and black dots for the computational and experimental results, respectively.

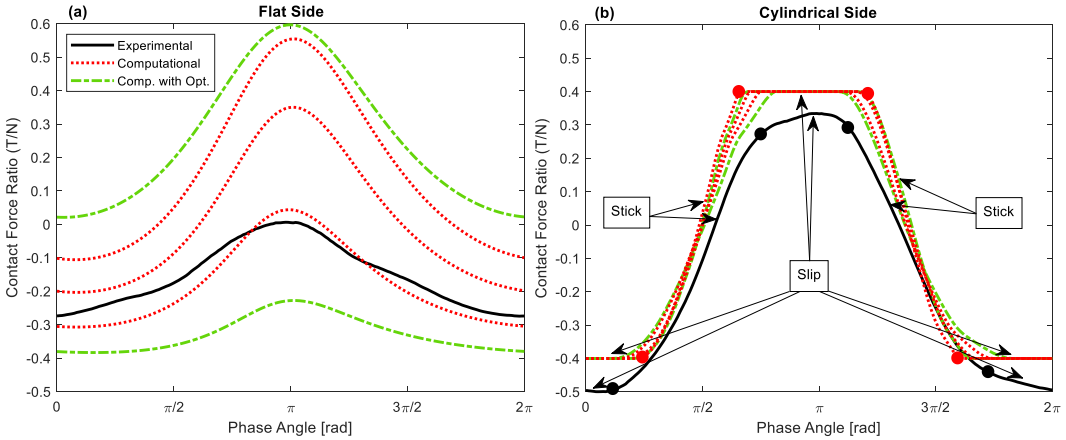

Figure 59: Contact force ratio of 80 N excitation case in one full vibration cycle at ω = 529 Hz for the right damper: (a) Flat side, (b) Cylindrical side

Figure 60a and Figure 60b show the tangential forces on the right damper for both flat and cylindrical sides, respectively. This set of forces corresponds to the one used to produce the results in Figure 59. Since the contact surfaces on the flat side are almost in the full stick condition, the tangential force on this side is non-unique as shown in Figure 60a. It is also clear in Figure 60a that the limit forces obtained computationally with the optimization algorithm successfully bound the variability range in which the experimental result is also present. This is one of the key results of the current study and proves the effectiveness of the optimization method once more. Focusing the tangential forces on the cylindrical side in Figure 60b, it is known that the slip condition significantly lowers the uncertainty caused by the non-uniqueness of tangential forces on this side. However, variability is still visible. This is explained by the fact that the forces at the cylindrical and flat contacts are coupled, i.e. the uncertainty at the flat side influences the variability at the cylindrical side. Hence, the tangential force on the cylindrical side also varies due to different force balances, as shown in Figure 60b. The curves follow a common pattern and share a similar behavior.

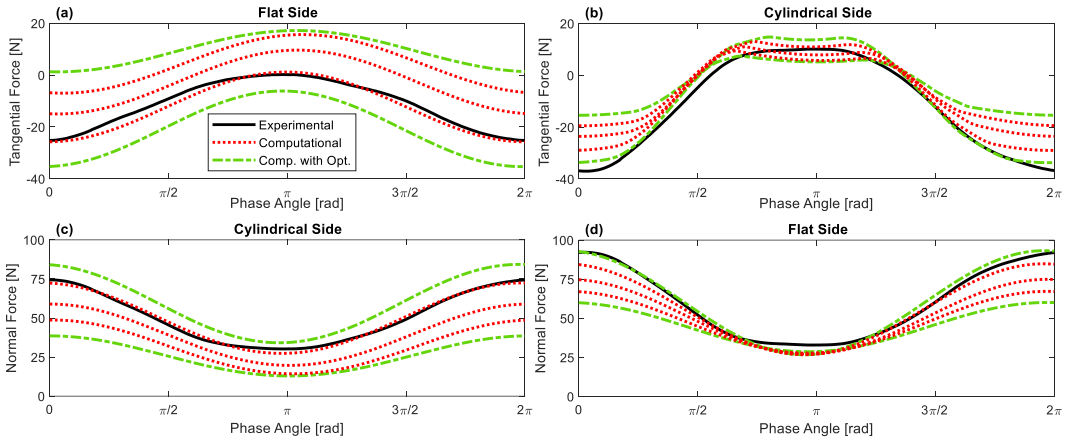

Figure 60: Contact forces on the right damper for 80 N excitation case at ω = 529 Hz

The damper induced cross coupling (see Figure 51c) has an important impact on the behavior of normal forces; it can be observed how the normal force on one side is mostly affected by the tangential force on the opposite side. Figure 60c depicts the normal forces on the cylindrical side, where a variability range is seen, as expected, due to the uncertainty of tangential forces on the flat side. This variability is also bounded by the limit forces obtained with the optimization algorithm. Figure 60d shows the normal forces on the flat side, which follow a similar pattern to that of the tangential forces on the cylindrical side shown in Figure 60b. It can also be noticed in the all results that experimental results are successfully captured by one of the computationally obtained curves, both in amplitude and in overall trend.

In Figure 61, the contact forces produced at the left damper contacts are shown. The trends are the same as those shown for the right damper. The variability range of non-unique tangential forces for the fully stuck flat side is successfully predicted with the method proposed in the previous chapter. The experimental results are computationally obtained with a high accuracy. All of these observations not only show the superior performance of the method, but also support the fact that the dynamic response variability is created by the uncertainty related to the non-uniqueness of tangential forces.

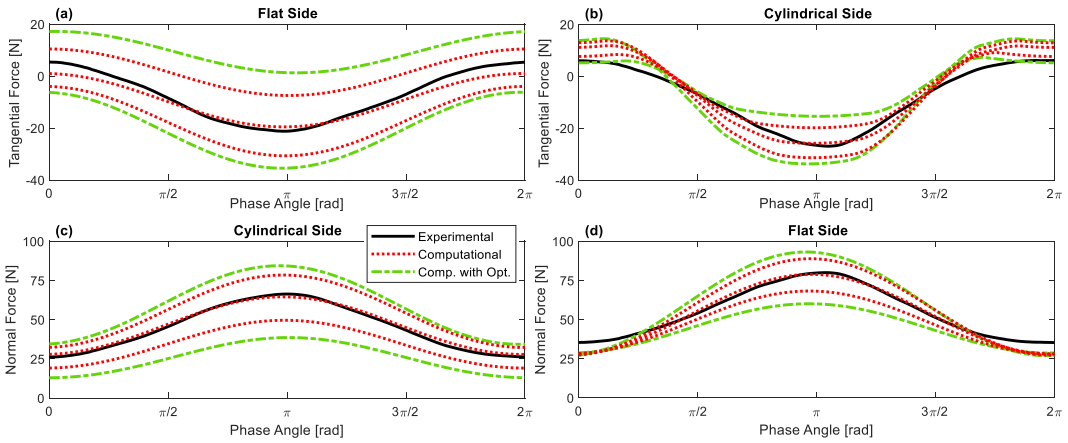

Figure 61: Contact forces on the left damper for 80 N excitation case at ω = 529 Hz

- Contact Forces for 20 N Excitation Case

This case has a larger variability range than the 80 N excitation (see Figure 57). In order to investigate the limiting cases, the contact forces are studied at the resonance of the two boundaries of the variability range, i.e. at ω = 549 Hz and at ω = 536 Hz.

First, the contact status is investigated once again, in order to better interpret the force results. In this case, the relative displacement between the damper and the blade is measured on one side in each recording, by using a differential laser. On the computational side, the average of relative displacements of all contact points located at the same contact surfaces is taken. This means the average of the relative displacements of 10 points at the flat side, and of 6 points at the cylindrical side.

Figure 62 illustrates the hysteresis cycles with the corresponding tangential force and relative displacements for the contacts on the left damper. Figure 62a shows that the flat side is under a fully stuck condition, while the energy is dissipated with a micro slip on the cylindrical side as shown in Figure 62b. It should be noted that the amplitude of the relative displacement is so small, so the laser struggles to measure it smoothly. Hence, a zigzag behavior and unrealistic vertical lines are seen in the experiments. Nevertheless, the results give a clear indication on the contact status and the computational and experimental results share the same order of magnitude both in terms of force and displacement range.

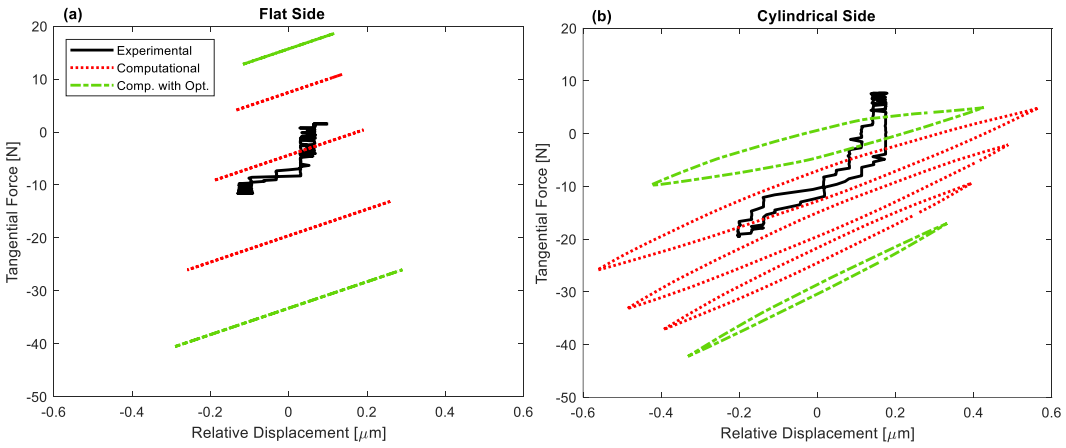

Figure 62: Hysteresis cycles of 20 N excitation case for the left damper: (a) Flat side, ω = 549 Hz, (b) Cylindrical side, ω = 544 Hz

Since the flat side is fully stuck, the variability range of the non-unique tangential forces is clearly visible in Figure 62a. The range is again bounded by the forces obtained with the optimization method. On the cylindrical side (see Figure 62b), it is very interesting to note that the static component of the forces is bounded by the optimization method, but the same phenomenon is not valid for the dynamic component and the amount of dissipated energy (internal area of the cycles). This is relevant; because, the optimization algorithm does not utilize the dissipated energy itself, but the loss factor, which is the proportion of the dissipated energy over the stored energy, as the objective function to minimize. This also explains the evidence shown in Figure 57c where some of the computationally obtained multiple responses (dotted red curves), which stay within the upper and lower limits (dash-dotted green curves), can exceed the boundaries at some specific frequencies.

Figure 63 shows the contact forces measured at ω = 549 Hz on the left damper. In this case, the non-uniqueness uncertainty and the damper induced cross coupling create a larger variability range than those of the previous results, in the tangential force of the flat side (see Figure 63a) and in the normal force of the cylindrical side (see Figure 63c), respectively. This is expected; as gross slip is achieved in the previous case, while a micro slip is dominant here. Hence, the behavior of the nonlinear response in the former was closer to a unique one than the latter. Regardless of the situation, the optimization method still works very-well and bounds the range including the experimental results, in Figure 63a and Figure 63c. The experimental and computational results match quite accurately in Figure 63b and Figure 63d, as well.

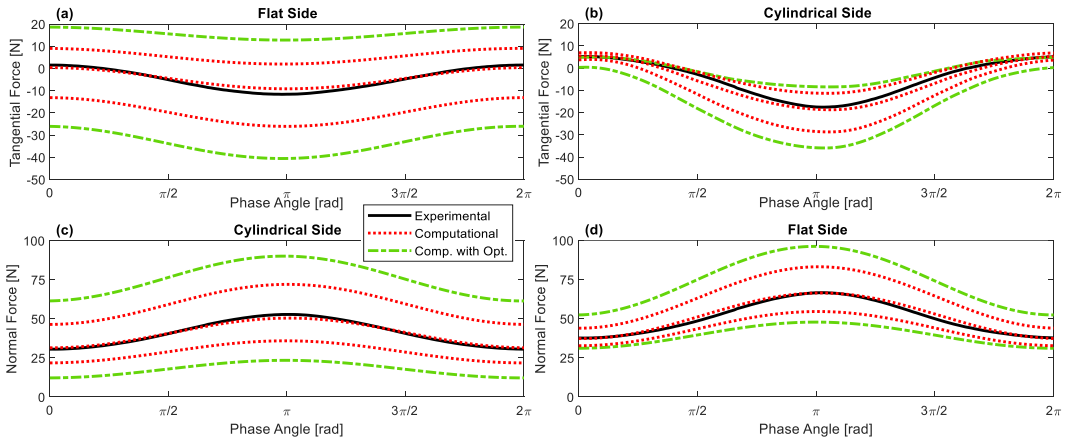

Figure 63: Contact forces on the left damper for 20 N excitation case at ω = 549 Hz

Figure 64 depicts the contact forces for the same conditions, but on the right damper. As expected, all the results show a coherent and a repetitive behavior. It should also be noted that, some of the computational tangential forces shown in Figure 64b have larger dynamic amplitudes than those predicted by the optimization algorithm. This is another example of the previous observation that the limits predicted by the optimization algorithm may be out-bounded by some of the nonlinear responses for limited portions of the vibration period at specific frequencies.

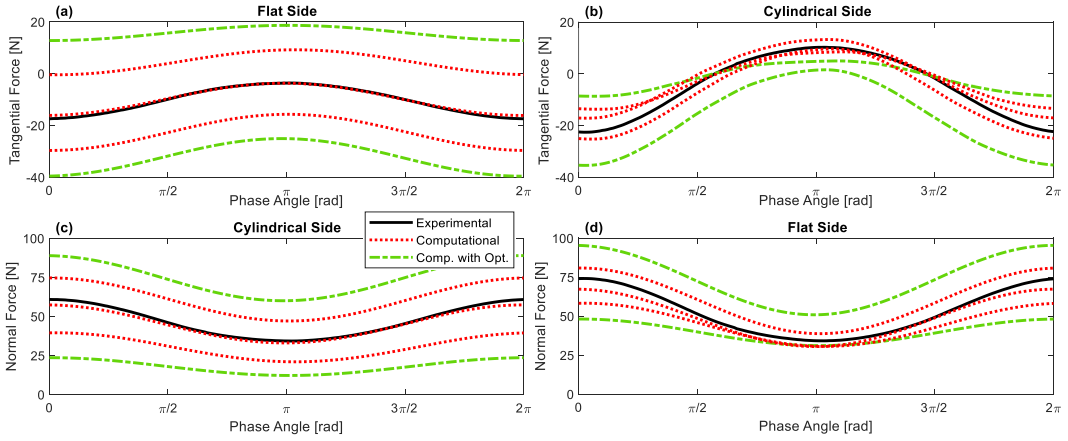

Figure 64: Contact forces on the right damper for 20 N excitation case at ω = 549 Hz

The contact forces are also investigated at the resonance of the lower limit (ω = 536 Hz), to check whether the method will be able to capture the range of variability. Figure 65 and Figure 66 illustrate the contact forces on the left and the right dampers, respectively. The results show the outstanding capability of the

optimization algorithm once more in determining the boundaries, together with well-matched experimental and computational responses.

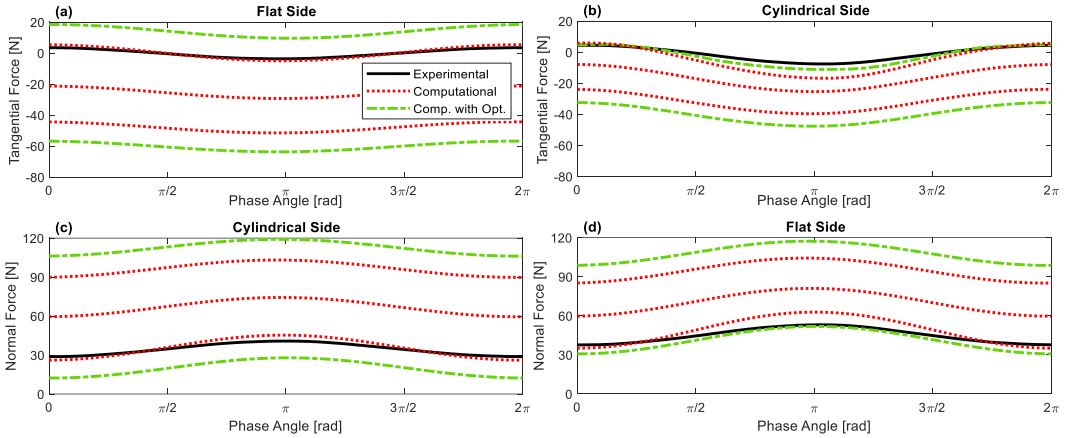

Figure 65: Contact forces on the left damper for 20 N excitation case at ω = 536 Hz

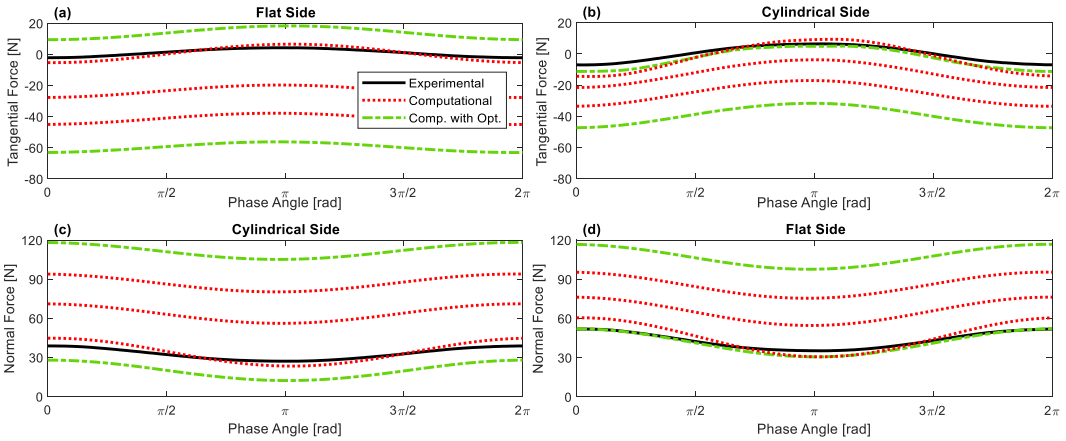

Figure 66: Contact forces on the right damper for 20 N excitation case at ω = 536 Hz

5.4.2 Multiple Nonlinear Responses with the Variability Range for 6.6 kg Pre-Load Case

This case study includes the heaviest pre-load applied to the damper; hence the pressure on the contact surfaces is the largest among investigated ones. This provides the contact pairs in the model to better represent the actual scenario, since a node-to-node perfect match is theoretically assumed in the simulations.

Figure 67 depicts all nonlinear responses measured and computed in the tests and simulations for different excitation amplitudes. A variability range is again clearly visible and it decreases with the increasing excitation level. The results show a great experimental-numerical match, as well as effective boundaries, also including the 100 N case. In addition to the general behavior of the frequency response, the resonance amplitudes are also given in Figure 68 for a direct comparison; since most of the attention in the under-platform damper design is given to the maximum vibration levels as it is directly related to the maximum stress on the blade or the computation of the largest stresses. It is also interesting to note in Figure 67 and Figure 68 that the variability ranges for different excitation levels overlap, a phenomenon also observed for 4.6 kg case. This underlines the importance of the computation of multiple responses and boundaries. Otherwise, if the overall behavior is not captured and the attention is focused only to particular curves, one may incur in the misinterpretation of the system kinematics. It may even lead to observe a hardening behavior of the response with an increasing excitation level. For instance, the upper boundary of the 80 N case is higher than the lower boundary of the 50 N case, and these two responses can be obtained in two different particular analyses or experiments. The correct inherent kinematics is only determined, once the full range of variability has been tracked.

Figure 69 shows the evolution of the loss factor which is used as the objective function to be minimized in the optimization algorithm. The solid line represents the values obtained during the computation of lower boundary, while dash-dotted line is for the upper boundary. As shown in Figure 69, the value of the loss factor is bigger with larger excitation levels, since the number of slipping nodes increases as the forcing becomes large. This condition makes the dampers more dissipative, which results in higher proportions of dissipated energy over the stored energy, i.e. loss factor. It should also be noted that the lower boundary for a particular excitation level is characterized by bigger loss factors than those computed for the upper boundary. This is also relevant, because the contacts spend more time in the stick state during the analysis of upper boundary, while more slip occurs in the lower boundary case.

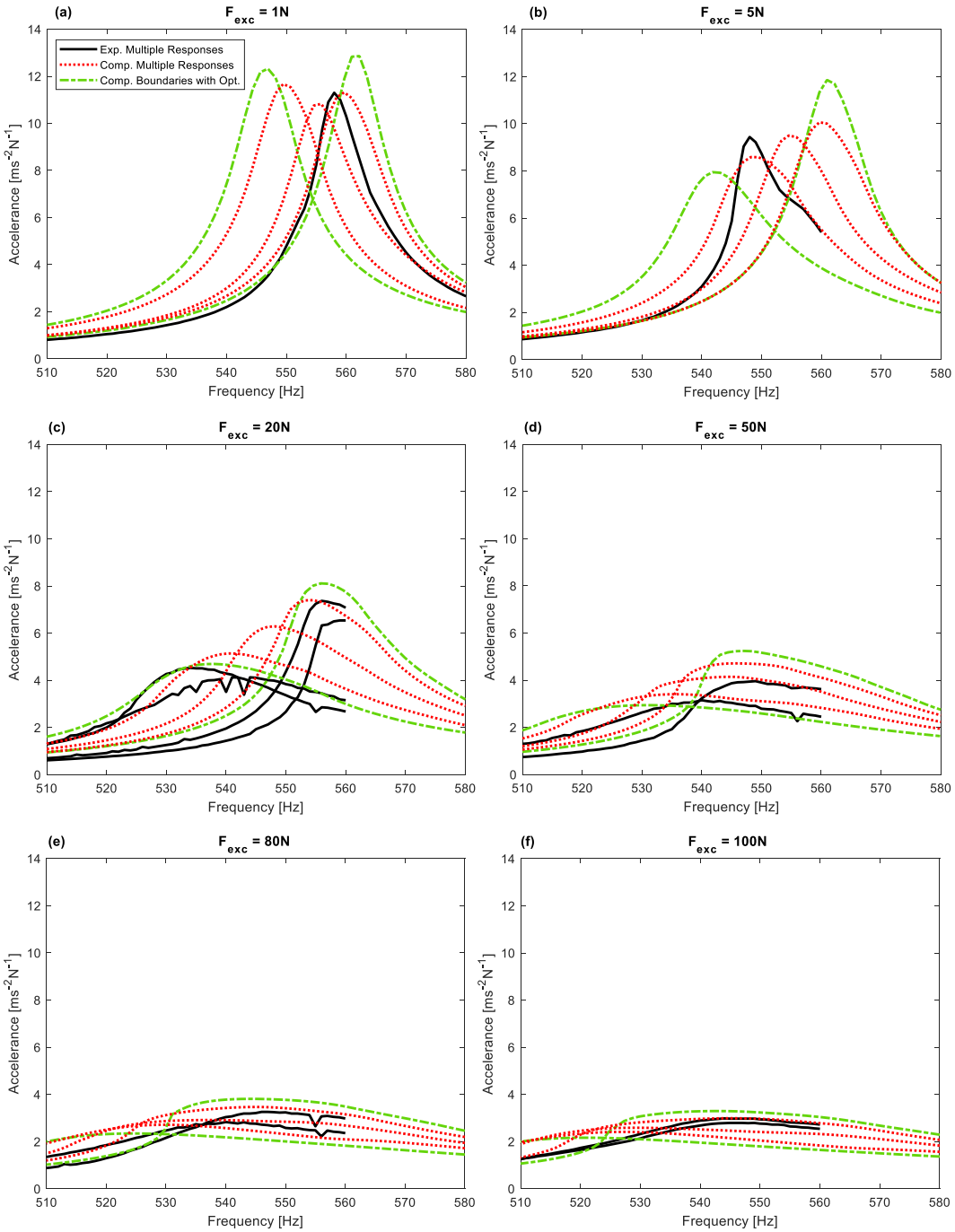

Figure 67: Nonlinear response amplitude of the blade tip for different excitation levels with 6.6 kg pre-load

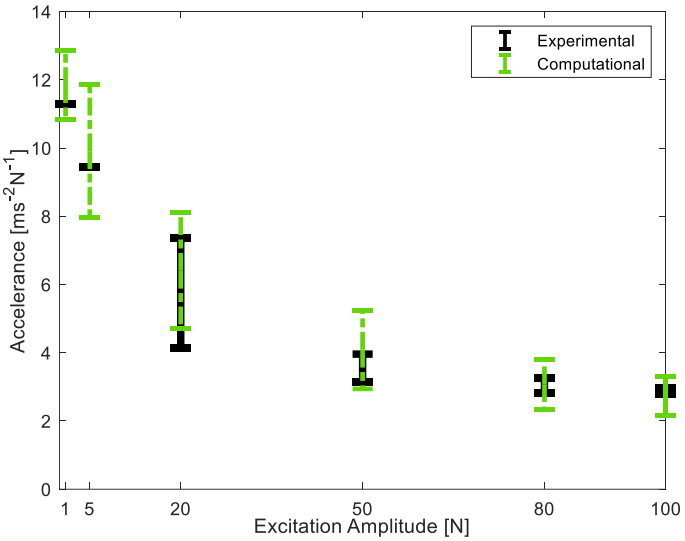

Figure 68: The variability range of resonance response amplitudes for different excitation levels with 6.6 kg pre-load

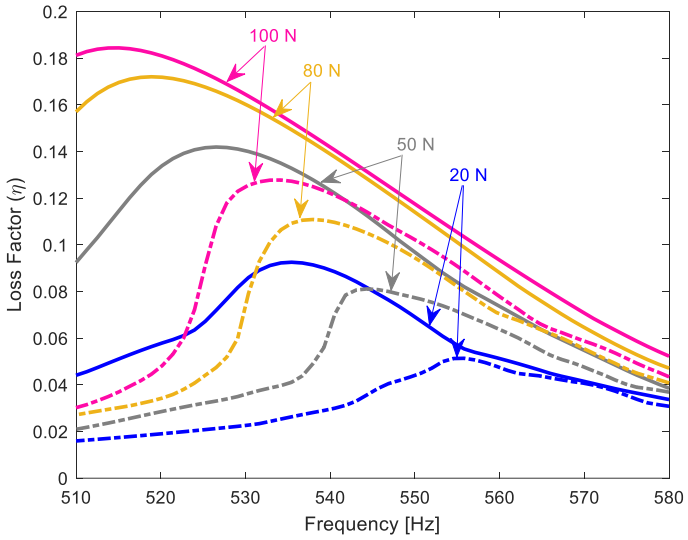

Figure 69: Loss factors corresponding to the boundaries for different excitation levels with 6.6 kg pre-load (solid line: lower boundary, dash-dotted line: upper boundary)

5.4.3 Multiple Nonlinear Responses with the Variability Range for 2.6 kg Pre-Load Case

In this case, the pre-load is decreased to a smaller value (2.6 kg) to further challenge the numerical optimization method. Figure 70 shows the nonlinear response amplitudes of the blade tip for various excitation levels. Although some of the experimental responses are captured computationally, the results are not as satisfactory as in the previous cases. . The differences are clearer in the variability range of resonance response amplitudes, as shown in Figure 71. It should be noted that this case with the lowest pre-load is the one where the nonlinearity is the largest. It is apparent that there is a missing point in the model, which provides a deviation between the experimental and computational results. Since the pre-load is very low, the contacts in the experiments may not be stable enough and some partial loss of contact may occur. Full contact may not have been achieved and the pressure distribution on the contact surfaces can be non-uniform. This explains the differences detected between the experimental response and the computational results, the latter being produced under the assumption of an ideal contact condition.

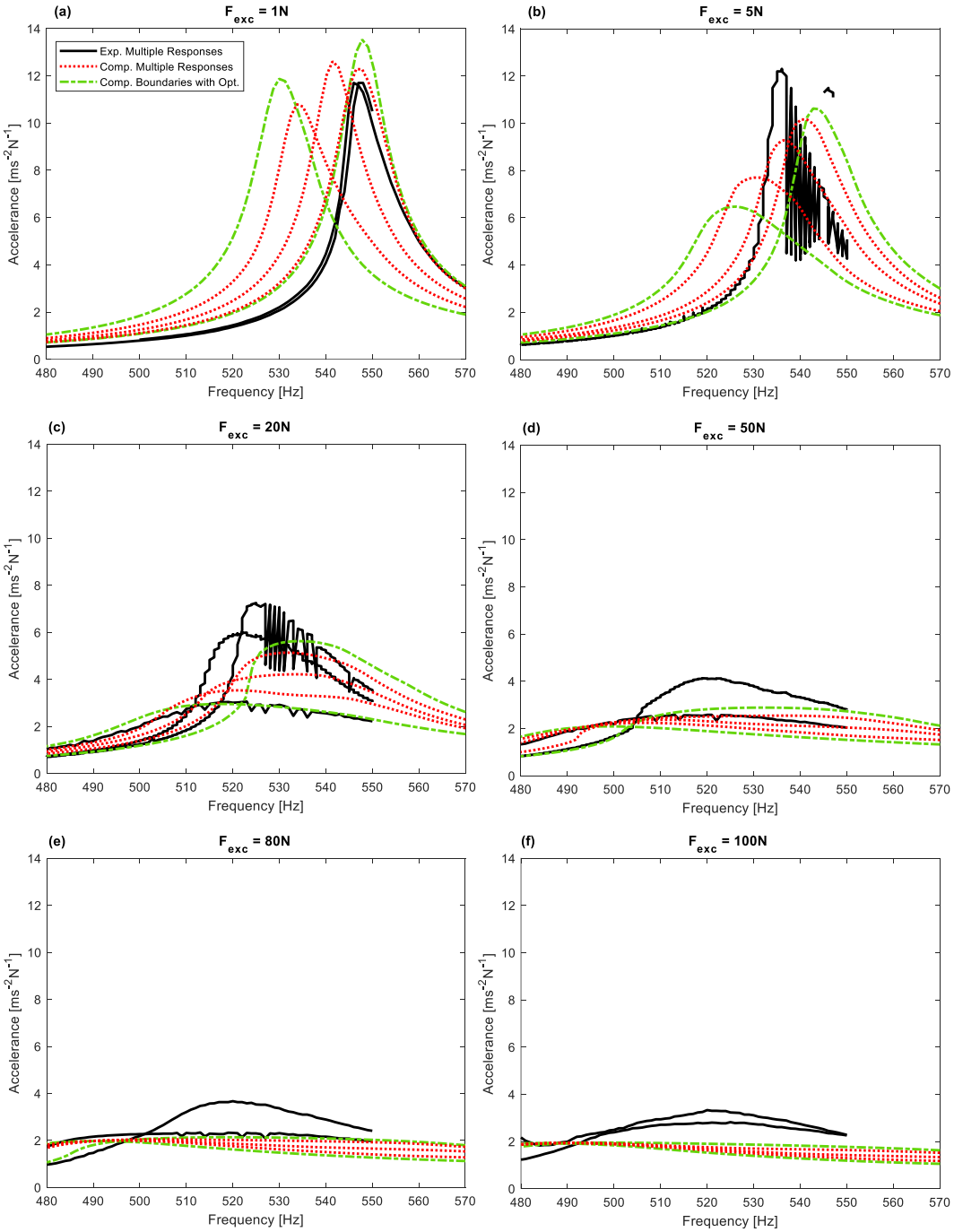

Figure 70: Nonlinear response amplitude of the blade tip for different excitation levels with 2.6 kg pre-load

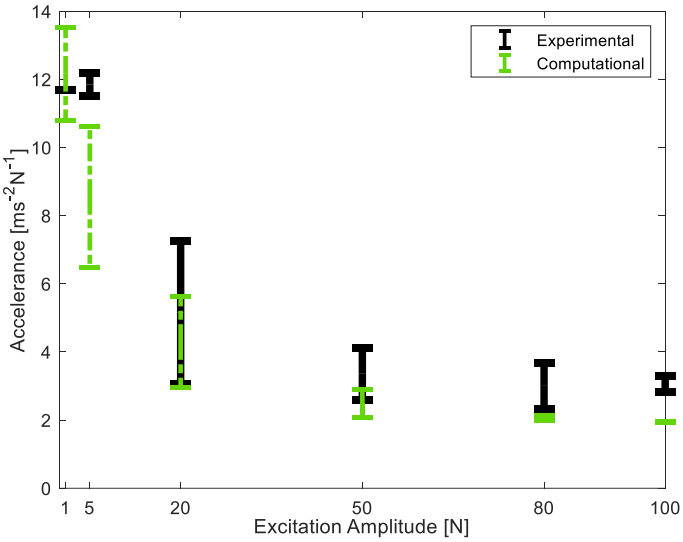

Figure 71: The variability range of resonance response amplitudes for different excitation levels with 2.6 kg pre-load

5.5 Summary

This chapter presents a joint study which aims to challenge the developed method with a test data. A dedicated experimental campaign has been previously used to measure the variable responses and contact forces (Botto & Umer, 2018; Botto et al., 2018), while the developed numerical method is utilized to estimate the boundaries of the variability range computationally. A large number of investigated cases show that different static conditions with the same contact parameters can give rise to a large variability in the nonlinear response, due to the non-uniqueness of friction forces. Experimental and computational results are in a good agreement, and the numerically calculated limits with the method proposed successfully bound the variability range in most of the cases.

This chapter underlines the importance of taking into account the non-unique contact forces, since fretting wear is not persuasive for the response variability of two consecutive tests. It also presents the first study in the literature, where a comparison is performed between experiments and simulations in the context of non-unique contact forces.

Chapter 6

Experimental and Computational Investigation of the Uncertainty on a Blade with Mid-span Dampers

This chapter[5] addresses three main subjects. Firstly, a novel test setup is developed to experimentally study the nonlinear dynamic behavior of a turbine blade coupled with two mid-span dampers. To this end, a representative turbine blade and mid-span friction dampers are originally designed, and they are assembled to the special test rig which has been shown in the previous chapter. Secondly, the variability of the dynamic response of the blade under the same nominal conditions is investigated in detail. Lastly, the computational and experimental comparison is performed.

6.1 Experimental Campaign

6.1.1 Description of the Test Setup

The entire test rig is a large assembly composed of three main substructures. Figure 72 depicts the complete picture of the test setup. Although some of the

[5] Part of the work described in this chapter has been previously published:
"Ferhatoglu, E., Botto, D., & Zucca, S. An experimental investigation on the dynamic response variability of a turbine blade with mid-span dampers. *ASME Turbo Expo 2022 Turbomachinery Technical Conference and Exposition*, (accepted)"

substructures have been explained in the previous chapter, they will be very briefly explained once more for the sake of completeness.

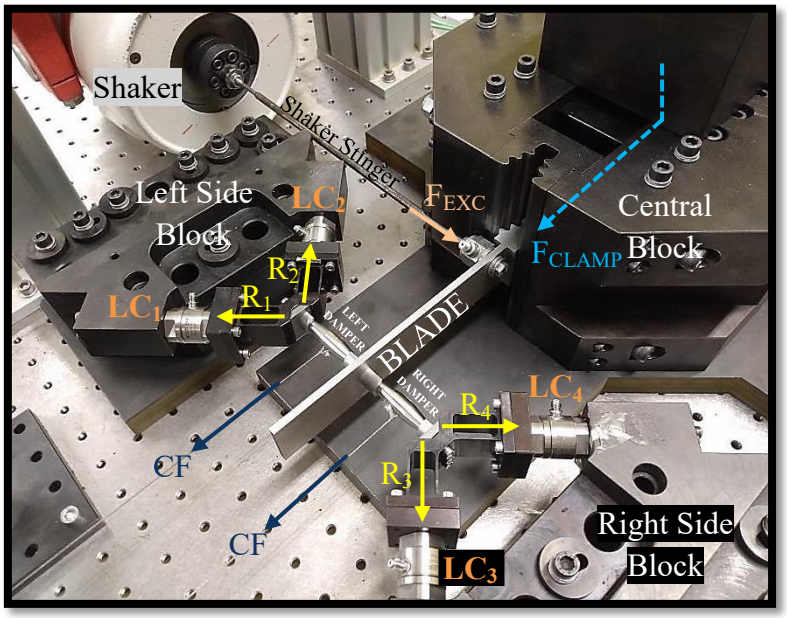

Figure 72: A view of the assembled test setup

The first substructure consists of one central and two side blocks, which form the main frame of the test rig. The central block has a clamping mechanism inside. Basically, it applies a large static force (F_{CLAMP}) from the bottom and sticks the blade root to its female fir-tree slot. In this way, a possible source of friction at the blade root is prevented. Side blocks are bulky entities that are bolted to the table. They carry auxiliary components on themselves to measure contact forces. One of the components is an L-shaped force de-coupler. This element distributes the reaction forces (R) in two perpendicular directions. The forces are then measured by a load cell (LC) that is attached between the de-couplers and the side blocks. This first substructure has been already manufactured previously at Politecnico di Torino. The details about the design of these parts and the clamping mechanism can be extensively found in the study of Botto and Umer (2018).

The second substructure is the blade itself. It imitates the last stage blades of steam turbines utilized in industrial applications (Drozdowski et al., 2015; Siewert et al., 2017; Szwedowicz et al., 2008), and it is originally developed for academic purposes in the scope of this thesis. The top view of the blade model, together with the parts at the right side, is depicted in Figure 73. The blade has a rectangular cross section and is a slender beam with 4 mm thickness and 160 mm

length. At the mid-span of the blade, there are two cylindrical slots on which the damper can engage and come into contact with the blade. In the experiments, the blade is harmonically excited by an electromagnetic shaker (F_{EXC}), from a position close to the root (see Figure 72).

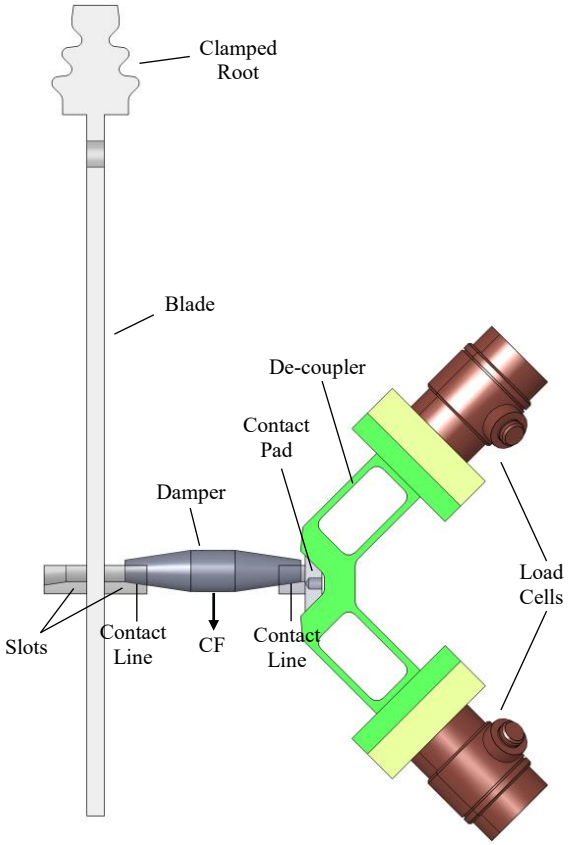

Figure 73: A top view of models for the right side

The third substructure consists of the dampers and contact pads. The dampers are designed of the pin type geometry, as similar to their industrial counterparts (Drozdowski et al., 2015; Siewert et al., 2017; Szwedowicz et al., 2008). They have a non-uniform cross section throughout their horizontal axes and three different portions with a total length of 40 (15+10+15) mm. The ends and the middle portion are cylindrical with 5 mm and 9.5 mm diameters, respectively. These dimensions ensure an 8.53° inclined cylindrical contact region on each side.

Dead weights are applied from the middle portion of the dampers, which creates a static pre-load simulating the centrifugal force (CF) effect. The pre-load presses the dampers in between the blade and contact pads. These pads are directly bolted to the de-couplers and provide a frictional surface mimicking the contact region of a dummy adjacent blade. They have exactly the same contact regions of the slots on the real blade's mid-span. In this way, the contact surfaces become similar at each side of the damper. It should also be noted that the axes of the mating pairs are intentionally designed eccentric to ensure a line contact in the tests. This feature is an imitation of real life applications, implemented by making the radius of the damper curvature smaller than that of the slots and pads. It should also be noted that the material of all structures in the experimental campaign is steel.

6.1.2 Measurement Procedures

The experiments are performed with a conventional force controlled stepped-sine methodology around the first lateral in-plane resonance region. Frequency sweeps are done by defining a lower and an upper limit in which the resonance frequency is included. The Simcenter SCADAS Mobile data acquisition system is utilized for acquiring the time signals. The sampling frequency and windowing are properly taken into account to measure the data correctly. Several parameters are recorded during the tests, and their measurement procedures are explained in the following.

The first quantity measured is the reaction forces on the load cells, from which the contact forces can be easily derived. Figure 74a depicts the force balance on the right de-coupler. R_3 and R_4 are the measured forces by load cells, while T and N represent the tangential and normal forces on the contact pad. α and θ are 45° and 8.53°, respectively, and they are design parameters of the de-coupler and the contact pad. The geometry of the components is purposely designed in such a way that forces intersect exactly at the middle point of the contact line. Thus, all forces act on the same point, and the possibility of a moment due to a force eccentricity is prevented. The contact forces can be derived with two coupled force balances in the horizontal and vertical directions as follows

$$\begin{aligned} T\cos(\theta) + N\sin(\theta) - R_3\cos(\alpha) - R_4\cos(\alpha) = 0 \\ T\sin(\theta) - N\cos(\theta) + R_3\sin(\alpha) - R_4\sin(\alpha) = 0 \end{aligned} . \tag{6.1}$$

The accuracy of this calculation method is deeply investigated by Botto and Umer (2018) with the same de-coupler mechanism by including several parameters such as the elasticity of the de-couplers or the degree of separation in forces. It has been reported that it enables an accurate measurement of contact forces with a deviation less than 1%. Figure 74b also shows the force balance achieved on the damper. T' and N' are the contact forces at the de-coupler side of the damper with the same magnitude of T and N but in opposite directions. Contact forces at the blade side, T" and N", can also be computed with force balance equations by neglecting the inertia of the damper. They can be written as

$$\begin{aligned} T^{"}\cos(\theta) + N^{"}\sin(\theta) - T^{'}\cos(\theta) - N^{'}\sin(\theta) = 0 \\ -T^{"}\sin(\theta) + N^{"}\cos(\theta) - T^{'}\sin(\theta) + N^{'}\cos(\theta) - CF = 0 \end{aligned} . \quad (6.2)$$

In this way, all forces on contact interfaces can be easily obtained. There are two assumptions that are worthy to mention for Eq. (6.2). The first one is that the bending on the damper, caused by the pre-load, is negligible. This assumption is simply confirmed with a preliminary analysis by assuming the damper as a simply supported beam. The static deformation is extremely small (less than 1μm), and the effects of the bending can be ignored. The second assumption is that the inertia of the damper is neglected, since the mass of the dampers are only 15.3 grams. Nevertheless, it will be numerically shown in Section 6.2.3 that the effect of the inertial forces can be safely ignored. It should also be noted that CF is applied by using steel ropes that pass through two successive pulleys. A static test is initially performed to quantify the friction between the rope and pulleys. It is measured that the actual force transmitted to the dampers is 95% of the dead weights. As a result, a correction of 0.95 is applied in the CF. The procedures of measuring contact forces on the de-coupler and the damper at the left side can be similarly followed as explained above.

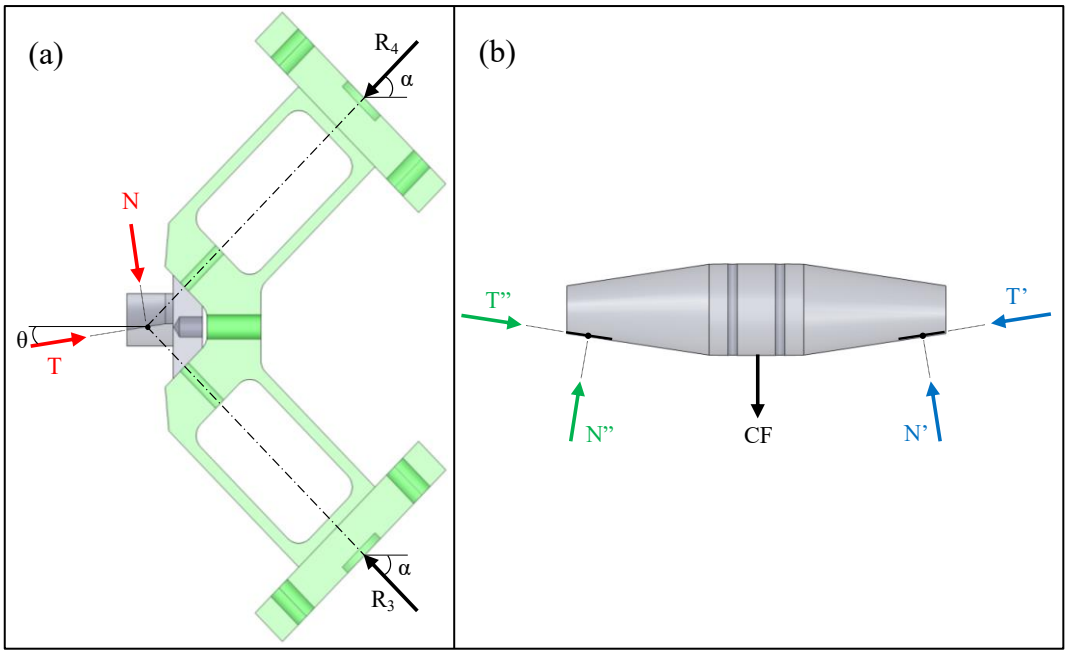

Figure 74: Force balances on (a) The contact pad and (b) The damper

A differential laser is also used in the experiments while the test setup is in operation. The laser measured two different parameters to extract the inherent kinematics of the damper. The first one is the relative displacement between two ends of the damper. The laser is pointed in parallel, from the direction of the dead weights to the two positions located at both ends of the right damper, as shown in Figure 75a. The distance between the two points (h) is 20 mm. This measurement enables the prediction of the damper's rigid rotational motion around its vertical axis (see Figure 75a), with a simple geometrical relation. The second parameter measured by the laser is the relative displacement between the damper and the blade. This measurement is done to construct the hysteresis cycles. However, it should be underlined that there are limitations on the exact measurement of the relative displacement due to the lack of space in the test campaign for this particular measurement. Nevertheless, the main aim here is only to qualitatively interpret the behavior of hysteresis cycles with roughly measured relative displacements. A quantitative assessment of contact parameters is out of scope here. Figure 75b and Figure 75c show the laser points and the position of laser heads, respectively. One of the heads is directed to a point located on a close region to the contact slot of the blade, while the other head is pointed on top of the damper. Here, a reflective tape is attached via an additional indenter wrapped around the damper, since the middle portion of the damper is perfectly circular

and does not have any indentation to reflect the light back to the laser. Moreover, the laser has to be inclined (around 12°-15°) to be able to take the measurements. Even though the final results cannot be assumed perfectly accurate, they are illustrative for a qualitative interpretation. The last parameter recorded is the response of the blade with an accelerometer attached to the blade tip as shown in Figure 75b.

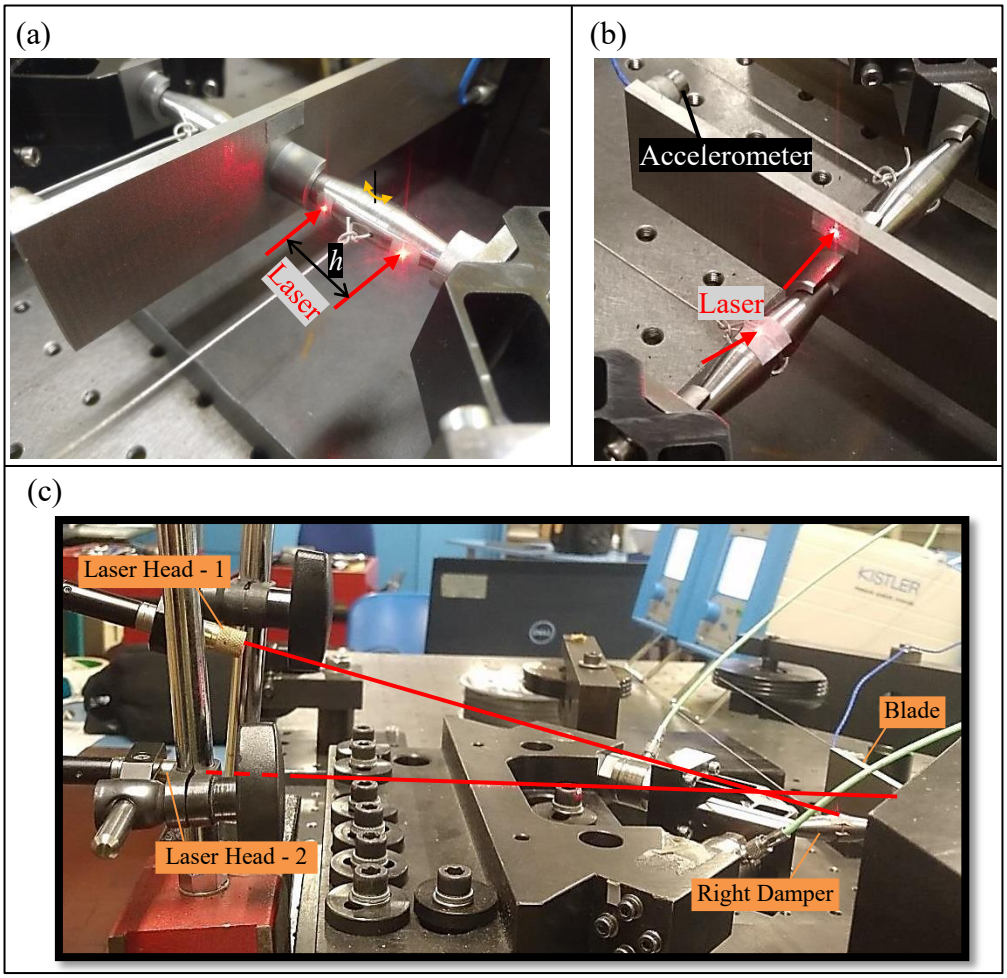

Figure 75: (a) Laser points for the rotational motion, (b) laser points for relative displacements, (c) a back view for the position of the laser heads

6.2 Experimental Results and Discussion

6.2.1 Linear Response of the Blade

To characterize the blade's linear behavior, frequency sweeps are performed initially for the free blade. A sensitivity analysis is also done on the clamping force to minimize the friction introduced from the fir-tree root. F_{CLAMP} is set to a large enough value that minimizes the damping at the blade root.

The normalized response of the blade for an increasing level of excitations is shown in Figure 76a. It can be seen that the response overlaps except for the case with the lowest excitation. It is necessary to highlight the fact that it is practically impossible to completely prevent the damping at the blade root as well as the material damping in the blade, no matter how large clamping force is applied. The results depicted in Figure 76a can be assumed reasonable enough to state that the damping at the blade root is negligible. It should also be underlined that the vibration amplitudes will drastically decrease after engaging the dampers when compared to the free blade case. It will further reduce the friction at the root, and the most dominant damping will be provided from the contacts between the blade and dampers. The response of the free blade is given with a larger frequency interval in Figure 76b. It shows that the interested mode is a well-separated one with the natural frequency measured at 122.25 Hz.

It is also worth mentioning that the frequency step has been set to 0.25 Hz. A smaller frequency step would capture the resonance peaks better; however, it should be underlined that the free blade is a slender structure that has a considerable amount of vibration at the resonance particularly with higher excitations. Not to damage the blade, the resonance region was needed to be passed sufficiently fast while at the same time capturing the steady-state response. On the other hand, when the excitation amplitude is decreased below 1 N, it is observed that the force controller of the data acquisition system was struggling to keep the excitation amplitude constant at that small value. So, the minimum value is chosen 1 N.

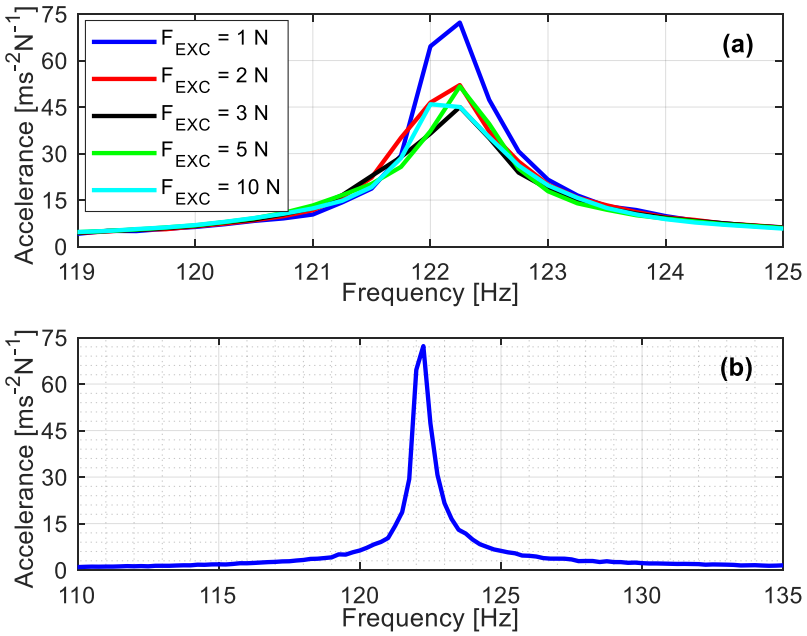

Figure 76: Linear response of the blade without dampers

6.2.2 Nonlinear Response of the Blade

The nonlinear dynamic behavior of the blade coupled with the dampers is extracted with several tests. Firstly, frequency sweeps are performed with an increasing order of excitation levels, while the centrifugal forces (CF) are constant on the damper. Three dead weights (5.6 kg, 3.6 kg and 1.6 kg) are separately loaded to investigate the dissipation capability of the damper under different circumstances.

Figure 77 illustrates the normalized response amplitudes of the blade obtained with various excitation levels around the first resonance region. It is obvious that the resonance frequency of the system considerably shifted to higher values when compared to the free blade case. This is due to the engaging position of mid-span dampers. They are located relatively far from the blade root, which brings a considerable amount of hardening to the system. It is clear in Figure 77 that the mid-span dampers efficiently work and reduce the vibration amplitudes of the blade by dissipating the energy. In all cases, the normalized response smoothly decreases and shows a softening behavior, while the excitation increases. Moreover, the resonance region slightly shifts to the left with decreasing pre-loads, as can be seen from Figure 77a towards to Figure 77c. This observation is quite relevant; because, contact pressure on the frictional surfaces tend to increase

with larger pre-loads and this ensures the increase of contact stiffness, which results in obtaining higher resonance frequencies. It is also interesting to note that the response amplitudes corresponding to the same excitation level among different cases is smaller for those obtained with low pre-loads. For instance, the response curve measured with 5 N excitation in Figure 77c is more damped than its counterpart shown in shown in Figure 77a; because, the higher pre-load in the latter makes the response behavior closer to that of the fully stuck linear configuration.

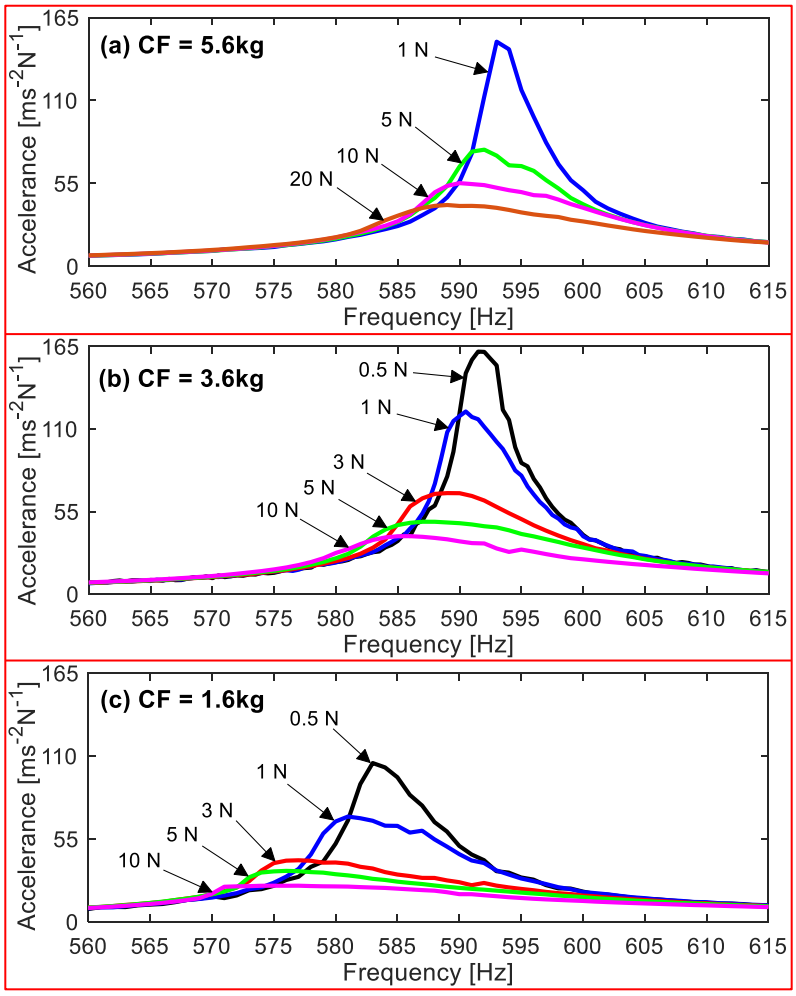

Figure 77: Nonlinear response of the blade with an increasing order of excitation levels

It is worth mentioning that the direct comparison of the accelerance amplitudes shown in Figure 76 and Figure 77 can be misleading in the interpretation of the dissipative capabilities of MSDs. Some curves in Figure 77

surpass the blade's linear response shown in Figure 76, and this observation might be interpreted as the vibration level increases after engaging the dampers. It should be noted that the accelerance is a quantity obtained by the multiplication of the steady state displacement amplitude with the square of the excitation frequency. Since the resonance frequency of the coupled blade-damper configuration is approximately 5 times of the value for the stand-alone blade, the actual comparison of the displacement amplitudes should be done by dividing the values of the coupled blade-damper configuration to 25. As a result, the displacement amplitudes become much smaller with the presence of the damper, compared to the free blade case.

It is shown in each case study that the frequency sweeping strategy with an ascending order of harmonic forcing under the same pre-load gives consistent results. All observations about the nonlinear dynamic behavior of the blade coupled with mid-span dampers can be considered coherent. The next part presents the variability of the nonlinear response measured under the same nominal circumstances with purposely defined loading sequences.

6.2.3 The Variability of the Nonlinear Response

The variability phenomenon is a frequent occurrence in laboratory conditions. In this chapter, it is investigated by following a particular testing strategy that enables the comparison of the response obtained in different tests but with the same inputs.

Table 7 gives the complete picture of the experimental procedure. Before explaining the procedure, it is worth defining the terminology used in it. One complete run means a full frequency sweep throughout the frequency range defined. Each run is performed with one specific pre-load and excitation level. All the measurements (nonlinear response, contact forces and relative displacements) are done simultaneously during the runs. The procedure consists of four steps. In Step 1, the excitation amplitude at which the tests will be performed is first decided, and the dampers are loaded with 6.6 kg dead weights. Step 2 consists of eight consecutive frequency runs with the defined excitation level, but different pre-loads. More specifically, in Step 2, the first run is performed with 6.6 kg. Having completed the first run, the experiment stops, and one kg dead weight is removed. The second run of the Step 2 starts again with 5.6 kg, and a full sweep is completed. The practice of decreasing pre-loads is maintained until the end of the

fourth run conducted with 3.6 kg. The fifth run is again performed with 3.6 kg without touching to dead weights, and then they are gradually loaded back with one kg intervals in between the frequency sweeps, until to complete the eighth run with 6.6 kg. In step 3, the dampers are completely unloaded and reloaded back with 3.6 kg. Step 4 is accomplished with the identical logic of the second step, but with a reverse loading sequence of dead weights, i.e. they are increased first and then decreased. This approach nearly simulates the actual working environment of turbine blades in the laboratory conditions, as the centrifugal forces change with increasing and decreasing rotor speeds.

Each run takes almost one minute. The time interval between the runs is also around 15-20 seconds, which was spent for unloading/loading the dead weights and starting the next run. Thus, the entire procedure is completed in approximately 20 minutes, as there are 16 runs. This procedure gives 16 different response curves all of which are measured with the previously defined excitation level. Since four particular pre-loads are used in the tests, the curves can be separated into 4 subsets each of which contains 4 different runs corresponding to the same pre-load. As an example, the subset of 4.6 kg pre-load is composed by the 3rd, 6th, 10th and 15th runs.

Table 7: The loading sequence of the dampers for a prescribed excitation level

Step 1	Step 2		Step 3	Step 4	
	Run	CF [kg]		Run	CF [kg]
Load the dampers	1	6.6	Remove and reload the dampers	9	3.6
	2	5.6		10	4.6
	3	4.6		11	5.6
	4	3.6		12	6.6
	5	3.6		13	6.6
	6	4.6		14	5.6
	7	5.6		15	4.6
	8	6.6		16	3.6

This testing strategy is applied with four different excitation amplitudes (F_{EXC}), 1 N, 3 N, 5 N and 10 N, to investigate the damper kinematics under various forcing. At the end, 16 different sets are collected with four different excitations and pre-loads. For brevity, the results are presented in six subsets with two excitation levels (1 N and 5 N) and three dead weights (3.6 kg, 4.6 kg and 6.6 kg). These subsets are shown in Table 8, and intentionally selected as

demonstrators. For each subset, a parameter, which simply represents how close the system is to full stick conditions, is defined. It is computed with the ratio of CF/F_{EXC}, and normalized with respect to the first subset. It means that the highest the ratio, the closest the system is to the fully stuck configuration. In this way, different conditions in which the slip is low (Subset 1), moderate (Subsets 3, 4) and high (Subset 6) will be shown in the following. It is worth mentioning that this ratio is just an illustrative parameter that will help in the interpretation of the results.

Table 8: Subsets of experimental results

Subset	CF [kg]	F_{EXC} [N]	Ratio (%)	Runs
1	6.6	1	100	1, 8, 12, 13
2	4.6	1	70	3, 6, 10, 15
3	3.6	1	55	4, 5, 9, 16
4	6.6	5	20	1, 8, 12, 13
5	4.6	5	14	3, 6, 10, 15
6	3.6	5	11	4, 5, 9, 16

Figure 78 depicts the frequency response curves measured around the first resonance region. To make a meaningful comparison, the results of subsets are separately given in each subfigure. Each subset contains frequency responses measured with the same inputs (F_{EXC} and CF) but in different runs as shown in Table 8. It is clear that the response is non-unique and it varies in all subsets, even if all user controlled conditions at the macro scale testing environment are kept identical. This phenomenon may seem as a black box for the designers, since the response itself does not give an insight about its non-repeatability. In this study, the underlying mechanism is investigated through additional measurements thanks to developed test rig.

The first notable observation is that the variability is larger in some subsets. In particular, on the one hand for 1 N excitation, the response behavior shows a lower variability with the highest pre-load in Figure 78a, while the scattering increases with decreasing pre-loads towards Figure 78c. On the other hand for 5 N forcing, the behavior is exactly opposite. The largest variability is obtained for 6.6 kg case in Figure 78d and it decreases with reducing dead weights towards Figure 78f. To investigate the underlying reason of this observation, hysteresis cycles are measured in each test to illustrate the amount of slip.

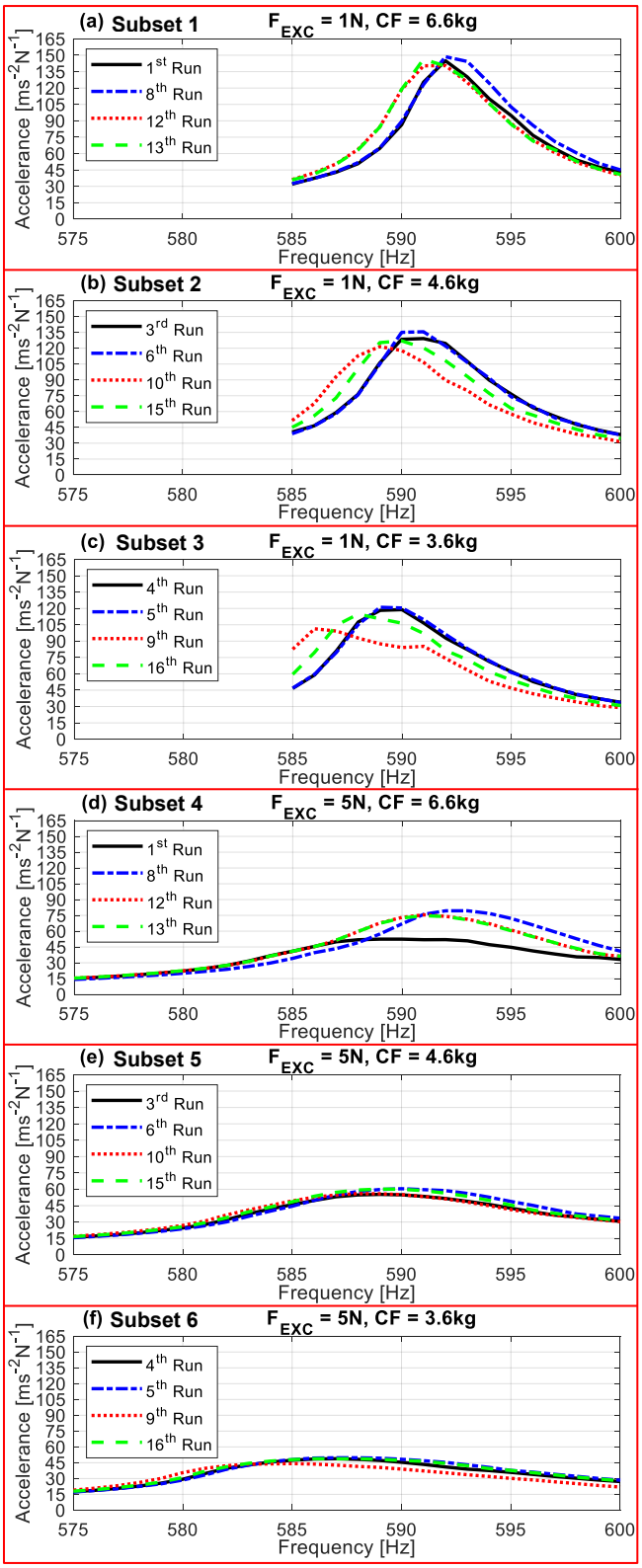

Figure 78: The variability of nonlinear response

- Hysteresis Cycles

Figure 79 depicts the hysteresis curves measured at the steady state conditions during which the system is at the corresponding resonance frequencies. The results are presented for the 1st, 3rd, 4th and 6th subsets, to investigate the cases with the largest and lowest variability. One sample is given from each subset, for clarity. It can be noticed in Figure 79 that there is a zigzag behavior in the data; because, the differential laser struggles to smoothly measure the extremely low relative displacements (less than 0.7 μm). To ease the readability of results, hysteresis cycles are heuristically (i.e. manually) redrawn by using dotted and dashed lines. It is clear in all subsets that damping is present with a slip motion, as the inside area of the hysteresis cycles gives the dissipated energy. The shapes of the hysteresis curves indicate that micro slip occurs in all subsets. To check whether the gross slip is also achieved, the ratio of tangential forces to normal ones (T/N) is investigated. During the gross slip, the ratio is expected to be a constant value (coefficient of friction); but, it does not reach this limit (as shown in Figure 80), indicating that gross slip is never achieved in the experiments.

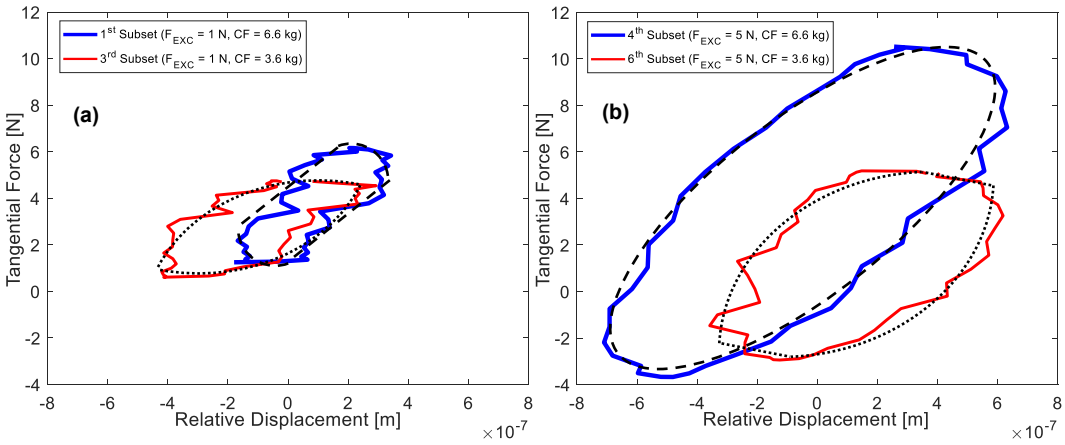

Figure 79: Hysteresis cycles

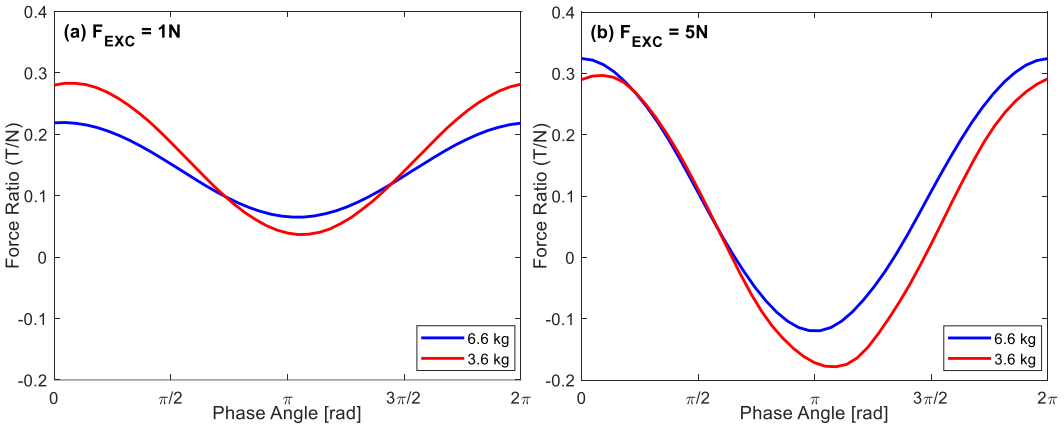

Figure 80: Contact force ratio

In Figure 79a, the hysteresis shape of the 1st subset (F_{EXC} = 1 N, CF = 6.6 kg) has clearer stick region with more straight lines, while the curve of the 3rd subset (F_{EXC} = 1 N, CF = 3.6 kg) has more uncertain stick-to-slip transition region. This indicates that the micro slip in the 1st subset is less dominant than that in the 3rd. The amount of the slip in the former is also slightly less. These observations are relevant, because the 1st subset is the one closest to the fully stuck configuration among all cases, since it includes the lowest excitation (1 N) and the highest pre-load (6.6 kg), as also shown in Table 8 with the ratio of CF/F_{EXC}. Regarding 5 N excitation in Figure 79b, the shapes of the hysteresis cycles show that the motion of the damper approaches to a near gross slip in both subsets. It is interesting to note that the micro slip in the 4th subset is more dominant than the 6th one. This observation is also relevant; because, the 6th subset is the one closest to the gross slip conditions, with the lowest pre-load (3.6 kg) and the highest excitation level (5 N) among the presented subsets.

All these observations show that there is a link with the amount of micro slip and the response variability in the system. Indeed, once the micro slip is the dominating motion in the contacts, i.e. the 3rd and 4th subsets, the variability is larger as shown in Figure 78c and Figure 78d. The repeatability of the response increases towards to the fully stuck (the 1st subset) or gross slip (the 6th subset) conditions, as the response approaches to a unique one as shown in Figure 78a and Figure 78f. This observation is fully consistent with the hypothesis of Chapter 3 that the response variability is caused by the non-uniqueness of friction forces. According to this idea, the response may vary considerably if a dominating micro slip behavior occurs in the contacts, due to the uncertainty present in the static component of the tangential forces. It also states that the response of the system should be unique during the gross slip or fully stuck contact behavior, as observed

in a similar manner in the experiments of the current work. This is the first indication that the variability in our experiments is caused by the non-uniqueness of friction forces. If there was one another main factor dominant on the response variability in the tests, it would have affected all the data regardless of the contact conditions.

- Rigid Rotation of the Damper

Accuracy of the measured contact forces and the relative displacement between the damper and the blade may be affected by the rigid rotation of the damper around its vertical axis, which is also indirectly measured as shown in Figure 75a. However, this quantity is recorded with additional tests separately, since the laser orientation had to be changed from the previous one used for the measurement of the relative displacement between the blade and the damper.

In the experiments, the measured quantity is the relative displacement (referred to as Δd), whose amplitude is measured in the range of 1-2 μm, between the directed points of the laser. The distance between the laser measuring points (h) on the damper is 20 mm (see Figure 75a). Hence, the angle of the rotation can be computed with a simple geometrical formulation, as $\tan^{-1}[\Delta d/h]$. Figure 81 shows directly the computed angle of the damper rotation, measured with two different pre-loads and excitation values, for one full vibration cycle at the corresponding resonance frequency. It can be seen that even the maximum angle of the rotation is considerably small (less than $6\text{x}10^{-3}$ degrees). The inertia force (F_i) due to the maximum amplitude of the damper rotation ($\theta \approx 6\text{x}10^{-3}$ deg $\approx 1.05\text{x}10^{-4}$ rad) is also computed at the resonance frequency ($\omega \approx 590$ Hz) as the multiplication of mass moment of inertia of the damper ($I \approx 1490$ g·mm^2, calculated by the design software) with the angular acceleration ($\ddot{\theta}$),

$$\begin{aligned} F_i &= I\ddot{\theta} = I\omega^2\theta \\ &\approx (1490\times10^{-9})(2\pi\times590)^2(1.05\times10^{-4}) \\ &\approx 0.002\text{N} \end{aligned} \tag{6.3}$$

The amount of the rotation angle and the computed inertia force proves that the rigid rotation of the damper is negligible and can be safely ignored.

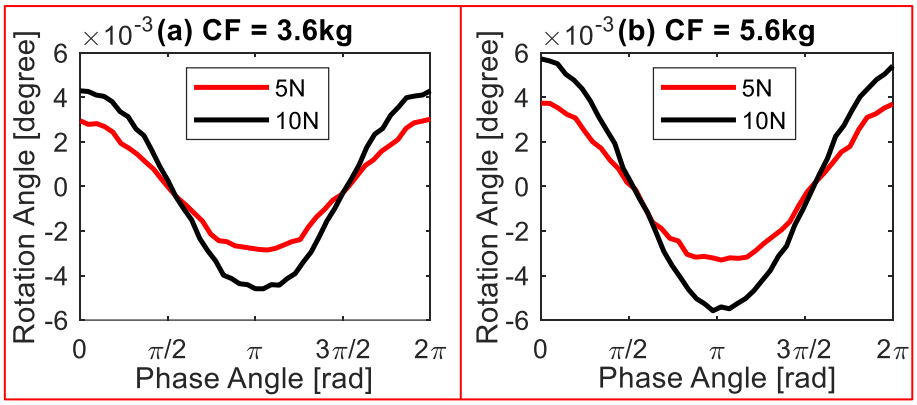

Figure 81: The angle of the damper rotation

- Non-unique Contact Forces

Measurement of the contact forces gives an ability to interpret the inherent kinematics of the damper. To better understand the underlying reason of the response variability, contact forces corresponding to each response curve obtained under the nominally same set of inputs are directly compared at their resonance frequencies. The contact forces will be shown for the time intervals in which the force equilibrium is achieved on the de-coupler and damper at steady state. Three subsets of six cases are particularly selected for the demonstration purposes. Two of them are the ones in which the variability is the largest with the dominating micro slip behavior (the 3rd and 4th subsets, see Figure 78c and Figure 78d), while the third one has the lowest variability with a near gross slip motion (the 6th subset, see Figure 78f). In this way, it is expected that the main factor that causes the variability will be identical for the overlapping response curves, while the same factor should differ for non-overlapping ones.

The 4th subset (F_{EXC} = 5 N, CF = 6.6 kg) is the one with the largest micro slip motion (see Figure 79b) and response variability (see Figure 78d). All contact forces on the left damper are shown for its de-coupler and blade sides in Figure 82a and Figure 82b, respectively. Moreover the upper and lower graphs of each subfigures depict the tangential and normal forces, respectively. Type and color properties of the curves are kept identical with the corresponding runs given in Figure 78d. Each graph shows the dynamic and static components together. It is worth mentioning that the static components are simply computed by averaging the dynamic part over one vibration cycle.

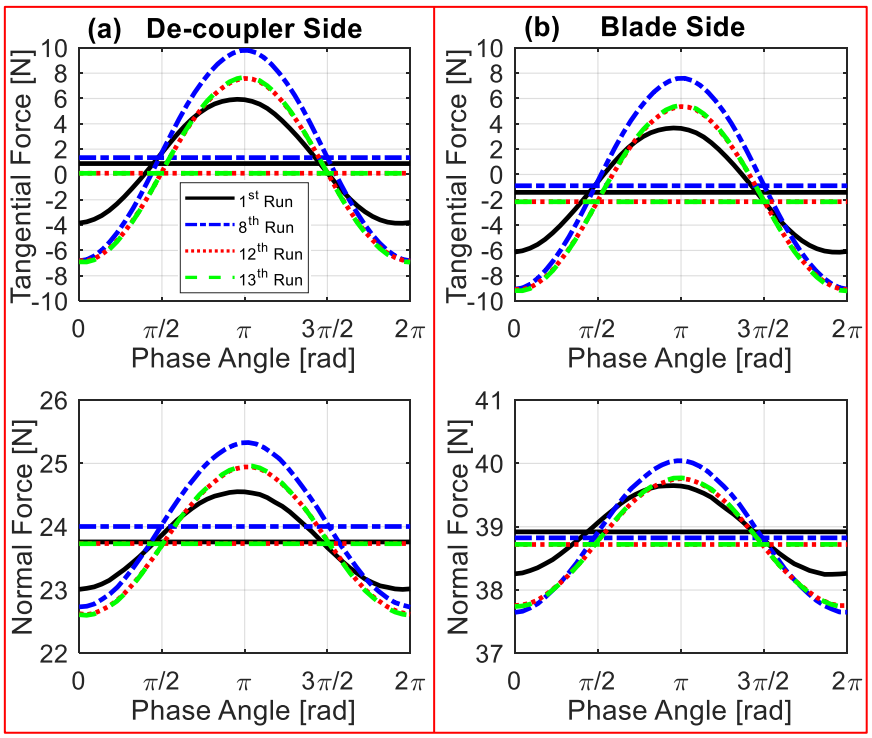

Figure 82: Contact forces on the left damper for the 4th subset (F_{EXC} = 5 N, CF = 6.6 kg)

The first remarkable observation in Figure 82 is that dynamic components of the contact forces measured in the 1st and 8th runs are notably different from those overlapping ones of the 12th and 13th runs. While the amplitude is the largest for the least damped case (the 8th run in Figure 78d), it takes its lowest value for the most damped one (the 1st run in Figure 78d). It is also in the mid-range for the overlapping responses (the 12th and 13th runs in Figure 78d) staying in the interval of the upper and lower boundaries. This observation is quite relevant, because it is expected from an engineering point of view that contact forces increase with higher vibration amplitudes and decrease with the lower ones.

Secondly, it can be seen that the static components are not unique, even though the applied pre-load is nominally the same for all runs. It is an indication of an uncertainty that varies the static components and, thus, enables the static force equilibrium on the damper in different ways. To better illustrate it, Table 9 numerically gives the static components of contact forces with the notations given in Figure 74b. As an example, force balance of the 1st run can be written in the horizontal (x) and vertical (y) directions with Eq. (6.2) as

$$F_x = (38.92 - 23.76)\sin(8.53) - (1.41 + 0.86)\cos(8.53) = 0.0038$$

and

$$F_y = (1.41 - 0.86)\sin(8.53) + (38.92 + 23.76)\cos(8.53) - 6.66 \times 9.81 \times 0.95 = 0.0004$$

respectively. Since the resultant forces are almost 0 (the deviations are due to round-off errors), the damper is said in balance. The same procedure can be applied for the 8th, 12th and 13th runs, too, and it can be understood that the force equilibrium on the damper is non-unique. It should also be noted that this computation is just a crosscheck of Eq. (6.2), after obtaining the contact forces by using the same equation. Lastly, it is worthy to mention that the exact mass of the dead weight is 6.66 kg, as shown in these balance equations. Its last digit was omitted throughout the thesis for simplicity. This fact applies the other dead weights, as well.

Table 9: Static components of contact forces on the left damper for the 4th subset (F_{EXC} = 5 N, CF = 6.6 kg)

Runs	T'	N'	T''	N''	Resultant Force	
					X Dir.	Y Dir.
1st	0.86	23.76	-1.41	38.92	0.0038	0.0004
8th	1.33	24	-0.89	38.82	0.0028	-0.008
12th	0.097	23.73	-2.15	38.72	0.0013	-0.0042
13th	0.092	23.73	-2.16	38.72	-0.0037	-0.0019

For the sake of completeness, contact forces on the right damper for the same set are also given in Figure 83. The non-uniqueness of the static components is present on this damper, as well. The values are numerically given in Table 10 from which the non-unique force equilibria corresponding to different runs can be easily demonstrated. However, it should be noted in Figure 82 and Figure 83 that the variability pattern of the static components of the tangential forces closely matches that of the response variability shown in Figure 78d. In other words, the static tangential forces and the response of the 12th and 13th runs overlap very well in all figures; and, the curves of the 1st and 8th runs are distinct and separated from them. These observations show that there is a relation between the response variability and the corresponding non-unique static components of the tangential forces.

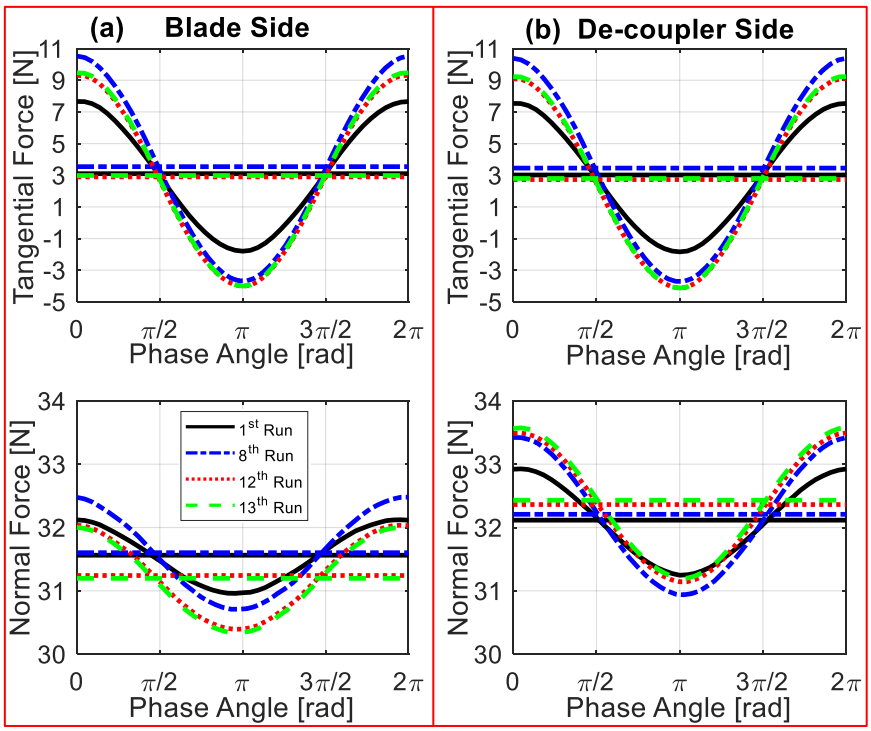

Figure 83: Contact forces on the right damper for the 4th subset (F_{EXC} = 5 N, CF = 6.6 kg)

Table 10: Static components of contact forces on the right damper for the 4th subset (F_{EXC} = 5 N, CF = 6.6 kg)

Runs	T'	N'	T''	N''	Resultant Force	
					X Dir.	Y Dir.
1st	3.01	32.12	3.1	31.56	0.0059	0.0014
8th	3.45	32.21	3.54	31.6	-0.0015	-0.0005
12th	2.73	32.36	2.89	31.24	-0.0079	-0.005
13th	2.8	32.43	2.98	31.2	-0.0044	0.0009

To make further investigations on the same phenomenon, the results measured in the 3rd subset (F_{EXC} = 1 N, CF = 3.6 kg) are given for the right damper in Figure 84. The response variability is also large for this case, as shown in Figure 78c. It can be seen in Figure 84 that the amplitudes of all forces in each subfigure is approximately equal; but, some of the static components of the tangential forces is again notably different than the other ones. In particular, the curves of the 4th and 5th runs exactly overlap; yet, the static tangential component of the 16th run is slightly different from them, while the one for the 9th run is considerably far. Like in the previous case, this pattern is also totally in-line with the response variability pattern, as shown in Figure 78c. On the other hand, contact forces at the left

damper for the same subset is also given in Figure 85. Here, the curve measured in the 9th run breaks the trend, while the rest of the static tangential forces comply with the variability pattern. Nevertheless, it can be inferred that static component of the tangential forces is non-unique, which phsyically corresponds to different static force equilibria on the damper. This phenomenon accordingly causes the response variability, even though the results of one run is out of the common pattern presented in totally sixteen cases. It can be noted that this is the second observation supporting the hypothesis of Chapter 3 which states that the non-repeateability of the nonlinear response is caused by the non-unique static component of the tangential force.

It can also be noted that there is an offset in the normal force values of de-coupler and blade sides at the left damper. This is probably resulted by a misalignment in the assembly, even though everything seemed properly aligned during the tests. It should be underlined that the entire structure is a complex system and it is composed of several subcomponents. The difficulties in the assembling procedures always create problems in laboratory conditions. Nevertheless, the contact forces and all other measurements are recorded in a reasonable and consistent manner, where the coherence of the results is ensured.

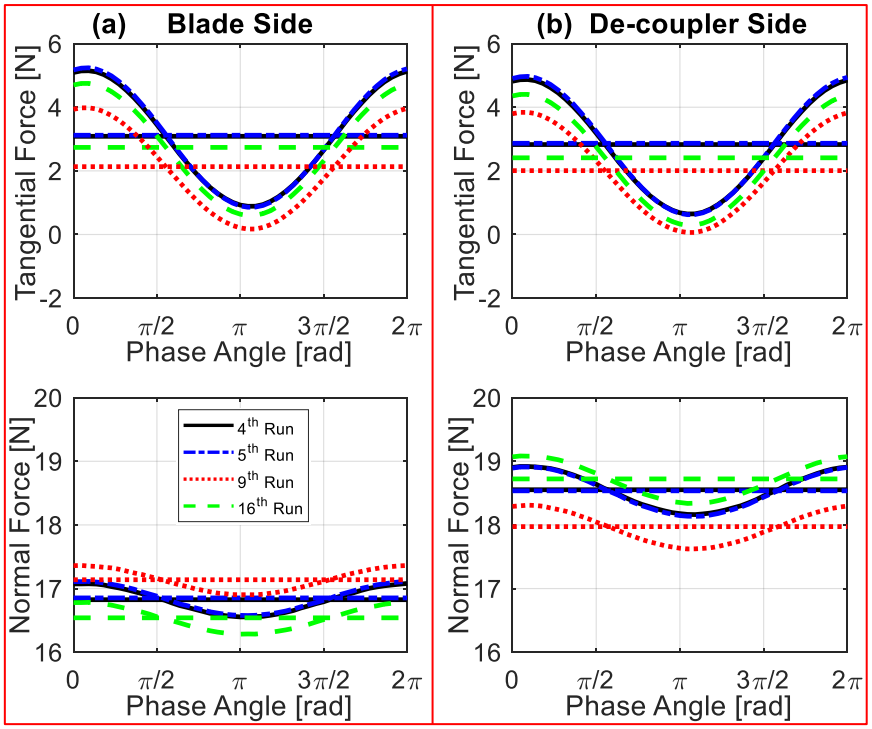

Figure 84: Contact forces on the right damper for the 3rd subset (F_{EXC} = 1 N, CF = 3.6 kg)

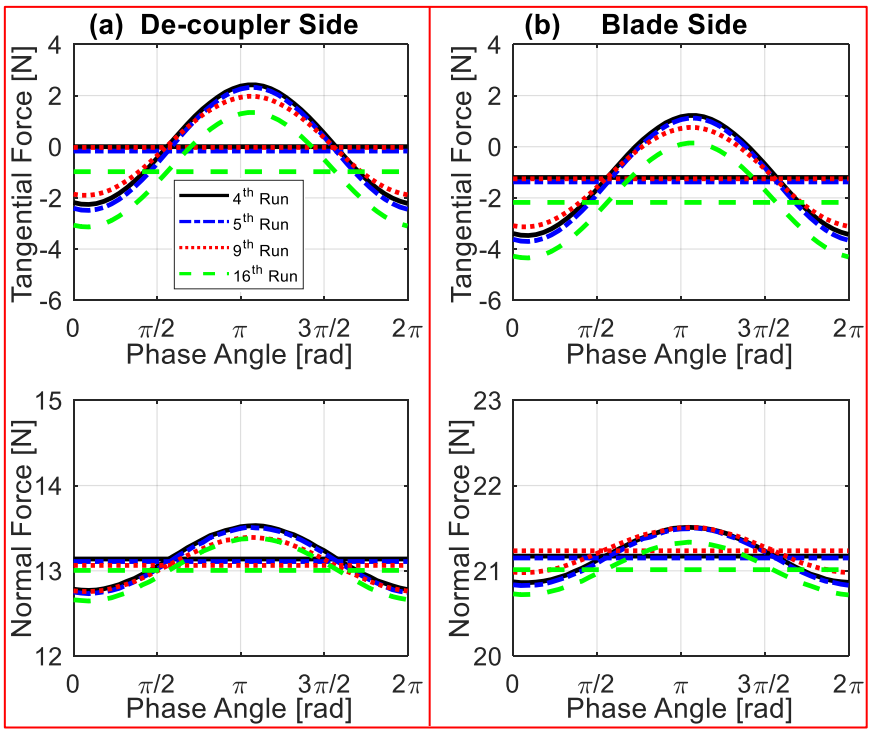

Figure 85: Contact forces on the left damper for the 3rd subset (F_{EXC} = 1 N, CF = 3.6 kg)

It is observed in the results of the investigated subsets that the non-uniqueness of static tangential forces creates a variability range in the nonlinear vibration amplitudes. These two subsets (the 3rd and 4th) are the ones with the largest variability range. Now, this observation is further challenged whether it will be still consistent with the results of the 6th subset (F_{EXC} = 5 N, CF = 3.6 kg). This case is intentionally selected, because it is the one where the response behavior is closest to a unique pattern with the highest repeatability (see Figure 78f). Figure 86 and Figure 87 illustrate the corresponding contact forces at the resonance frequency of each run for the right and left dampers, respectively. A similar variability pattern between the response and the static components of the tangential forces is also valid here. The behavior of three runs (the 4th, 5th and 16th runs) is similar to each other in both Figure 86 and Figure 78f, while the last one (the 9th run) is slightly different from them. In Figure 87, the curve of the 16th run becomes distant from the 4th and 5th ones, but the general pattern is still preserved.

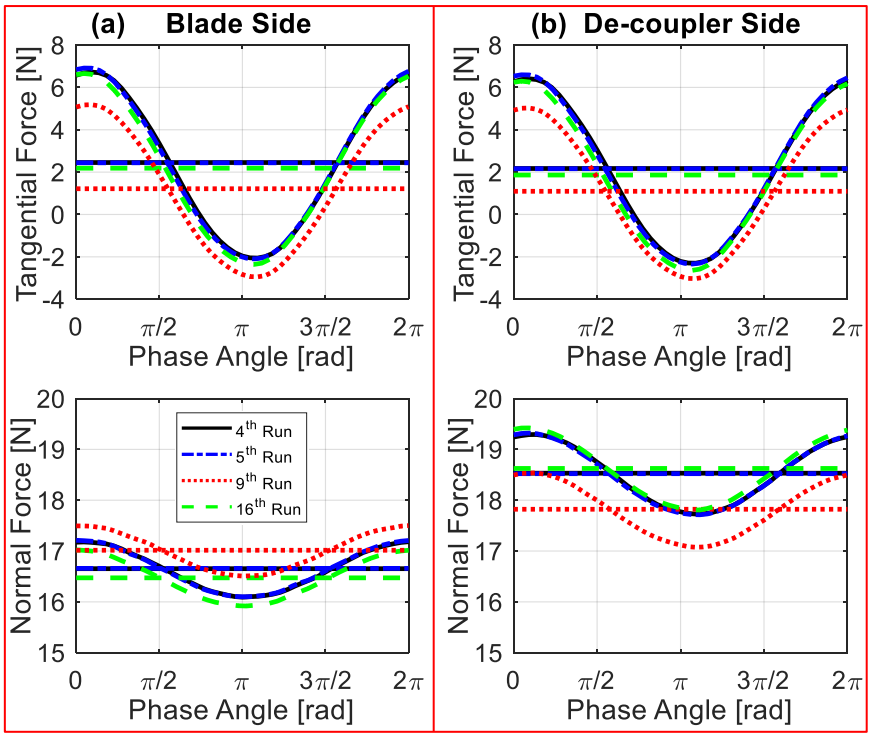

Figure 86: Contact forces on the right damper for the 6th subset (F_{EXC} = 5 N, CF = 3.6 kg)

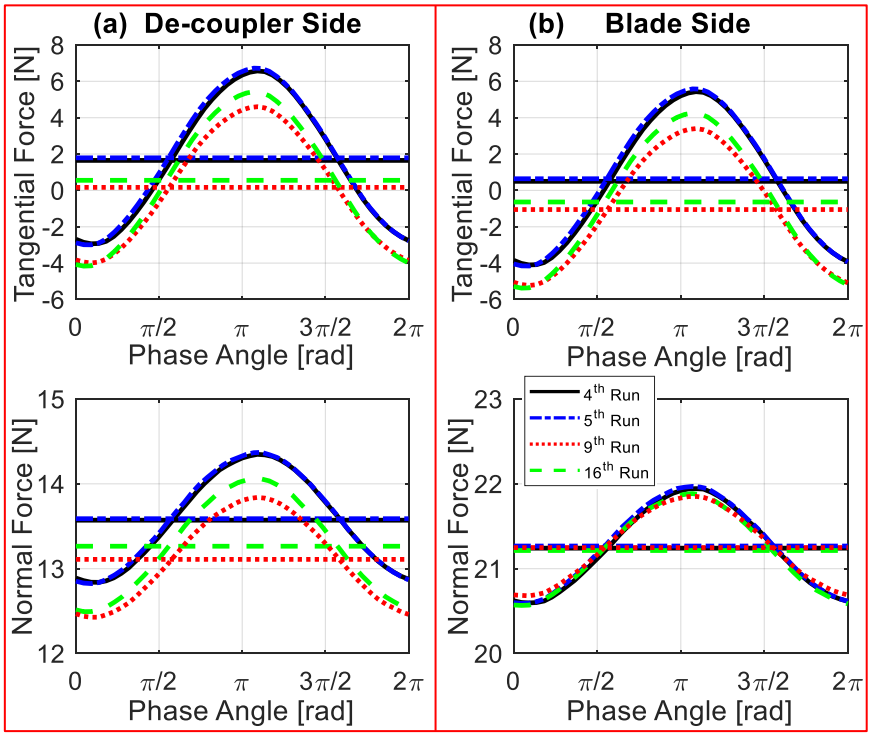

Figure 87: Contact forces on the left damper for the 6th subset (F_{EXC} = 5 N, CF = 3.6 kg)

All the results show that there are mutually strong compliances on the variability pattern of the response and the static component of the tangential forces, which shows a parallelism to the hypothesis of Chapter 3. This is also supported with other results presented in the previous parts, in which it is shown that the range of the response variability is largely affected by the amount of micro slip motion occurring in the frictional surfaces. As a result, it can be understood that the response variability, observed in our experiments under the same nominal conditions, is mostly caused by the non-uniqueness of the static tangential components. It is worth mentioning that other uncertainties may also be inevitably present in the nonlinear nature of the frictional systems, which may contribute to the response variation. For instance, tribological effects at the contact surfaces or dissimilar thermal expansion of different components may be relevant to change the micro conditions of frictional interfaces, even if macro scale conditions are nominally same. Moreover, some uncertainties may be physically connected to each other within the repeatability concept of systems with frictional structures. This research area is still highly active and requires further investigations to address all the concerns. In this thesis, their detailed investigation is out of scope, and the results are highly consistent with the uncertainty of the non-unique tangential forces.

- The Evolution of the Contact Forces

It is shown that the achievement of the static force equilibria in different ways provides the variability in the nonlinear response. Monitoring the change of contact forces from beginning to the end of a frequency sweep gives an insight to visualize the entire process.

Figure 88 shows the measured contact forces at the de-coupler side of the right damper for the 4th subset that has the largest variability (F_{EXC} = 5 N, CF = 6.6 kg). The forces are measured through the entire frequency sweep in the 1st run that corresponds to the black response curve in Figure 78d. The evolution of the forces is shown for the dynamic and static components together. In this particular case, the sweep is performed from higher to lower frequencies. The amplitude of the dynamic part increases through the resonance, and then decreases with lowering frequencies. This behavior is expected, because the larger the vibration amplitudes, the higher the contact forces. However, it is interesting to note that the static part is not constant and evolves in such a way where it directly decreases after starting the experiment, then slightly increases around the resonance region.

After a certain point, it reaches to a saturation value at which it approximately remains the same until the end of the test. It should be noted that these forces are recorded in the 1st run, where the damper has just been loaded with the dead weights. This mobile characteristic of the static components is a repetitive behavior for the initial runs after the damper has just been loaded (1st and 9th runs).

For the sake of comparison, the evolution of static contact forces, which corresponds to successive runs for the same subset, is shown for the right and left dampers in Figure 89 and Figure 90, respectively. Unlike to the 1st run, the static components are almost constant throughout the entire sweep for the 8th, 12th and 13th runs where the dampers had been loaded before and some other runs have already been performed in advance. Hence, these results show that removing the damper and then reloading it back may somehow create different contact conditions, where the static balance may be mobile during the sweep. The main reason of this phenomenon cannot be fully revealed in the current study, since the exact contact conditions at the micro scale is a black box. However, it can be said that the conformity of the asperities formed in the 1st runs continuously change during the micro slip around the resonance, until a saturation point as the contact states approach to an almost fully stuck condition at the out-of-resonance. Then, in the seven successive runs, the final conformity of the 1st run is nearly maintained, since the damper is not removed; which enables a constant static force throughout the entire sweeps. This interpretation is also consistent with the so-called “bedding-in” phenomenon (Sever et al., 2008) which is referred to as the fact that a certain amount of time is needed during the tests until smooth surfaces are achieved in the frictional interfaces after starting the experiment. In the literature, this practice is popular to increase the repeatability of the nonlinear response. However, it should also be underlined that the variability phenomenon is not an error but a consequence of physical uncertainties present in the contact interfaces.

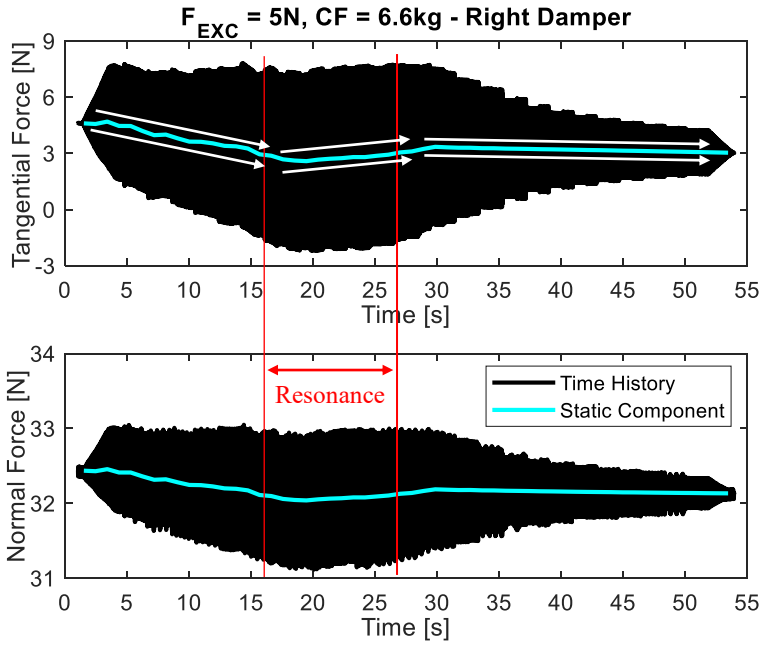

Figure 88: The evolution of the contact forces on the right damper in the 1st run of the 4th subset (F_{EXC} = 5 N, CF = 6.6 kg)

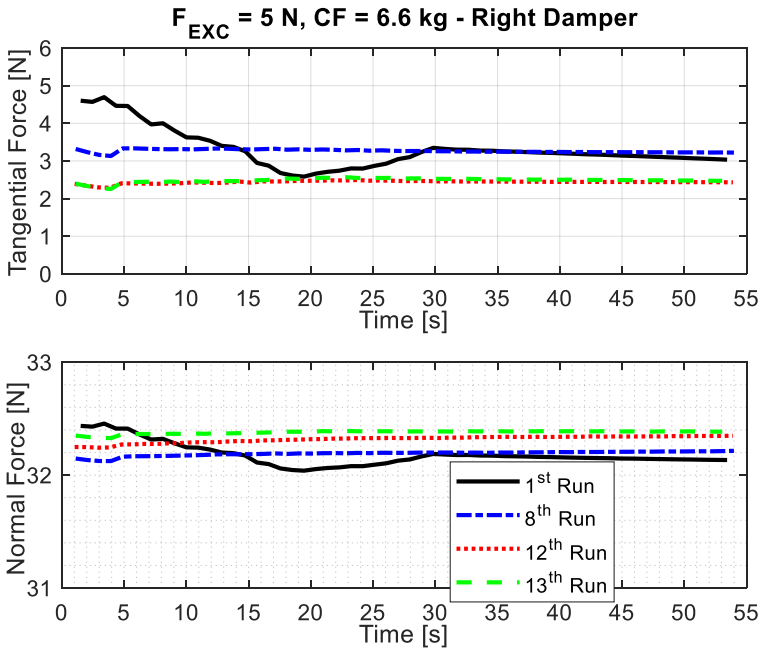

Figure 89: The evolution of static contact forces on the right damper in different runs for the 4th subset (F_{EXC} = 5 N, CF = 6.6 kg)

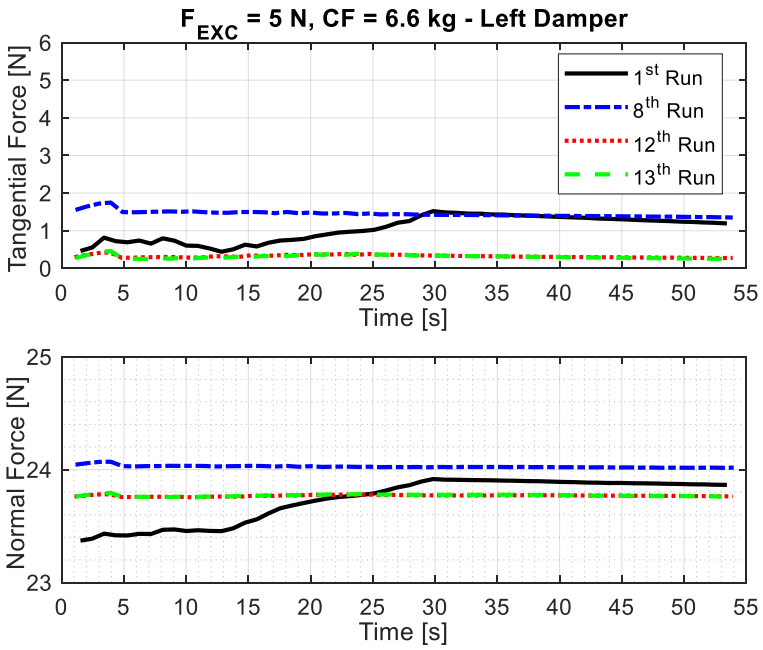

Figure 90: The evolution of static contact forces on the left damper in different runs for the 4th subset (F_{EXC} = 5 N, CF = 6.6 kg)

- An Overall View of the Variability

The generic pattern of the non-unique frequency response has been shown in Figure 78; but, for the sake of completeness, the variability maps of the resonance amplitude and resonance frequency for the entire test data are also given in Figure 91 and Figure 92, respectively. Here, the full data totally contains 64 points which are shown with markers and presented in 3D graphs with respect to the pre-load and excitation levels. The data is grouped for each excitation level and connected for each pre-load; because the experiments are performed at a fixed excitation, while varying the pre-loads in each set (see Table 7). The colors represent the consecutive tests in a ramping up or down of the pre-loads in one set.

Figure 91 and Figure 92 show that the pattern of the variability is generally in line with the one presented in the previous parts. It is smaller when the configuration is close to the fully stuck and the gross slip conditions (low excitation – high pre-load; high excitation – low pre-load), although red curve in 10 N case slightly disrupts it. The range is larger when the case contains a dominant micro slip condition (low excitation – low pre-load; high excitation – high pre-load; moderate excitation – moderate pre-load). It is also interesting to note that .the difference between multiple responses is larger in the amplitudes

(10% - 60%) rather than the resonance frequencies (<1%). This indicates that the variability cannot be ignored, particularly in the amplitudes.

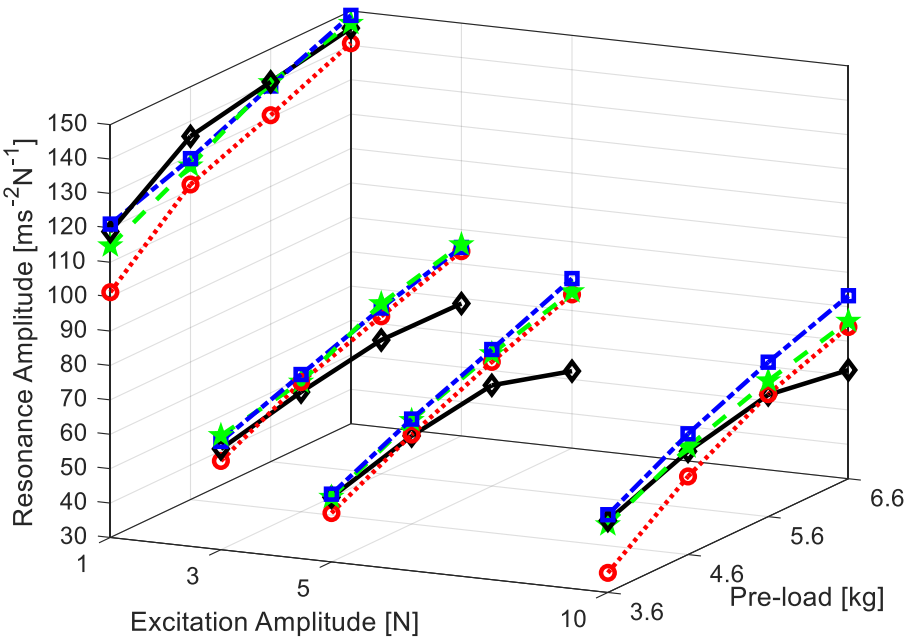

Figure 91: The variability map of the resonance response amplitude

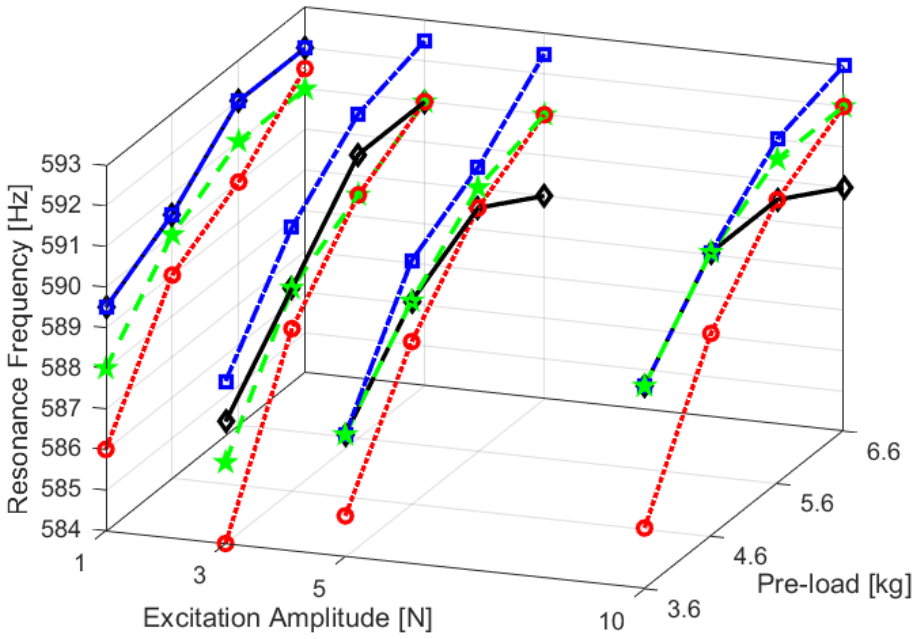

Figure 92: The variability map of the resonance frequency

6.3 Comparison of Computational and Experimental Results

This section first describes the tuning process of the computational model and then compares the results. It should be mentioned that a considerable amount of time is spent on the entire procedure, since a large amount of matching iterations is performed to be able to match the computational results with their experimental counterparts better. Hence, all steps leading to the most accurate results and including even the non-matching ones, but deemed beneficial, will be briefly explained.

6.3.1 Linear Analyses

In this part, it is first aimed to match the natural frequency of the finite element model of the blade (non-reduced, i.e. full model) with its experimental counterpart, by performing modal analyses. Then, the second step is to compare the linear response of the reduced order blade model with the test results, by performing linear forced response analyses in Matlab.

The resonance frequency of the first lateral bending mode of the blade without dampers is measured at 122.25 Hz in the experiments, as shown with its corresponding linear response in Figure 76. In the computational side, there are three main factors that may affect the accuracy of the blade's natural frequency: the type of the utilized finite elements, the mesh density and the clamping conditions of the blade. The first two ones can be implemented only in the finite element software, while the third one can be adjusted either in the finite element software (Ansys) or in Matlab. A sensitivity analysis with different iterations is performed and all the observations will be presented in the following part; but, a brief explanation on the effecting factors is first needed.

- The Type of the Finite Elements and the Mesh Density

A common and straightforward practice for meshing an academic blade is to use 3D solid finite elements. It should be noted that this is not a rule of thumb, and different strategies can be followed depending on the application. In the sensitivity analysis of this study, two different tetrahedral solid elements are tried. The first one is Solid185, as named in the Ansys terminology, and has 8 nodes in a single element, while the second one is Solid186 that contains 20 nodes in one 3D element. The latter can be considered to give more accurate results than the

former for the same number of elements, since it is a higher order element type; but, the computational burden is also expected to increase due to a larger number of nodes.

Regarding the mesh density; the higher number of finite elements utilized in the model, the better accuracy in the results; but a compromise should be taken into account between the accuracy and the size of the model. In the sensitivity analysis, several iterations are performed with different mesh densities, by assigning an average element length in each iteration model. The density is adjusted with respect to the blade and it refers to the number of elements present in the thickness of the blade span. For instance, if the blade thickness is swept by two elements, the mesh density is named as 2 Element model. Hence, the more number of elements, the higher density.

- The Clamping Conditions of the Blade

The fixed boundary conditions in the experiments can never be considered perfect, no matter how large clamping force is applied. On the other side, imposing zero displacements to the clamping nodes implies a seamless constraint in the computational model. To address this phenomenon properly in the model, a relieving strategy is followed in the finite element software. In particular, instead of fully clamping the blade from all nodes located on the fir-tree root, the constraints are applied to only some of the clamping nodes, selected arbitrarily but uniformly, on the root. This is called as relaxed configuration, since it allows a relieving on the boundary conditions and makes the system less stiff compared to the fully clamped one.

- The Comparison of the Results

Table 11 summarizes the first part of the sensitivity analysis, which refers to the modal analyses performed in Ansys. The first four models are constructed by using Solid185 element type with different mesh densities and clamping conditions. The results are not satisfactory enough, as the experimental one is around 122.25 Hz. Even though the higher mesh density decreases the error, it is still around 7% which can be considered as a large error for the linear systems. It is also seen that a modification on the clamping conditions does not affect the results considerably for this particular case. In the fifth model, the element type is changed to Solid186 to increase the accuracy and the results abruptly overlapped.

This shows that use of the higher order element type is a necessary condition for obtaining an accurate model. To check if there is a further improvement, in the sixth model, the mesh density is increased. It is seen that the natural frequency already reached to the saturation and an additional contribution to the model accuracy is not present. Different models (7-10) are also built for the investigation of the different parameter effects on the results. It is demonstrated that the effect of the element type is the most dominant one among three factors, as long as Solid186 is utilized in the model.

Table 11: First part of the sensitivity analysis

Model Number	Element Type	Mesh Density	Clamping Condition	Natural Freq. [Hz]	Error (%)
1	Solid185	3 Elements	Full	137.1	12.2
2	Solid185	3 Elements	Relaxed	137.0	12.1
3	Solid185	4 Elements	Full	131.1	7.2
4	Solid185	4 Elements	Relaxed	131.0	7.1
5	Solid186	4 Elements	Full	122.1	0.12
6	Solid186	5 Elements	Full	122.1	0.12
7	Solid186	2 Elements	Full	122.4	0.12
8	Solid186	2 Elements	Relaxed	121.9	0.29
9	Solid186	1 Element	Full	122.6	0.29
10	Solid186	1 Element	Relaxed	122.1	0.12

The second part of the sensitivity analysis deals with the matching of the computationally and experimentally obtained linear responses of the blade without coupling the dampers to it. For this purpose, the 6^{th} model is selected, although it is the one with the largest size due to its intense mesh; but, this does not create a problem in terms of model size and computational time, since a reduced order model is used in the forced response analyses. The physical retained nodes for the reduced order model are the excitation and response monitoring nodes.

Figure 93a depicts the normalized linear forced responses of the blade tip, where the computational ones are obtained with three different damping values. It can be seen that the resonance frequency of the computational curves closely match with the experimental one. Moreover, the amplitude of the red curve is also comparable with test results. However, there is a notable difference between the

experimental and computational curves around the lower part of the resonance region. The response of the former is much wider than the latter, as indicated with arrows. It is crystal clear that there is a missing point in the computational model somewhere, although the matching of red (computational) and black (experimental) curves may be considered partially acceptable as long as it is justified. To check its prospective impacts on the nonlinear response behavior, a preliminary nonlinear response analysis is performed with roughly estimated contact parameters. It should be noted that the detailed and real nonlinear analyses will be elaborated in the next section and this preliminary analysis is just done to have an initial idea whether the current model can give a prospective matching on the nonlinear response. Figure 93b depicts a general picture about the matching accuracy of the nonlinear responses presented for two different excitation levels. It is interesting to note that although the amplitudes are comparable in both curves, the phenomenon that occurs in the linear case appears here, too. Hence, these results show that the linear model needs to be further tuned.

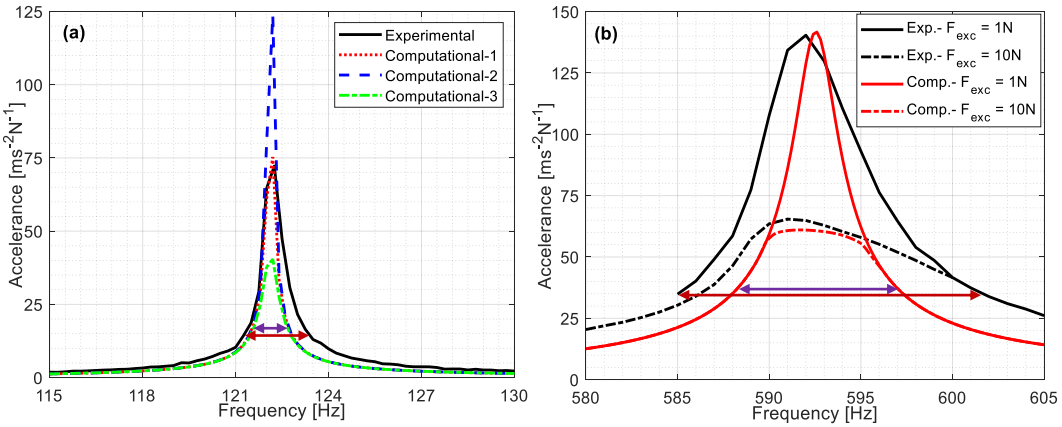

Figure 93: An unsuccessful matching of the (a) Linear responses, (b) Preliminary nonlinear responses

In order to be able to match the linear responses better, the second part of the sensitivity analysis is performed. Here, the idea of clamping conditions is changed. In particular, all the constraints applied in the finite element software are removed and reduced order model is re-computed by also including the clamping nodes into the retained master nodes. The constraints are then applied in Matlab by grounding the model from these clamping nodes with linear springs whose stiffness values can be adjustable. This gives an ability to simulate non-perfect boundary conditions with elastic spring elements. Here, the main aim is to be able to widen the lower part of the red linear response curve shown in Figure 93a. For

this purpose, the value of the linear stiffness elements is correspondingly tuned, and the new response curve computationally obtained is shown in Figure 94a. It is clear that the width of the experimental and computational curves almost become equal, but the resonance frequency shifted to left. This is relevant, because the root is not perfectly clamped now and some elasticity is introduced with springs. The error is still around 2.5% that cannot be assumed minor. Nevertheless, the preliminary nonlinear analysis is repeated in this case, as well, to see the effects of widening. Figure 94b illustrates the nonlinear response curves obtained with 1 N and 10 N excitations. Unlike the previous case, the matching accuracy of the results is good enough. The width of the lower parts becomes comparable for both excitation levels, in addition to resonance frequency and amplitudes. It can be understood that the behavior of the nonlinear response does not become true, unless the linear responses obtained both experimentally and computationally overlapped properly.

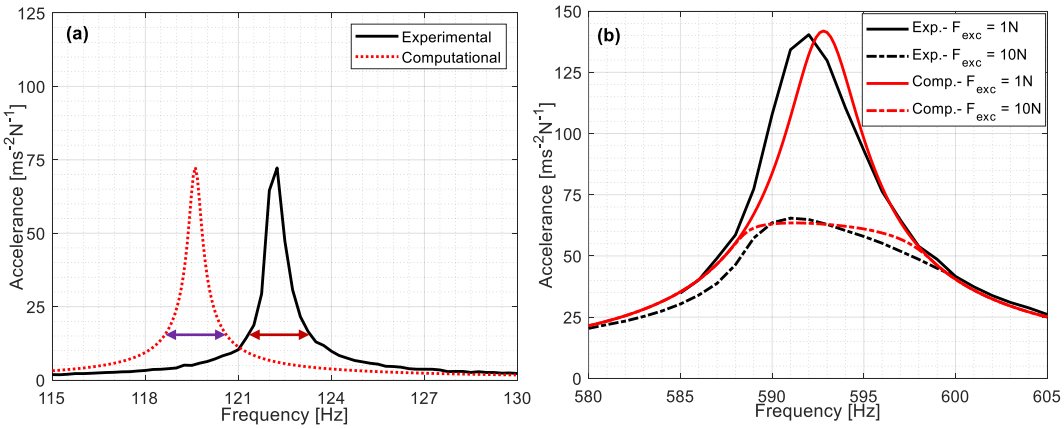

Figure 94: (a) Another unsuccessful matching of the linear responses, (b) A promising matching of preliminary nonlinear responses

A reasonable justification of the unmatched natural frequencies could be the blade's interaction with the shaker, and contributions of the sensor masses on the blade dynamics. In the finite element model, these were not modeled and their impacts are assumed negligible, since the shaker stinger is attached to a close position to the root and the sensor masses are relatively low. Nevertheless, additional linear springs and lumped masses are correspondingly implemented in the Matlab to imitate these factors. Unfortunately, no further improvement is observed for the phenomenon shown in Figure 93, even though the resonance frequency slightly increased due to the stinger stiffness.

It is observed in the computational linear response that a decrease in the width of the lower resonance region always accompanies, as the resonance frequency increases with the stiffness contributions to the model. To make the computational linear response shown in Figure 94 move to the right as a whole, the density of the model is decreased in Ansys. Finally, the responses overlapped with a negligible amount of difference as shown in Figure 95. It is worth mentioning that the assigned density (7450 $kg.m^{-3}$) is 4% lower than the measured actual value (7770 $kg.m^{-3}$) and this was the last remedy to be able to tune the model. It should also be noted that the tuning of the linear model plays a vital role on the tuning of the contact element properties that will be used for the nonlinear analyses. It prevents an artificial contribution that may come from the blade root and enables the correct calibration of contact stiffness values.

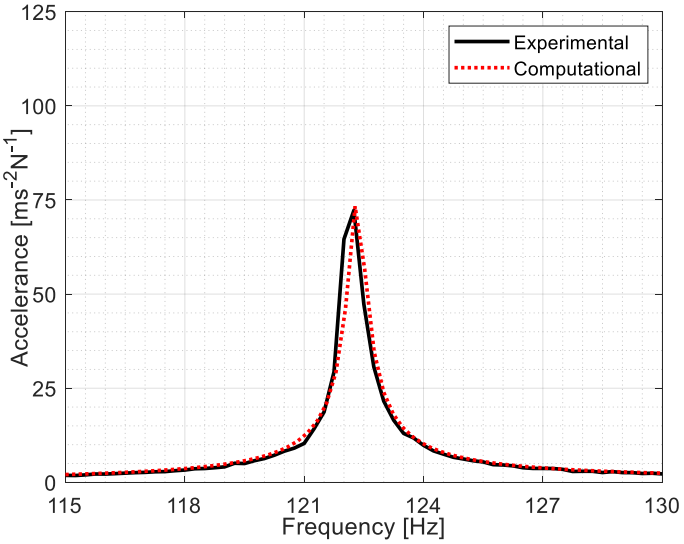

Figure 95: Final match of the linear responses

6.3.2 Nonlinear Analyses

This section presents the thorough procedure of the comparison of the nonlinear results. The ultimate goal is to computationally estimate the measured variability range of the nonlinear responses and the contact forces in the tests. It should be noted that the computational method developed in Chapter 4 is utilized to predict the boundaries. For the comparison of the results, the pre-load of 5.6 kg case with four different excitation levels (1 N, 3 N, 5 N and 10 N) is selected purposely; because, an abundant amount of extra tests in addition to the ones shown in the previous section is performed for 5.6 kg pre-load case, in order to be able to

increase the variability range. Moreover, similar to the previous part, an extensive effort is spent on the matching procedure, where all steps will be summarized and discussed in detail.

- Main Finite Element Models

Figure 96 shows the finite element models of the structures used throughout the entire process. The mesh of the blade is the final version of the previous part. The dampers and the auxiliary components are also meshed with the same element type and mesh density used for the blade, for the sake of coherence. It can be noted that the central block and side blocks are excluded in the models and they are assumed rigid. Contact pads and load cells are also merged with the de-couplers (as similar to the case of the previous chapter), since they are tightly bolted together. It is also worth highlighting that the elasticity of the load cells is properly assigned to approximate its actual rigidity defined in their user manuals. The dampers have no boundary conditions, which make them free to move as in the laboratory conditions. Hence, the entire model is composed of five different bodies. It is worth stating that there are no contact element constraints in the finite element software, and they will be introduced in Matlab. Similarly, the blade root is free from clamping boundary conditions in Ansys and it is clamped with linear springs in Matlab, as explained in the previous part. On the contrary, the load cells are clamped in the Ansys from their ends which are farer from the dampers. The Craig-Bampton approach (Craig & Bampton, 1968) is used for the reduced order model. Clamping nodes (at the blade root), response monitoring node (at the accelerometer position on the blade tip), excitation force nodes (at the position nearby the root, where the shaker stinger is bolted to the blade) and centrifugal force, i.e static force, application nodes (on the hollows of the damper) are selected as the physical master nodes together with 150 modal coordinates as the master degrees of freedom in the reduction process.

- *Tuning Process of the Models*

The first step in the computational model is the decision of the number of contact points as well as the calibration of the contact element features and linear damping ratio of the structure. To tune the numerical values finely, a study that simultaneously contains the effects of different parameters is performed. For instance, the contact stiffness values are calibrated with respect to the hysteresis cycles, the resonance frequency of the response curves and keeping into account the nonlinear response variability. The most optimized values that give

satisfactory computational results for each parameter are determined. The procedure is explained in detail in the following.

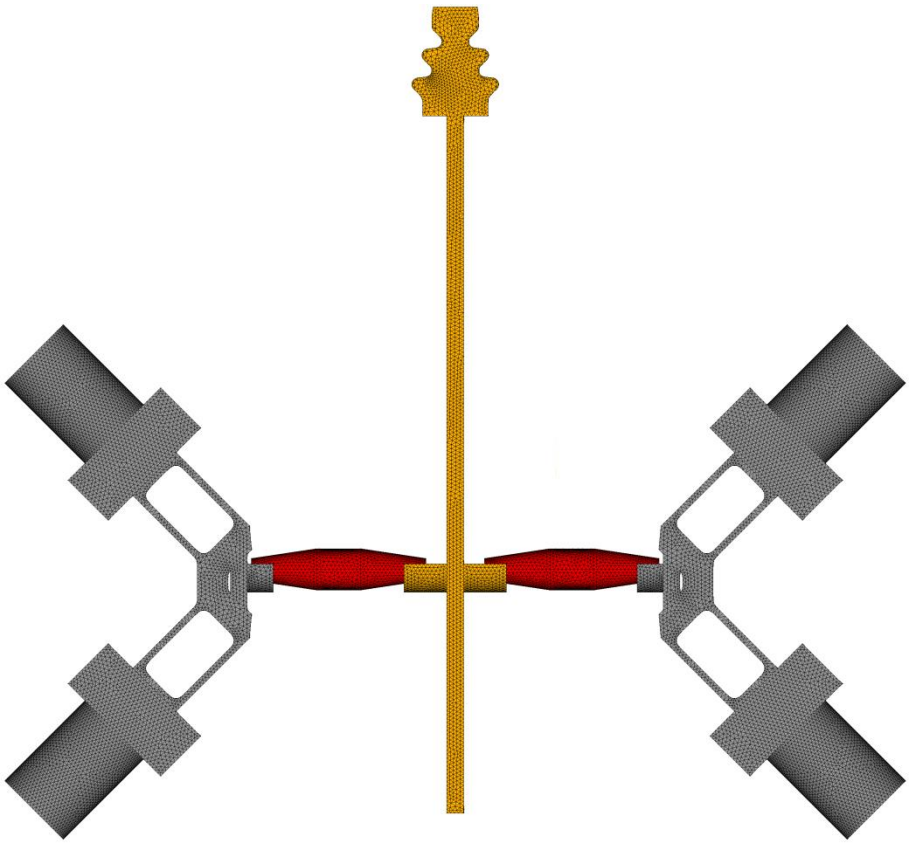

Figure 96: A top view of the finite element models of the blade, dampers and auxiliary components

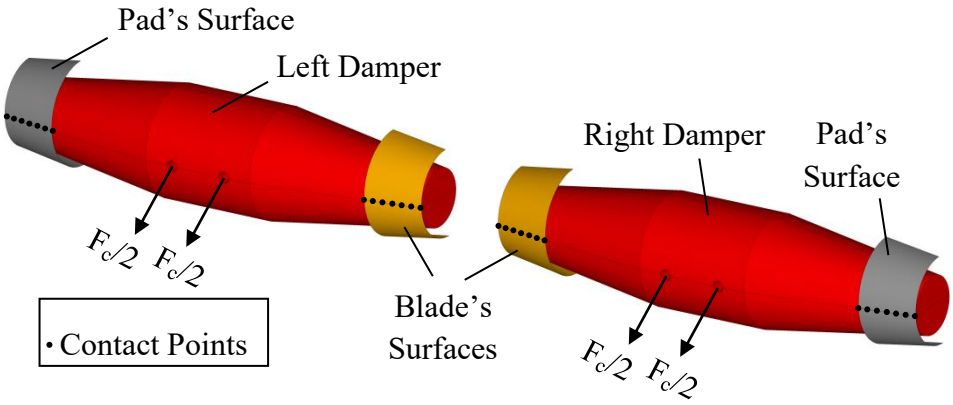

Figure 97: A view of dampers together with the contact surfaces

Figure 97 shows the dampers coupled with the contact surfaces of the pads and blade. Since the dampers and the blade as well as the contact pads have different radius of curvatures, a theoretical line contact occurs in the frictional interfaces. Seven contact points, where the Jenkins elements are utilized in each one, are chosen on the lines.

A two-step tuning strategy is followed in the calibration of the system features. The initial values of the contact element properties (k_t, k_n and μ) and the linear damping level of the system are first estimated by simultaneously considering the measured hysteresis cycles, the response excited with 1 N, and the contact force ratio (T/N) of the case excited with 10 N. These cases are purposely selected and will be explained in the following. The final values are then calibrated with respect to the variability range of the non-unique nonlinear response and contact forces, recorded in the experiments.

Figure 98a depicts the hysteresis cycles measured for the right damper (see Figure 75b for the laser points). Two cases with the minimum (1 N) and the maximum (10 N) excitations are shown for the sake of comparison. It is clear that there is a micro slip in both cases. To estimate the tangential contact stiffness value (k_t), a peak-to-peak straight line is plotted for the former, while the stick region of the latter is idealized with another line. The slope of the both lines (k_t) is same and numerically equals to 11.5 x 10^6 N/m. The similarity between the results of two different cases shows that the estimated value is coherent. However, it should be noted this value is a rough estimation and it needs to be corrected; because, although the measurement of contact force on the damper is reliable, the recorded relative displacement is representative, since the direct measurement of the relative displacement of the friction surfaces is not possible. Moreover, there is a slight inclination (around 15 degrees) at one of the differential laser heads due to the fact that there was a lack of space during the positioning of the laser (see Figure 75c). These conditions make the real contact stiffness value lower than the previously estimated one, since the actual relative displacement is greater than the measured one. As a result, keeping into account all these facts, k_t is estimated with a range of 4-9 x 10^6 N/m for the first nonlinear analyses.

It is worth underlining that a measurement, from which the normal contact stiffness (k_n) can be directly extracted, is not made in the experimental campaign. However, the response of the case with 1 N excitation can be used to tune its value with a calibration performed on the resonance frequency, since k_t is already defined in a range. 1 N excitation case is intentionally selected, because this case gives the configuration closest to the fully stuck linear condition of the damper.

Figure 98b shows the response curves, where a micro slip is apparent in the experimental one, as the shape of the response has a slight softening behavior. On the other hand, the computational one is computed for fully stuck linear conditions. Here, the effect of contact stiffness values are dominant on the resonance frequency values (axis of abscissa), while the damping is effective on the resonance amplitudes (axis of ordinate). After a calibration study on the resonance frequencies, it is seen that k_n can also be estimated in the range of 4-9 x 10^6 N/m, similar to the k_t values. It is worth highlighting that the equivalency of the contact stiffness values (k_t and k_n) is in line with the observation made in the second chapter where the contact stiffness values were comparable to each other also for an industrial application of mid-span dampers. Moreover, the numerical values are also in the same order of level, which increases the reliability of the defined ranges for the contact stiffness parameters. Regarding the linear damping of the system, a proportional viscous damping is assumed in the system and the numerical value of this fully stuck condition gives a reference value ($\zeta = 0.33\%$). The actual real damping ratio should be lower than this one due to the presence of micro slip in the experiments, and it is defined in the range of 0.15% - 0.3%.

The last parameter for the initial nonlinear analyses is the coefficient of friction. It is tuned with respect to the contact force ratio (T/N), obtained for the case with 10 N excitation, for one vibration cycle. This case is also purposely selected; because, it gives the configuration closest to the gross slip of the damper. Theoretically, the force ratio (T/N) should be equal to the friction coefficient (μ) in case of having a gross slip; however, in our experiments, gross slip is never achieved as explained in the previous part and also as shown in Figure 98c , since the ratio never takes a constant value over one full vibration cycle. Nevertheless, the amplitude of the curve gives an insight about it and helps to estimate a lower reference value ($\mu \approx 0.6$). The actual coefficient of friction should be greater than this one due to the absence of gross slip in the experiments, and it is defined in the range of 0.6 - 0.85.

Table 12 summarizes the defined ranges for all the parameters, for the sake of brevity. It should be noted that these values are for the initial nonlinear analyses and the final values will be finely tuned according to the boundaries to be estimated for the variability range of the nonlinear response and contact forces.

Table 12: The range for the system properties

k_t, Tangential Stiffness [N/μm]	k_n, Normal Stiffness [N/μm]	μ, Friction Coefficient	ζ, Damping Ratio [%]
4 – 9	4 – 9	0.6 – 0.85	0.15 – 0.3

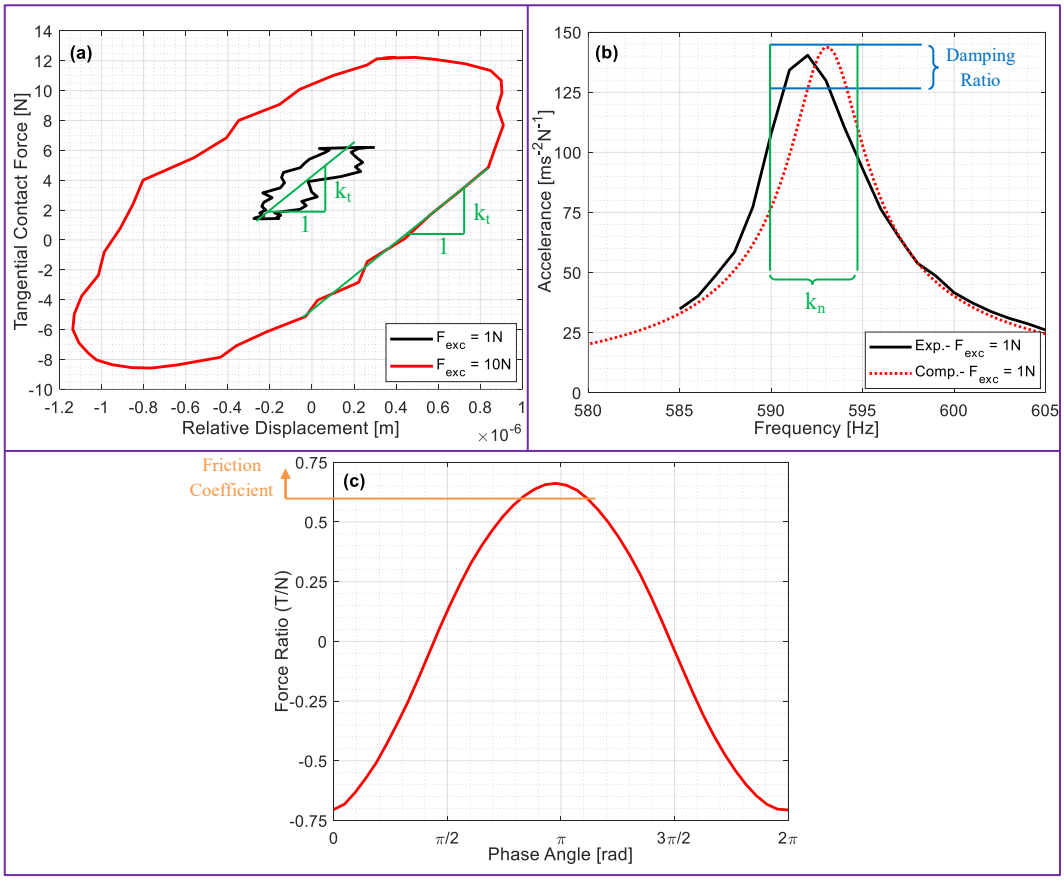

Figure 98: (a) Hysteresis cycles, (b) Responses for 1N excitation, (c) Force ratio for 10N excitation

- The Comparison of the Results

Having defined the initial ranges for the contact parameters, the second step of the tuning strategy is performed together with the nonlinear response analyses. The main aim here is to computationally predict the variability range of the non-unique nonlinear response and contact forces. The contact stiffness parameters are finely calibrated so that the most satisfactory results are obtained. It should be noted that there is a great challenge here; because, as shown in the previous part,

an offset is present in the normal force value of the left damper, which indicates a misalignment in the application of the static pre-load is present in the experiments. To compensate it in the computational model, several iterations with five different configurations are performed to match the results. The entire process as well as a detailed discussion will be presented with its all steps.

Configuration 1:

In the first configuration of the model, pre-loads are symmetrically taken into account, even though there is a misalignment in the tests. This configuration is an initial attempt to see the general picture of the results in overall. Figure 99 shows a representative simple sketch of the first configuration. Regarding the contact parameters, the tangential contact stiffness (k_t) value is set to 4.65 N/μm and distributed evenly to all contact elements (by dividing it to the number of contact elements, 7). The normal contact stiffness (k_n) is taken 6.75 N/μm with the same idea, while the friction coefficient (μ) is assumed 0.6 and kept constant for all contact elements. Damping ratio (ζ) is also set to 0.2 %.

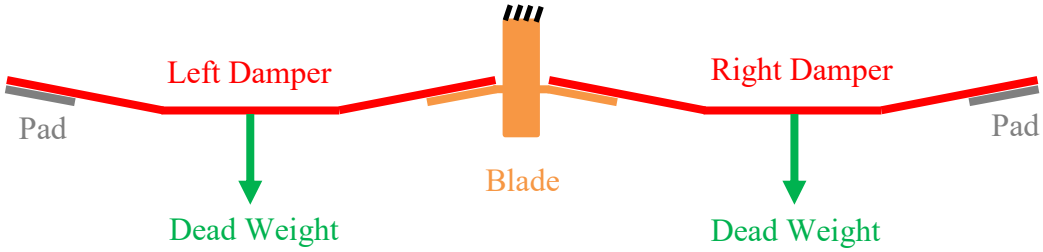

Figure 99: A simplified sketch of the 1st configuration

Figure 100a-d show the nonlinear response curves obtained with four different excitation levels. Experimental ones are obtained under the same nominal conditions in the tests. On the computational side, the boundaries are computed with the optimization method developed in Chapter 4. It is seen that the upper boundary is computed always around the resonance regime of the experimental curves, while the lower boundary shows a strong softening behavior and its resonance frequency shifts towards to the lower values with increasing excitation. To investigate this phenomenon, the contact conditions of the lower boundary at the resonance frequencies are investigated. It is realized that a full separation occurs at some of the contact points, in addition to the damping in the

frictional interfaces. This means that the optimization algorithm converges to a contact condition so that the system's loss factor is the maximum. The number of points undergoing full separation increases, which results in a higher stiffness loss, with larger excitations. On the other hand, the surfaces are always in contact for the upper boundary and even no damping is present for the 1 N and 3 N cases. It should be noted that these boundaries are the theoretical limits in which the experimental curves can reach, and the variability range of the test data is successfully captured with the boundaries predicted.

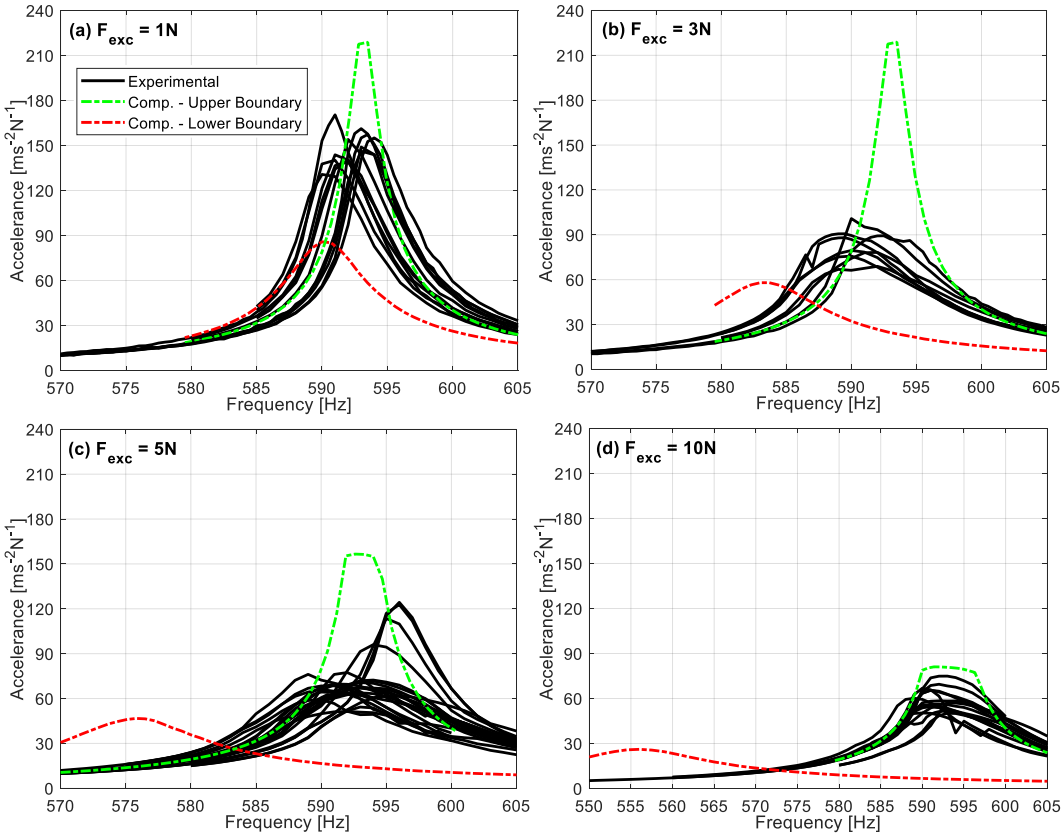

Figure 100: Nonlinear Response variability and boundaries for the 1st configuration

In addition to the response variability, the computational method is expected to capture the variability of the static tangential contact forces that causes the main uncertainty phenomenon in the system. For this purpose, contact forces are investigated at the corresponding resonance frequencies. Figure 101 depicts the contact forces measured and computed on the de-coupler sides of the left and right dampers, for 10 N excitation case as the demonstrator. Each graph shows the dynamic and static components together. The dynamic components of the upper

boundary are comparable with the experimental ones, while those of the lower boundary are evidently smaller. This is relevant, because the response curve of the upper boundary case (for F_{exc} = 10 N) is close to the experimental responses, so the contact forces are also expected to be more or less similar. Moreover, the static tangential forces are also computationally captured; however, the offset in the normal force of the left damper is not estimated properly, since the application of the pre-loads is symmetric in the model and this cannot reflect the actual case scenario. To compensate the difference, the next configuration is studied.

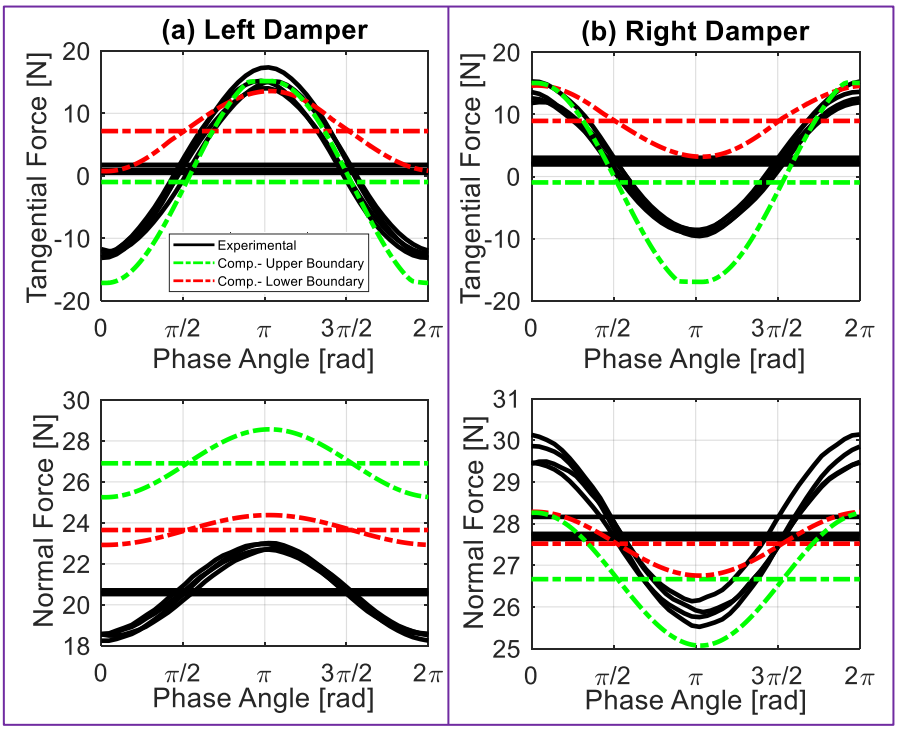

Figure 101: Contact force variability for the 1st configuration (F_{exc} = 10 N)

Configuration 2:

In the second configuration, the position of the dead weights on the dampers is changed to be able to naively imitate the misalignment in the model. This is done by considering the experimental normal force values. Pre-loads are shifted to the blade side on the left damper, while slightly moved to the pad side on the right damper. Figure 102 depicts the simplistic sketch of the 2nd configuration. Since the application of pre-loads may affect the dynamic behavior of the system, all

analyses are repeated to see the effects. In this configuration, contact parameters are also slightly updated to k_t = 4.6 N/μm, k_n = 8.5 N/μm and μ = 0.8 for a better accuracy.

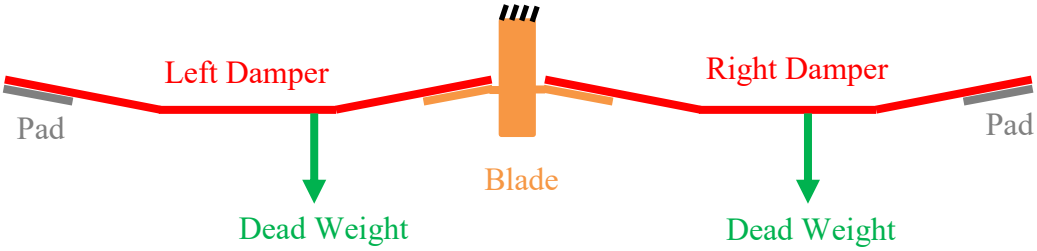

Figure 102: A simplified sketch of the 2nd configuration

Figure 103 shows the nonlinear responses for different excitation levels. The trend of the boundaries is similar to the one of the previous configuration, which shows that the position of the pre-loads on the damper does not sharply affect the computational response behavior. On the other hand, its effect is dominant on the contact forces, as shown in Figure 104. In particular, the computational normal load on the left damper changes considerably and the offset in the test data is almost captured with the static normal force corresponding to the upper boundary curve. It is also interesting to note that the variability range of the static tangential forces is perfectly captured on the left damper, while there is a small deviation for the right one. To compare the contact forces obtained also for the cases with the other excitation amplitudes, Figure 105 presents the results for 1 N forcing level. Unfortunately, the results are not as satisfactory as the 10 N case. The static components of the computational results are apparently distant from their experimental counterparts, and this implies that further tuning is needed to improve the accuracy.

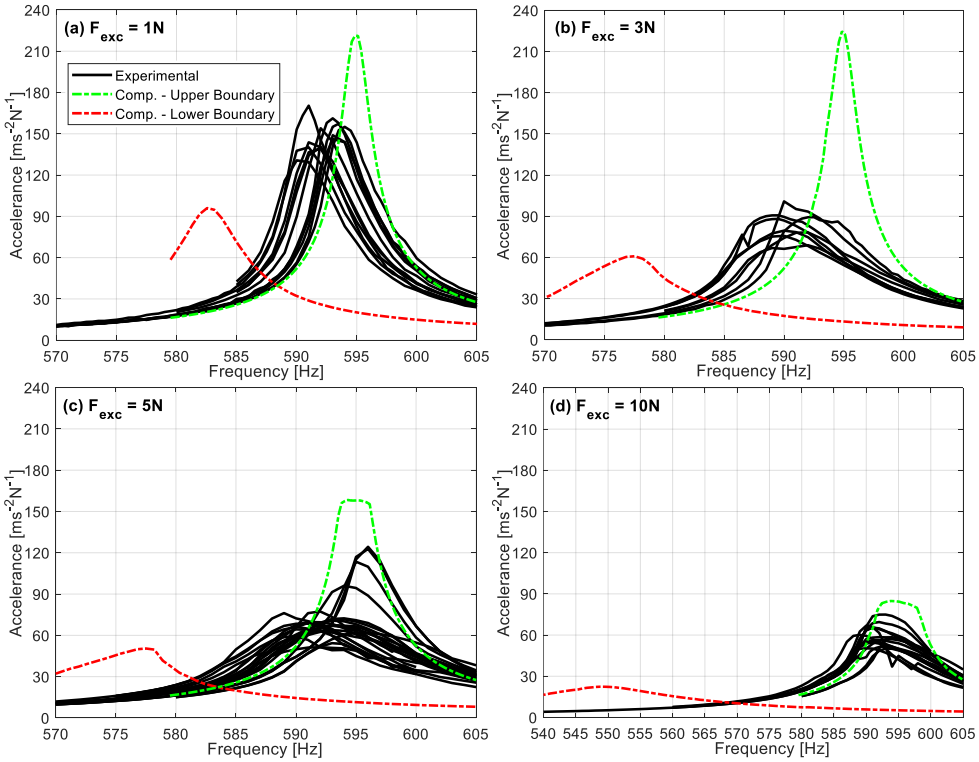

Figure 103: Nonlinear response variability and boundaries for the 2nd configuration

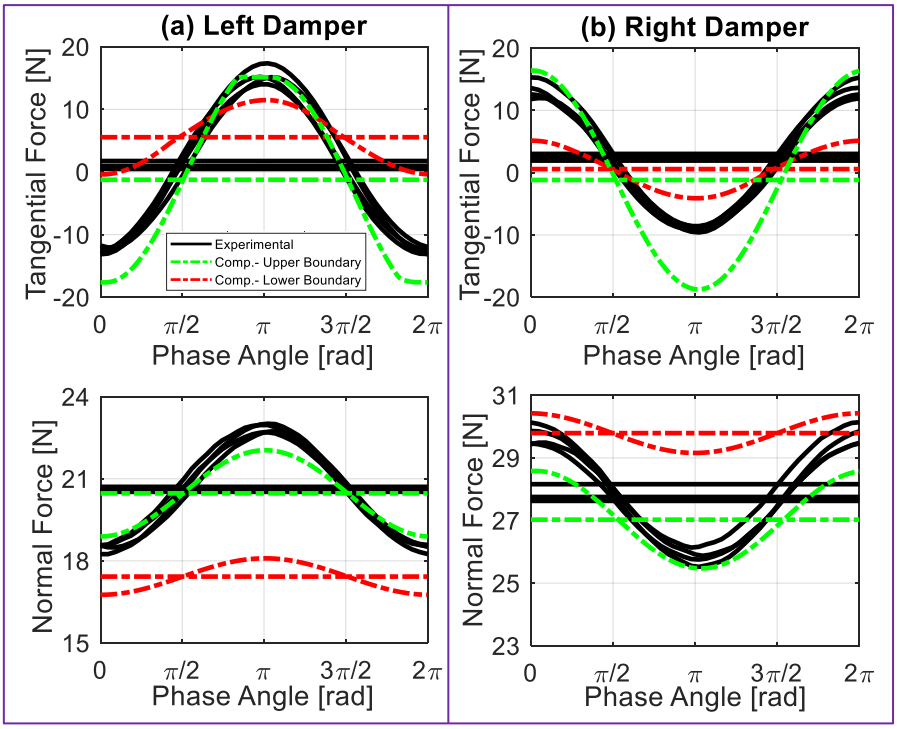

Figure 104: Contact force variability for the 2nd configuration (F_{exc} = 10 N)

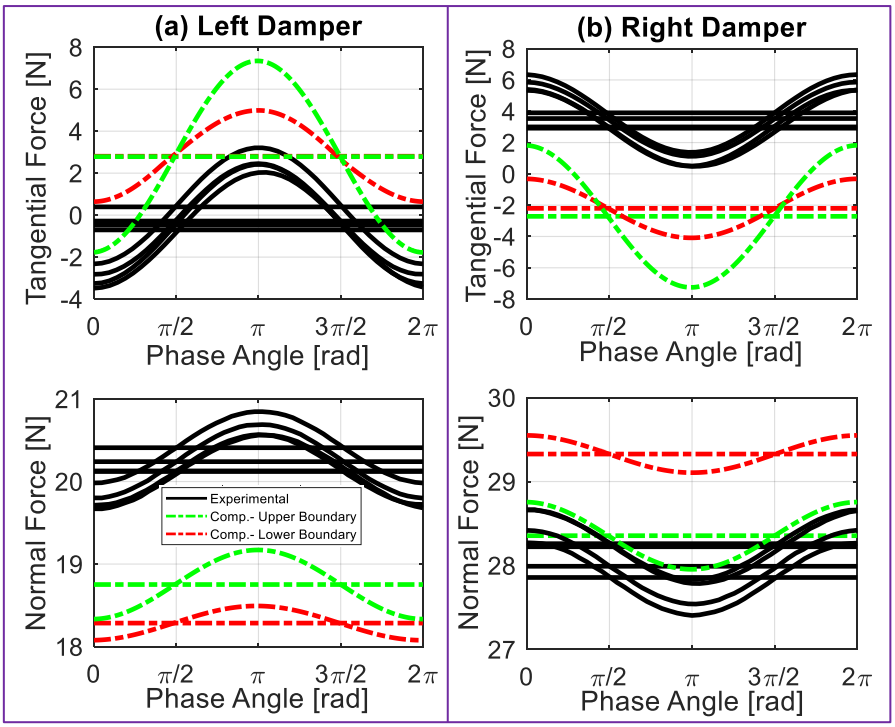

Figure 105: Contact force variability for the 2nd configuration (F_{exc} = 1 N)

Configuration 3:

In this configuration, the pre-loads on the dampers are inclined to better introduce the misalignment into the model and to match the results for all excitation cases. A sensitivity analysis is performed for the inclination angle and they are assigned as 3 and 5 degrees for the left and right dampers, respectively. The contact parameters are also kept the same of the previous case.

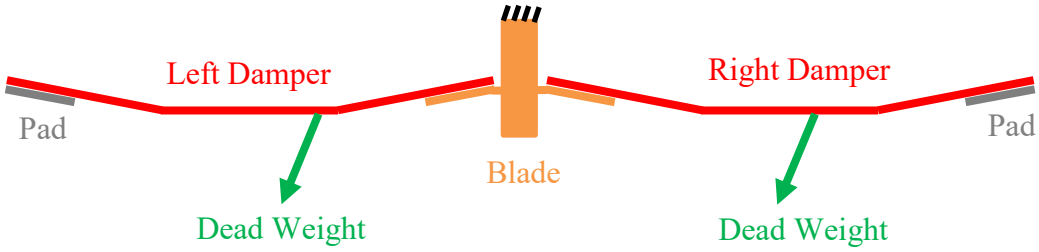

Figure 106: A simplified sketch of the 3rd configuration

Figure 107 illustrates the nonlinear response variability and boundaries for the 3rd configuration. Experimental curves are again successfully captured by the computationally obtained boundaries. Contact forces are also given in Figure 108 - Figure 111 for the increasing level of excitations. The results show that the dynamic amplitudes are in the same level order for all cases and the static tangential forces are bounded by the optimization algorithm, where small deviations are inevitably present. Nevertheless, they can be assumed negligible and the experimental and computational results are coherent. This shows that the misalignment is finally modeled in the third configuration with satisfactory results.

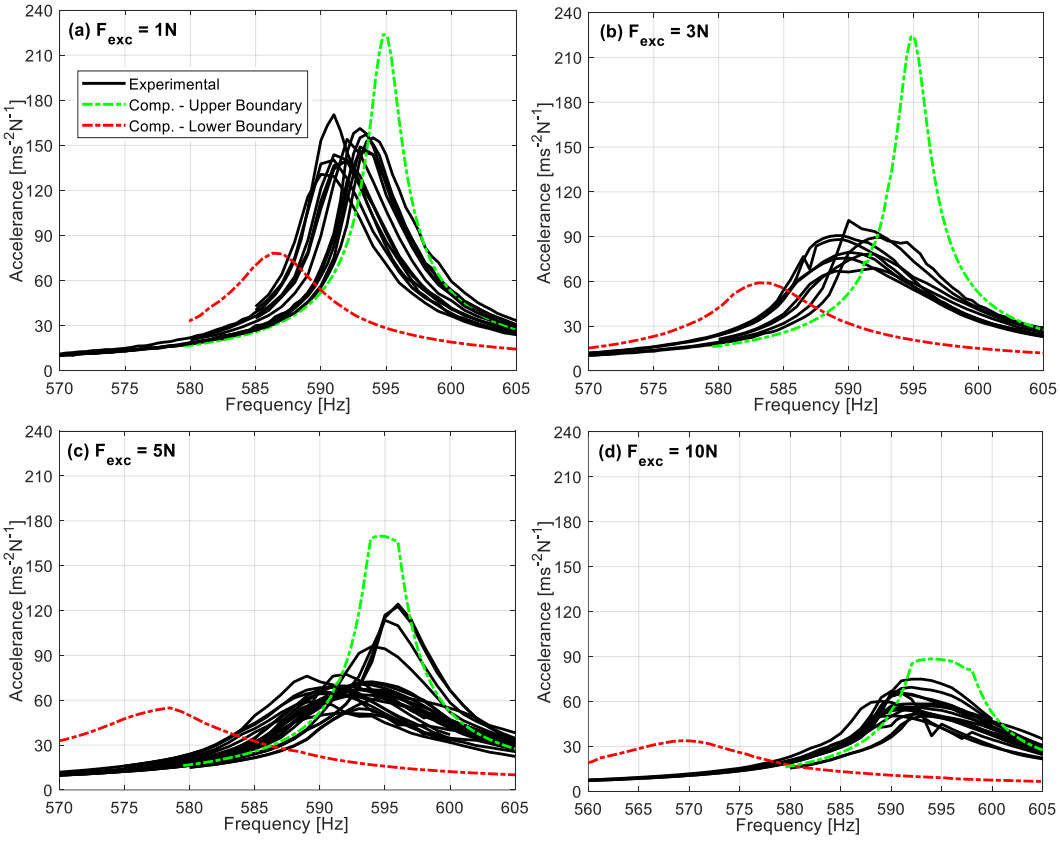

Figure 107: Nonlinear response variability and boundaries for the 3rd configuration

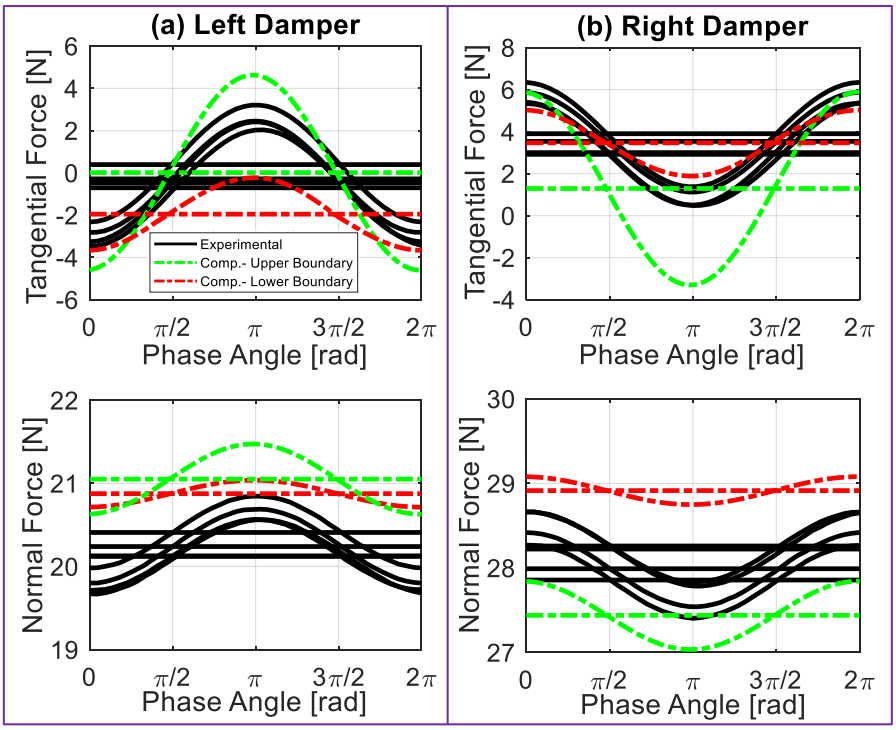

Figure 108: Contact force variability for the 3rd configuration (F_{exc} = 1 N)

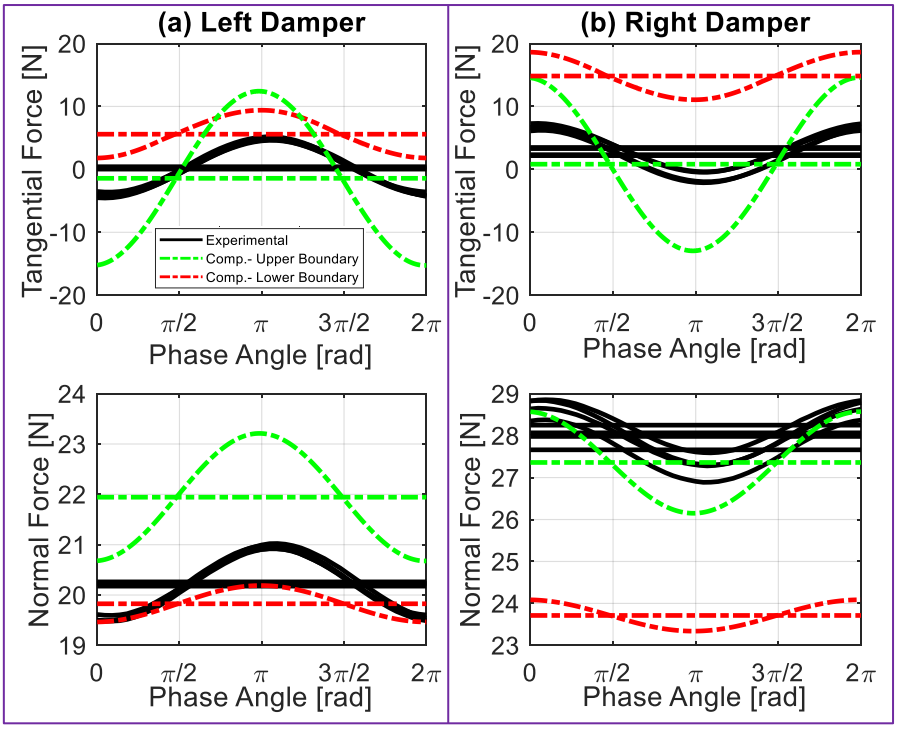

Figure 109: Contact force variability for the 3rd configuration (F_{exc} = 3 N)

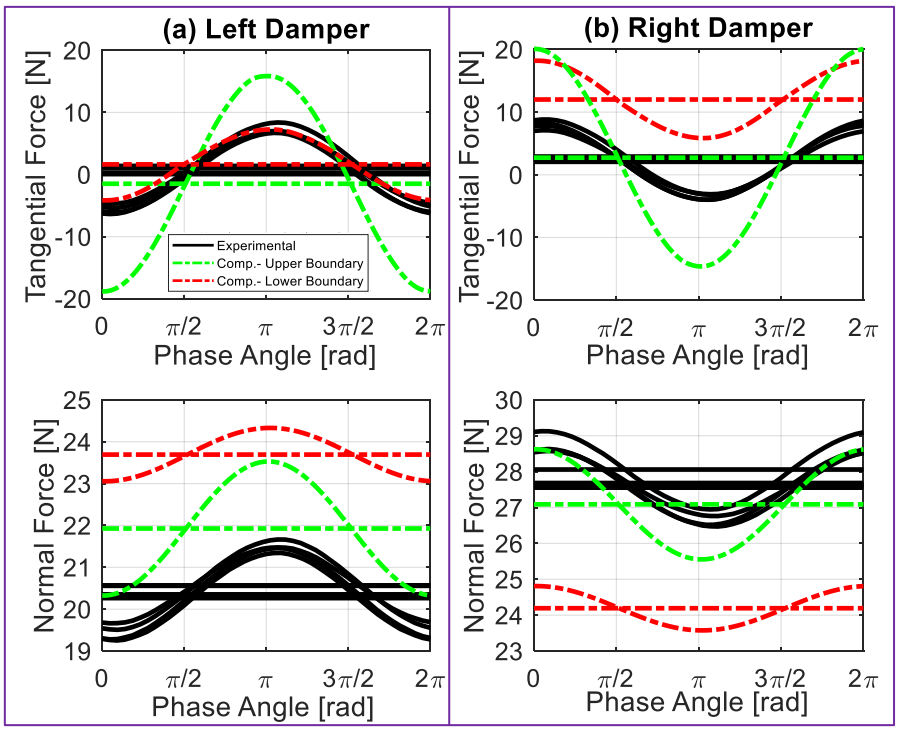

Figure 110: Contact force variability for the 3rd configuration (F_{exc} = 5 N)

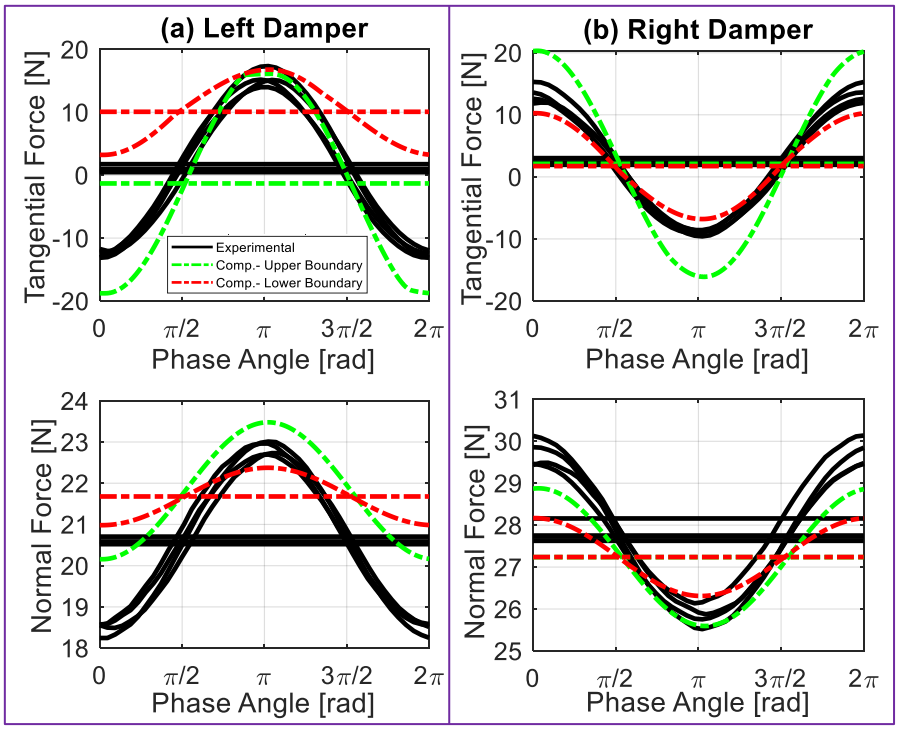

Figure 111: Contact force variability for the 3rd configuration (F_{exc} = 10 N)

Configuration 4:

To further enhance the accuracy of the results, the left damper is rotated as shown in Figure 112. This is modeled by introducing initial gaps into the contact elements. The defined value of the gaps is different for each contact points and it is linearly proportioned through the contact line. Different values of the rotation angle are assigned to check the effect of the damper rotation on the results and the case with 0.35 degree of rotation angle will be presented here. The contact parameters are kept same with the previous configuration.

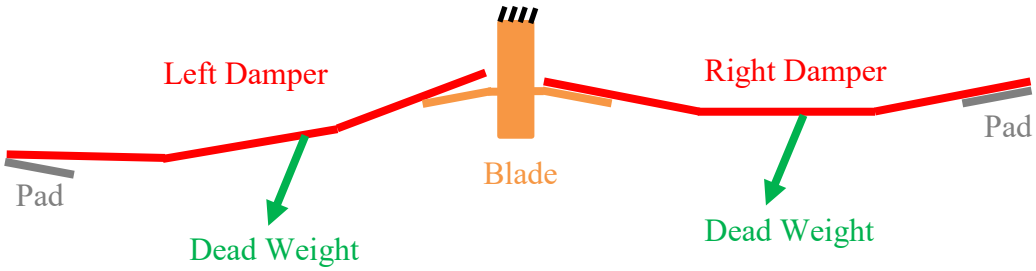

Figure 112: A simplified sketch of the 4th configuration

Figure 113 shows the nonlinear response curves for the 4th configuration. It is interesting to note that the resonance frequencies of the boundaries (including even the upper one) for the lower excitations are considerably lower than the experimental ones, while the one for 10 N excitation case is similar to the previous configurations. This is due to the full separation of some contact nodes, where the defined initial gap is relatively high and cannot be closed due to low vibration levels in the small excitation cases. The number of the fully separated contact points decreases with higher forcing levels, and more mating points come into contact correspondingly. This makes the resonance frequency of the upper boundary curve shift to right as can be seen from Figure 113a to Figure 113d. Since the nonlinearity level increases together with stick-slip-separation for higher excitations, the optimization algorithm struggles to find the minimum value of the loss factor, which results in jumping behavior of the upper boundary curves as shown in Figure 113c and Figure 113d. It should be noted that the algorithm converges even for jumping responses, but the value of the loss factor is not the global minimum in the system. Since the nonlinear responses do not match as expected, the contact forces are not given for this configuration.

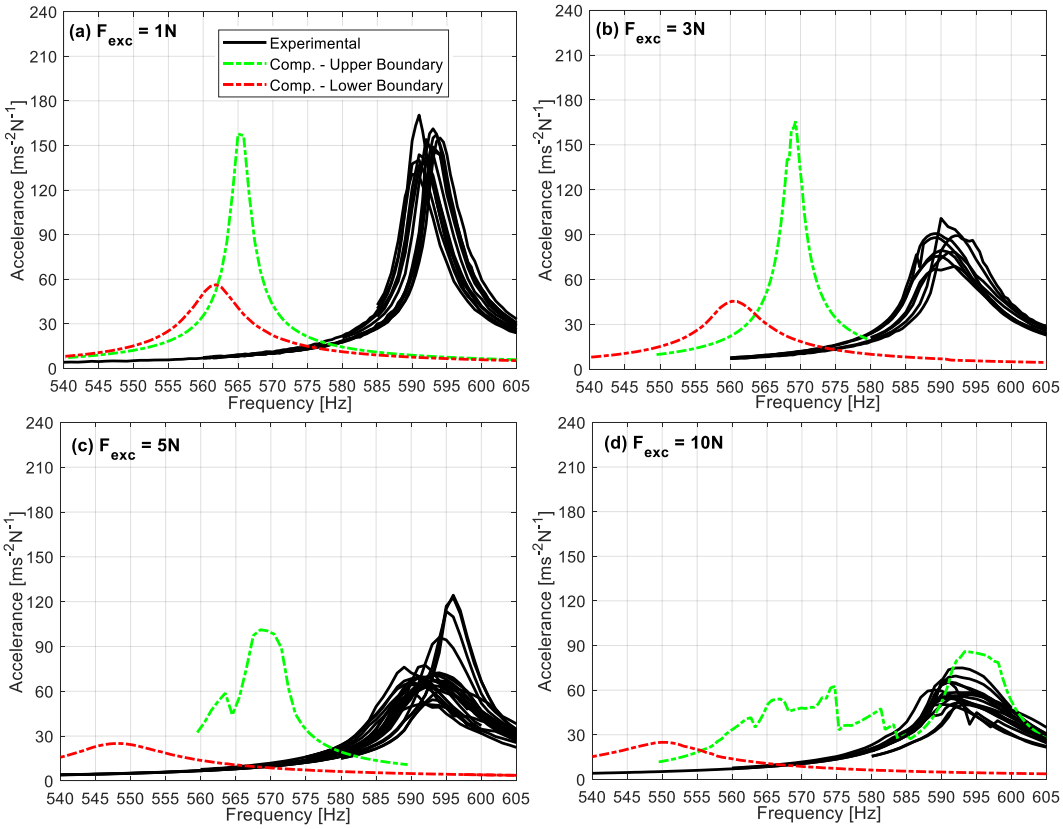

Figure 113: Nonlinear response variability and boundaries for the 4th configuration

Configuration 5:

The idea of rotating the damper is applied for the other direction, too, to check if the same behavior will be obtained (see Figure 114). The trend of the response is obtained similarly as shown in Figure 115. These results show that the further effort to model the misalignment with the rotation of the damper does not give satisfactory results, and the most consistent ones are obtained in the third configuration.

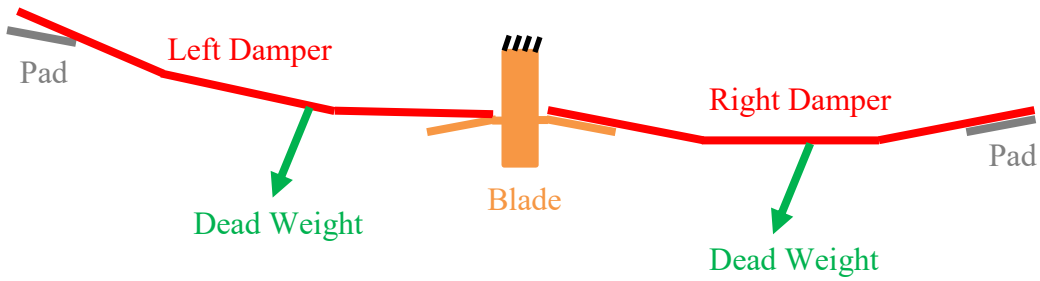

Figure 114: A simplified sketch of the 5th configuration

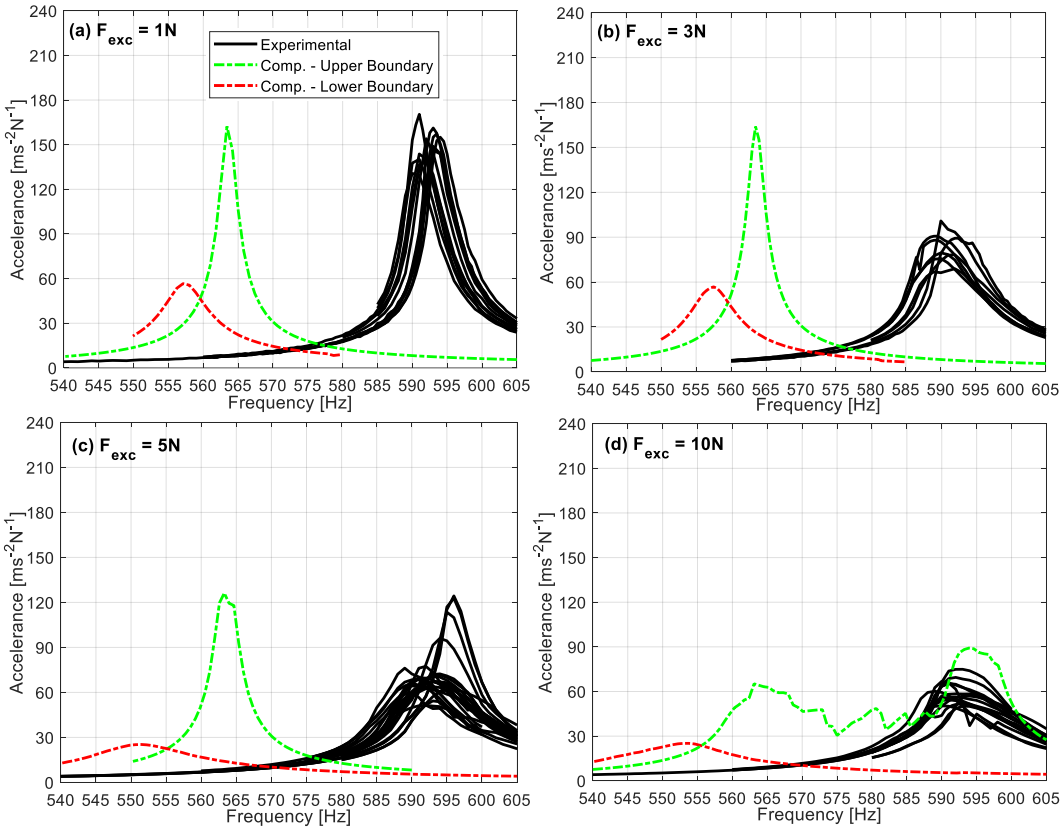

Figure 115: Nonlinear response variability and boundaries for the 5th configuration

- Manual Nonlinear Response Analyses

The predicted variability range in the third configuration successfully captures the experimentally obtained data with the calibrated contact parameters, which was the main objective of the current section. However, since the computational range is apparently larger than the experimental one, additional nonlinear response analyses are performed without using the optimization algorithm, to see if any curve can be obtained in between the boundaries. These analyses are called here as the manual analyses, where the initial guess of the multiplier coefficients is not a variable anymore and defined by the user. A considerable amount of manual analyses are performed; but, it is seen that the solver has severe convergence problems at the very first frequency point, unless the initial guess (at $t = t_{ini}$) for the tangential force is assigned as $T(t_{ini}) = k_t\, u(t_{ini})$. Here, u is the tangential relative displacement between the contact pairs. Convergence problem is directly related to the weak initial guesses of the response. As explained previously, in the determination of the lower boundary curve, full separation occurs at some of the contact nodes, while all the points are in contact for the

upper boundary case. The optimization algorithm successfully finds these configurations, since it perturbs the unknowns during the search of the minimum loss factor. However, the initial guesses assigned for the response in the manual analyses is the one obtained with the configuration of fully stuck linear case. Since contact points do not have a separation state in this configuration, the solver of the classical Newton-Raphson algorithm does not converge and cannot find variable results.

Figure 116 shows manually obtained nonlinear response for the 3rd configuration, in addition to the ones given in Figure 107. It is interesting to note that manually obtained curve is closer to the upper boundary. This is relevant; because, converged configuration of the manual analysis is the one where all points are in contact in the frictional surfaces. The manual analysis stays also within the range predicted by the optimization algorithm.

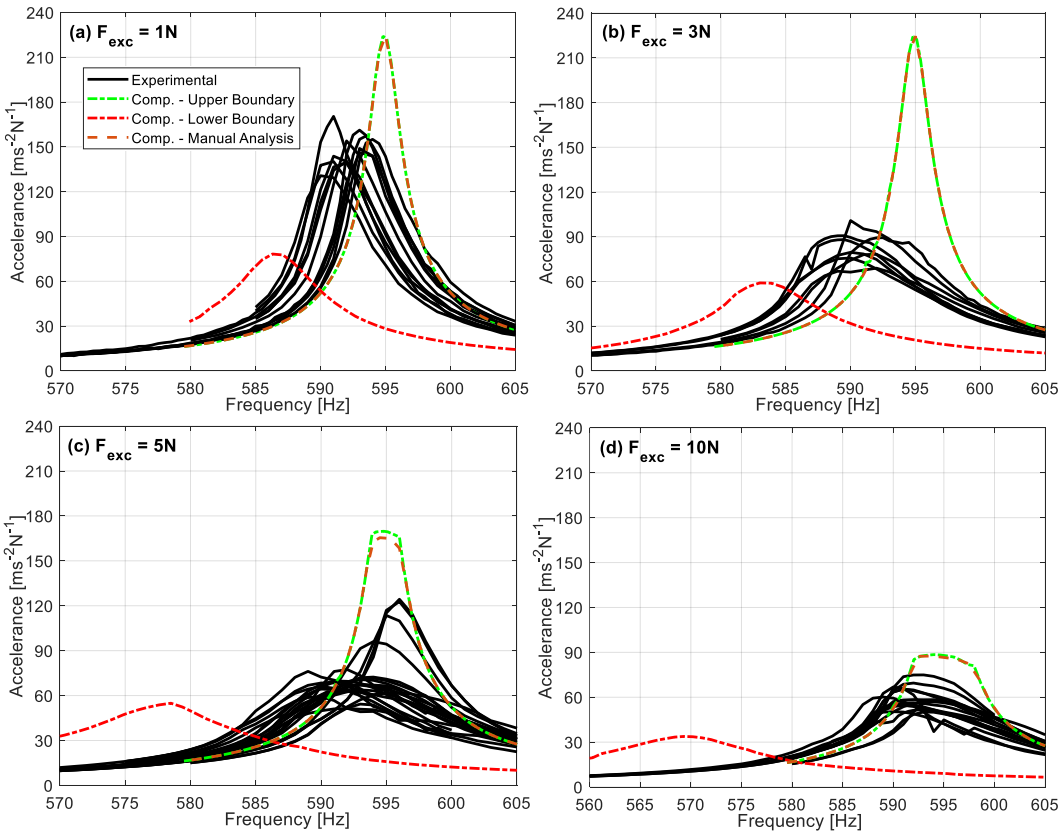

Figure 116: Nonlinear response variability together with the manual analysis

6.4 Summary

In this chapter, three topics are presented. The first one is the design of a novel test rig that consists of an academic turbine blade coupled with mid-span dampers. The components are originally designed and the experimental campaign allows the measurement of key features that enables the underlying kinematics of the non-uniqueness uncertainty. Secondly, experimental characterization is performed with purposely defined loading sequence, and several observations are made to explain the non-repeatability of the nonlinear response. It is shown that different static balances resulted by the non-unique static tangential forces creates the response variability range, even if all user controlled inputs are kept identical. The last part presents a thorough comparison between the computational and experimental results. The variability range obtained in the experiments is computationally predicted by using the developed method with the optimization algorithm. A tuning procedure to calibrate the contact parameters is conducted for the determination of the most accurate nonlinear response and contact force results. The performance of the developed method is shown with successfully captured ranges.

Chapter 7

Conclusions and Future Directions

7.1 Overview of the Thesis

The occurrence of friction is an unavoidable fact in engineering systems including contact interfaces. The friction is implemented even intentionally into turbine bladed disks to be able to suppress undesired stress and vibration levels. Together with its positive outcomes, a big challenge is also accepted in the modeling and simulations: uncertainties. In this thesis, the effects of one of these uncertainties on the dynamic behavior of turbine bladed disks coupled with contact interfaces are thoroughly investigated. In particular, the studied phenomenon is the non-uniqueness of friction forces, which create a variability range in the dynamic response amplitudes under the same nominal conditions. The brief overview of the thesis is given in the following.

The first step in the thesis is to develop a nonlinear solver that is capable of determining the nonlinear vibration response of turbine blades coupled with frictional interfaces. For this purpose, the harmonic balance methodology is used to convert the time domain differential equations to a set of nonlinear algebraic equations in frequency domain. Several techniques are applied before solving these equations to partially relieve the high computational burden. First, the algebraic equation set is derived only for the fundamental sector by utilizing the cyclic symmetry conditions. The reduced order model is then constructed by using the Craig-Bampton Component Mode Synthesis. Additional contribution to the solution speed is also supplied by the use of receptance notation and by re-

ordering the linear and nonlinear degrees-of-freedoms in the reduced order model. The final set of equations is solved by using the Newton-Raphson Method with Pseudo Arc-length Continuation. Once the solver is ready, the dissipation capability of a different type of dampers, the so-called mid-span dampers, designed for the steam turbines of Baker Hughes is studied. It is computationally shown that mid-span dampers efficiently reduce excessive vibration amplitudes. It was also interesting to note that the nonlinear response is non-unique and varies considerably in the simulations, even if all user-controlled inputs are kept same. It is inferred that the variability of the response is related to an uncertainty present in the contact forces.

To investigate the underlying kinematics of the variability phenomenon, a simple academic model that imitates a wedge damper pressed in between two turbine blades is constructed and studied. It is revealed that the non-unique static components of tangential forces for the fully stuck contact points changes the equivalent stiffness and damping capability of slipping points, which in turn enables the possibility of multiple responses. A numerical method is developed by utilizing limit tangential forces to estimate the response limits for wedge dampers modeled with macro slip contact elements at its each side. It is also shown that the range of non-unique responses is directly dependent to the damper geometry, where the range increases with more interaction between tangential and normal forces.

Such a variability range raises the interest of response boundaries, regardless of the system complexity. To meet this need, a new systematic approach is developed for realistic structures to determine the response boundaries. In this method, an optimization algorithm is used to minimize the system's loss factor. The performance of the method is computationally demonstrated on an academic turbine blade with contacts present in the shrouds and roots separately. It is shown that the method is satisfactorily capable of finding the response limits by minimizing the positive and negative values of the loss factor. Together with the superior performance of the method, numerical drawbacks are also presented. The method is then validated with an extensive experimental data obtained for a previously designed turbine blade coupled with under-platform dampers. It is shown that the method computationally captures the variability range obtained in the tests.

The next step was to develop a novel test rig to experimentally study the variability phenomenon. To this end, an academic turbine blade coupled with

mid-span dampers are originally designed and manufactured. A purposely defined loading sequence is applied in the tests to obtain non-unique responses. It is shown that multiple responses are due to different static balances resulted by the non-unique static tangential forces. The developed computational method is then challenged with the experimental data to estimate the boundaries of the response variability range. The tuning procedure of the contact parameters and the model is presented in detail. The comparison of the results revealed that the method predicts the response boundaries successfully once more.

7.2 Contributions to the Literature

The current study has several novel aspects that contribute to some open research area in the literature. These can be summarized as follows.

1- The dynamic response behavior of industrial steam turbines with mid-span dampers is shown by studying different resonance regions with several pre-loads and excitation levels. The coupled Harmonic Balance Method is utilized as the first time in the dynamic solution of mid-span dampers.

2- The thesis reveals the underlying kinematics of the non-unique tangential forces. It is shown how the uncertainty results in a variability range in the vibration response under the same nominal conditions. Even though this phenomenon has been previously studied in the literature, this thesis highlights its importance with different features taking place in the contact interfaces during vibration cycles.

3- Two novel numerical methods are proposed to determine the response boundaries of the variability range. The first approach is particularly developed for wedge dampers whose each side is modeled with macro slip elements, while the second one is a generalized approach for turbomachinery applications and utilizes an optimization algorithm to systematically detect the response limits regardless of the system complexity.

4- The developed method with the optimization algorithm is computationally demonstrated on turbine blades with different configurations of damping technologies and it is then experimentally validated on a turbine blade coupled with under-platform dampers. Here, the comparison of computational and experimental results is the first study performed in the literature within the context of non-unique contact forces.

5- A novel test setup with an academic turbine blade and mid-span dampers is developed to experimentally study the uncertainty phenomenon. The experimental campaign enables the investigation of the blade-damper interaction with its original features. Experimentally obtained variability range is then computationally predicted by utilizing the developed method. This study contributes to our understanding of the uncertainty phenomenon with a purposely designed experimental campaign.

7.3 Future Work

The observations made throughout the thesis bring impactful contributions to the literature as discussed in the previous section. The research area expanded with this thesis shall be carried further with the following points.

1- The developed optimization scheme is shown with numerically-calculated gradients. The analytical computation of jacobian and hessian matrices would relieve the high computational burden. Moreover, the use of a global optimization method may increase the robustness of the method. These subjects are candidates for the future research, which requires a sophisticated background in the nonlinear optimization field.

2- The developed optimization scheme can be applied to detect the boundaries of backbone curves. In this work, the first requirement is the development of a dedicated solver that is capable of directly determining the resonance response amplitudes of the system. Then, the optimization scheme can be implemented to this solver to track the maximum and minimum backbone curves. This approach would be highly relevant from the engineering point of view, since most of the attention is focused on the resonance vibration level during the design of turbine blades.

3- The developed optimization scheme can also be used to investigate how the boundaries change with fretting wear in the contacts. For this purpose, the wear algorithm would be correspondingly implemented into the developed method, which may further increase the computational burden.

4- Comparing the effects of the use of different contact elements on the response variability range would bring an impactful contribution to the literature. This work enables the application of the optimization scheme to predict the response boundaries, probably with different constraints. It also provides the

measurement of the performance of the developed method under different conditions.

5- The developed method can be used for an assessment of a mistuning problem. In the literature, the contact mistuning is mostly modeled by changing the value of contact stiffness in each blade. A different version of mistuning can be defined by using the uncertainty phenomenon in the static contact forces, and the optimization algorithm can be utilized to estimate the response boundaries of mistuned bladed disks.

References

Allara, M. (2009). A model for the characterization of friction contacts in turbine blades. *Journal of Sound and Vibration*, *320*(3), 527-544.

Botto, D., & Umer, M. (2018). A novel test rig to investigate under-platform damper dynamics. *Mechanical Systems and Signal Processing*, *100*, 344-359.

Botto, D., Gastadi, C., Gola, M. M., & Umer, M. (2018). An experimental investigation of the dynamics of a blade with two under-platform dampers. *Journal of Engineering for Gas Turbines and Power*, *140*(3).

Brake, M. R. W., Schwingshackl, C. W., & Reuß, P. (2019). Observations of variability and repeatability in jointed structures. *Mechanical Systems and Signal Processing*, *129*, 282-307.

Butlin, T., Ghaderi, P., Spelman, G., Midgley, W. J. B., & Umehara, R. (2019a). A novel method for predicting the response variability of friction-damped gas turbine blades. *Journal of Sound and Vibration*, *440*, 372-398.

Butlin, T., Spelman, G., Ghaderi, P., Midgley, W. J. B., & Umehara, R. (2019b). Predicting response bounds for friction-damped gas turbine blades with uncertain friction coupling. *Journal of Sound and Vibration*, *440*, 399-411.

Byrd, R. H., Hribar, M. E., & Nocedal, J. (1999). An interior point algorithm for large-scale nonlinear programming. *SIAM Journal on Optimization*, *9*(4), 877-900.

Byrd, R. H., Gilbert, J. C., & Nocedal, J. (2000). A trust region method based on interior point techniques for nonlinear programming. *Mathematical programming*, *89*(1), 149-185.

Cameron, T. M., & Griffin, J. H. (1989). An alternating frequency/time domain method for calculating the steady-state response of nonlinear dynamic systems. *Journal of Applied Mechanics*, *56(1)*, 149-154.

Chan, T. F., & Keller, H. B. (1982). Arc-length continuation and multigrid techniques for nonlinear elliptic eigenvalue problems. *SIAM Journal on Scientific and Statistical Computing*, *3*(2), 173-194.

Chen, J., Zang, C., Zhou, B., & Petrov, E. P. (2021). High-fidelity calculation of modal damping caused by friction at blade roots for single blades and tuned bladed disc assemblies. *Proceedings of the Institution of Mechanical Engineers, Part C: Journal of Mechanical Engineering Science*, *235*(15), 2810-2831.

Charleux, D., Gibert, C., Thouverez, F., & Dupeux, J. (2006). Numerical and experimental study of friction damping blade attachments of rotating bladed disks. *International Journal of Rotating Machinery*, *2006*.

Ciğeroğlu, E., & Özgüven, H. N. (2006). Nonlinear vibration analysis of bladed disks with dry friction dampers. *Journal of Sound and Vibration*, *295*(3-5), 1028-1043.

Cigeroglu, E., An, N., & Menq, C. H. (2009). Forced response prediction of constrained and unconstrained structures coupled through frictional contacts. *Journal of Engineering for Gas Turbines and Power*, *131*(2).

Claeys, M., Sinou, J. J., Lambelin, J. P., & Todeschini, R. (2016). Modal interactions due to friction in the nonlinear vibration response of the "Harmony" test structure: Experiments and simulations. *Journal of Sound and Vibration*, *376*, 131-148.

Cowles, B. A. (1996). High cycle fatigue in aircraft gas turbines—an industry perspective. *International Journal of Fracture*, *80*(2), 147-163.

Craig Jr, R. R., & Bampton, M. C. (1968). Coupling of substructures for dynamic analyses. *AIAA journal*, *6*(7), 1313-1319.

Denimal, E., Wong, C., Salles, L., & Pesaresi, L. (2021). On the Efficiency of a Conical Underplatform Damper for Turbines. *Journal of Engineering for Gas Turbines and Power*, *143*(2), 021020.

Drozdowski, R., Völker, L., Häfele, M., & Vogt, D. M. (2015). Experimental and numerical investigation of the nonlinear vibrational behavior of steam turbine last stage blades with friction bolt damping elements. In *Turbo*

Expo: Power for Land, Sea, and Air (Vol. 56796, p. V008T26A007). American Society of Mechanical Engineers.

Drozdowski, R., Völker, L., Häfele, M., & Vogt, D. M. (2016). Numerical and experimental analysis of low-pressure steam turbine blades coupled with lacing wire. *Proceedings of the Institution of Mechanical Engineers, Part A: Journal of Power and Energy*, *230*(3), 332-342.

Eriten, M., Polycarpou, A. A., & Bergman, L. A. (2011). Surface roughness effects on energy dissipation in fretting contact of nominally flat surfaces.

Ewins, D. J. (2010). Control of vibration and resonance in aero engines and rotating machinery–An overview. *International Journal of Pressure Vessels and Piping*, *87*(9), 504-510.

Firrone, C. M., Zucca, S., & Gola, M. M. (2011). The effect of underplatform dampers on the forced response of bladed disks by a coupled static/dynamic harmonic balance method. *International Journal of Non-Linear Mechanics*, *46*(2), 363-375.

Gastaldi, C., & Gola, M. M. (2015). An improved microslip model for variable normal loads. In *Proceedings of the 9th IFToMM International Conference on Rotor Dynamics* (pp. 169-179). Springer, Cham.

Gastaldi, C., & Gola, M. M. (2016a). On the relevance of a microslip contact model for under-platform dampers. *International Journal of Mechanical Sciences*, *115*, 145-156.

Gastaldi, C., & Gola, M. M. (2016b). Testing, simulating and understanding under-platform damper dynamics. In *ECCOMAS*.

Gastaldi, C. (2018). Modeling Friction for Turbomachinery Applications: Tuning Techniques and Adequacy Assessment of Heuristic Contact Models. *Contact and Fracture Mechanics*, 97.

Gastaldi, C., Gross, J., Scheel, M., Berruti, T. M., & Krack, M. (2021). Modeling complex contact conditions and their effect on blade dynamics. *Journal of Engineering for Gas Turbines and Power*, *143*(1), 011007.

Griffin, J. H. (1980). Friction damping of resonant stresses in gas turbine engine airfoils. *Journal of Engineering For Gas Turbines And Power*, *102*(2), 329-333.

Jaiswal, B. L., & Bhave, S. K. (1994). Experimental evaluation of damping in a bladed disk model. *Journal of sound and vibration*, *177*(1), 111-120.

Jamia, N., Jalali, H., Taghipour, J., Friswell, M. I., & Khodaparast, H. H. (2021). An equivalent model of a nonlinear bolted flange joint. *Mechanical Systems and Signal Processing*, *153*, 107507.

Janovský, V. (1981). Catastrophic features of Coulomb friction model. *The mathematics of finite elements and applications*, 259-264.

Jenkins, G. M. (1962). Analysis of the stress-strain relationships in reactor grade graphite. *British Journal of Applied Physics*, *13*(1), 30.

Klarbring, A. (1990). Examples of non-uniqueness and non-existence of solutions to quasistatic contact problems with friction. *Ingenieur-Archiv*, *60*(8), 529-541.

Krack, M., Salles, L., & Thouverez, F. (2017). Vibration prediction of bladed disks coupled by friction joints. *Archives of Computational Methods in Engineering*, *24*(3), 589-636.

Laxalde, D., Thouverez, F., & Lombard, J. P. (2010). Forced response analysis of integrally bladed disks with friction ring dampers. *Journal of Vibration and Acoustics*, *132*(1).

Lavella, M., & Botto, D. (2011). Fretting wear characterization by point contact of nickel superalloy interfaces. *Wear*, *271*(9-10), 1543-1551.

Menq, C. H., & Griffin, J. H. (1985). A comparison of transient and steady state finite element analyses of the forced response of a frictionally damped beam. *Journal of Vibration and Acoustics*, *107*(1), 19-25.

Menq, C. H., Griffin, J. H., & Bielak, J. (1986). The forced response of shrouded fan stages. *Journal of Vibration and Acoustics*, *108*(1), 50-55.

Mitra, M., Zucca, S., & Epureanu, B. I. (2016). Adaptive microslip projection for reduction of frictional and contact nonlinearities in shrouded blisks. *Journal of Computational and Nonlinear Dynamics*, *11*(4), 041016.

Mitsopoulou, E. N., & Doudoumis, I. N. (1987). A contribution to the analysis of unilateral contact problems with friction. *Solid Mechanics Archives*, *12*(3), 165-186.

Mulvihill, D. M., Kartal, M. E., Nowell, D., & Hills, D. A. (2011). An elastic–plastic asperity interaction model for sliding friction. *Tribology international*, *44*(12), 1679-1694.

Petrov, E. P. (2004). A method for use of cyclic symmetry properties in analysis of nonlinear multiharmonic vibrations of bladed disks. *Journal of Turbomachinery 126*(1), 175-183.

Petrov, E. P., & Ewins, D. J. (2003). Analytical formulation of friction interface elements for analysis of nonlinear multi-harmonic vibrations of bladed disks. *Journal of Turbomachinery*, *125*(2), 364-371.

Petrov, E. P., & Ewins, D. J. (2006). Effects of damping and varying contact area at blade-disk joints in forced response analysis of bladed disk assemblies. *Journal of Turbomachinery*, *128*(2), 403-410.

Panning, L., Popp, K., Sextro, W., Götting, F., Kayser, A., & Wolter, I. (2004). Asymmetrical underplatform dampers in gas turbine bladings: theory and application. In *Turbo Expo: Power for Land, Sea, and Air* (Vol. 41715, pp. 269-280).

Pesaresi, L., Salles, L., Jones, A., Green, J. S., & Schwingshackl, C. W. (2017). Modelling the nonlinear behaviour of an underplatform damper test rig for turbine applications. *Mechanical Systems and Signal Processing*, *85*, 662-679.

Sanliturk, K. Y., Ewins, D. J., & Stanbridge, A. B. (2001). Underplatform dampers for turbine blades: theoretical modeling, analysis, and comparison with experimental data. *Journal of Engineering For Gas Turbines And Power*, *123*(4), 919-929.

Schwingshackl, C. W., Petrov, E. P., & Ewins, D. J. (2012). Measured and estimated friction interface parameters in a nonlinear dynamic analysis. *Mechanical Systems and Signal Processing*, *28*, 574-584.

Seinturier, E. (2007). Forced response computation for bladed disks industrial practices and advanced methods. *Lecture Series-Von Karman Institute For Fluid Dynamics*, *2*, 5.

Sever, I. A., Petrov, E. P., & Ewins, D. J. (2008). Experimental and numerical investigation of rotating bladed disk forced response using underplatform friction dampers. *Journal of engineering for gas turbines and power*, *130*(4).

Siewert, C., Panning, L., Gerber, C., & Masserey, P. A. (2008). Numerical and experimental damping prediction of a nonlinearly coupled low pressure steam turbine blading. In *Turbo Expo: Power for Land, Sea, and Air* (Vol. 43154, pp. 531-542).

Siewert, C., Panning, L., Wallaschek, J., & Richter, C. (2010). Multiharmonic forced response analysis of a turbine blading coupled by nonlinear contact forces. *Journal of Engineering for Gas Turbines and Power*, *132*(8).

Siewert, C., Sieverding, F., McDonald, W. J., Kumar, M., & McCracken, J. R. (2017). Development of a Last Stage Blade Row Coupled by Damping Elements: Numerical Assessment of Its Vibrational Behavior and Its Experimental Validation During Spin Pit Measurements. In *Turbo Expo: Power for Land, Sea, and Air* (Vol. 50954, p. V008T29A018). American Society of Mechanical Engineers.

Srinivasan, A. (1997). Flutter and resonant vibration characteristics of engine blades. *Journal of Engineering For Gas Turbines And Power*, *119*(4), 742-775.

Stender, M., Jahn, M., Hoffmann, N., & Wallaschek, J. (2020). Hyperchaos co-existing with periodic orbits in a frictional oscillator. *Journal of Sound and Vibration*, *472*, 115203.

Stingl, B., Ciavarella, M., & Hoffmann, N. (2013). Frictional dissipation in elastically dissimilar oscillating Hertzian contacts. *International Journal of Mechanical Sciences*, *72*, 55-62.

Szwedowicz, J., Secall-Wimmel, T., & Dünck-Kerst, P. (2008). Damping performance of axial turbine stages with loosely assembled friction bolts: The nonlinear dynamic assessment. *Journal of Engineering for Gas Turbines and Power*, *130*(3).

Tang, W., & Epureanu, B. I. (2017). Nonlinear dynamics of mistuned bladed disks with ring dampers. *International Journal of Non-Linear Mechanics*, *97*, 30-40.

Voldřich, J., Lazar, J., & Polach, P. (2015). Nonlinear Vibration Analysis of Steam Turbine Rotating Wheel Equipped with the LSB48 Blades. In *Proceedings of The 14th IFToMM World Congress, Taipei, doi* (Vol. 10).

Yamashita, Y., Shiohata, K., Kudo, T., & Yoda, H. (2012). Vibration characteristics of a continuous cover blade structure with friction contact surfaces of a steam turbine. In *10th International Conference on Vibrations in Rotating Machinery* (pp. 323-332).

Yang, B. D. (1996). *Contact kinematics of friction interfaces and applications to the prediction of resonant response of frictionally constrained turbine blades*. PhD Thesis, The Ohio State University.

Yang, B. D., & Menq, C. H. (1998a). Characterization of contact kinematics and application to the design of wedge dampers in turbomachinery blading: Part 1—Stick-slip contact kinematics. *Journal of Engineering For Gas Turbines And Power*, *120*(2), 410-417.

Yang, B. D., & Menq, C. H. (1998b). Characterization of contact kinematics and application to the design of wedge dampers in turbomachinery blading: part 2—prediction of forced response and experimental verification. . *Journal of Engineering For Gas Turbines And Power*, *120*(2), 418-423.

Yuan, J., Fantetti, A., Denimal, E., Bhatnagar, S., Pesaresi, L., Schwingshackl, C., & Salles, L. (2021). Propagation of friction parameter uncertainties in the nonlinear dynamic response of turbine blades with underplatform dampers. *Mechanical Systems and Signal Processing*, *156*, 107673.

Zucca, S., Berruti, T., & Cosi, L. (2016). Experimental and numerical investigations on the dynamic response of turbine blades with tip pin

dampers. In *Journal of Physics: Conference Series* (Vol. 744, No. 1, p. 012131). IOP Publishing.

Zucca, S., Botto, D., & Gola, M. M. (2008). Range of variability in the dynamics of semi-cylindrical friction dampers for turbine blades. In *Turbo Expo: Power for Land, Sea, and Air* (Vol. 43154, pp. 519-529).

Zucca, S., Firrone, C. M., & Gola, M. (2013). Modeling underplatform dampers for turbine blades: a refined approach in the frequency domain. *Journal of Vibration and Control*, *19*(7), 1087-1102.

Zucca, S., & Firrone, C. M. (2014). Nonlinear dynamics of mechanical systems with friction contacts: coupled static and dynamic multi-harmonic balance method and multiple solutions. *Journal of Sound and Vibration*, *333*(3), 916-926.